UNIVERSITY OF SOUTHAMPTON
Natural and Environmental Sciences
School of Chemistry

STUDIES OF THE CORROSION OF MATERIALS FOR BIPOLAR PLATES IN FUEL CELLS

by
Alicja Juskowiak-Brenska

Thesis for the degree of Doctor of Philosophy

August 2011

Abstract

Studies were undertaken to investigate the corrosion processes of materials for metal bipolar plates in fuel cells based on a poly(benzimidazole) membrane filled with H_3PO_4.

In addition to mild steel, stainless steel, nickel, electroplated Ni and Ni/graphite, the focus was on Ni-Cr alloys and the influence of composition on the rate of corrosion. The medium chosen was phosphoric acid pH 2 at 353 K and a potential of + 100 mV was considered in order to mimic the conditions at an oxygen cathode in a fuel cell. Stainless steel showed good corrosion resistance but was considered too expensive. Mild steel corroded rapidly and although a Ni electroplate lowered the corrosion rate its performance was insufficient. The graphite in the coating was necessary to reduce the contact resistance of the bipolar plate with the electrocatalyst layer.

The replacement of the Ni layer by a NiCr layer was therefore studied.

The quality of Ni and Ni/C electroplates was determined by AC impedance in H_2SO_4 at 293K. Nyquist plots showed semi-circles from which the corrosion resistance was easily determined. Layers with thickness > 3 μm showed corrosion resistances similar to bulk Ni but those < 1 μm showed very high corrosion rates indicating pits and corrosion of the underlying mild steel.

The corrosion of the Ni-Cr alloys was investigated using (a) commercial, bulk materials and (b) a high throughput technique whereby a wedge modification of physical vapour deposition was used to produce 10 x 10 arrays of electrodes with variable composition – the voltammetry at all 100 electrodes was then recorded simultaneously. Small additions of Cr to Ni led to a large drop in the rate of corrosion but it is shown that the microstructure of the alloy, determined by electron microscopy and X-ray diffraction, can be as important as the composition.

Contents **Page**

List of Symbols

C_{dl}	Double layer capacitance
d	Lattice plane spacing
E	experimental potential vs. reference electrode
E_e	Equilibrium potential for a couple vs. reference electrode
E_e^0	Equilibrium potential when $c_O=c_R$
ΔE	Equilibrium cell voltage
E_{corr}	Corrosion potential
F	The Farraday constant
f	Frequency of AC impedance
IR	The voltage drop across the electrolyte
I	Current
j	Current density
j_o	Exchange current density
j_c	Partial cathodic current
j_a	Partial anodic current
j_{corr}	Corrosion current
α	Transfer coefficient
α_a	Anodic transfer coefficient
α_c	Cathodic transfer coefficient
M	Molecular weight
n	Number of electron or reflection
η	Overpotential
η_a	Anodic overpotential
η_c	Cathodic overpotential
λ	Wavelenght
R	Gas constant or resistance
R_u	Uncompensated resistance between working and reference electrode
R_{ct}	Contact resistance
θ	Angle of reflection
T	Temperature
t	Time
V_{cell}	Cell voltage
Z	Impedance
ω	Maximum of frequency

Acknowledgements

I would like to express my gratitude to my supervisor Professor Derek Pletcher for his invaluable suggestions, guidance and encouragement that helped me in all the time of my research. I would like to thank Professor Frank Walsh who has supported and given new ideas. Also I would like to thank Professor Andrea E. Russell for many helpful comments and motivation.

I am especially grateful to all members of the group: Maria, Clelia, Hartini and Jacek.

I would like to express my heartfelt thanks to Professor Brian Hayden, Dr. Alexandros Anastasopoulos, Tallal Aljohani, and Jacek Lapinski who have prepared samples.

I do thank all University staff for all the help and rendering during my study.

I gratefully acknowledge the financial support from Corus.

Special thanks to all my friends: Michal, Magda, Agnieszka, Ola and Angie for their constant support and kindness. Most especially to my family, and dear husband, Karol whose patient love enabled me to completed this work.

Declaration of Authorship

I, Alicja Juskowiak-Brenska

declare that the thesis entitled

Studies of the Corrosion of Materials for Bipolar Plates in Fuel Cells

and the work presented in the thesis are both my own, and have been generated by me as the results of my own original research. I confirm that:

- this work was done wholly or mainly while in candidature for a research degree at this University;
- where any part of this thesis has previously been submitted for a degree or any other qualification at this University or any other institution, this has been clear stated;
- where I have consulted the published work of others, this is always clearly attributed;
- where I have quoted from the work of others, the source is always given. With the exception of such quotations, this thesis is entirely my own work;
- I have acknowledged all main sources of help;
- where the thesis is based on work done by myself jointly with others, I have made clear exactly what was done by others and what I have contributed myself;
- None of this work has been published before submission, or [delete as appropriate] parts of this work have been published as: [please list references]

Signed:……...

Date:……..

Chapter 1

Introduction

1.1 Fuel cells

Fuel cells [1-9] are capable of contributing in several ways to an energy economy that is sustainable and compatible with our environment. Alongside solar and wind energies, bio fuels, natural gas, hydroelectric power, fuel cells can provide clean energy and play

a major role in the solution to a whole range of green challenges, such as global warming and harmful effects of local pollutants, for instance those from cars in the urban environment. Fuel cells may also be able to provide economic benefits due to their high efficiency, low noise and being environmentally friendly [10-13]. Fuel cells can produce energy from a few W to hundreds of kW, depending upon their size and the application. They can be used as power supplies in buses, boats, cars, laptops, mobiles etc. Before fuel cell powered vehicles will become common, however, it is essential to reduce the cost and to miniaturise components.

Fuel cells are classified by the electrolyte contacting the two electrodes [14]. Also the electrolyte determines the operating temperature and structure/materials for the fabrication of the fuel cell. Five types of fuel cell have been under development: phosphoric acid fuel cell (PAFC), solid oxide fuel cell (SOFC), molten carbonate fuel cell (MCFC), alkaline fuel cell (AFC) and proton exchange membrane fuel cell (PEM). The first successful application of fuel cell was achieved by alkaline fuel cell used in NASA Apollo space programme. Figure 1.1 presents a photograph of fuel cell stack from laboratories in the University of Southampton.

A key performance measure of a fuel cell is the voltage output, as a function of the current density drawn, ie. the polarization curve as presented in Figure 1.2. The Power of the fuel cell can be calculated:

$$\text{Power} = I \cdot V_{cell} \tag{1.1}$$

The cell voltage is given by

$$V_{cell} = \Delta E_e - IR - \eta_c - \eta_a \tag{1.2}$$

Where: ΔE_e – is the equilibrium cell voltage, η_c- cathodic overpotential, η_a- anodic overpotential, and IR –the voltage drop across the electrolyte.

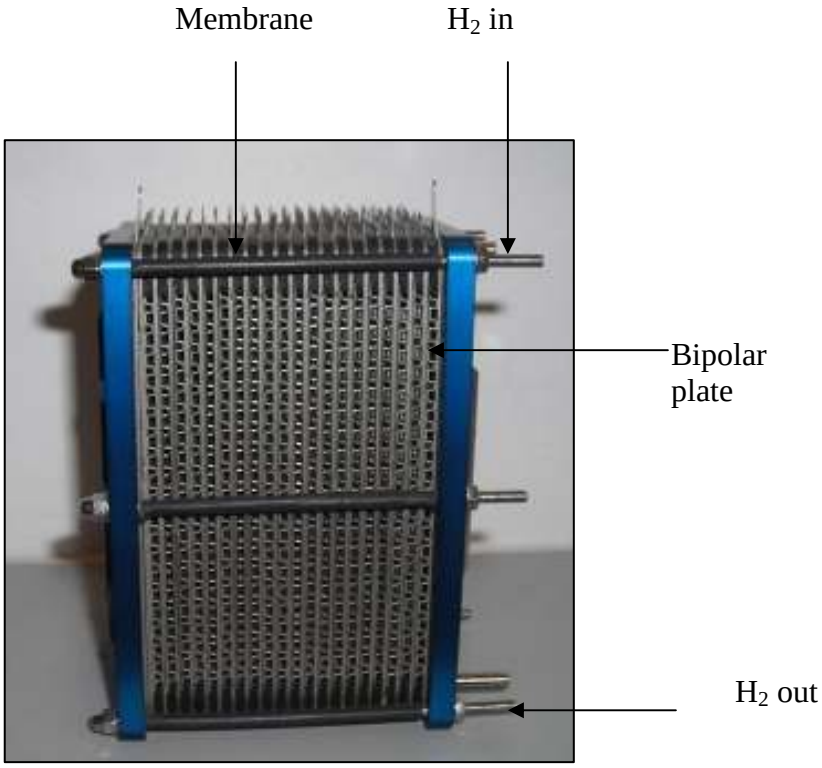

Figure 1.1 *Fuel cell stack.*

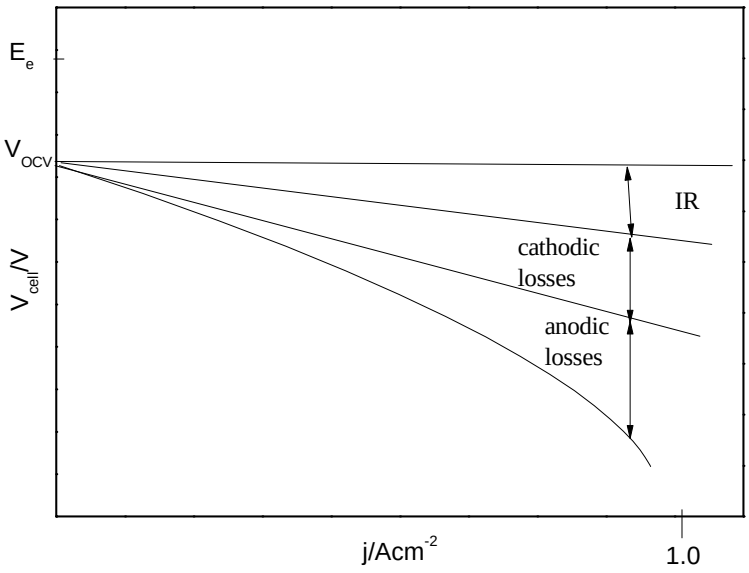

Figure 1.2 *Power density curves of fuel cell* [6].

1.2 PEM H_2/O_2 Fuel Cells

In a PEM fuel cell, hydrogen and oxygen are converted directly to electricity with only one chemical product – water. Hence it is a clean energy source with zero-emissions and operated in the low temperature range 85-105ºC. It is a most promising energy source [1-3, 15], particularly for portable applications.

A PEM fuel cell consists of a membrane, catalyst layers and bipolar plates. The fuel is hydrogen and hydrogen ions pass through the membrane and reach the cathode side, where they are consumed in the reduction of oxygen to produce water [4, 6, and 14]:

$$\text{Anode side} \qquad 2H_2 \rightarrow 4H^+ + 4e^- \qquad (1.3)$$

$$\text{Cathode side} \qquad O_2 + 4H^+ + 4e^- \rightarrow 2H_2O \qquad (1.4)$$

$$\text{Overall} \qquad O_2 + 2H_2 \rightarrow 2H_2O + \text{electricity} \qquad (1.5)$$

Figure 1.2.1 presents a picture of a PEM fuel cell to show the components.

The function of the membrane is to separate the H_2 and O_2 reactants and to provide a medium for proton transport from anode to cathode. The membrane [16] is often considered to be the heart of a PEM fuel cell. The most common membrane used in PEM systems is Nafion^{TM} (produced by DuPont), because of its chemical, mechanical and thermal stability. Nafion^{TM} functions at temperatures below - 353 K. At temperatures above 353 K Nafion dehydrates and loses conductivity. There are now a number of alternative membrane polymers as well as materials working at higher temperature - for such conditions poly-benzimidazole (PBI) doped with phosphoric acid is a common choice of membrane.

Two membrane structures are shown in figure 1.2.2.

a)

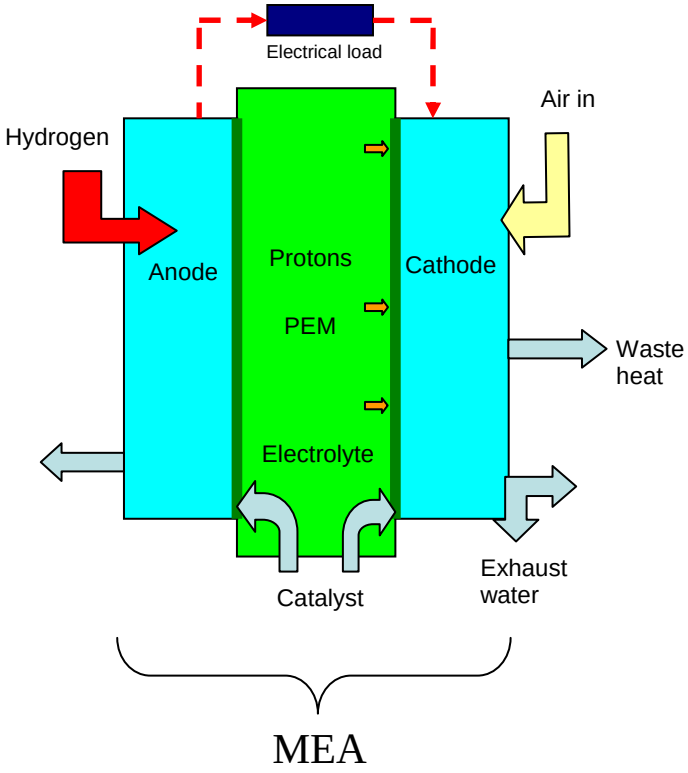

b)

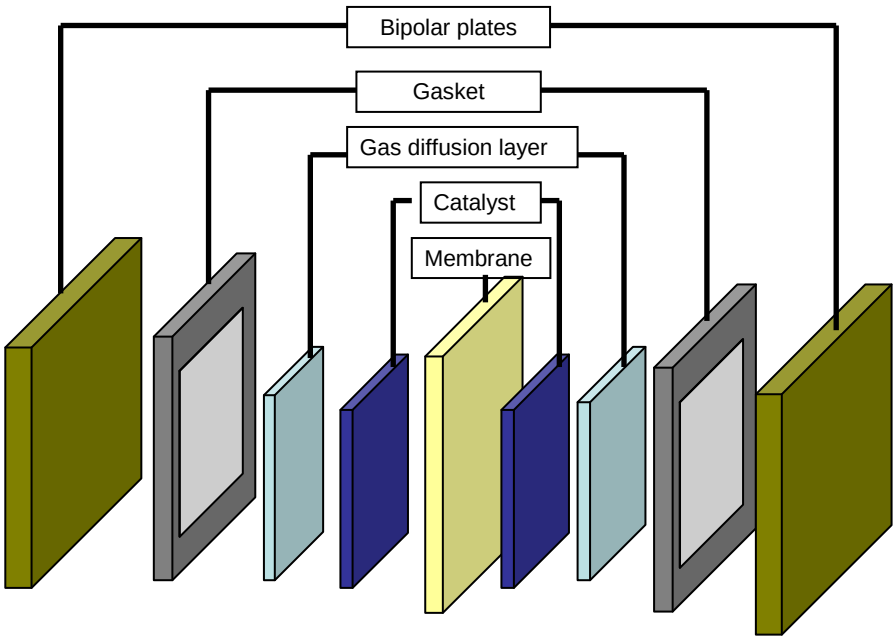

Figure 1.2.1 *Scheme of fuel cell stack a) graphical explanation, b) the components of the single PEM fuel cell.*

a)

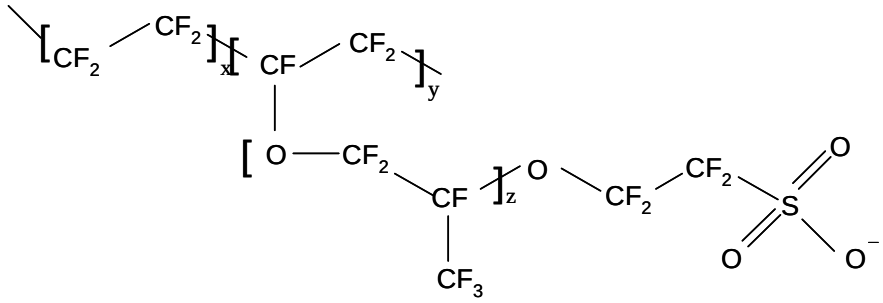

x =5 - 15
y = 600 - 1500
z = 1- 3

b)

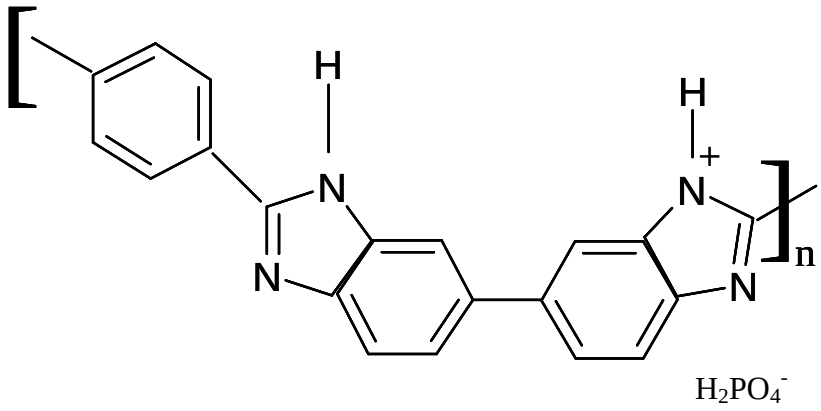

Figure 1.2.2 *Chemical structure of Nafion and poly-benzimidazole (PBI).*

1.2.1 Bipolar plates

The voltage and power output of a single fuel cell is usually too low to be useful. Therefore a series of cells is usually arranged in series within a stack where the electrical connection between cells is made by a bipolar plate. In the stack, the cells need to be 'chemically' isolated from their neighbours but electrically connected. This separation is achieved with a bipolar plate. Thus bipolar plates have two key functions:

(a) Separation of gases H_2 and O_2 in neighbouring cells

(b) Electrical pathway between neighbouring cells and must have a very low resistance.

They also serve to remove the excess heat from the stack. Figure 1.2.1.1 presents a sketch of a PEM fuel cell stack showing the bipolar plates.

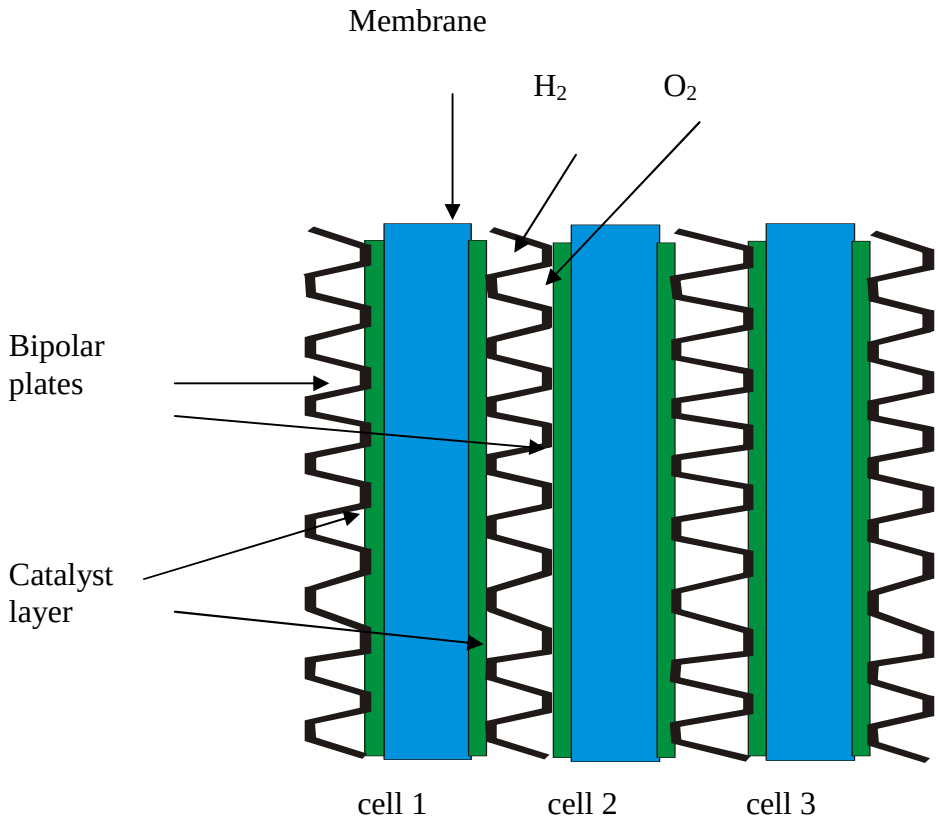

Figure 1.2.1.1 *Sketch of a fuel cell stack with segregation of neighbouring cells by bipolar plates.*

The bipolar plates serve [5] to distribute the fuel gas and air uniformly over the active areas as well as to remove heat from the active area, conduct current from cell to cell, and prevent leakage of gases and coolant and separating individual cells in the stack. Figure 1.2.1.2 presents some examples of the channel designs within the bipolar plate tested in fuel cell design.

Figure 1.2.1.2 *Examples of metallic bipolar plate with different shapes and flow channels.*

Bipolar plates operate in an environment where corrosion is probable. The environment is likely to be acidic. One side is exposed to reducing gas (H_2) at a potential where active corrosion is likely, while the other is exposed to an oxidising gas (O_2) at even more positive potentials. Corrosion of the bipolar plate could lead a) loss of material integrity,

b) an increase in contact resistance c) poisoning of the polymer electrolyte by products of corrosion. Poisoning [17] of the membrane is a particular problem with metallic bipolar plates. Metal ions poison the membrane and adversely influence the cell performance.

Therefore, a bipolar plate must have a high resistance to chemical and electrochemical corrosion. These factors limit the materials that can be used for bipolar plates (see figure 1.2.1.3); the possibilities are limited to non-porous graphite and carbon, composites and metals. Conventionally, non-porous graphitic carbon is the most commonly used bipolar plate material because of its high stability and

conductivity [18] and excellent resistance to corrosion. The disadvantages of carbon plates are the cost of fabricating the channel network essential to the operation of the bipolar plate, brittleness and weight. Because of its brittle nature, graphite bipolar plate cannot be made very thin and usually have a thickness of few millimetres.

Metals are very good candidates for bipolar plates, because of their conductivity and mechanical properties that permit manufacture from thin sheet or foil. The limitation of metallic plates is, however, corrosion leading to multivalent cations that increase the resistance of the membrane and therefore lower power output of the cell.

Examples of pure metals that have been examined as bipolar plates are Ni, Al, Ti. Also very attractive are steels and other metal alloys. Stainless steels (especially SS 316 L) have been widely used for bipolar plates. Many authors have presented data to show the long term stability to corrosion of stainless steel [19-22]. In an acid environment stainless steels passivate but the effect of passivation of the surface is to increase the contact resistance and thereby reduce fuel cell efficiently. Stainless steels are also expensive.

Wang et al. [23] studied the influence of Cr additions in stainless steels, and came to the simple conclusion that steels with higher Cr content presented better corrosion resistance. Wind et al. [13] concluded that Fe and Ni atoms dissolve to form ions in solution while Cr atoms lead to a passivating layer. Also a similar behaviour of Cr was reported by Lee et al [4] for stainless steel ~ 70 % of Fe, 18% Cr and 12 % Ni. In acidic environment both Ni and Fe oxides are unstable and corrode very fast, while Cr very rapidly became covered by oxide.

Amongst the various methods developed to fabricate metallic plates can be included machining, die casting, stamping, electroforming, stretch forming, powder metal forming, hydroforming and wire bonding (see figure 1.2.1.4).

Several authors have investigated the reduction of the contact resistance of metallic bipolar plates various types of treatments and surface coatings [24-27]. The coatings of metallic bipolar plates should avoid defects such as pinholes which can create corrosion and metallic ions poisoning the membrane.

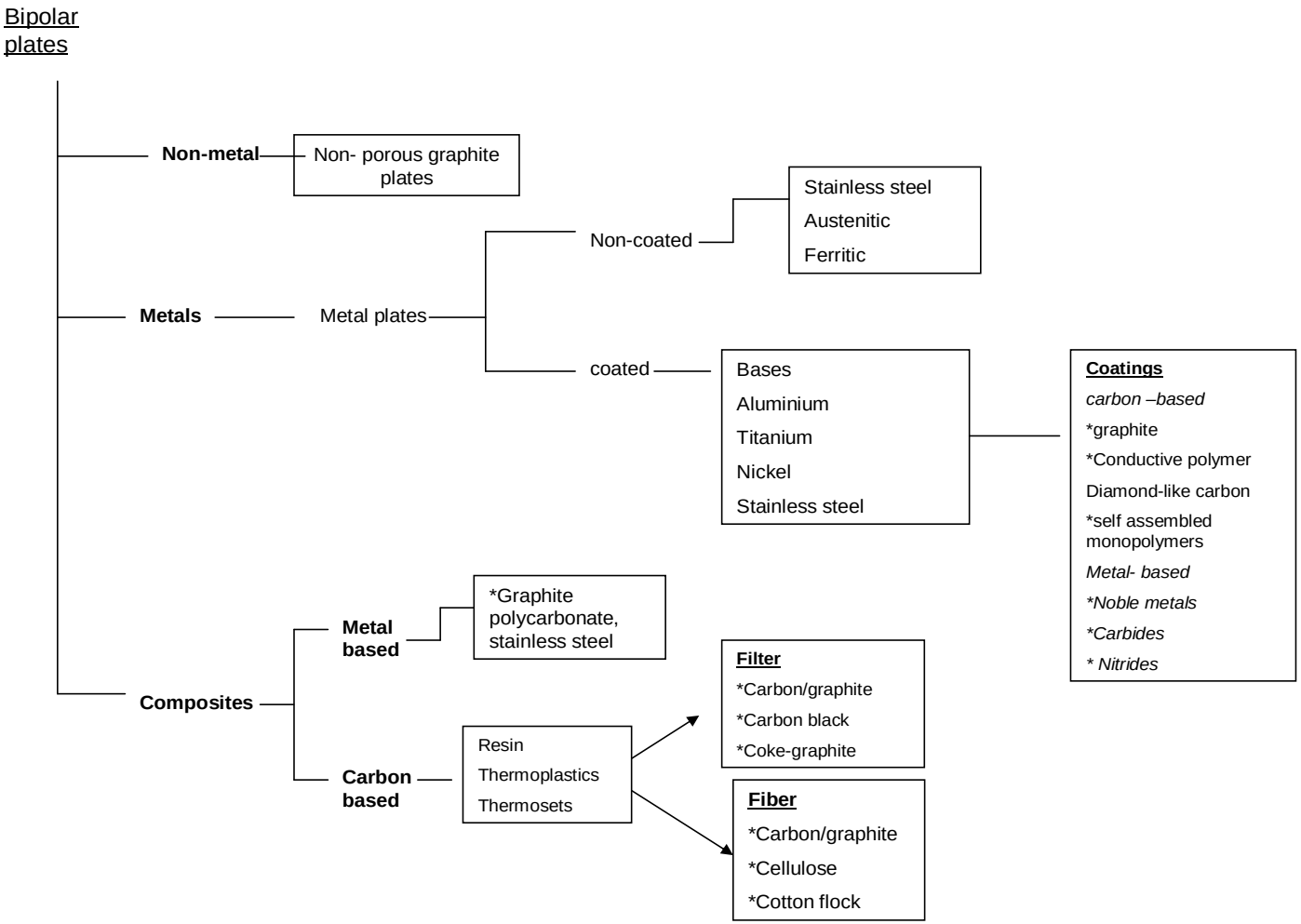

Figure 1.2.1.3 *Categorisation of materials might use as bipolar plates in PEM fuel cell systems.* [14]

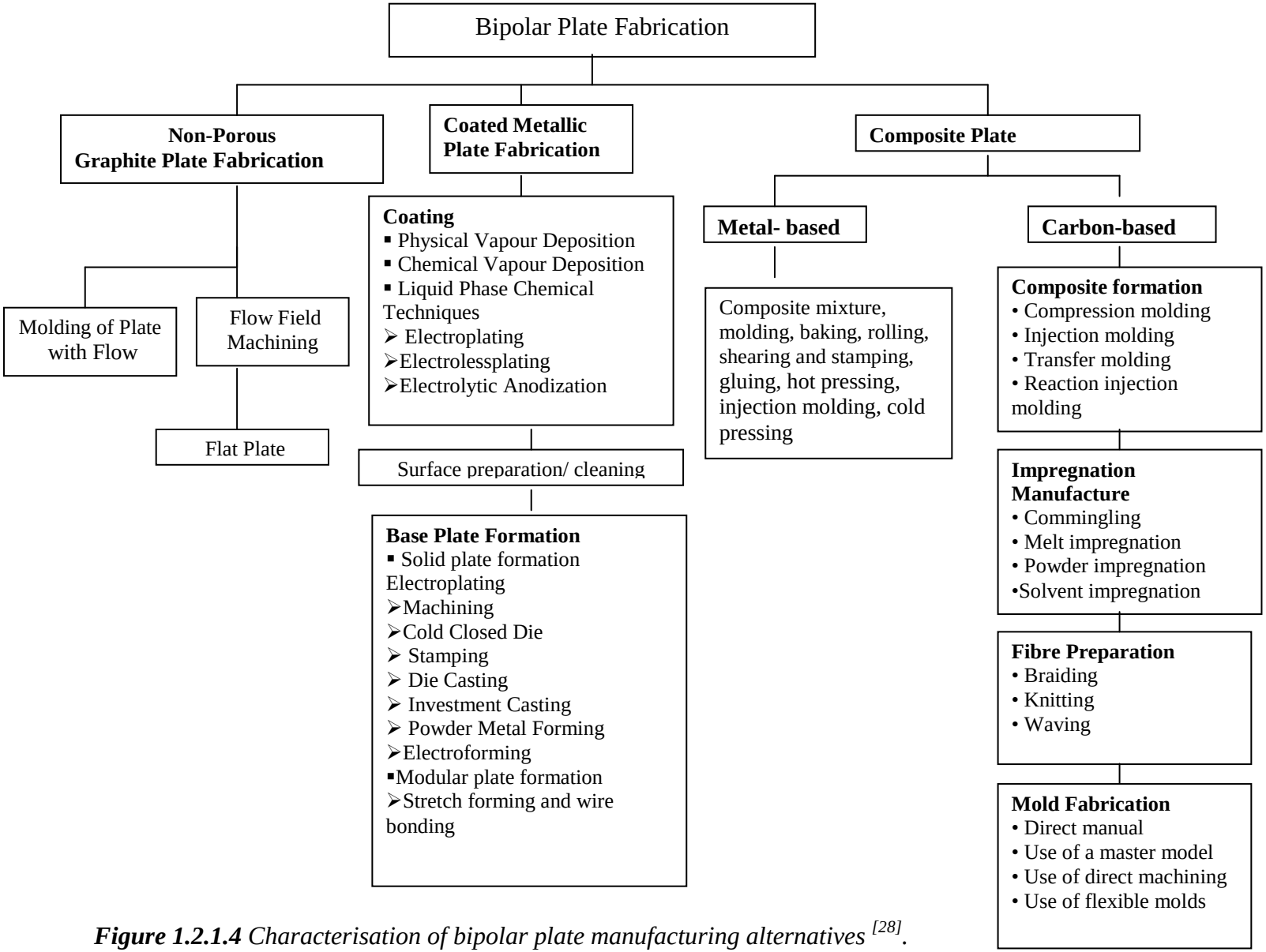

Figure 1.2.1.4 *Characterisation of bipolar plate manufacturing alternatives* [28].

Table 1.1 *Performance essential for PEM fuel cell bipolar plates.*

Property	Unit	Value
Tensile strength	MPa	>41
Flexural strength	MPa	>59
Electrical conductivity	S cm^{-1}	>100
Corrosion rate	μA cm^{-2}	< 1
Contact resistance	mΩ cm^2	<20
Hydrogen permeability	$cm^3(cm^2s)^{-1}$	$<2.10^{-6}$
Mass	kg/kW	<1
Density	g cm^{-3}	<5
Thermal conductivity	W $(m\ K)^{-1}$	>10
Impact resistance	j m^{-1}	>40.5

*[29]

*R.A. Antunes, M. C.L Oliveira, G. Ett, V. Ett *International Journal of Hydrogen Energy* **Vol. 35**, 8 (2010) 3632-3647

1.3 Corrosion Process

1.3.1 Electron transfer

Electrode reactions are the heterogeneous processes involving charge transfer electrons or ions to or from the electrode surface (typically a metal). Therefore, reactions of metal ions can be represented by the reaction:

$$Fe^{3+} + e^{-} \leftrightarrow Fe^{2+} \tag{1.6}$$

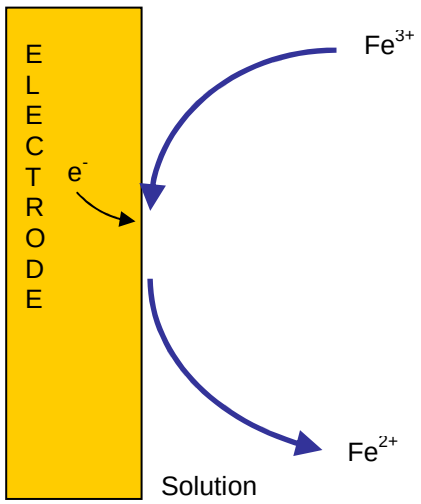

Figure 1.3.1.1 *A simple single electron transfer.*

The equilibrium potential can be calculated from the Nernst equation:

$$E_e = \mathrm{E}_e^0 + \frac{2.3RT}{nF}\log\frac{c_o}{c_R} \tag{1.7}$$

where E_e is equilibrium potential, E_e^0 the formal potential for the O/R couple. It can be seen that the formal potential can be measured using a solution where $c_O = c_R$.

At the equilibrium potential no net chemical change can be occur and the measured current density is zero, j=0 since $j_a = j_c$ where j_a~ partial anodic current density and j_c ~ partial cathodic current density.

When the discharge electron transfer reactions are occurring in the potential region away from the equilibrium potential, the rate of the net chemical change is the measured current density, j, given by

$$j = j_0\left[\exp\left(\frac{\alpha_a nF}{RT}\eta\right) - \exp\left(-\frac{\alpha_c nF}{RT}\eta\right)\right] \qquad (1.8)$$

Where j ~ is a current density, j_0 ~ exchange current density, n is the number of electron, F the Faraday constant (96485 C mol^{-1}), α_a and α_c are the anodic and cathodic transfer coefficients, η ~ overpotential, R ~ gas constant, T~ temperature.

At potentials away from the equilibrium potential, one term in equation (1.8) will dominate and the expression simplifies to

$$j = j_0 \exp\left(\frac{\alpha_a nF}{RT}\eta\right) \quad \text{or} \quad -j = j_0 \exp\left(-\frac{\alpha_c nF}{RT}\eta\right) \qquad (1.9)$$

and these are commonly written

$$\log j = \log j_0 + \frac{\alpha_a nF}{RT}\eta \qquad (1.10)$$

and

$$\log -j = \log j_0 - \frac{\alpha_c nF}{RT}\eta \qquad (1.11)$$

These equations provide a way to determine the equilibrium potential, the exchange current density and the transfer coefficients by plotting a Tafel plot, i.e. a plot of log j vs. E

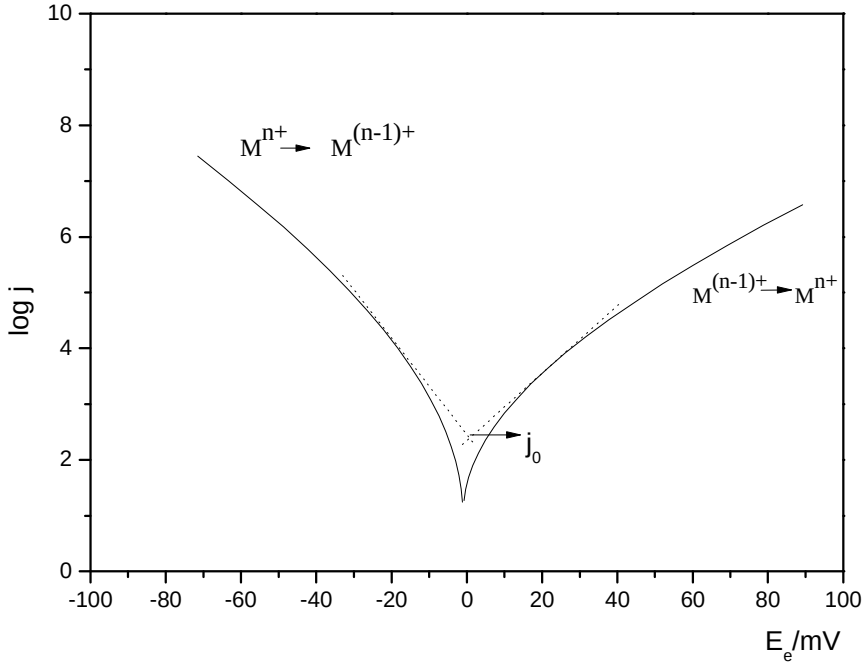

Figure 1.3.1.2 *Tafel plot for the analysis of log j vs. E_e.*

1.3.2 Corrosion

Corrosion [30-33] is the oxidation of a metal or other material under open circuit conditions. This process leads to a corrosion layer on the metal surface or ions in solutions.

The basis for understanding of electrochemical corrosion came from mixed potential theory[33]. When the metal is placed into an aqueous solution, no net current can flow and its surface takes up a potential often referred to as the corrosion potential.

The corrosion potential is a mixed potential and corresponds to the potential when the total rate of all anodic reactions and all cathodic reactions occurring at this potential on the metal surface are equal [34].

In a general corrosion reaction, the metal atom is removed after having been oxidized to its ion. In this reaction the number of separated electrons is equal to the valence of produced metal ion.

$$M \rightarrow M^{n+} + ne^{-} \qquad (1.12)$$

Possible cathodic reactions in aqueous media are:

- Hydrogen evolution

$$2H^+ + 2e^- \rightarrow H_2 \text{ (acidic solutions)} \quad (1.13)$$

$$2H_2O + 2e^- \leftrightarrow H_2 + 2HO^- \text{ (neutral or alkaline solutions)} \quad (1.14)$$

- Reduction of dissolved oxygen ,

$$O_2 + 4H^+ + 4e^- \leftrightarrow 2H_2O \text{ (acidic solutions)} \quad (1.15)$$

$$O_2 + 2H_2O + 4e^- \leftrightarrow 2HO^- \text{ (neutral or alkaline solutions)} \quad (1.16)$$

The thermodynamics of possible corrosion reactions as a function of pH are summarised in Pourbaix diagrams [35-36]. These diagrams apply only to one particular medium, most commonly a medium where no complexing agents are present. They present how the potential for oxidation/reduction reactions and the identity of the most stable species vary with pH. Figure 1.3.2.1 presents Pourbaix diagrams for Ni, Cr and Fe in pure water. The diagrams include regions where 'corrosion',' passivity' and 'immunity' are predicted. In the corrosion region the stable species are dissolved ions. Passivity is where the metal is protected by layer of an oxide or a hydroxide. Immunity is where the metal itself is stable.

In the diagrams horizontal lines are for reactions involving only ion charge transfer:

$$Ni - 2e^- \rightarrow Ni^{2+} \quad (1.17)$$

Vertical lines are for hydrolysis reactions that do not involve charge transfer:

$$Ni^{2+} + 2OH^- \rightarrow Ni(OH)_2 \quad (1.18)$$

Sloping lines correspond to reactions that involve both charge transfer and proton transfer, e.g.

$$OH^- + Ni(OH)_2 - e^- \rightarrow NiO(OH) + H_2O \quad (1.19)$$

Also included in the Pourbaix diagrams are two parallel lines that show the thermodynamic stability of water. The higher line corresponds to the oxygen/water couple $O_{2(g)}/H_2O_{(l)}$; at higher potential (above the line) water will oxidise with oxygen evolution.

The lower line is for the hydrogen the $H^+/H_{2(g)}$ couple and at lower potential (below the line) hydrogen evolution will occur. More importantly, the relative positions of these lines compared to those for a reaction involving metal species indicates whether the corrosion reactions are thermodynamically favourable; in general, corrosion through reaction of the metals with oxygen is always favourable while corrosion via reaction with protons/water depends on pH and the particular metal.

The corrosion resistance of Ni is strongly dependent on the pH and the presence of oxygen. In acid and neutral solutions nickel corrodes with ions Ni^{2+} and $NiOH^+$.

In alkaline solutions nickel passivates by formation of $Ni(OH)_3^-$ and $Ni(OH)_4^{2-}$ (depends of the pH range). Ni^{2+}, β-$Ni(OH)_2$/NiO and $Ni(OH)_3^-$ are further oxidised to β or γ phases at very high potential.

Limitations for Pourbaix diagrams are (a) they apply to one specific medium and consider only thermodynamics (equilibrium is assumed) (b) no information about the kinetics of reactions and therefore the corrosion rate is included , (c) they apply only to one temperature (d) passivation by layers of oxides and hydroxides have a strong influence on rates. Pourbaix diagrams are seldom available for alloys. In the case of binary alloys, some useful information can be obtained by considering the Pourbaix diagrams for the individual metals.

a)

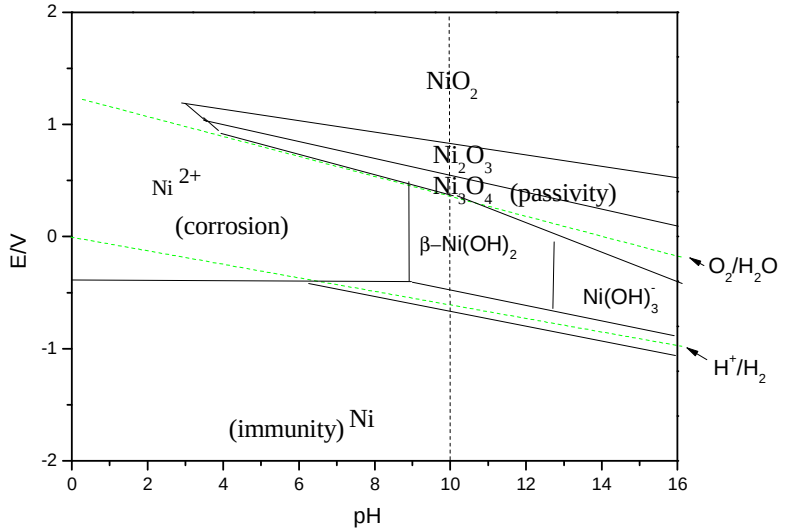

b)

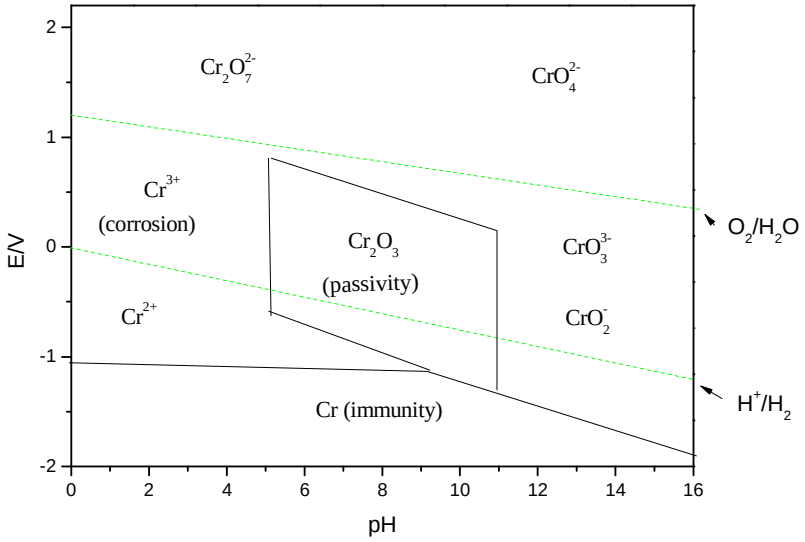

c)

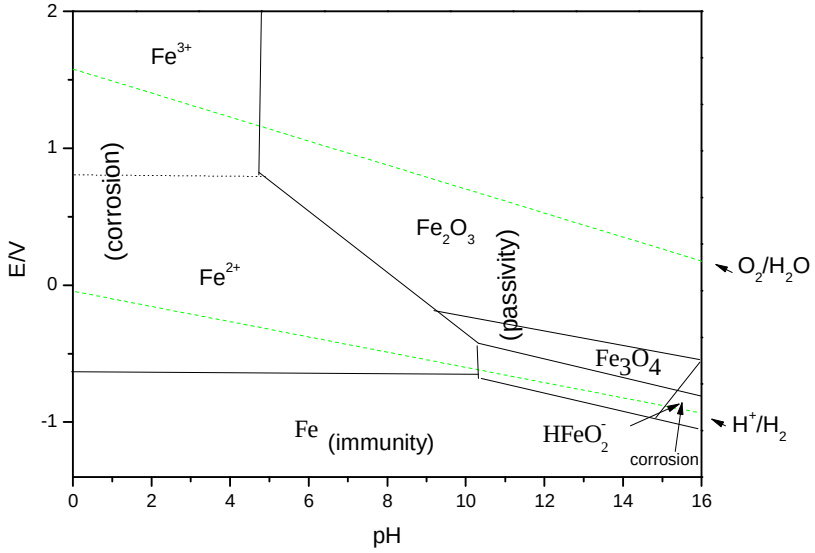

Figure 1.3.2.1 *Pourbaix diagrams for a) Ni [90], b) Cr and c) Fe in pure water [35].*

The open circuit potential for a corroding metal is commonly referred to as the corrosion potential E_{corr}. At the corrosion potential, there is no net current flowing and therefore the total rate of the anodic reaction – oxidation of M must equal to the total rate of the cathodic reaction – eg. hydrogen evolution:

$$j_{corr} = j_a = -j_c \qquad (1.20)$$

The corrosion potential is a mixed potential involving the M/M^{n+} and H+/H couples. As can be see from the figure, the mixed potential occurs when the major anodic current is metal dissolution and the major cathodic reaction is the evolution of H_2.
The E_{corr} and $j_{corr,}$ respectively the corrosion potential and the corrosion current density, can in theory, be found experimentally from steady state current density/ potential data as shown in figure 1.3.2.2. The current density at the corrosion potential is called the corrosion current density, j_{corr}, and it is related to metal loss by Faraday's law:

$$\Delta w = \frac{j_{corr} M}{nF} \qquad (1.21)$$

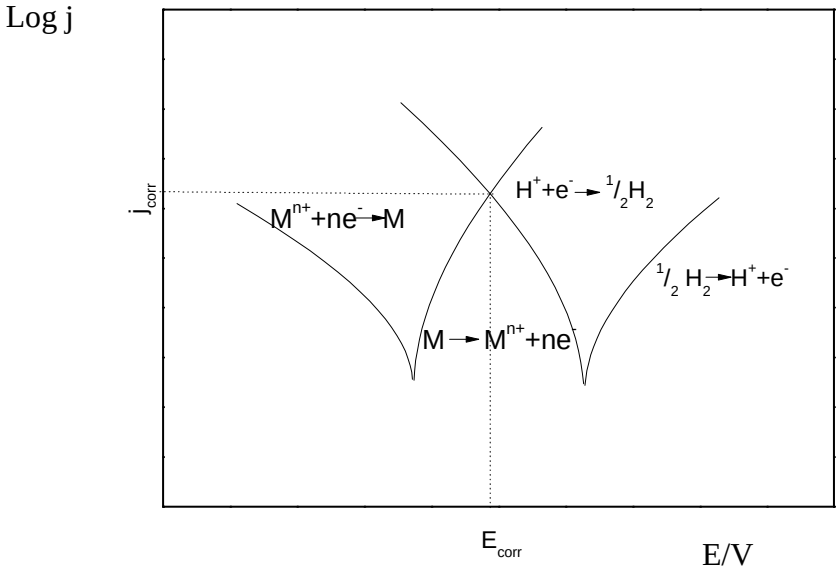

Figure 1.3.2.2 *Corrosion processes showing anodic and cathodic components.*

There are several types of corrosion [33]. Uniform corrosion assumes that corrosion is occurring with the same rate over all the surface. Perhaps more common and certainly more hazardous are a number of types of localised corrosion (pitting, crevice corrosion, deposit corrosion, selective corrosion, intergranular corrosion, layer corrosion, erosion corrosion, cavitation corrosion, fretting corrosion) where loss of metal is concentrated at particular sites.

Corrosion can be important in many environments [33, 37] - water (pure or with presence of HCO_3^-, Cl^-, SO^{2-}_4, other salts), seawater, the atmosphere (SO_x, NO_x), molten salts, inorganic solvents, soils, gases, bases, acids.

Most studies seek a way to slow down corrosion and hence to achieve 'corrosion protection'. Methods to achieve protection can include: (a) controlling the electrode potential to values where cathodic or anodic protection occurs, (b) using inhibitors to reduce the corrosion process, (c) coating protective layer – organic (eg. a paint) or inorganic, usually a passivating layer formed in situ.

1.3.3 Passive layers

Passivity layers are important to the properties of metals since they are responsible for the stability of many metals and alloys in common use, even when the Pourbaix diagram (ie. thermodynamics) predicts that conditions are very favourable for corrosion. Fundamentally, an insoluble film of metal salt, or oxide, is formed on the electrode by a reaction such as that in the equation

$$M + X^+ \rightarrow MX + e^- \qquad (1.22)$$

The film formed then limits the rate of further corrosion since there must be a mechanism for charge to pass through the layer. Hence, it must conduct electrons or it must allow ions to migrate through the layer.

The first step of passivation is commonly the adsorption of an oxygen layer on the surface. The second step is the movement of surface metal atoms out into layer of adsorbed oxygen atoms, where they exchange electrons and effectively constitute a monolayer of oxide/hydroxide. The properties of the passivating film will commonly determine the rate of corrosion of the metal underneath the film. In theory, passive

layers and barrier layers are well known, as presented in figure 1.3.3.1. Amongst these several models can be distinguish: (a) an absorbed layer on the metal surface (described above), (b) a thin barrier layer on metal surface (e.g. internal and outer oxide layers on Fe surface), (c) a barrier layer formed on less protective layer (e.g. cobalt), (d) a barrier layer which has been covered with hydrated deposit layer (Ti in acidic solutions), (e) the barrier film covered with porous layer of the same composition (anodic oxidation of Al).

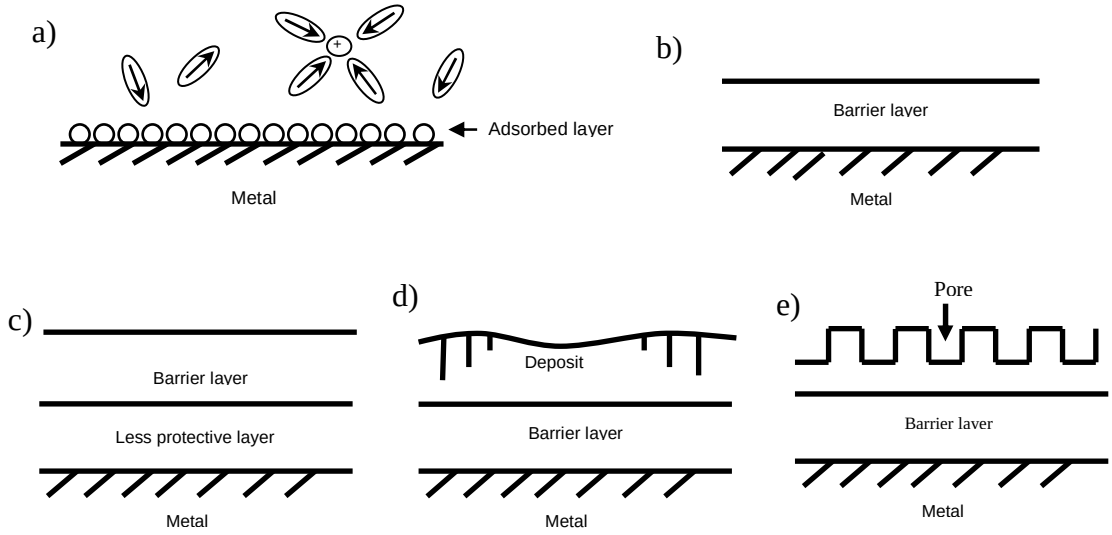

Figure 1.3.3.1 *Types of passive films (a, b) and barrier layers (c, d, e) on metal surface* [38].

1.3.4 Role of special sites

Metals are built of crystals grains, the exact structure depends on the element and its history, particularly thermal treatments and mechanical working. The structure leads to the possibility of mechanism of corrosion, eg. intergranular or crevice corrosion.
Intergranular corrosion occurs when the major metal mass loss occurs at the boundary between grains (although the balancing cathodic processes may occur over the whole surface); the rate of intergranular corrosion depends on the grain size and regularity as well as the orientation of crystals. Crevice corrosion takes place when metal loss is limited to active sites, and the formation of a crevice commonly leads to a high rate and disasterous corrosion.

Also this kind of corrosion can take a place between metal and non-metallic material. Figure 1.3.4.1 presents sketches to illustrate crevice and grain boundary corrosion.

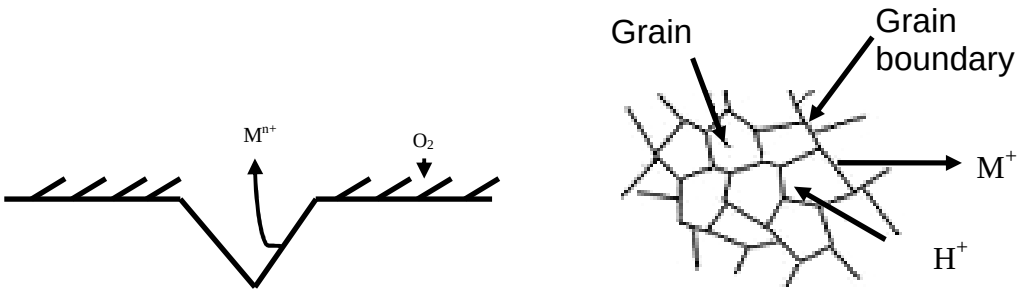

Figure 1.3.4.1 *Illustrations of a) crevice and b) intergranular corrosion.*

1.3.5 Corrosion of studied materials

1.3.5.1 Corrosion of steels

Steel is an alloy consisting of iron and carbon (0.2 ~ 2.1%) mixed with other elements. According to the percentage carbon, steel can be described as mild steel (up to 0.25 % C), medium carbon steel (0.25 - 0.45% C) and high carbon steel (0.45 - 1.50% C). In other steels, C and/or Fe can be substituted by addition of elements such as nickel, molybdenum, chromium, or copper and become a stainless steel.

Properties of steels (hardness, strength, weldability, formability, plasticity, mechanical properties, resistively) vary strongly with their composition. Also the treatment of the steel during production (the cooling and hardening regimes) is very important. Stainless and mild steels have been used as substrate materials in this thesis.

Table 1.2 *Compositions of stainless and mild steels.*

steel	% Cr	% Mo	% Ni	% Fe	% C	% Mn	% Si	% P	% S	% Cu
316	16-18.5	2-3	10-14	balance	<0.03	<2.0	<1.0	0.045	0.035	-
904L	19-23	4-5	23-28	balance	0.02	2.0	1.0	0.045	0.035	1-2
Mild	-	-	-	balance	0.08	0.4	-	0.03	0.03	-

Stainless steel has been studied by many authors [34, 39-41] and it exists as three different structures: ferritic (b.c.c), austenitic (f.c.c) and martensitic (metastable austenic phase f.c.c changing with temperature to b.c.c). For example, the magnetic properties change with the structure. Figure 1.3.5.1.1 presents the phase diagram for iron-carbon steels while figure 1.3.5.1.2 shows structure of austenitic, martensitic and ferritic steels.

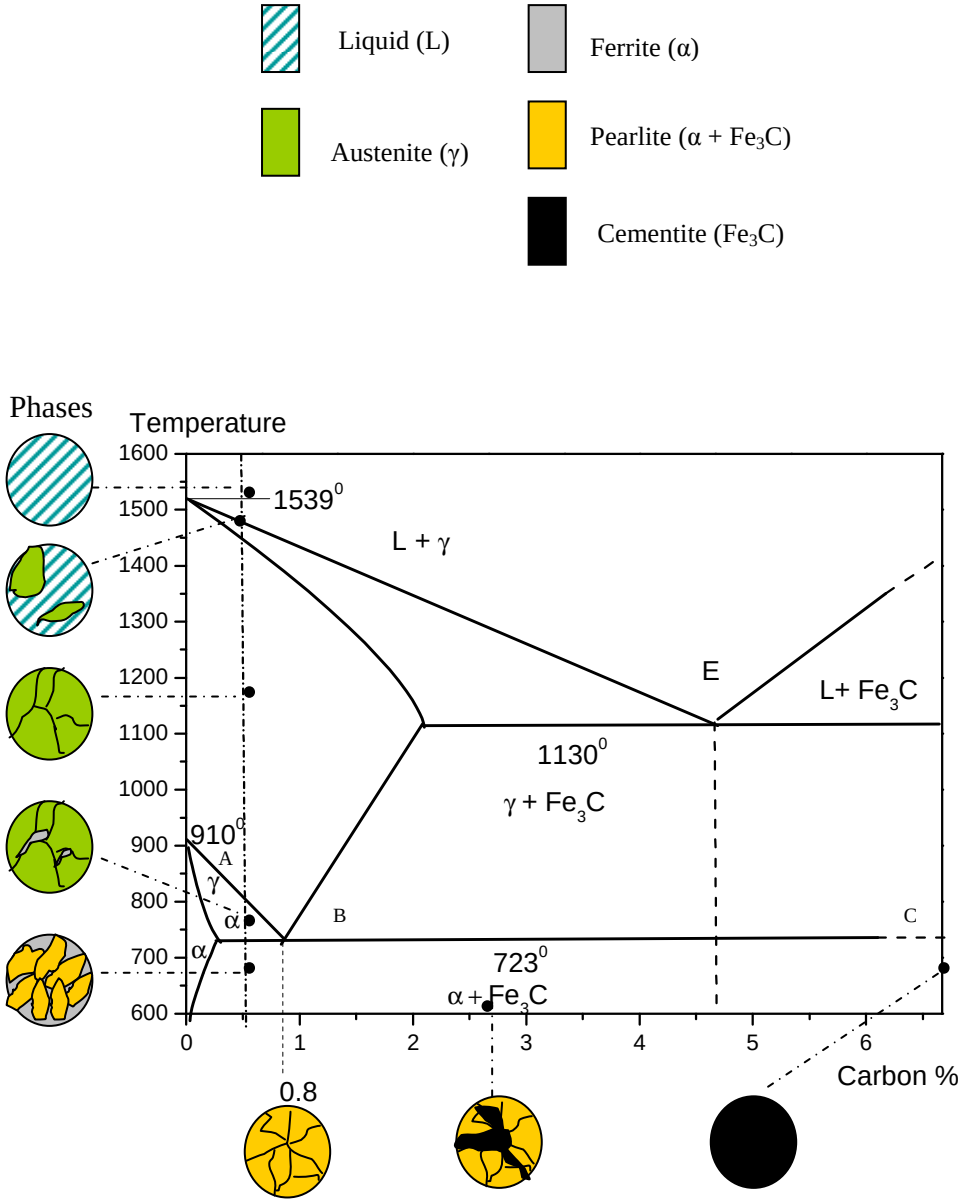

Figure 1.3.5.1.1 *Phase diagram for iron-carbon steels* [37, 42].

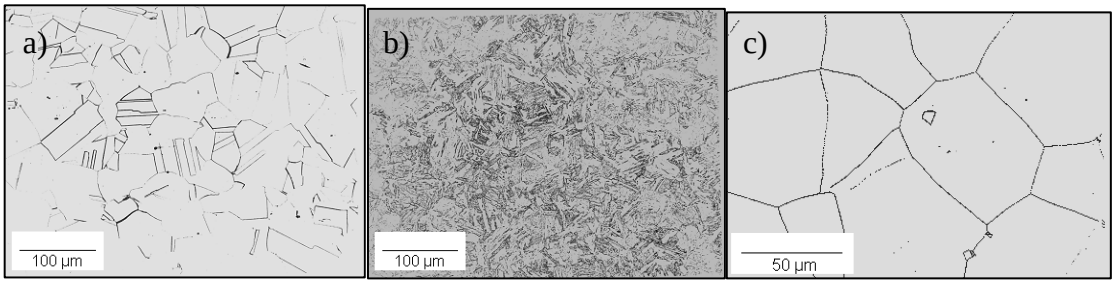

Figure 1.3.5.1.2 *SEM images of microstructure of a) austenitic b) martensitic c) ferritic steels* [30, 37, and 43].

Additions in SS 904 L especially of Mo, Mn [46-47] and Cr play an important role.
The function of Cr [23, 44] in stainless steel is to increase the resistance to corrosion and it has a strong influence on anodic behaviour. Most of authors suggest that Cr_2O_3 has a critical role in the of passivation process of stainless steel [23, 30]. Formation of a thin surface film occurs and this is the reason why many stainless steels contain 17-18 % of Cr.
Also it is well known that addition of Mo and Ni increase resistance to corrosion in acidic solutions and stabilise the passive film by eliminating the active sites. Mo [15] changes the polarity of the passive film and has shown repassivation behaviour. Mn can increase solubility of nitrogen and is responsible for austenite formation. The effect of elements on the structure of stainless steel is summarised by a Schaeffler-Delong diagram [80]. The diagram is based on the way that the alloying elements influence the steel structure. Nickel promotes the formation of austenite and chromium stabilises ferrite:

Chromium equivalent = %Cr + 1.5 x %Si + %Mo

Nickel equivalent = %Ni + 30 x (%C + %N) + 0.5 x (%Mn + %Cu + %Co)

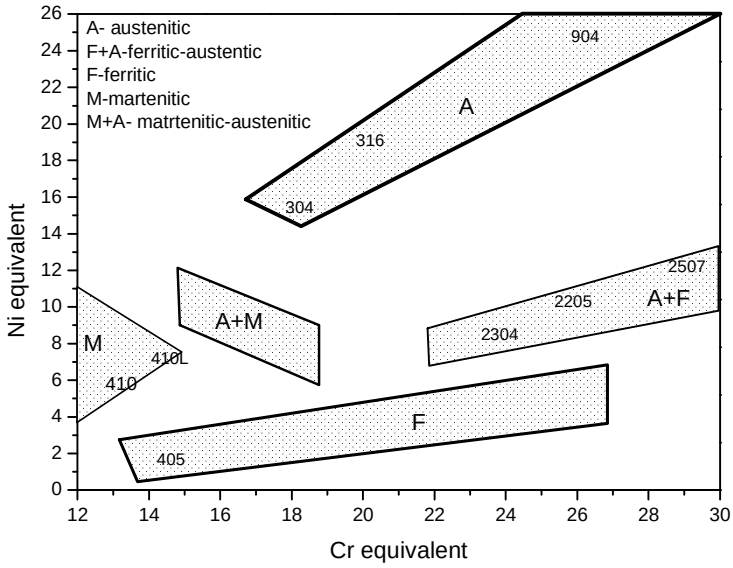

Figure 1.3.5.1.3 *The Schaeffler-Delong diagram [80] with alloying phases of A-austenitic, F+A-ferritic-austenitic, F-ferritic, M-martenitic and M+A- martenitic-austenitic.*

Figure 1.3.5.1.4 summarises the influence of alloying elements on the properties of austenitic stainless steels.

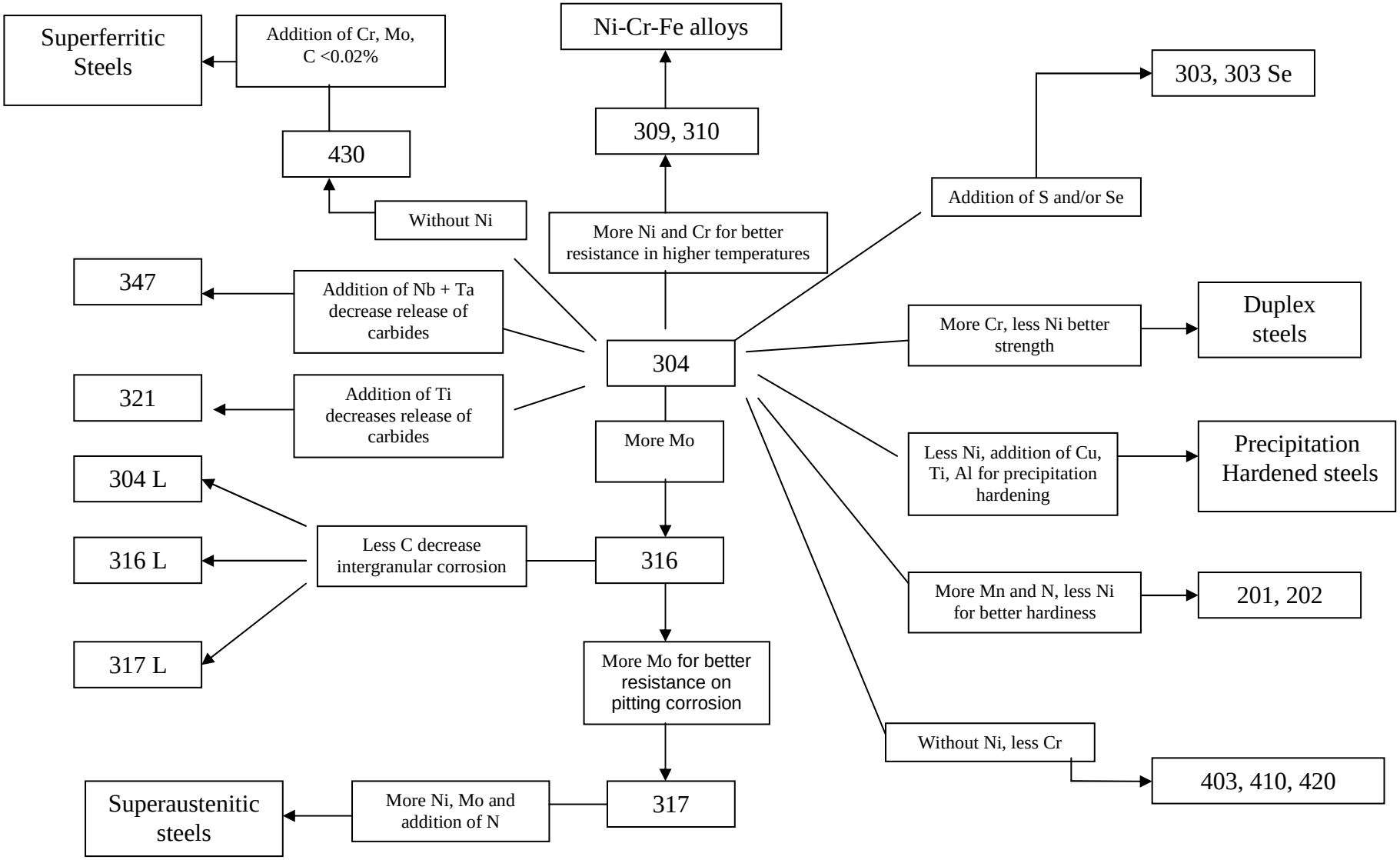

Figure 1.3.5.1.4 *The influence of alloying elements on the properties of the steel* [45].

Mild steel is the cheapest type of steel and is also the most common steel in our lives (e.g. bullets, chains, hinges, knives, pipes, bolts, screws, tubes, girders etc.). The main addition is carbon. Unfortunately, mild steel corrodes significantly in many environments. It rusts in humid air while the rate of dissolution can be very high in acid medium [46] because of the absence of an effective barrier layer and the consequent formation of soluble products.

In contrast, the addition of chromium to stainless steels allows the formation of an effective protective layer on the surface. The rate of uniform corrosion is low in many environments. When corrosion is observed, it is usually a form of localised corrosion such as pitting, crevice, stress corrosion cracking or intergranular corrosion.

In general, the main products of the anodic corrosion of stainless steel are [44-45] oxides. The first step may be

$$Fe + 2H_2O \longrightarrow FeOOH + 3H^+ + 3e^- \quad (1.23)$$

$$Ni + H_2O \longrightarrow NiO + 2H^+ + 2e^- \quad (1.24)$$

$$Cr + H_2O \longrightarrow CrO + 2H^+ + 2e^- \quad (1.25)$$

involving nucleation and growth of a layer on the electrode surface. Thereafter, nickel and, even more so, chromium oxides are oxidised further to more protective layers.

$$2CrO + H_2O \longrightarrow Cr_2O_3 + 2H^+ + 2e^- \quad (1.26)$$

while with iron there is a greater tendency to form soluble material

$$\gamma FeOOH \rightleftharpoons \alpha\ FeOOH \rightleftharpoons Fe_2O_3 \quad (1.27)$$

1.3.5.2 Corrosion of Ni, Cr, and Fe

The corrosion of nickel, chromium, and iron has generated a very extensive literature [46-54] but very few in media similar to that of interest in this thesis (ie. phosphoric acid, pH 2 – see project objectives). These three metals are first series transition metals with the electronic configurations for Ni [Ar] $3d^8 4s^2$, Cr [Ar] $3d^5 4s^1$, and Fe [Ar] $3d^6 4s^2$. Parshutin et al. [46] has suggested that pure Ni in concentrated phosphoric

acid is almost not corroded, while in diluted phosphoric acid it corrodes rapidly. It is likely that the initial oxidation of the metal is faster in the strong acid but passivation is more effective in concentrated phosphoric acid. In both cases NiO is presumed to be the surface layer although the orthophosphate would explain the behaviour better. MacDougall [50] has presented a model of the breakdown of oxide films on a nickel surface. Initially, nucleation then growth of the nickel oxide layer occurs. At some point in the formation of the layer, breakdown occurs perhaps due to stress and pores are formed that allow nickel (II) to go into electrolyte. A sketch of these processes has been presented on figure 1.3.5.2.1.

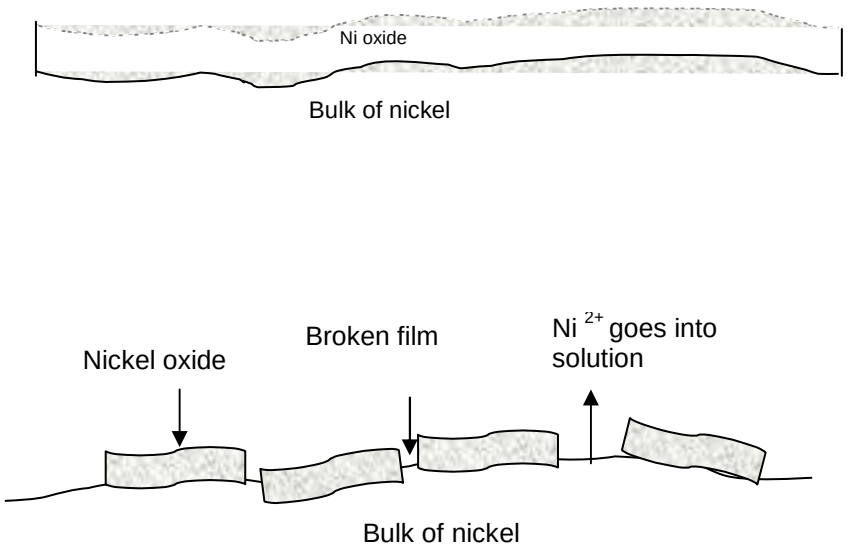

Figure 1.3.5.2.1 *Simple characterisation of nickel (a) oxide formation and (b) break down of oxide layer [50].*

In most environments, chromium has the tendency for the quick formation of a passive layer on its surface. This film has good barrier properties and leads to a very low rate of corrosion. Many authors have been suggesting that small addition of chromium [57, 30] to steel changes the behaviour. Also chromium in Ni-Cr-Mo alloys is important to their use as bio steels [30].

Iron is one of the most common elements in the world. Atenas et al. [58] suggests that the corrosion processes of iron depend strongly on the electrolyte. This is because oxidation of iron surfaces can lead to a passive layer or soluble Fe (II). Many authors [59-60] suggested that the typical layer formed on iron surface contains two layers: an inner magnetite Fe_3O_4 and outer maghemite γ-Fe_2O_3 layer.

1.3.5.3 Corrosion of graphite

Carbon materials are available in many different forms (rods, powders, felts, foams etc) and structures. They are very attractive for many industrial applications because of their electrochemical and chemical properties [37, 44, 61-62]: thermal conductivity, gas and liquid adsorption, compressibility, elasticity and electrical conductivity. Many authors [44,61] have shown that the anodic processes occurring on carbon electrodes depend on the conditions- pH, concentration, and specific nature of electrolyte and, more importantly, on the kind of carbon.

In this thesis graphite particles have been employed. Each particle of graphite is a composition of single crystals (figure 1.3.5.3.1).

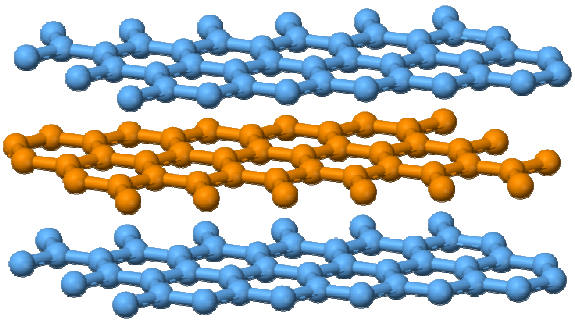

Hexagonal form of graphite with the layer sequences ABAB

Figure 1.3.5.3.1 *Crystalline structure of graphite [63].*

Some papers conclude that the properties of graphite depend strongly on the level of the impurities. Guenbour et al. [61] highlighted the role of oxygenation/deoxygention of the surface on graphite corrosion. Graphite corrosion can be described in two steps:

$$C + H_2O \rightarrow C(O)_{ads} + 2H^+ + 2e^- \quad (1.28)$$

then

$$(1) \qquad 2C\,(O)_{ads} \rightarrow CO_2 + C \quad (1.29)$$

or /and

$$(2) \qquad C(O)_{ads} + H_2O \rightarrow CO_2 + 2H^+ + 2e^- \quad (1.30)$$

The rate of graphite corrosion can be influenced by:

- catalysis by metals species (Pt, Pt alloys, Ni, Ni alloys, MnO_2) that assist the formation of an oxidising intermediate, M-OH

- intercalation of anions. The layer structure of graphite allows ions or molecules to move into the structure. In anodic conditions, anions are likely to migrate into the structure.

$$C + X^- \rightarrow C^+X^- + e^- \quad (1.31)$$

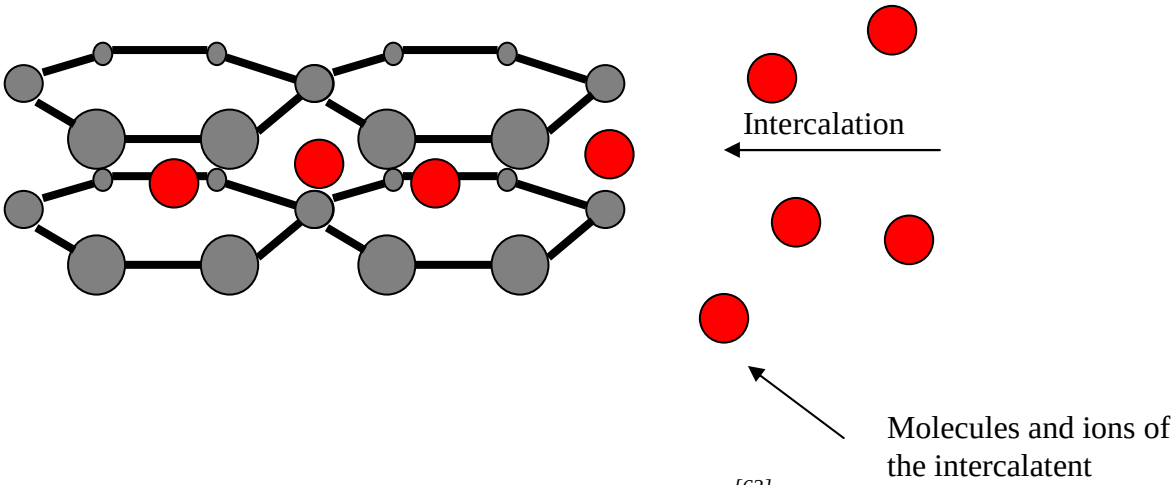

Figure 1.3.5.3.2 *Illustration of the intercalation process* [63].

- erosion - corrosion of graphite – this results from mechanical friction on the graphite surface.

.

1.3.5.4 Corrosion of Ni-Cr alloys

The corrosion of Ni-Cr alloys in sulphuric acid, phosphoric acid and sodium hydroxide has been previously reported [64-67, 69]. McCafferty [67-68 and 70-71] has investigated formation of the passivating oxide film on the surface binary alloys.
The studies suggested that the bridging Cr-O-Cr is responsible to the formation of the passive layer. This, however, depends on the percentage concentration of Cr in the Ni-Cr alloys. At high concentrations of Ni compared to Cr the structure of the passive layer is formed by the network of Ni-O-Ni bridges [67-68]. Bojinov and coworkers [65, 72-73] investigated transpassive dissolution (conversion to Cr (VI) or Cr^{3+} in solution) of Ni-Cr alloys in sulphate solutions and in 14.8 M phosphoric acid. Betova at al. [74] concluded that in the transpassive dissolution process for Ni, Cr and Ni-Cr alloys the limiting reactions occur at the anodic film/electrolyte interface. It has been shown that Ni and Cr dissolution are limited by the anion-assisted and oxidative dissolution. Ni-Cr alloys have smaller transpassive potential range than pure metals Ni and Cr.
Also Kasprova [75] suggested that Ni- rich Ni-Cr alloys are highly resistive to corrosion in oxidizing acids, and, even in nitric acid solutions with the presence of F^- at high temperature, the dissolution of the Ni-Cr alloys is minimal. The presence of the Cr within the Ni matrix results in the increasing stability of the Ni-Cr alloys [76]. The slow dissolution of the alloys compared to Ni [77] explains the resistive nature of the Ni-Cr alloys in oxidizing acids. Ni-Cr alloys may well be a material for bipolar plates in fuel cells.
Applications for Ni-Cr alloys [78-81] include: superconductors, dentistry (composite of Ni-Cr alloy with porcelain), aircraft gas turbines, high electrical resistivity, steam turbine power plants, nuclear power systems, chemical and petrochemical industries. These all result from the high resistance to alloy oxidation even under extreme conditions.

1.4 Methods to corrosion study

1.4.1 Weight loss test

In this method, a weighed sample of the metal/alloy is exposed to attack in the environment of interest (gaseous or aqueous solution) or an environment designed to give accelerated corrosion but also information relevant to the environment of interest. After a period of time, the metal sample is washed, dried, and weighed. The weight loss is then used to estimate an average corrosion depth.

1.4.2 Spray salt testing

A commonly used example of a weight loss experiment is the salt spray test. The sample is placed in a cabinet with controlled environment and sprayed with a salt solution. Particular salt spray procedures include:
:

- Scab test - sample is exposed to air and sprayed twice a week with 5 % sodium chloride solution and dried. (5% NaCl + T)
- Neutral salt test - spraying solution contains 5 % sodium chloride with pH between 6.5-7.2 at a controlled temperature (5% NaCl + T, pH)
- Acetic acid salt spray – the solution is a mixture of aqueous acetic acid with 5 % of sodium chloride with pH 3.1- 3.3 at a controlled temperature (5% NaCl + CH_3COOH+T, pH)
- Copper accelerated acetic acid salt spray test- basic sprayed solution (with 5% of sodium chloride) with addition of acetic acid and cupric chloride (5% NaCl + CH_3COOH + $CuCl_2$ + T, pH).

Humidity and temperature as well as the composition of the atmosphere are important in atmospheric corrosion. Testing may include exposure to corrosive gases such as SO_2, H_2S or CO_2.

1.4.3 Cyclic Voltammetry

Cyclic voltammetry [82] is a basic electrochemical method that can define the changes to the surface and/or solution adjacent to the surface during electron transfer across the surface/solution interface. It is particularly useful for initial studies of a system. In this method the working electrode is polarised versus a reference electrode with the potential changed linearly with time. In this technique the key parameters are; potential limits, potential scan rate and numbers of cycles. Peak shapes indicate the type of reaction occurring while differences of the potentials between the peaks characterise the kinetics of electron transfer and charge balance indicates the chemical stability of the products of electron transfer. Data analysis will use the number and shape of the peaks, peak potential and peak current densities, charges connected with the peaks and the presence of other features and the way that these quantities vary with potential limits and potential scan rate. Figure 1.4.3.1 presents graphs of cyclic voltammograms for fast and slow electron transfer reactions for the two limiting cases of (a) electroactive species and reaction product soluble in solution (b) reaction involving the formation or conversion of a surface film.

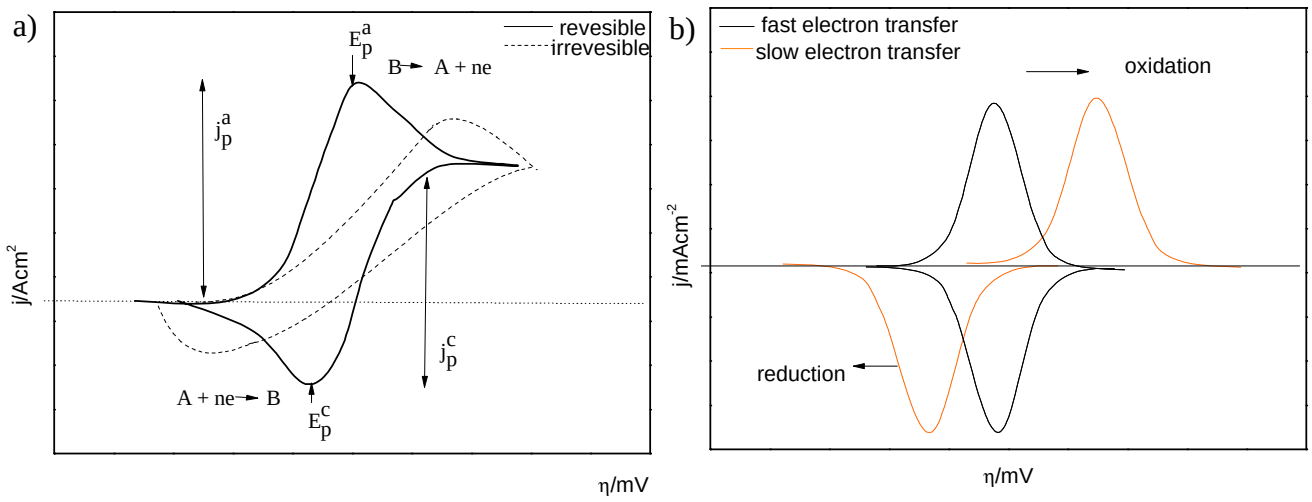

Figure 1.4.3.1 *Graphical illustrations of cyclic voltammograms of a) solution reaction and b) surface changes.*

In the study of corrosion, voltammetry is a simple approach to estimating the corrosion potential and corrosion resistance and gives a quick and visual indication as to the active corrosion region, the occurrence of passivation, the stability, and nature of oxidation products, the cathodic process leading to corrosion and the role of mass transport in the corrosion process. The current densities give an immediate estimate of the rate of corrosion as a function of potential.

1.4.4 Electrochemical Impedance Spectroscopy EIS

In electrochemical impedance spectroscopy [83-94], a low amplitude sinusoidal current (or potential) perturbation is applied to the electrode/solution interface and the response of the potential (or current) is monitored; this measurement is repeated as a function of the frequency of the perturbation and the overall response is interpreted with the aid of an equivalent circuit that mimics the behaviour of the electrode/solution interface. EIS is a powerful tool to study the mechanisms of electrochemical reactions and in corrosion science has also been used to investigate localized corrosion process such as crevice and pitting corrosion, cracking, stress, fatigue and corrosion under the protective layer. It is a very sensitive method to measure the porosity of coatings metals and measures electrical resistance. EIS [95] is a good method to characterise quantify and explaining corrosion effects. This technique is suited to investigate the passive layer breakdown phenomena and also provide information about the localized the corrosion of coating /steel system.

The father of the impedance spectroscopy is Oliver Heaviside [85]. Impedance data is interpreted in terms of an equivalent circuit, ie an electronic circuit containing resistances, capacitances etc, that behaves in the same way as the electrode reaction under study. The idea of electrical resistance can be defined by Ohm's law $R = V/I$, but this relationship only applies to the simple circuit element, the resistor. Impedance is the 'resistance' of more complex circuit elements. The impedance [94] at high frequency ($Z = R_1$) is smaller than at low frequency ($Z = R_1+R_2$). Figure 1.4.4.1 presents graphical interpretations of impedance data for iron in sulphuric acid in the most common ways, Nyquist and Bode plots. In a Nyquist plot, the imaginary component of the impedance is plotted vs the real component. In Bode plots, the real and imaginary components of the impedance and/or the phase shift are plotted as a function of frequency (usually as a log/log plot).

Simple electrode reactions are interpreted in terms of the Randles circuit, see figure 1.4.4.1. Components of the Randles circuit are:

- R_u depends on the geometry of the electrode, position of the Luggin capillary

  and conductivity of the solution,

- R_{ct} relates to the charge transfer kinetics for the electrode reaction,

- C_{dl} depends on the electrode material, electrode area, and electrolyte.

The Nyquist plot for such an electrode reaction is a simple semi-circle and the components of the equivalent circuit are immediately found:

- R_u is the intercept on the real axis.
- R_{ct} – from the diameter of the semi-circle.
- Double layer capacitance (C_{dl}) from the frequency, ω_{max}, at the maximum of the circle.

The Bode plot allows the estimation of same parameters but its real advantages lie in the study of more complex reactions where the equivalent circuit contains more independent RC elements. The frequencies (and hence timescales) related to each RC element is immediately clear from the features on the plot.

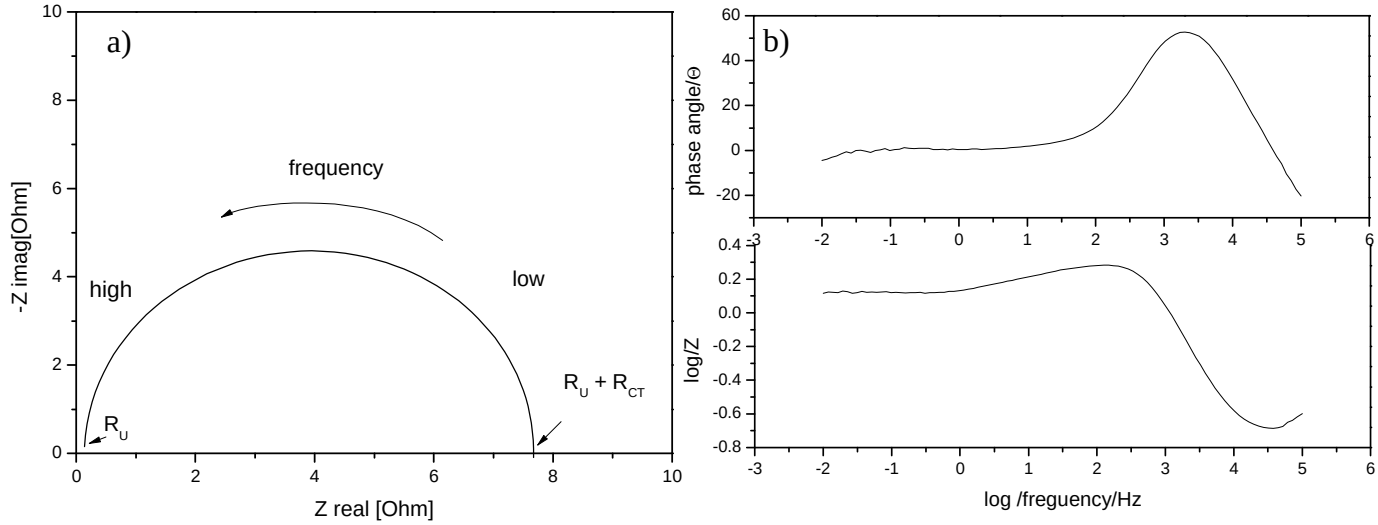

Figure 1.4.4.1 *Graphical interpretation of Electrochemical Impedance Spectroscopy a) Nyquist plot [96], b) Bode plots of Fe in 1 M of sulphuric acid.*

In this thesis, electrochemical impedance spectroscopy has been used to investigate the porosity and corrosion resistance of electrodeposited thin layer of Ni and/ or Ni/C on steel and to characterise processes occurring (Chapter 3).

1.4.5 X-Ray Diffraction (XRD)

XRD is a technique for the determination of bulk structure [97-101] – of commercial metals and alloys, electrodeposited layers and surface films. In this technique a beam of X-rays impinges investigated sample and is scattered in all directions.
The mathematical form of this process is described by Bragg's law,

$$n\lambda = 2d\sin\theta \qquad (1.32)$$

Where: n – is the order of reflection, λ - the wavelength, d – is the lattice plane spacing, θ – is the angle of reflection.

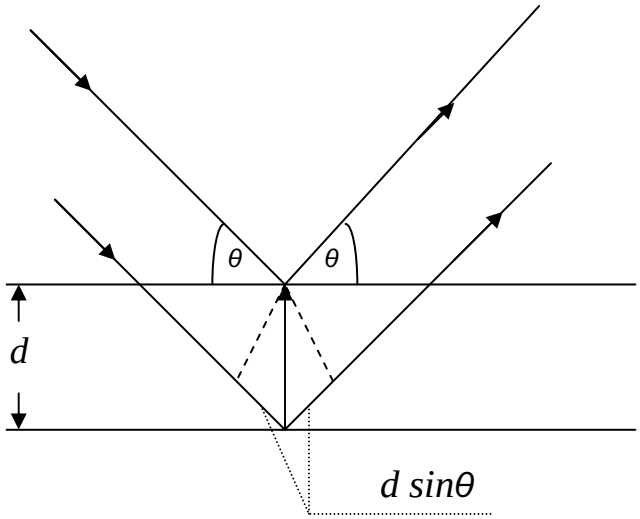

Figure 1.4.5.1 *Graphical explanation of Bragg's law with reflection of X-ray* [100].

The scattered X-rays result in Bragg reflections was operating at wide angles 10 - 90º. The identification of Ni-Cr alloy and pure Ni and Cr phases were performed with the ICDD database and literature.
Many authors [101-102] suggest that for low concentration of Cr in Ni - Cr alloys, Cr atoms simply replace Ni atoms in the nickel f.c.c lattice γ phase structure. At higher concentrations Cr, two phases are observed, the f.c.c phase and the b.c.c [99] form

related to Cr (α, γ phases). Also Cr has a good solubility in Ni. Nickel has been characterised by five typical peaks at ~ 44.52º, ~ 51.86º, ~ 76.4º, ~ 92.98º, and ~ 98.48º associated with the lattice planes (111), (200), (220), (311) and (222) – f.c.c lattice structure. Chromium has been described by peaks at ~ 44.36º, ~ 81.68º associated with the planes (110) and (211) and b.c.c lattice structure (Figure 1.4.5.2). Typical crystal structure for Ni atoms in crystal lattice with sequence ABCABC, atoms are close packed, and coordination number equals 12, while Cr has 8.

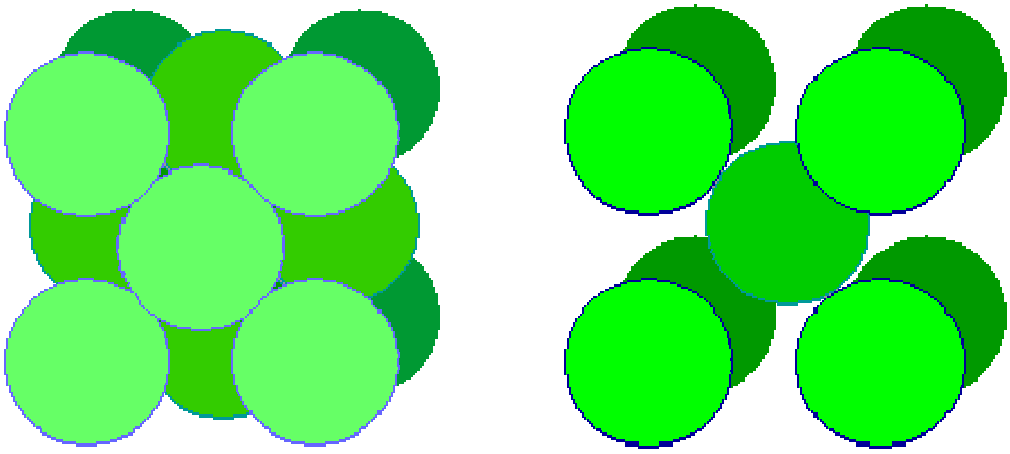

f.c.c for Ni b.c.c for Cr

Figure 1.4.5.2 *Crystal structure of Ni and Cr.*

1.5 Objective of thesis

In this thesis, the objective has been to study the rate of corrosion of materials that might be used for bipolar plates in a PEM fuel cell. In order to achieve this it was necessary to select conditions appropriate to the materials in this role. The sponsor for the work was mainly interested in fuel cells with membranes with phosphoric acid as the electrolyte in a polymer matrix. They therefore surmised that the bipolar plate, separated from the membrane by catalyst layers might be exposed to phosphoric acid but at a lower concentration than within the membrane – pH 2 was selected. The temperature agreed for the investigation was 353 K. The two sides of the bipolar plate are exposed to oxygen and hydrogen and are in electrical contact with the two catalyst layers. The sponsors were more concerned about corrosion on the oxygen reduction side. It is known experimentally that oxygen reduction typically takes place at potentials in the range 700 – 900 mV vs. SHE and the environment is strongly acidic. Because of the higher pH of the medium selected for the study, it was considered that the potential equivalent to that at the bipolar plate should be less positive. Experiments were therefore focused on potentials of ~ + 600 mV vs. SHE.

The sponsors wished the base material for the bipolar plate to be mild steel. In a related project [103] the objective was therefore to find a protective coating for the mild steel that also had the required low contact resistance. The approach was to deposit first a layer of nickel/graphite and then to enhance the corrosion resistance of the nickel with the deposition by physical vapour deposition (PVD) of a further layer on the nickel surface, perhaps followed by a heat treatment to alloy the deposited metal with nickel. This required the development of a nickel graphite surface with a low contact resistance and a distribution of graphite particles that did not lead to significant ‘shadowing’ during PVD. The metal selected to enhance the corrosion resistance of the nickel was chromium.

This thesis reports studies of the corrosion of both base materials and the surfaces produced during the parallel project. Hence, during the study various materials such as pure metals, steels and alloys have been investigated. Some of the studied materials have been tested ‘as received’, other with protective layer on the surface. Mild and stainless steels have been suitably pre-treated and covered with protective layer of Ni or/and Ni/C. The main materials studied include (Figure 1.1.2.5):

- Pure metals (Ni, Cr, Fe).
- Steels (stainless steel 904 L, mild steel, Ni coated mild steel, Ni/C coated mild steel).

- Steel coated with protective layer.
    - ❖ Ni coated mild steel with different thicknesses of layer (0.1 – 10 µm).
    - ❖ Ni coated stainless steel with different thicknesses of protective layer (0.1 – 10 µm).
    - ❖ Ni/C on Ni coated mild steel with different thicknesses of protective layer (1-10 µm).
    - ❖ Cr (20 and 80 nm) layer on Ni coated mild steel.
- Ni-Cr alloys (Ni90Cr10, Ni80Cr20, Ni50Cr50).
    - ❖ Foils and rods.
- Ni-Cr alloys modified by PVD.
    - ❖ As deposited.
    - ❖ Heat treated (2 hour at 523 K).
- Graphite – has been use to comparison.

Investigating protective layer has been deposited by electroplate method and PVD.

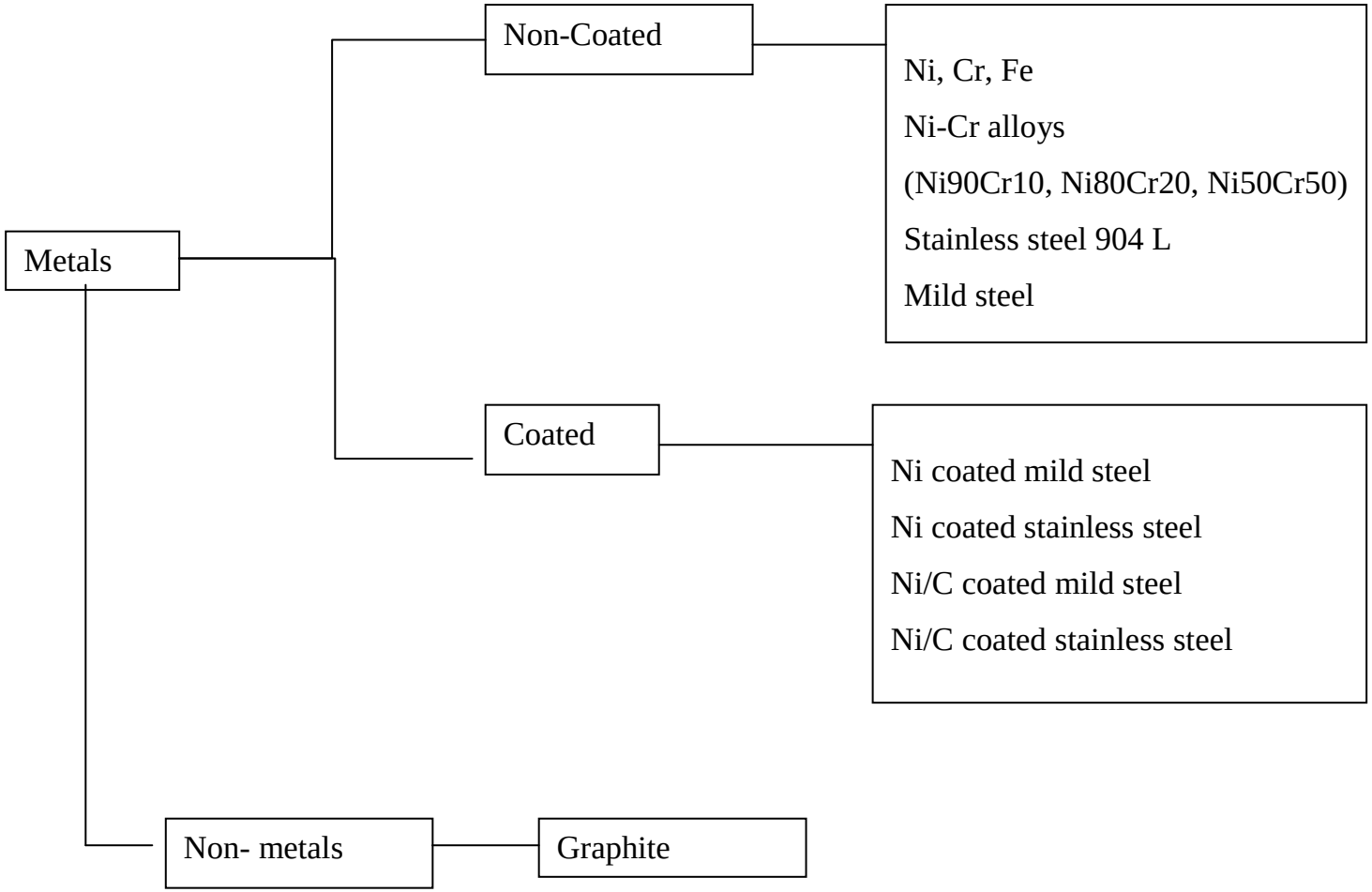

Figure 1.5.1 *Studied materials as candidates on bipolar plates.*

1.6 References

[1] L. Carrette, K. Friedrich, U.Stimming *CHEMPHYSCHEM* 2000, **1**, 162-193.
[2] M.J. Cropper, S. Geiger, D.M. Jolie *Journal of Power Sources* **131** (2004) 57-61.
[3] Steele B.C.H., Heinzel A., Nature (Lond.) 414 (2001) 345.
[4] S. Lee, C. Huang, J. Lai, Y. Chen *Journal of Power Sources* **131** (2004) 162-168.
[5] E. Middelman, W. Kout, B. Vogelaar, J. Lenssen, E. de Waal *Journal of Power Sources* **118** (2003) 44-46.
[6] S.Haile, *Acta Materialia* **51** (2003) 5981- 6000.
[7] M. Neergat, A.K. Shukla, *Journal of Power Sources* **102** (2001) 317–321.
[8] M. Ghouse, H. Abaoud, A. Al-Boeiz, M. AbdulHadi *Applied Energy* **60** (1998) 153-167.
[9] J. P. Vanhanenen, P. S. Kauranenen, *Int .J. Hydrogen Energy*, **Vol. 22**, No. 7, pp. 707-713, 1997.
[10] A.Bauen, *Ins.J.Hydrogen Energy* **28** (2003) 695-701.
[11] C. K. Dyer, *Journal of Power Sources* **106** (2002) 31-34.
[12] M. Nurdin, in: Proceedings of the Fuel Cell Home Conference, 2001, pp. 17-28.
[13] J. Wind, R. Späh, W. Kaiser, G. Böhm *Journal of Power Sources* **105** (2002) 256-260.
[14] A. Hermann, T. Chaudhuri, P. Spagnol *International Journal of Hydrogen Energy* **30** (2005) 1297-1302.
[15] S. Lister, G. McLean *Journal of Power Sources* **130** (2004) 61-76.
[16] S .E. Iyuke, A.B. Mohamad, *Journal of Power Sources* **114** (2003) 195-202.
[17] A.A. Shah, F.C. Walsh *Journal of Power Sources* **185** (2008) 287- 301.
[18] R. Makkus, A. Janssen, F. de Bruijn, R. Mallant *Fuels Cell Bulletin* **No 17.**
[19] M. Li, C. Zeng, S. Luo, J. Shen, H. Lin, C. Cao *Electrochimica Acta* **48** (2003) 1735-1741.
[20] F. Dundar, E. Dur, S. Mahabunphachai, M. Koç *Journal of Power Sources* **195** (2010) 3546-3552.
[21] A.S. Woodman, E.B. Anderson, K.D. Jayne, and M.C. Kimble, *Development of Corrosion-Resistant Coatings for Fuel Cell Bipolar Plates,* American Electroplaters and Surface Finishers Society 1999, AESF SUR/FIN '99 Proceedings, 6/21-24.
[22] D.R. Hodgson, B. May, P.L. Adcock, D.P. Davies Journal of Power Sources **96** (2001) 233-235.
[23] H. Wang, M. Sweikart, J. Turner *Journal of Power Sources* **115** (2003) 243-251.
[24] Y. Wang, D. Northwood *Electrochimica Acta* **52** (2007) 6793-6798.
[25] N. Cunningham, D. Guay, J. Dodelet, Y. Meng, A. Hill, A. Hay *Journal of the Electrochemical Society* **149** (7) A905-A911 (2002).
[26] T. Matsuura, M. Kato, M. Hori *Journal of Power Sources* **161** (2006) 74-78.
[27] M. Brady, K. Weisbrod, I. Paulauskas, R. Buchanan, K. More, H.Wang. M. Wilson, F. Garzon, L. Walker *Scripta Materialia* **50** (2004) 1017-1022.
[28] V. Mehta, J. Cooper *Journal of Power Source* **114** (2003) 32-53.
[29] R.A. Antunes, M. C. L Oliveira, G. Ett, V. Ett *International Journal of Hydrogen Energy* **Vol. 35**, 8 (2010) 3632-3647.
[30] Karol Przybyłowicz *Metaloznawstwo WTN*, Warsaw 2007.
[31] S.A. Bradford *Corrosion control*, 2nd edition, ASM International, 2002
[32] L. L. Shreir, R. A. Jarman, G.T. Burstein *Corrosion Metal/ Environment reaction*, Vol.1 third edition (1994).

[33] E. Mattsson *Basic Corrosion Technology for Scientists and Engineers*, J. Wiley& Sons New York, 1989.
[34] K.H. Lo, C.H. Shrek, J.K.L. Lai *Materials Science and Engineering* ***R*** **65** (2009) 39-104.
[35] E. McCafferty *Introduction to Corrosion Science*, Springer New York, 2010.
[36] B. Beverskog, I. Piugdomenech *Corrosion Science*, **Vol.39**, No. 5, pp. 969-980, 1997.
[37] W.D. Callister *Materials Science and Engineering an Introduction* seventh edition, USA, 2007.
[38] H.J. Engell Passivity of Metals- N. Sato Passivaty of Metals and Passivating Films, Electrochemical Society, New Jersey (1978).
[39] S. S.Dihrab, K. Sopian, M. A. Alghoul, M.Y.Sulaiman *Renewable and Sustainable Energy Reviews* **13** (2009) 1663-1668.
[40] J.S.Kim, W.H.A. Peelen, K.Hemmes, R.C. Makkus *Corrosion Science* **44** (2002) 635-655.
[41] A. Iversen *Corrosion Science* **48** (2006) 1036-1058.
[42] B.L. Bramfitt, A.O.Benscoter *Metallographer quide;practices and procedures for Irons and Steels*, Material Park USA, 2002
[43] G.F. Vander Voort, *Metallography: Principles and Practice*, ASM International, Materials Park, OH, 1999
[44] H.Iken, R. Basseguy, A. Guenbour, A. Ben Bachir *Elecrochimica Acta* **52** (2007) 2580-2587.
[45] P.A. Schweiter *Fundamentals of metallic Corrosion, Atmospheric and media Corrosion of Metals*, Corrosion Engineering Handbook 2nd Edition, CRC Press Taylor & Francis Group, USA 2007.
[46] H.P Sachin, G. Achary, Y. A. Naik, T. V. Venkatesha *Materials Chemistry and Physics* 104 (2007) 422-428.
[47] A. Pardo, M. C. Merino, A. E. Coy, F. Viejo, R. Arrabal, E. Matykina *Corrosion Science* **50** (2008) 1796-1806.
[48] B. Leffler, *STAINLESS- stainless steels and their properties*
[49] V.V. Parshutin, N.L. Bogdashkina, G.P. Chernova *Protection of Metals* **Vol. 43** (2007) 59-65.
[50] B. MacDougall, M. Cohen *Passivity of Metals*, ed. R.P. Frankanhal and J. Kruger, elctrochem. Soc. Princeton, New York, 1978.
[**51**] V. Maurice, S. Cadot, P. Marcus *Surface Science* **458** (2000) 195-215.
[**52**] T. Ossowski, A. Kiejna *Surface Science* **602** (2008) 517-524.
[53] T. Jukna, J. Baltrušaitis, V. Sinkevičius, D. Viržonis *Thin Solid Films* **516** (2008) 2943-2947.
[54] D. Sazou *Electrochimica Acta*, **Vol. 42** No. 4, pp 627-637, 1997.
[55] V. Alonzo, F. Berthier, L. Priester *Materials Science and Engineering* **A249** (1998) 158-166.
[56] C. L. Briant, K.S. Kumar, N. Rosenberg, H. Tomioka *International Journal of Refractory Metals & Hard Materials* **18** (2000) 9-11.
[57] T. Kamimura, M. Stratmann *Corrosion Science* **43** (2001) 429-447.
[58] G.M. Atenas, E. Mileczarski, J.A. Mielczarski *Journal of Colloid and Interface Science* **289** (2005) 157-170.
[59] H. J. Engell *Passivity of Metals - H. Uhlig History of Passivity, Experiments and Theories*, pp.1-27, Electrochemical Society, New Jersey (1978).

[60] H.J. Engell *Passivity of Metals* -F.M. Delnick, N. Hackerman *The Passivity of Metals and Passivating Films*, pp 29-57, Electrochemical Society, New Jersey (1978).
[61] A. Guenbour, H.Iken, N. Kebkab, A. Bellaouchou, R. Boulif, A. Ben Bachir *Applied Surface Science* **252** (2006) 8710.
[62] L. Xiaowei, R. Jean-Charles, Y. Suyuan *Nuclear Engineering and Design* **277** (2004) 273-280.
[63] M. Wissler, *Journal of Power Sources* **156** (2006) 142-150.
[64] M. Chakravortty, P. K. Paramguru and J. K. Jena, *Hydrometallurgy*, **59** (2001) 45.
[65] M. Bojinov, G. Fabricius, P. Kinnunen, T. Laitinen, K. Mäkelä, T. Saario and G. Sundholm, *Electrochim. Acta*, **45** (2000) 2791.
[66] M. Bojinov, G. Fabricius, P. Kinnunen, T. Laitinen, K. Mäkelä, T. Saario and G. Sundholm and K. Yliniemi, *Electrochim. Acta*, **45** (2002) 1697.
[67] E. McCafferty, *Corr.Sci*., **42** (2000) 1993.
[68] E. McCafferty, *Corr. Sci.*, **44** (2002) 1393.
[69] E. McCafferty *Corrosion Science* **50** (2008) 3622-3628.
[70] J.M.Marioli, L.E.Sereno *Electrochimica Acta*, **Vol. 40**, No.8, pp.983-989, 1995.
[71] E. McCafferty *Corrosion Science* **47** (2005) 1765-1777.
[72] E.M. Lehockey, G. Palumbo, P. Lin, A.M. Brennenstuhl, *Scripta Mineralia*, **Vol. 36**, No.10, pp. 1211-1218, 1997.
[73] M. Bojinov, T. Tzvetkoff *J. Phys. Chem. B* **107**, 2003, 5101-5112.
[74] I. Betova, M. Bojinov, T. Tzvetkoff, *Electrochimica Acta* **49** (2004) 2295-2306.
[75] O.V. Kasprova, *Protection of Metals*, **Vol. 36**, No.6, 2000, pp. 524-532.
[76] A.M. Rana, A.F. Khan, A. Abbras, M.I. Ansari *Materials Chemistry and Physics* **80** (2003) 228-231.
[77] K. Heusler, *Corrosion Science*, **Vol. 39** No. 7, pp. 1177-1191, 1997.
[78] Y.Zhang, X. Peng, F.Wang *Materials Letters* **58** (2004) 1134-1138.
[79] M. Danişman, N. Cansever *Journal of Alloys and Compounds* **493** (2010) 649-653.
[80] A. Ul-Hamid *Materials Chemistry and Physics* **80** (2003) 135 -142.
[81] J. M. Marioli, L. E. Sereno *Electrochimica Acta*, **Vol. 40**, No.8 pp. 983-989, 1995.
[82] D. Pletcher *A First Course in Electrochemistry*, 2nd Edition, Cambridge 2009.
[83] D. Loveday, P. Peterson, B. Rogers Part 2 Applications of EIS to Coatings JCT *Coatings Tech* **October 2004.**
[84] K. Darowicki, S. Krakowiak, P. Ślepski Electrochimica Acta **49** (2004) 2909-2918.
[85] C. Liu, Q. Bi, A. Leyland, A. Matthews *Corrosion Science* **45** (2003) 1243-1256.
[86] D. D Macdonald *Electrcochimica Acta* **51** (2006) 1376-1388.
[87] J. Hwang, K. S. Kirkpatrick, T. O. Mason, E. J. Garboczi *Solid State Ionics* **98** (1997) 93-104.
[88] P. Agarwal, M. E. Orazem, L. H. Garcia-Rubio *J. Electrochem. Soc*. **Vol. 139**, No 7 (1992).
[89] N. Wagner, T. Kaz, K. A. Friedrich *Electrochimica Acta* **53** (2008) 7475-7482.
[90] V. Freger, S. Bason, *Journal of Membrane Science* **302** (2007) 1-9.
[91] J. R Macdonald *Solid State Ionics* 176 (2005) 1961-1969.
[92] J. R. Macdonald *Electrochimica Acta*, Vol. 35, No. 10 (1990) 1483-1492.
[93] D. E. Tallman Electrochemical Impedance, February 2, 2009.

[94] F.C. Walsh *A simple Electrochemical Impedance Spectroscopy Analysis of an electrodeposited Nickel coating on steel*, Summer School, Southampton, August 2009
[95] J. R Macdonald *Encyclopedia of Physical Science and Technologies* (2004) 111-124.
[96] D. Loveday, P. Peterson, B. Rogers Part 1 Fundamental of Electrochemical Impedance Spectroscopy *JCT Coatings Tech* **October 2004.**
[97] B. D. Cullity *Podstawy dyfrakcji promieni rentgenowskich* PWN (1964).
[98] C. Giacovazzo, H. L. Monaco, G. Artoli, D. Viterbo, G. Ferraris, G. Gilli, G. Zanotti, M. Catti *Fundamentals of Crystalography*, 2nd edition, Oxford 2002.
[99] C. Hammond *The Basics of Crystallography and Diffraction, 3rd edition* Oxford University Press 2009.
[100] P. J. Goodhew, J. Humphreys, R. Beanland *Electron Microscopy and Analysis* 3rd edition, London 2001.
[101] T. D. Xiao, S. Torban, P. R. Strutt and B. H. Kear *NanoStructured Materials* , **Vol. 7**, No.8, pp. 857-871 (1996).
[102] L. Karmazin Materials Science and Engineering, **54** (1982) 247-256.
[103] J. Lapinski Optimization of protective coating for steel-based bipolar plates in PEM fuel cell, 2010

Chapter 2

Experimental

2.1 Chemicals and solutions.

All chemicals used during the study are listed in Table 2.1, along with their supplier and purity.

Table 2.1 *Chemicals used in the study.*

Name	Chemical formula	Producer/Grade
Phosphoric acid	H_3PO_4	Fisher/98 %
Sulphuric acid	H_2SO_4	Fisher/99%
Sodium sulphate	Na_2SO_4	Acros/99%
Sodium fluoride	NaF	AnalaR®/99%
Potassium sulphate	K_2SO_4	Fisher/99.5%
Nitric acid/70%	HNO_3	Fisher /reagent
Potassium chloride	KCl	Fisher/analytical reagent
Oxalic acid dihydrate	$HO_2CCO_2H \cdot 2\ H_2O$	Avocado/98%
Hydrochloric acid	HCl	Fisher /98%
Methanol	CH_3OH	Fisher/99%
Mercury	Hg	Aldrich/99
Mercury (I) chloride	$HgCl_2$	Aldrich/99.5
Mercury (I) sulphate	Hg_2SO_4	Aldrich/99
Boric acid	H_3BO_3	Alfa Aesar/98%
Nickel chloride hexahydrate	$NiCl_2 \cdot 6\ H_2O$	Alfa Aesar/98%
Nickel sulphate	$NiSO_4 \cdot 7\ H_2O$	Acros
Sodium dodecyl sulphate (SDS)	$C_{12}H_{25}SO_4Na$	Fisher
Chromic sulphate	$Cr_2(SO_4)_3 \cdot 15\ H_2O$	BDH/96-102 %
Acetone	CH_3COCH_3	Fisher
Nitrogen	N_2/oxygen free	BOC
Oxygen	O_2	BOC
Argon	Ar (5% of H_2)	BOC

Solutions were prepared using water from a Whatman Analyst Water Purifier system Nr 14039. Glassware was washed with Teepol - the multi-purpose detergent (Teepol Company) and rinsed thoroughly with deionised water.

2.2 Electrode materials and fabrication.

2.2.1 Working electrodes.

Working electrodes used during this study were fabricated from rods, foils and electroplated foils. A short length was cut from each rod (mainly Ni-Cr alloys), one end was connected to a copper contact wire using solder and then the sample was sealed into shrinkable tube (RadioSpares) by heating at ~ 353 K for 20 minutes; only a disc, area ~ 1 cm^2, was exposed to the solutions and this surface could also be readily polished. Foils were cut into small discs and mounted into a PTFE holder (see figure 2.2.1.1) whereby the disc was held by a gasket between the outer and inner parts of the holder. Contact was made by a Ni wire held in place by the gasket. In general, the discs made from the foils were used only for single experiments.

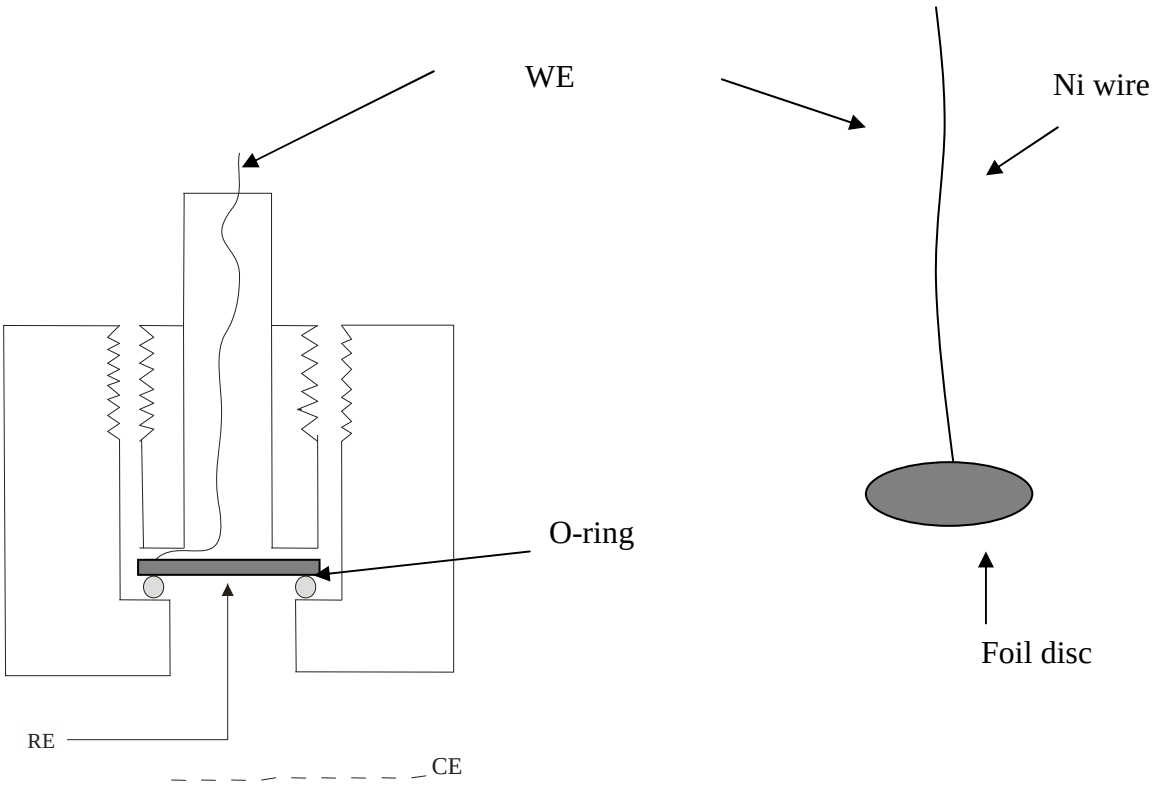

Figure 2.2.1.1 *PTFE holder and metal disc as WE.*

2.2.1.1 Corus samples.

Corus supplied a number of steel and coated steels as listed in Table 2.2.

Table 2.2 *List of materials supplied by Corus*

Material	**Composition**	**Short characterisation**
SS 904 L	Foil/ 0.15mm thick	Shiny surface with mirror finish effect
Mild steel	Foil/0.57 mm thick	Shiny surface with mirror finish effect
Ni coated Mild Steel	3µm layer of Ni electroplated on mild steel	Shiny surface with mirror finish effect
Ni/C (40 g/dm^3) coated Mild Steel	Mixed layer of Ni and C on mild steel	Matt/ grey surface

Table 2.3 *Compositions of stainless and mild steels.*

Steel	% Cr	% Mo	% Ni	% Fe	% C	% Mn	% Si	% P	% S	%Cu
316	16-18.5	2-3	10-14	balance	<0.03	<2.0	<1.0	0.045	0.035	-
904L	19-23	4-5	23-28	balance	0.02	2.0	1.0	0.045	0.035	1-2
Mild	-	-	-	balance	0.08	0.4	-	0.03	0.03	-

The Ni coated mild steel was electroplated from a Watts bath in an automated, reel to reel plating line in Dusseldorf. The Ni/C layer was plated on the same line but the electrolyte contained 40 g/l of dispersed C granules (5 µm of MF 5/99.5-99.9 NGC Naturgraphit Gmbh).

2.2.1.2 Commercial materials.

Pure metals and alloys purchased and used in this project are listed in Table 4.

Table 2.4 *List of commercial materials used during the study.*

Name	**Type**	**Supplier/grade**
Nickel	Foil/thickness 0.125 mm	Goodfellow/99.98 %
Chromium	Foil/thickness 0.5 mm	Goodfellow/99.98 %
Ni90Cr10	Rod/diameter 12 mm	Goodfellow/99.98 %
Ni80Cr20	Foil/thickness 0.125 mm	Goodfellow/99,98%
	Rod /diameter 10 mm	Goodfellow/99.98 %
Ni50Cr50	Rod/diameter 10 mm	Testbourne/99.95 %

2.2.1.3 Electrodeposited materials.

2.2.1.3.1 Ni coated mild steel.

Nickel coated mild steel samples were prepared by Jacek Lapinski[1] from a Watts bath (50 g/l $NiCl_2 \cdot 6H_2O$, 160 g/l $NiSO_4 \cdot 6 H_2O$ and 45 g/l boric acid adjusted to regulated pH = 3.5) and anionic surfactant sodium dodecyl sulphate (SDS) ~ 400 mg/l. The steel cathode (10 cm x 6 cm) was placed equidistant from two parallel Ni anodes on each side a beaker cell with a magnetic stirrer bar. The following the pre-treatment was used for mild steel: electrodegreasing with a current density j = - 15 to -80 mA cm^{-2} during time t = 15 to 30 s. Electrodeposition conditions: j = -10 mA cm^{-2} at a temperature 333 K, stirring conditions ~ 300 rpm and deposition time 30, 1500 and 3000 s corresponding to 1µm, 5 µm and 10 µm Nifilm thicknesses.

2.2.1.3.2 Ni graphite coated stainless steel.

Nickel graphite composite was prepared by Jacek Lapinski[2] in the following way; the substrate was stainless steel.

- The surface was electrodegreased with j = + 15 mA cm^{-2} during t = 1 minute, followed by dipping in H_2SO_4 (1:1) for t = 5 - 10 s.

- A Wood's strike with j = -100 mA cm^{-2} during t =30 s in an electrolyte consisting of 240 g dm^{-3} $NiCl_2 \cdot 6H_2O$ + 100 ml dm^{-3} concentrated HCl was used to create an initial layer. Temperature 333 K.

- The Ni layer was thickened using the Watts bath 50g/l $NiCl_2 \cdot 6 H_2O$, 160 g/l $NiSO_4 \cdot 6 H_2O$ and 45 g/l boric acid adjusted to regulated pH 3.5. Temperature 333 K. j = -100 mA cm^{-2} at a temperature 333 K, stirring conditions ~ 300 rpm and deposition time in seconds corresponding to 1µm, 5 µm and 10 µm Ni film thicknesses.

- As soon as possible after the Ni layer deposited onto the steel, the next layer of Ni with graphite particles (2 µm MF2/99.-99.9 or 5 µm MF2/99.-99.9 from NGC Naturegraphit Gmbh), concentration 1 – 10 g dm^{-3} was deposited onto the Ni in a flow cell. Flow rate 23 cm s^{-1}. Temperature 333 K. j = - 10 mA cm^{-2}

2.2.2 Cleaning.

Except where otherwise stated, electrodeposition used a fresh sample of foil (washed with acetone and rinsed well with water).

2.2.3 Heat treatment.

In an attempt to produce a Ni-Cr layer on Ni, 20 nm Cr was deposited on Ni coated mild steel and treated with different temperature and time in furnace (Lenton Thermal Design Ltd) under argon - Ar (5% of H_2).

2.2.4 Reference electrodes.

2.2.4.1 Hg/Hg_2SO_4

The reference electrodes were prepared in the laboratory using two concentric glass tubes, the outer one having a ceramic sinter in its end (figure 2.2.4.1.1)
Drops of mercury were placed into the glass until a platinum wire contact sealed into the inner glass tube was covered. A mixture of K_2SO_4 and Hg_2SO_4 (1:1) and a few drops of saturated K_2SO_4 was the placed onto the mercury layer and pressed with a wooden stick. The wool glass was inserted into the tube to hold the mercury and paste in place.

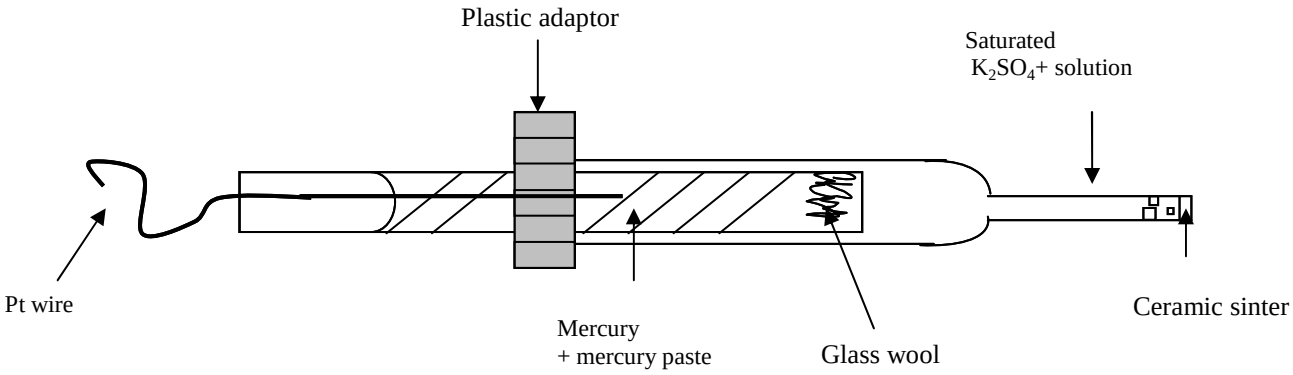

Figure 2.2.4.1.1 *Schematic representation of a reference electrode.*

The Hg/Hg_2SO_4 reference electrode was used to eliminate possible contamination of the electrolytes by Cl^- ions as this could have a strong influence on the corrosion behaviour of the metals and alloys.

2.2.4.2 Saturated calomel electrode (SCE).

A saturated calomel electrode was used as reference electrode in some experiments. The preparation procedure was the same as for the SMSE, except the solid was KCl and Hg_2Cl_2.

2.2.5 Counter electrodes.

In all experiments as counter electrode used was a Pt mesh.

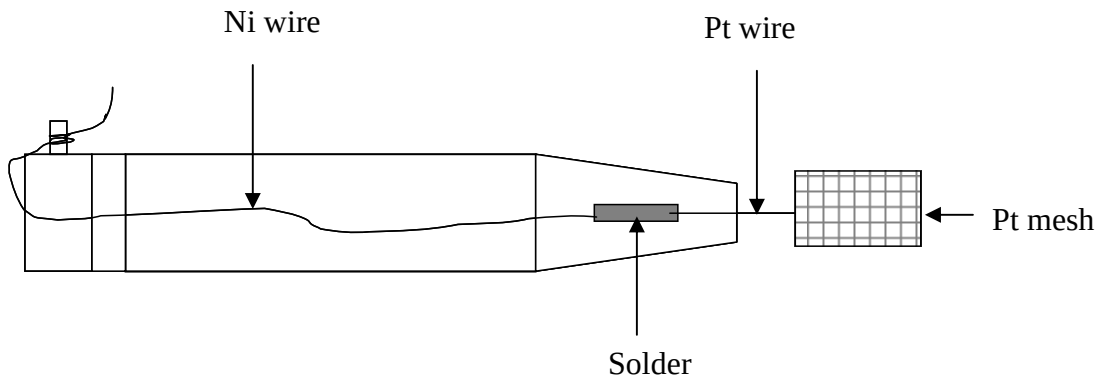

Figure 2.2.5.1 *Scheme of auxiliary electrode.*

2.3 Electrochemical cells.

2.3.1 Cyclic Voltammetry and Chronoamperometry.

Cyclic voltammetry (generally 20 mV s^{-1}) was used to define the dissolution and film formation reactions occurring as a function of applied potential for each of the materials (metals, alloys and electroplated samples). Glass, three electrode cells (see figure 2.3.1.1) were used and they had water jackets as most experiments were carried out at 353 K; commonly, the solutions under study were preheated and, during experiments, water was circulated through the jacket from a temperature controlled water bath (Julobo F12). In each cell, the working and reference electrode were separated by a Luggin capillary whose tip was placed ~ 2 mm from the working electrode surface. The counter electrode was placed in the same solution as the working electrode. The electrolyte (most commonly H_3PO_4, pH 2, without other additions) was either deoxygenated with N_2 or saturated with O_2 by bubbling a fast stream of gas through the solution for ~ 30 minutes.

Constant potential experiments were routinely carried out in a solution containing only phosphoric acid, pH 2, at + 100 mV and – 600 mV vs. $Hg/HgSO_4$. These potentials were selected as an estimate of those seen by a bipolar plate in contact with an O_2 reducing cathode and a H_2 oxidising anode at pH 2. The working electrode for these experiments was generally a foil and the cell was designed so that it was held with a gasket and clamp against a glass flange at the base of the cell. The temperature control and other procedures were as for cyclic voltammetry.

a)

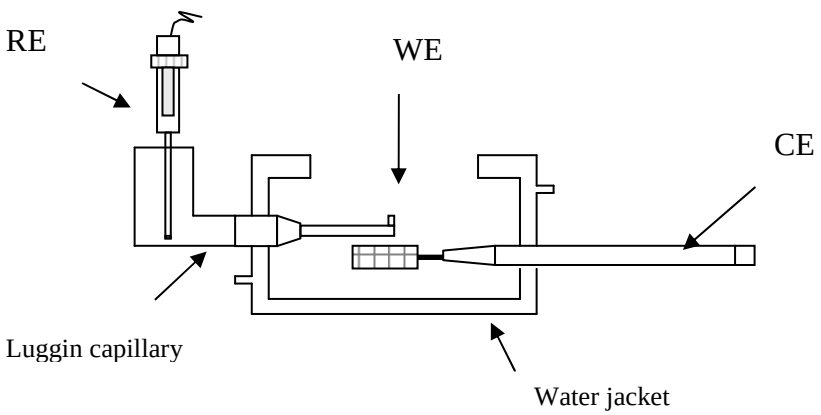

b)

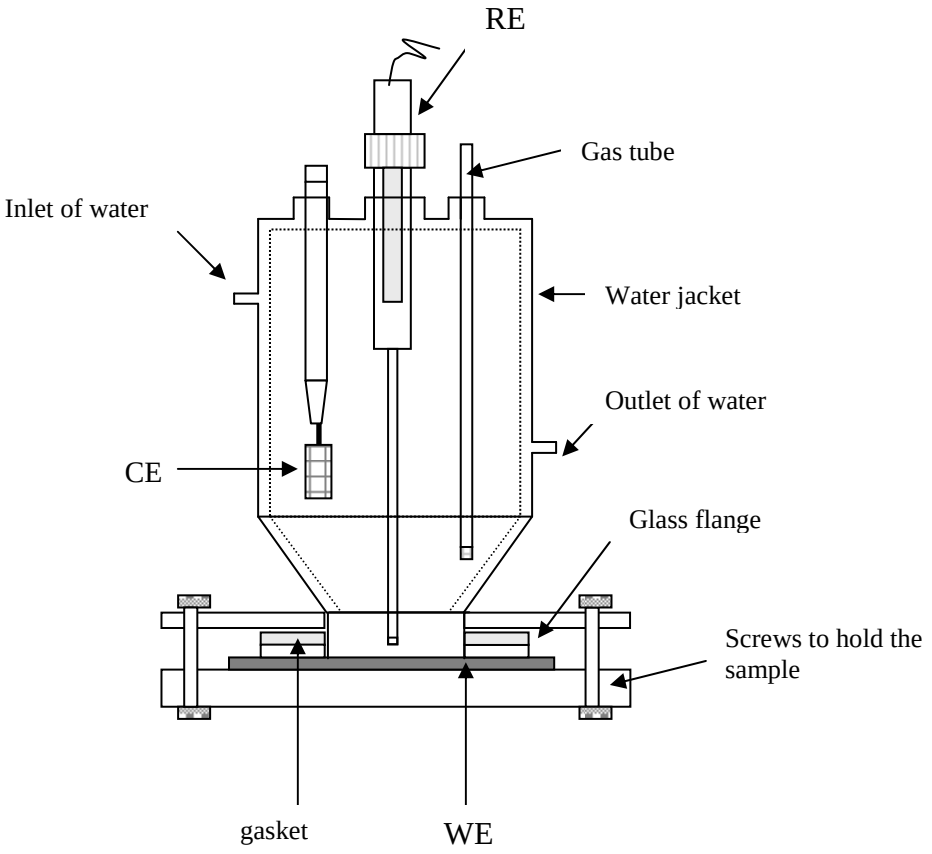

Figure 2.3.1.1 *Electrochemical cells used during study. Electrolyte volume ~ 150 cm^3. Electrode area 0.8 and 5 cm^2 for (a) and (b).*

2.3.2 Electrochemical Impedance Spectroscopy study.

Electrochemical impedance spectroscopy was used:

(a) to investigate the porosity of Ni layers electroplated onto steel. These experiments used 1 M H_2SO_4 as the electrolyte and were carried out 298 K and at the open circuit potential.

(b) to study the corrosion of materials in phosphoric acid, pH 2,at 353 K. Experiments were generally carried out at the open circuit potential both before and after passivation by applying a more positive potential.

The cell for impedance[3] (figure 2.3.2.1) studies were similar to that used for other experiments but had a larger working electrode, ~ 5 cm^2. Data was obtained using a potential modulation of $\pm$ 5 mV and the frequency was scanned from 10 kHz to 0.01 Hz with 100 data points.

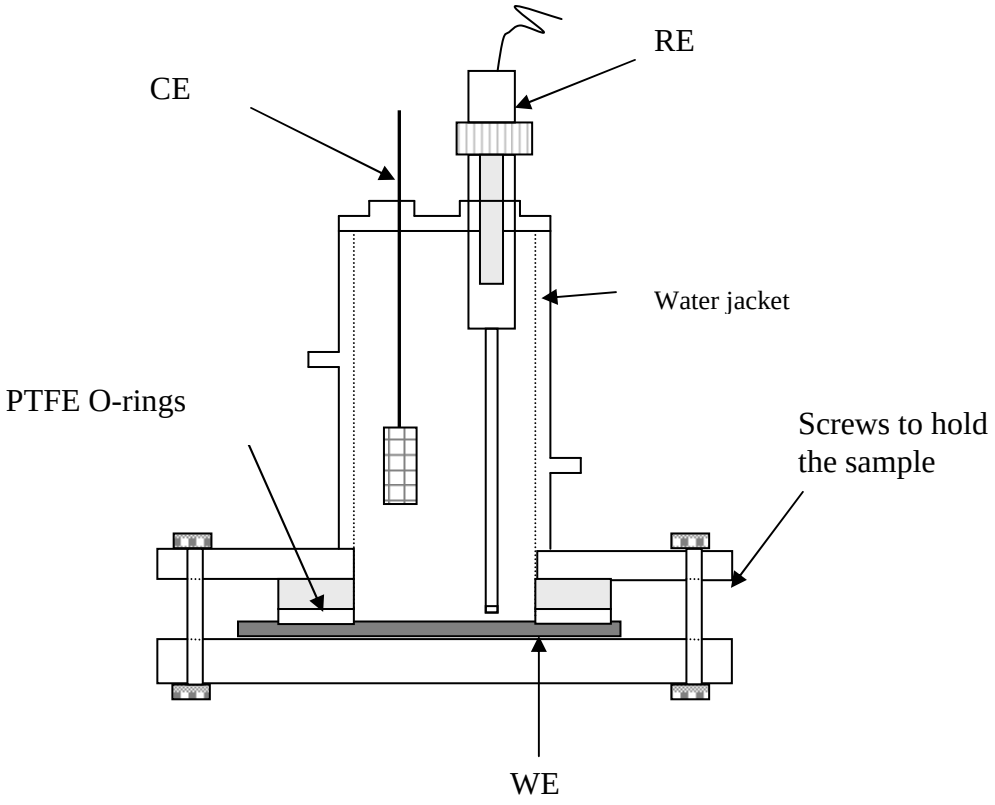

Figure 2.3.2.1 *Cells for electrochemical impedance spectroscopy stud. Electrolyte volume 50 cm^3.*

2.3.3 Electrochemical study for PVD samples.

In order to further understand the influence of the Ni-Cr alloy composition on the stability to corrosion, a combinatorial approach developed in Southampton was employed.10 x 10 arrays of individually connected electrodes (see figure 2.3.3.1) were produced (see later) with different, known composition were prepared by physical vapour deposition and their electrochemistry studied simultaneously. In the specially designed cell (see figure 2.3.3.2), the working electrode array fits into a PTFE holder that bolts on to the glass body of the cell and ensures good electrical contact with pads on a PCB board.

The three electrode system cell connected with holder and PCB, as CE used were a Pt mesh, Hg/Hg_2SO_4 as RE and array as WE (figure 2.3.3.2). Electrochemical cell linked with water bath. Electrolyte (phosphoric acid pH 2) heated up to 343 K and purged ~

30 minutes by argon. Standard conditions for cyclic voltammograms were to use scan rate 20 mVs^{-1} with potential window - 0.8 V to + 0.2 V vs. Hg/Hg_2SO_4.
Chonoamperometric experiments were carried out at constant potential + 100 mV vs. Hg/Hg_2SO_4 during 10 minutes.

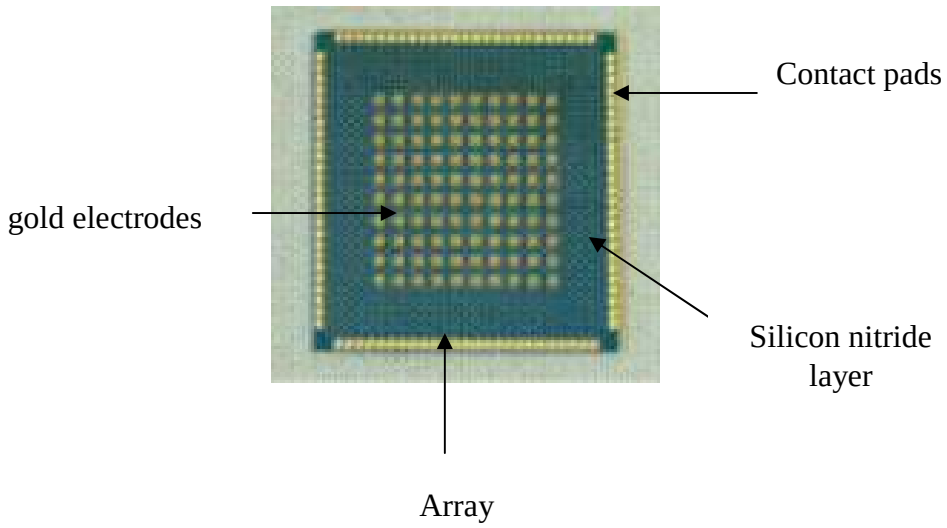

Figure 2.3.3.1 *Scheme of 100 elements working electrode array.*

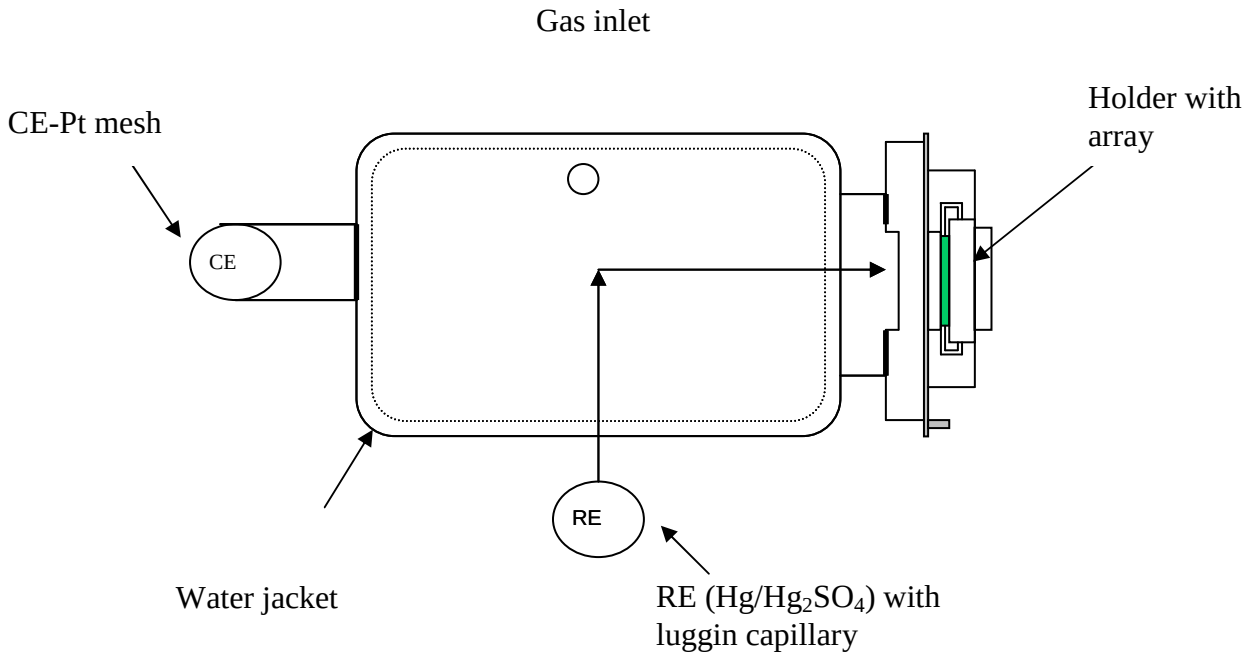

Figure 2.3.3.2 *Schematic view from above of the electrochemical cell with 10 x 10 arrays as working electrode. Electrolyte volume ~ 200 ml.*

2.3.3.1 Preparation of 10 x 10 arrays.

Thin films of alloys composed of different ratios of Cr and Ni were deposited onto a 10 x 10 array of Au pads with physical vapour deposition system. The deposition was carried out in an ultrahigh vacuum system with pressure 10^{-10} mBar [4, and 5].

'Wedges' of Cr and Ni were used to produce the 10 x 10 array and analyses of the deposits by EDX will be shown along side electrochemical data.

2.4 Preparation of materials for microstructures characterisation.

A small piece of the material to be studied was put inside a plastic tube (4 cm x 1 cm). The tube rinsed with release Argent (Buehler) to easier remove the encapsulated electrode from the plastic tube. Alloys were connected with steel wire, for better contact using a silver conductive paint (RS Components) and encapsulated in epoxy resin (mixture 15 ml of Epoxy Resin and 2 ml of EpoxyFix Hardener) by filling the tube and curing at 298 K for approximately 24 hours. After cutting away the plastic tube, the front face of the sample was polished and etched.

2.4.1 Cleaning of electrodes for microstructure characterisation.

The materials were polished successively with 120, 800, 1200, 3000 and 4000 grade emery paper (Struers) until examination of the surface by optical microscopy showed only fine scratches in the same direction. Then the samples were further polished with 6 µm diamond paste on OP –mol cloth and repeatedly polished with 1 µm diamond paste on a DP-mol cloth until scratches could not be seen with the optical microscope. Between each stage, the electrodes were washed with soap solution and then water and acetone before being dried. At the end of the preparation, the samples were cleaned with water in an ultrasonic bath.

2.4.2 Electrolytes for characterise the microstructure.

Table 2.5 presents the solutions used and the other conditions. Before structure investigation each material was electropolished at 298 K.

Table 2.5 *Materials and etching solutions.*

Name	Etch	Etching time
Ni	H_3PO_4 pH 2	5 mV~ 15 minutes
Ni90Cr10	10 % H_3PO_4	40 mA cm^{-2} ~ 90 s
Ni80Cr20	10 % H_3PO_4	40 mA cm^{-2} ~ 30 s
Ni50Cr50	10 % H_3PO_4	40 mA cm^{-2} ~ 60 s
SS 904 L	10 % oxalic acid	1 A ~ 2 min
Mild steel	10 % HCl	1 - 2 minutes
Iron	Nitrial	1 - 2 minutes

For each electro etch experiment the current was controlled by current supplier ISO-TECH IPS23030.

2.5 Electrochemical Equipment.

Potentiostat/Galvanostat model 263 A (Princeton applied Research) were used for cyclic voltammetry and constant potential corrosion tests. The potentiostat was controlled with a PC and data analysed with PC Data analysis software. For all EIS experiments Autolab (Potentiostat/Galvanostat) were used with FRA (Frequency Response Analysis) operating system software. The electrochemical experiments with arrays used instrumentation and software developed by Ilika.

2.6 Microstructures and morphological characterisation of materials.

For better characterisation of the surface materials studied an Optical Microscope (Olympus BHZ-UMA) and Scanning Electron Microscope (XL30 ESEM, Philips) were used.

SEM images of the different structures were obtained with a Back Scattered Electron (BSE) source. The most appropriate combination of voltage, vapour pressure, and spot size were used for each micrograph. The compositions of materials were determined by EDX (Energy Disperse X-ray) analysis. For analysis of 10 x 10 arrays were used JEOL JSM-5910 SEM with software to allow convenient and rapid data handling.

2.6.1 XRD.

Data were collected using a diffractometer, Siemens D5000 in a 2θ configuration.

The X-ray source was a monochromatic copper radiation $K_{\alpha 1}$ (1.5406 Å) passed directly onto a sample.

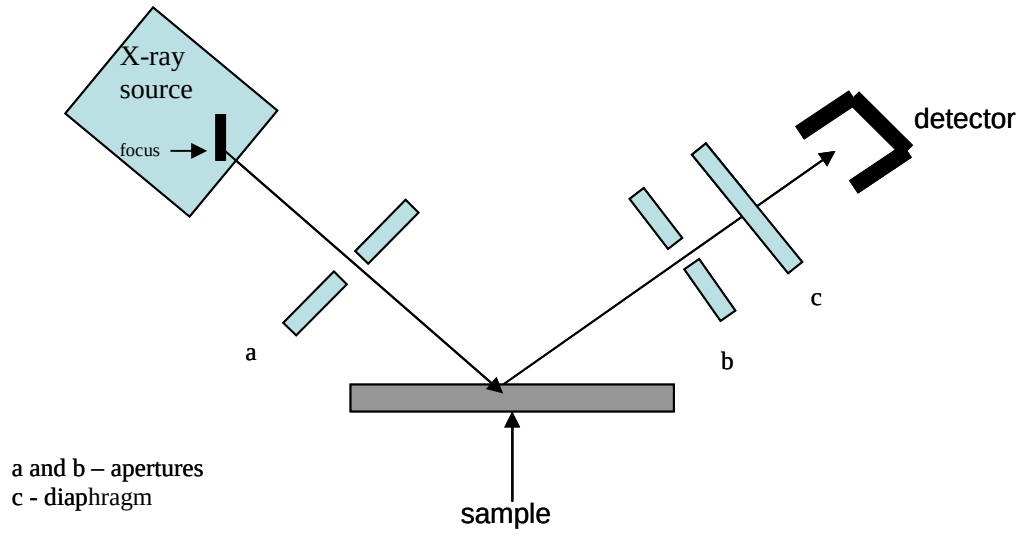

Figure 2.6.1.1 *Schematic representation of the Siemiens D5000 diffractometer.*

2.7 References

[1] J. Lapinski *Optimization of protective coating for steel-based bipolar plates in PEM fuel cell*, 2010
[2] J.Lapinski, D.Pletcher, F.Walsh *Surface and Coating Technology* **205** (2011), 5205-5209
[3] D.D. Macdonald *Electrochimica Acta* **51** (2006) 1376-1388
[4] S.Guerin, B.E. Hayden, D. C. A. Smith *J. Phys. Chem. B* 2006, **110** 14355-14362.
[5] S.Guerin, B.E. Hayden *J.Comb.Chem*.2006, **8**, 66-73.

Chapter 3

Studies of Base Materials and Electroplated Layers.

This chapter presents results and investigations of the metals as substrates or electrodeposits in the later studies. Most experiments used phosphoric acid, pH 2, at a temperature of 353 K as the electrolyte although the influence of temperature and phosphoric acid concentration were also undertaken.

- Study of metal substrate materials and electrodeposits.
- The porosity of the Ni electrocoating.
- Characterisation of influence Ni graphite layer on the corrosion rate.
- The behaviour of graphite in dilute phosphoric acid.

3.1 Base Materials

3.1.1 A short characterisation of metals and steels

This part presents results for pure metals (Fe, Ni and Cr) and steels (stainless steel, mild steel, Ni coated mild steel and Ni/C 40 g/dm^3 onto mild steel). Pure metals (Ni, Cr) can be use as protective layers for materials with a higher rate of corrosion. Steels have many of the properties required for the manufacture of bipolar plates although stainless steel is considered too expensive for use in bipolar plates.

A major concern is the stability of the steel to corrosion, particularly over the lifetime of the fuel cell, maybe 5 years. While much is known about the corrosion of steels in many environments, the environment within the fuel cell is unusual and less studied. In general, the corrosion resistance of steel may be increased substantially by the addition of chromium and other metals (ie. by using stainless steels). In fact, it is far from certain that any steel will have all the properties required, particularly a low electrical contact resistance since the stability to further corrosion probably results from a corrosion film on the steel surface. Hence, it is necessary to consider coated steels to reduce corrosion and also to lower the contact resistance.

Stainless steel and mild steel have been used as substrates for the deposition of different layer to study (thick Ni layer and/or Ni/C). The graphite powder in the Ni layer is intended to decrease the contact resistance between the bipolar plate and the MEA in the fuel cell.

3.1.2. Fe, Ni, Cr

Investigations of pure Ni, Ni coated mild steel, Ni/C coated mild steel; mild steel and stainless steel have been made in the electrolyte selected to mimic conditions within the cathode component of the fuel cell:

- phosphoric acid pH 2 (no other additives or electrolytes) at 353 K.

The media was selected to ‘mimic’ the environments in fuel cells based on MEA with poly-benzimidazole /H_3PO_4 electrolytes.

The behaviour and nature of three base metals Fe, Ni, and Cr have been characterised in deoxygenated phosphoric acid pH 2 at 353 K temperature. Cyclic voltammograms were recorded over the potential ranges where corrosion and passivation occur with a scan rate 20 mV s^{-1}. Following some trials with variable preparations of the surfaces, the metals were only washed with acetone and water as this seemed to give the most reproducible results.

In the case of iron, two sizes of the electrode have been used a) a 1 cm^2 disc cut out from Fe sheet and b) a 0.2 cm^2 disc fabricated from a rod. The larger electrode gave a voltammogram with very large currents and the current was essentially linear over the whole potential range; clearly IR drop was determining the response. When the size of working electrode was changed to 0.2 cm^2, the response was closer to that expected with a large anodic peak dominating the voltammogram (figure 3.1.2.1a). At the starting potential of – 1600 mV, a substantial cathodic current density is observed and hydrogen evolution can be seen to be occurring. The current crosses the zero current axis at - 980 mV, which is similar to the corrosion potential measured with a DVM. Close to the corrosion potential the current density is a linear function of potential and the slope can be used to estimate a corrosion resistance, $R_p \sim 14\ \Omega\ cm^{-2}$. An active corrosion region is located approximately between - 900 mV and + 100 mV. The anodic peak has a maximum current density, j_p= 193 mA cm^{-2} and the charge under the oxidation peak is ~ 12.5 C cm^{-2} corresponding to the loss of 3.5 mg cm^{-2} of Fe, a total change in the surface. Beyond the peak, the surface passivates to some extent but corrosion continues at a relatively high rate of j ~ 10 mA cm^{-2}. This corrosion continues on the reverse scan. Moreover, some reactivation is observed approaching the corrosion potential and this may suggest that the oxide layer leading to passivation becomes damaged. Also the current density for H_2 evolution at the negative end of the scan is higher in the reverse scan; probably the surface area of iron exposed to solution has increased as a result of the corrosion. On continuing the potential cycling, the anodic peak becomes smaller and passivation becomes more complete.

$$Fe \rightarrow Fe^{2+} \qquad (3.1)$$

The cyclic voltammograms for Ni were commenced at - 800 mV, where there is a small hydrogen evolution current. The corrosion potential is at E_{corr} = - 690 mV and the linear response close to the corrosion potential can be used to estimate a value for the corrosion resistance $R_p \sim 811\ \Omega\ cm^{-2}$. The active corrosion region extends from - 600 mV to - 350 mV. There is a well formed anodic peak at - 400 mV with current

density approximately ~ 13 mA cm^{-2}. This large anodic peak corresponds to significant dissolution of nickel and the charge under the oxidation peak is ~ 0.2 C cm^{-2}. Beyond the peak, the anodic current drops to ~ 3 mA cm^{-2}. Passivation is occurring but the surface is continuing to corrode at a significant rate. On the reverse scan corrosion continues and, indeed, over the potential range - 500 to - 750 mV the current is much higher on the reverse scan than forward one; it seems that surface in this region is more active for the corrosion after the scan to positive potentials. With continuous scans, the anodic peak gets smaller and the passivation process is more complete.

$$Ni \rightarrow NiO(OH) \qquad (3.2)$$

$$NiO(OH) \rightarrow NiO \qquad (3.3)$$

The cyclic voltammogram for chromium was commenced at - 1200 mV. At the initial potential, hydrogen evolution occurs at a low rate. The corrosion potential was - 900 mV. Close to the corrosion potential, the polarization resistance equals R_p ~ 8878 Ω cm^{-2}.

On the forward scan the currents are low over the whole potential range and although there is a small anodic peak, it is a minor feature and poorly formed. On the reverse scan, the current becomes cathodic negative to – 300 mV and even positive to this value, the anodic currents are very low. The origin of this reduction wave is uncertain. Experiments with an oxygen saturated electrolyte did not lead to an increase in the wave height ruling out oxygen reduction as the reaction occurring. Some reduction of a surface oxide is a possibility. With continuous cycling, the current density become is smaller and the response becomes even more featureless. It appears that chromium is largely passivated before the voltammetry is commenced.

$$Cr \rightarrow Cr_2O_3 \qquad (3.4)$$

Table 3.1 summarises the electrochemical data for pure metals taken from the voltammograms.

Ni, Cr, and Fe were also subjected to a test where the potential was held constant at + 100 mV vs. Hg/Hg_2SO_4 (calculated the potential for the bipolar plate in a fuel cell) in deoxygenated phosphoric acid pH 2 at 353 K for 1 hour and the current density was monitored. The results are presented in figure 3.1.2.2.

For all three metals, the current decreased with time. The potential corresponds to a value well positive to the anodic peaks in the voltammograms and hence where the

metals are passivated. But there were large differences in corrosion rate for the three metals.

The corrosion rates clearly decrease in the order Fe > Ni > Cr and the current densities at the end of the hour are reported in Table 3.2. The values range over a factor > 10^4 and clearly iron would be unsuitable for a bipolar plate while chromium would be much more promising.

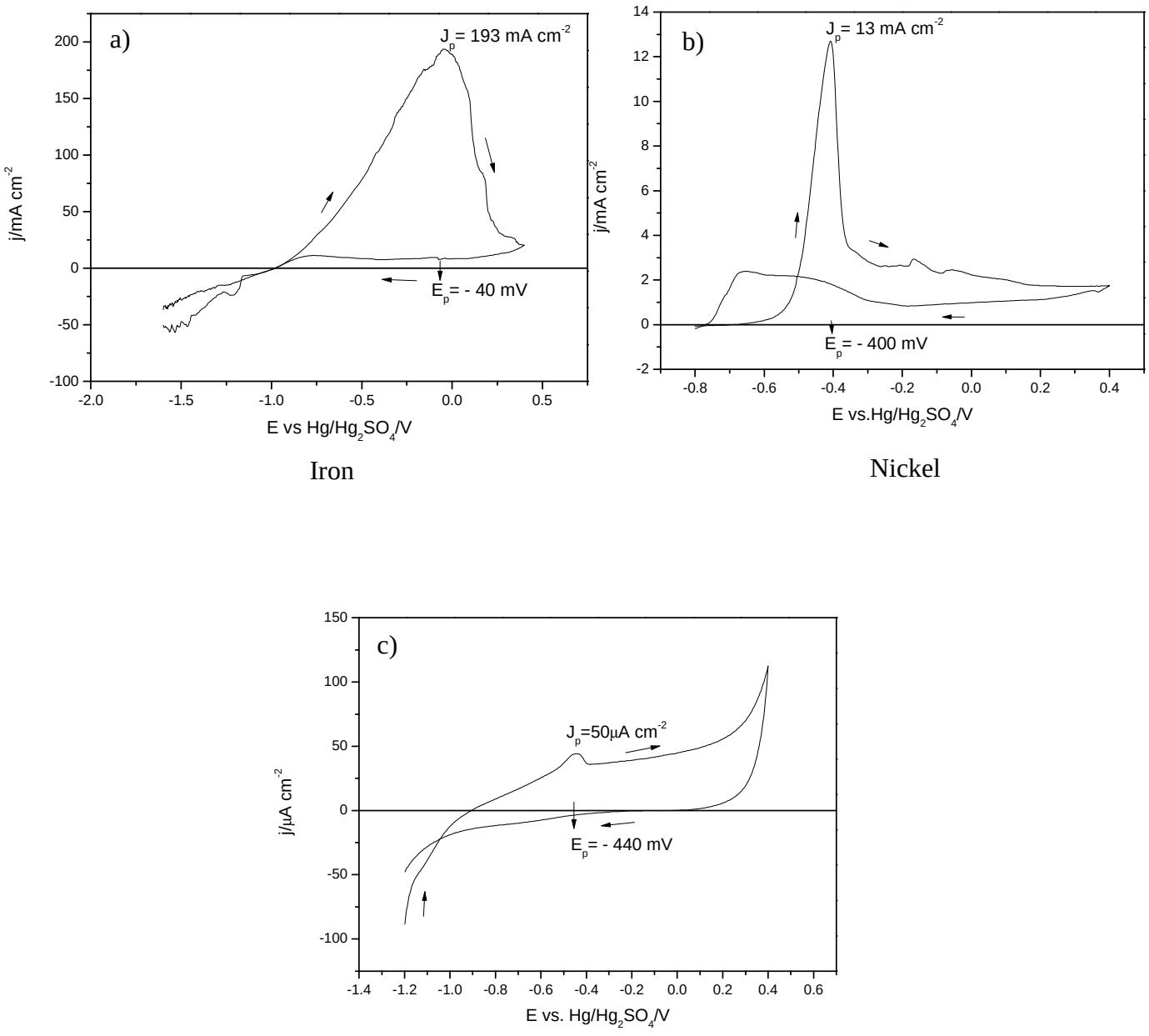

Iron

Nickel

Chromium

Figure 3.1.2.1 *Cyclic voltammograms of a) Fe, b) Ni and c) Cr in phosphoric acid pH 2 at 353 K. Potentials scan rate 20 mV s^{-1}.*

Table 3.1 *Electrochemical data of Fe, Ni, and Cr collected during studies for phosphoric acid.*

Material	**E_{corr}/mV**	**j_p/mA cm^{-2}**	**E_p/mV**	**Q/C cm^{-2}**
Fe	- 980	193	- 40	12.5
Ni	- 690	13	- 400	0.2
Cr	- 900	0.05	- 440	0.0014

Table 3.2 *Surface condition after 1 hour at constant potential $E_{= +100\ mV}$ for Fe, Ni and Cr.*

Metal	**j/mA cm^{-2}**
Fe	8
Ni	1
Cr	0.0002

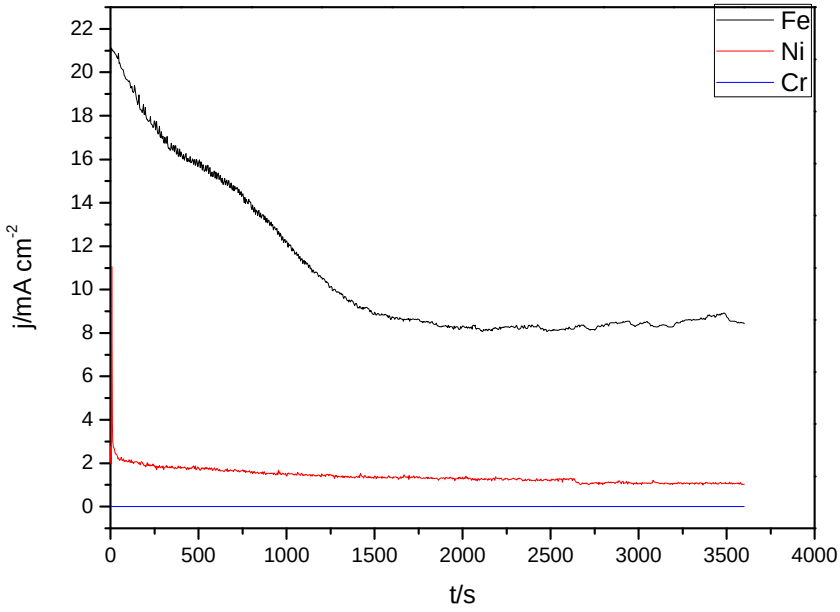

Figure 3.1.2.2 *I-t response for a potential step experiment of Fe, Ni and Cr electrodes at constant E = + 100 mV vs. Hg/Hg_2SO_4 in phosphoric acid pH 2.*

3.1.2.1 Influence of temperature on behaviour of Nickel

The influence of temperature on the behaviour of Ni in phosphoric acid, pH 2 was investigated. Cyclic voltammograms were recorded at temperatures of 298, 333, and 353 K (see figure 3.1.2.1.1). All the cyclic voltammograms presented were started at -800 mV vs. Hg/Hg_2SO_4 and the potential scan rate was 20 mV s^{-1}. At the initial potential, for all three temperatures, there were current densities for the hydrogen evolution were observed, which increased with temperature. The corrosion potentials, E_{corr} were - 690 mV at 353 and 333 K while at 298 K it was shifted to a less negative value, - 600 mV. Positive to the corrosion potential, an anodic peak is seen at all three temperatures. At 298 K, the peak occurs at ~ - 400 mV. The peak is quite sharp and the peak current density is low, < 1 mA cm^{-2}. Beyond the peak, there is evidence for further oxidation peaks but the current density drops to a relatively low value, << 0.1 mA cm^{-2}. On the reverse scan, there is evidence for a small cathodic current negative to – 200 mV. At 333 K, the voltammogram has changed in several respects. The anodic peak is much larger and also broader and it is clear that, in fact, there are at least two anodic processes. The anodic current density at the passivated surface is much larger and there is no evidence for cathodic current positive to the initial corrosion potential. At 353 K, the peak has become sharper again but the anodic peak current density is similar to that at 333 K, j_p~14 mA cm^{-2} compared to j_p~ 11 mA cm^{-2}.

On the reverse scan, reactivation is clearly seen and there is a potential range where the current density is higher than the forward scan.

Some features of the data are more clearly seen by replotting the voltammograms as log j vs. E, see figure 3.1.2.1.2. At 353 K, the reactivation process presents to a negative shift in the corrosion potential on the reverse scan. At the lower temperatures, the shift in corrosion potential is in the opposite direction; at 298 K, the positive shift is large.

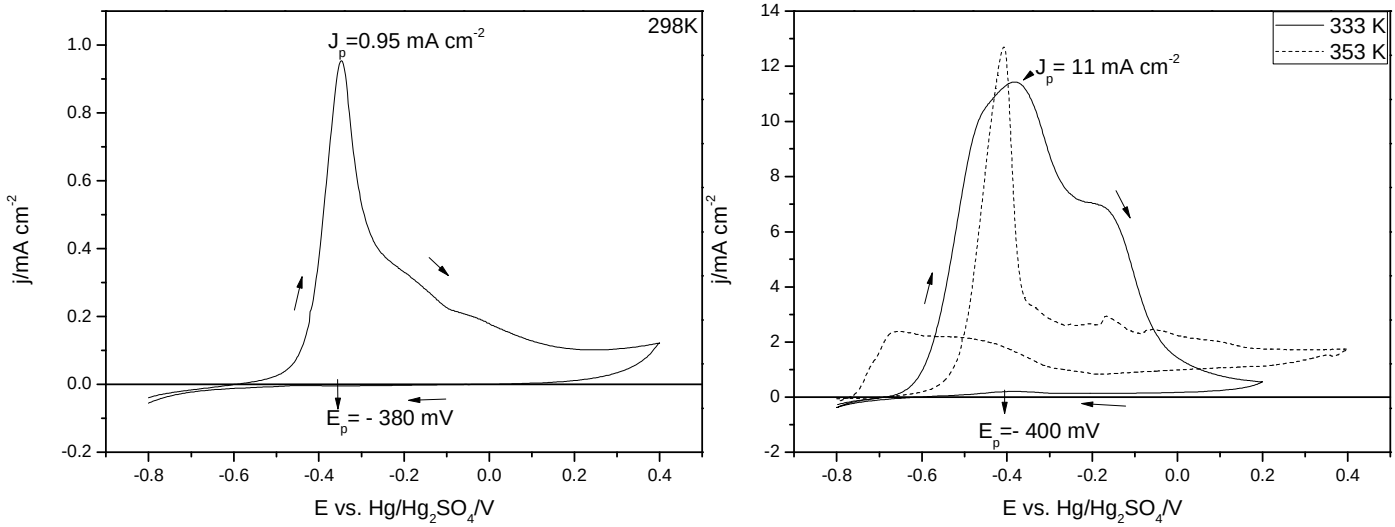

Figure 3.1.2.1.1 *Cyclic voltammograms of Ni in phosphoric acid pH 2 at 298, 333 and 353 K.*

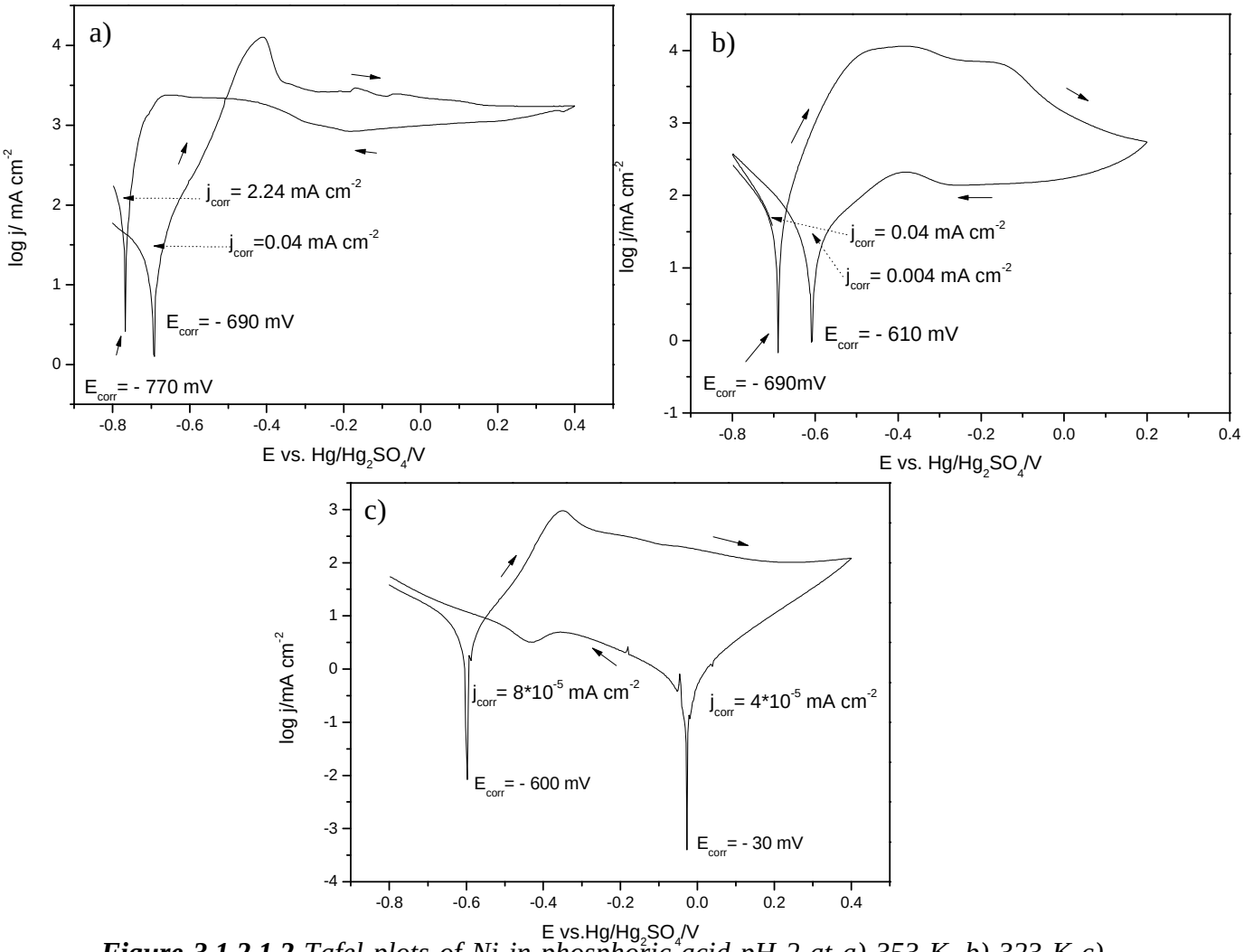

Figure 3.1.2.1.2 *Tafel plots of Ni in phosphoric acid pH 2 at a) 353 K, b) 323 K c) 298 K.*

This results from the cathodic process only seen on the reverse scan. It appears that on the reverse scan, there are both anodic and cathodic processes occurring but that they have totally different temperature dependences. The net current observed experimentally, therefore shows complex behaviour. Table 3.3 summarises the data from the voltammetry of Ni as a function of temperature. As expected, the rate of corrosion clearly increases with temperature but it is also clear that the changes in the voltammetry are not straightforward.

Table 3.3 *Influence of temperature on surface condition of nickel.*

T/K	**E_p/ mV**	**E_{corr}/ mV**		**j_p/ mA cm^{-2}**	**Q/ C cm^{-2}**	**j_{corr}/mA cm^{-2}**	
		Forward	**Reverse**			Forward	Reverse
298	- 380	- 600	- 30	0.95	0.02	$8 \cdot 10^{-5}$	$4 \cdot 10^{-5}$
323	- 400	- 690	- 610	11	0.3	0.036	0.004
353	- 400	- 690	- 770	14	0.2	0.04	2.24

Nickel, as well as chromium, was subjected to the test of holding the potential at +100 mV for 1 hour and monitoring the current. This experiment was used to probe the influence of pH and temperature. In the former case, the solutions were adjusted to the desired pH by addition of phosphoric acid to water and no other salt additions were made. The current densities at the end of an hour are reported in Table 3.4 and 3.5.

With both metals, their surfaces are largely passivated after this experiment and the rate of corrosion is determined by the properties of the corrosion layer. In all conditions the rate of corrosion of Cr is a factor of 1000 lower than that of Ni. The trends with pH and temperature are clear. The rates of continuing corrosion for Ni increase as the solution is made more acid while the rate of Cr corrosion is independent of pH. With increasing temperature the rate of corrosion of both Ni and Cr always increase.

Table 3.4 *Influence of pH on surface condition on Ni and Cr in phosphoric acid at 353 K.*

Material	**pH**		
	1	**2**	**3**
Ni	2.2 mA cm^{-2}	1.0 mA cm^{-2}	0.5 mA cm^{-2}
Cr	0.21 µA cm^{-2}	0.20 µA cm^{-2}	0.17 µA cm^{-2}

Table 3.5 *Influence of temperature on current density of Ni and Cr conditions in phosphoric acid pH 2.*

Material	**Temperature /K**		
	298	**333**	**353**
Ni	0.1 mA cm^{-2}	0.3 mA cm^{-2}	1.0 mA cm^{-2}
Cr	0.1 µA cm^{-2}	0.17µA cm^{-2}	0.20 µA cm^{-2}

3.1.3 Investigations of stainless and mild steels

The voltammetry of mild and stainless steels have been carried out in deoxygenated phosphoric acid pH 2 at 353 K. Figure 3.1.3.1 reports the voltammograms recorded at 20 mV s^{-1}.

The response for stainless steel shows relatively low current densities over the whole potential range - 750 mV to + 400 mV vs. Hg/Hg_2SO_4 but there are well formed waves during both the forward and reverse potential scans. At the initial potential, there is a low current for H_2 evolution but on the commencement of the scan, the current quickly becomes anodic. There is no anodic peak as found with the pure metals but an oxidation wave occurs at ~ - 500 mV. On the reverse scan, there is a reduction wave around – 100 mV. Clearly this reduction wave cannot be for the reverse reaction to the oxidation wave and the origins of the waves are not known. Hydrogen evolution is not a possible reaction at the potential of the reduction wave. Oxygen reduction is thermodynamically possible at this potential and hence some experiments were carried out in oxygen saturated solutions, see figure 3.1.3.3. While the presence of oxygen leads to a substantial positive shift in the corrosion potential (more clearly seen in the Tafel diagram), the current density associated with the anodic and cathodic waves are unchanged. Certainly, there is no evidence that the reduction wave results from oxygen reduction. The charges associated with both the anodic and cathodic processes are small and they are most likely redox reactions within the corrosion film present on the steel at the commencement of the experiments. With both the oxygenated and deoxygenated electrolyte, the apparent corrosion potentials on the reverse scan are similar and the value is determined by the currnet for this reduction process.

In contrast, the voltammogram for mild steel is rather featureless. Also the current densities are comparable with those at the stainless steel when a much higher rate of corrosion is to be expected. Indeed, the voltammogram is not consistent with other measures of the rate of corrosion but the experiment was repeated several times and the response was reproducible. This may imply that the mild steel has a protective film that survives this short timescale experiment but is easily broken down on a longer timescale.

a)

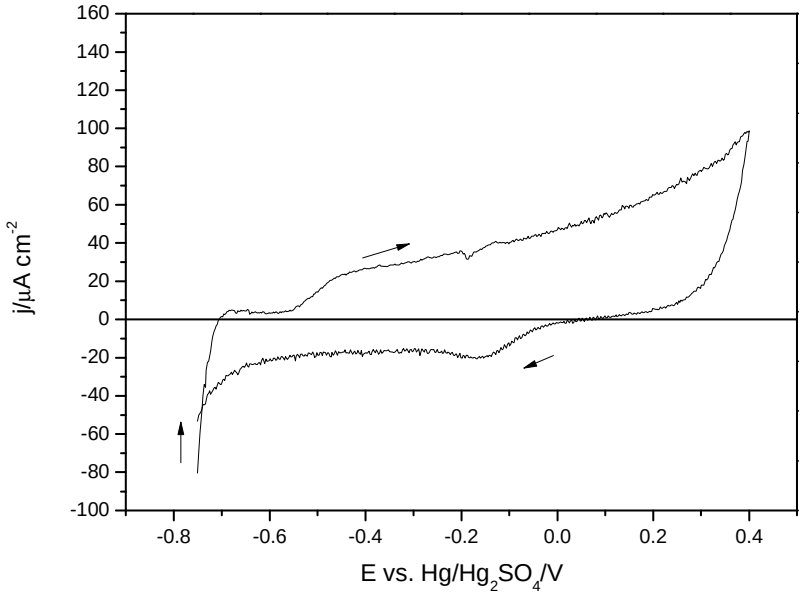

b)

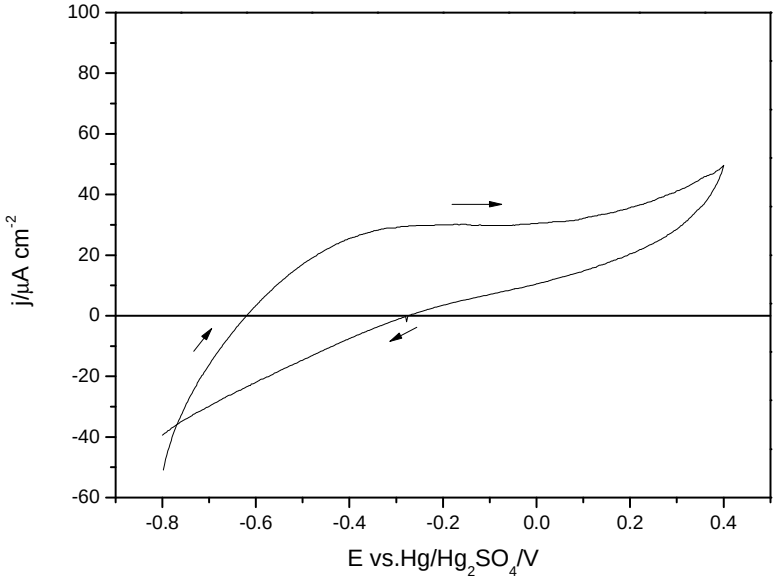

Figure 3.1.3.1 *Cyclic voltammograms of a) stainless steel 904 L, b) mild steel, in phosphoric acid pH 2 at 353K. Potential scan rate 20 mVs^{-1}.*

The two steels were subjected to the test of holding the potential at +100 mV for 1 hour in deoxygenated phosphoric acid pH 2 at 353 K and monitoring the current. At the end of the hour, the current density for the mild steel was 1.2 mA cm^{-2} and 0.04 μA cm^{-2} with the stainless steel. I believe that this difference better reflects the difference in corrosion rates of the two steels.

The electrochemical data for the two steels are collected together in Table 3.6.

The tendency for mild steel to corrode rapidly was further confirmed by recording an SEM image for a mild steel sample left around the laboratory for 2 years. See figure 3.1.3.2. By eye, the surface is covered by brown rust and the SEM image shows the heavy coverage by a poorly adherent film.

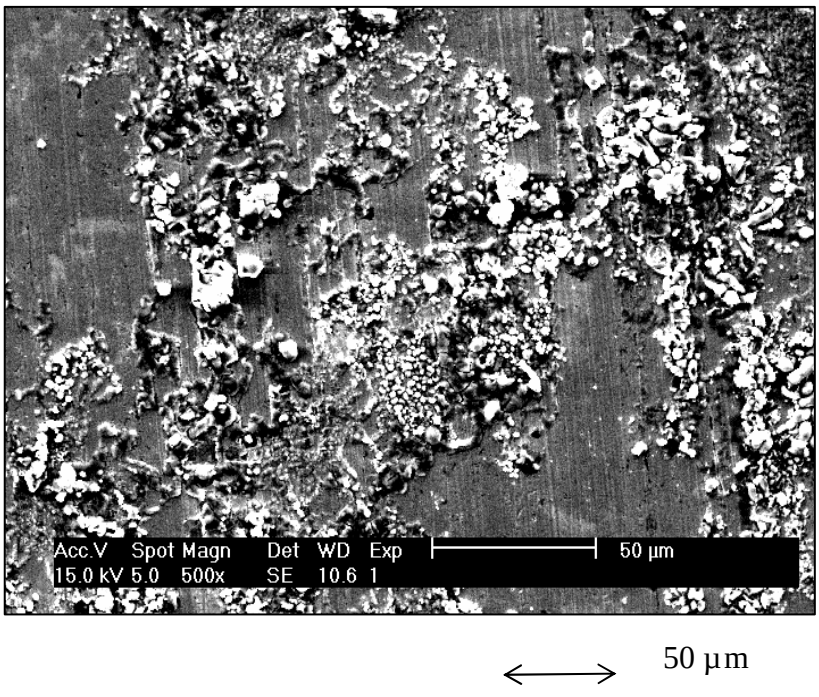

Figure 3.1.3.2 *SEM image of mild steel after exposure to the laboratory atmosphere for 2 years.*

a)

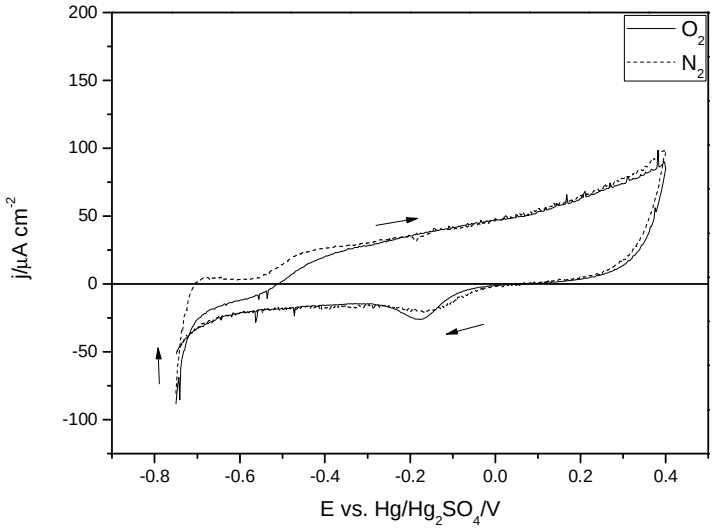

b)

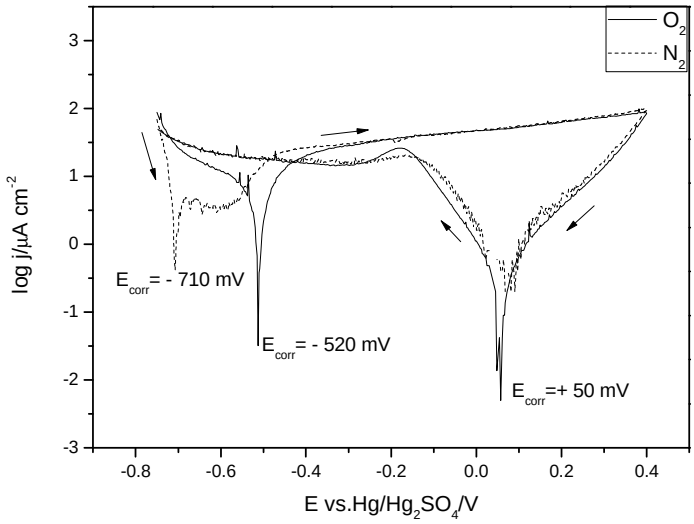

Figure 3.1.3.3 *Cyclic voltammograms (a) and Tafel plots (b) of stainless steel 904 L in phosphoric acid pH 2 oxygenated and deoxygenated conditions.*

Table 3.6 *Electrochemical data collected for stainless and mild steels.*

Material	**E_{corr}/mV**		**E_p/mV**	**Q/C cm^{-2}**	**j_{3600s} at $E_{+100\ mV}$**
	Forward	**Reverse**			
SS 904 L	-750	+ 80	No peak	0.05	0.04 µA cm^{-2}
Mild steel	- 620	- 270	No peak	0.03	1.2 mA cm^{-2}

3.1.3.1. Influence of pre-treatment at open circuit on the Stainless Steel 904 L surface condition

Discs of stainless steel were allowed to stand on open circuit in deoxygenated phosphoric acid pH 2 during 5 and 10 days at room temperature and then their voltammetry was compared with that for fresh samples of steel. The electrochemistry was again carried out in deoxygenated phosphoric acid pH 2 at 353 K. A typical cyclic voltammogram for the stainless steel after 10 days is presented in figure 3.1.3.1.1a. The overall response is not greatly changed from that for the fresh stainless steel. In general, the same features are seen and the current densities are similar although the anodic wave is more drawn out and the cathodic feature at ~ - 200 mV on the reverse scan is more peaked.

The 'treated' samples were also examined using the test of holding the potential for 1 hour at + 100 mV vs. Hg/Hg_2SO_4 in deoxygenated phosphoric acid pH 2 at 353 K. The current vs. time responses are shown in figure 3.1.3.1.1b. The exposure at open circuit of the stainless steel to the acid solution leads to a worsening in the performance of the steel. It can be seen that the current densities for the 'treated' stainless steel are much higher, particularly early in the experiment but still after 1

hour. The protective film on the surface of the stainless steel has been degraded during the stand in the acid solution.

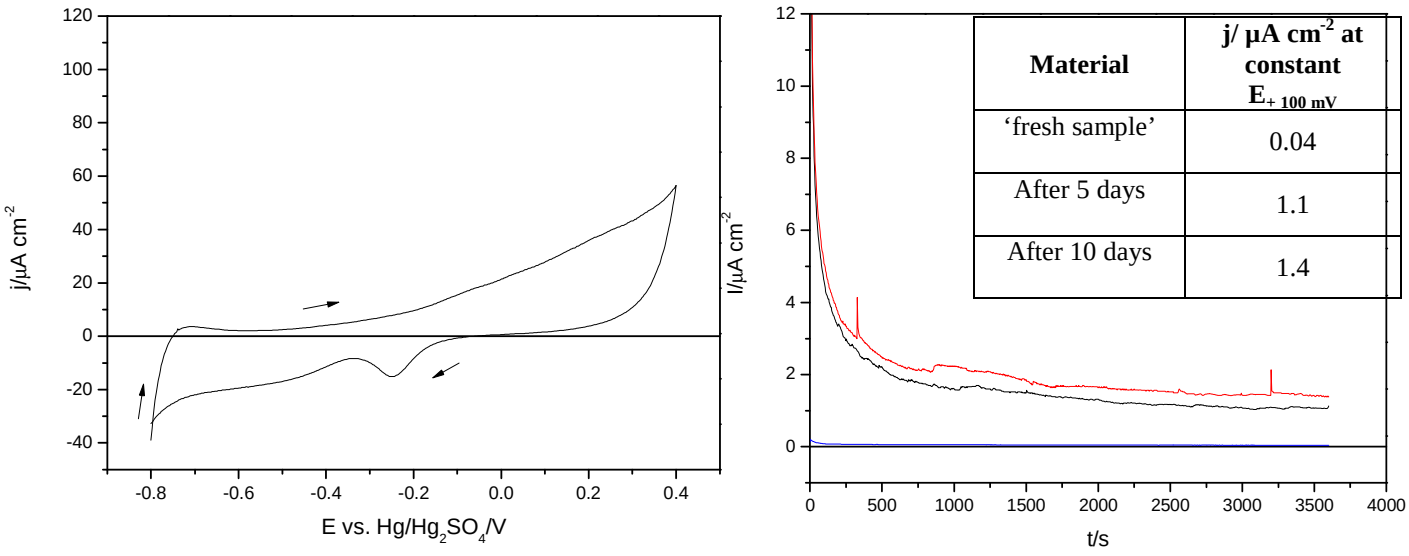

Figure 3.1.3.1.2 *Influence of phosphoric acid on stainless steel condition a) cyclic voltammogram of treated sample 'after 10 days' and, b) I vs. t for fresh (blue line), after 5 days (red line) and after 10 days (**black line**).*

3.1.4. 3µm Ni coated mild steel and Ni/C 40 g/dm^3 onto mild steel

In this section, the behaviour of mild steel with a 3 µm electrodeposit of Ni and a Ni/graphite deposit supplied by Corus are reported. The Ni coated mild steel was produced in a commercial reel-to-reel plating line employing a standard Watts bath for the deposition. The Ni/graphite was produced in a similar plating line but the Watts bath also contained 40 g dm^{-3} of graphite flakes with a mean dimension of 5 µm. Figure 3.1.4.1 shows an SEM image of the Ni/graphite layer and it can be seen that there is a high coverage by graphite.

In the absence of pinholes in the deposit, the voltammetry for the Ni coated mild steel would be expected to be very similar to that of bulk Ni (the electrodeposit contains some boron from the buffer). The voltammogram for the Ni electroplate in deoxygenated phosphoric acid pH 2 at 353 K is shown in figure 3.1.4.2 and it can be

seen that the response is, indeed, very similar to that for the pure Ni, figure 3.1.4.2b. The same features are evident and indeed the current densities (and charge densities) as a function of potential are very similar although the main anodic peak is more drawn out for the electrodeposit. The active and passive corrosion regions are clearly defined and with both surfaces the current density in the passive region is significant.

The inclusion of the graphite flakes in the layer also leads to only minor changes in voltammetry. Again the major feature is a large anodic peak but the peak current density is comparable to the Ni and Ni/steel samples. The corrosion potential is shifted negative and it is interesting to note that the reverse scan does not show reactivation of the corrosion process.

Both samples were examined using the test of holding the potential for 1 hour at + 100 mV vs. Hg/Hg_2SO_4 in deoxygenated phosphoric acid pH 2 at 353 K. The current densities along with data from the voltammetry are reported in Table 3.7. Both samples give corrosion rates after one hour comparable to the bulk Ni. The SEM image of the Ni coated mild steel after the 1 hour test is shown in figure 3.1.4.3. It can be seen that the surface layer has a number of pinholes.

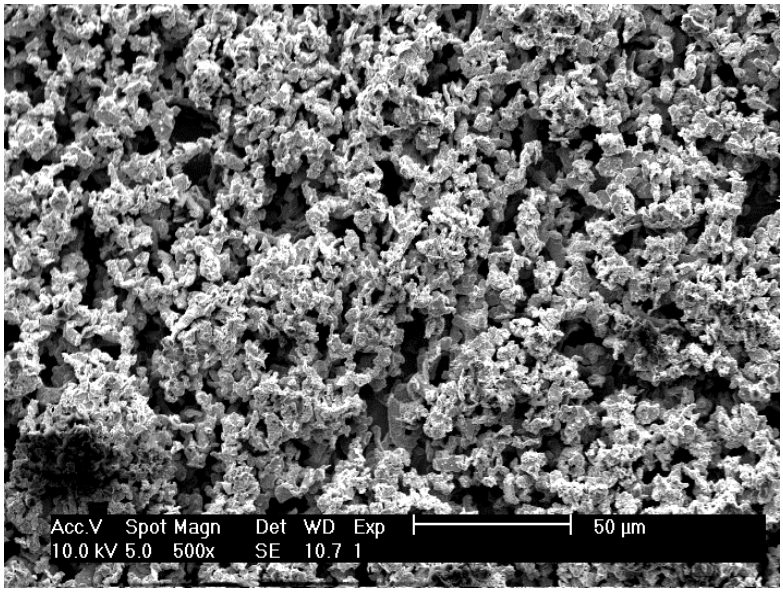

Figure 3.1.4.1 *SEM image of Ni/graphite layer.*

a)

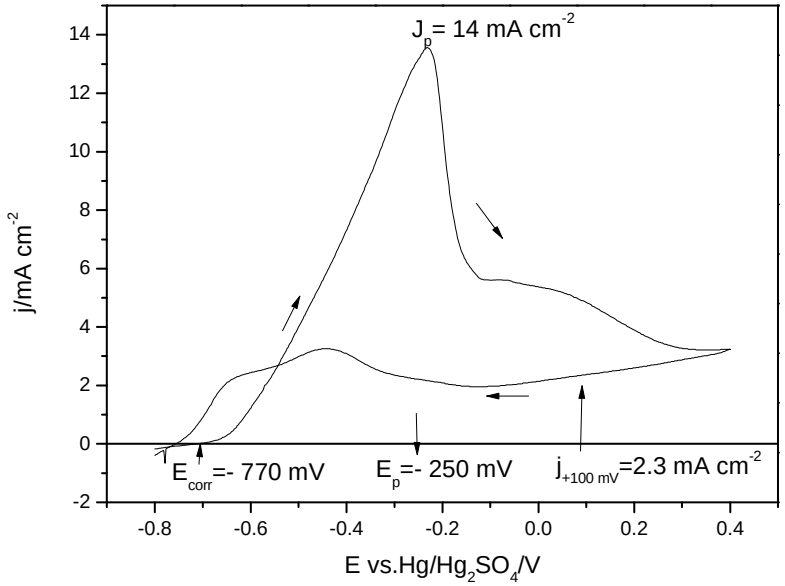

b)

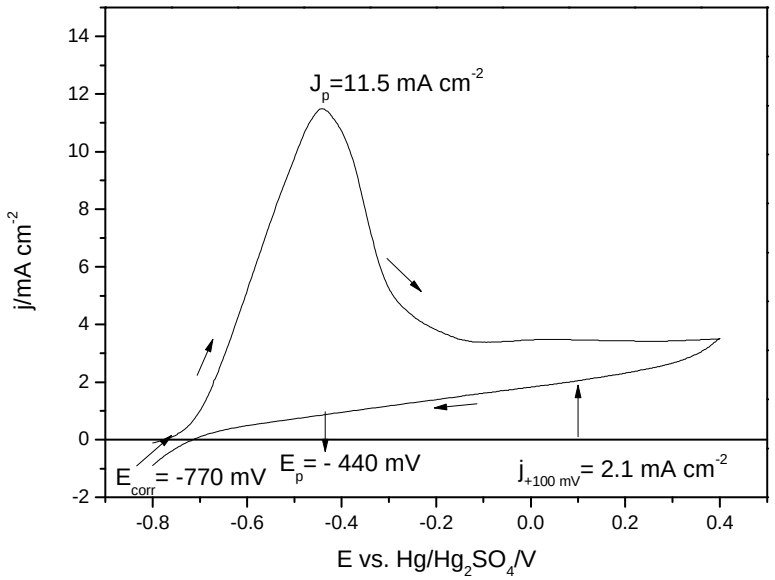

Figure 3.1.4.2 *Cyclic voltammograms of a) Ni coated mild steel, b) Ni/C 40 g/dm^3 coated mild steel in phosphoric acid pH 2 at 353K. Potential scan rate 20 mV s^{-1}.*

Table 3.7 *Electrochemical data for 3µm Ni coated mild steel and Ni/C 40 g/dm^3 onto mild steel.*

Material	**E_{corr}/mV**		**E_p/mV**	**J_p/ mA cm^{-2}**	**Q/C cm^{-2}**	**j_{3600s} at $E_{+100\ mV}$**
	Forward	**Reverse**				
Ni coated mild steel	- 720	- 720	- 250	14	0.7	1.8 mA cm^{-2}
Ni/ C 40 g/dm^3 mild steel	- 770	- 712	- 440	11.5	0.5	1.6 mA cm^{-2}

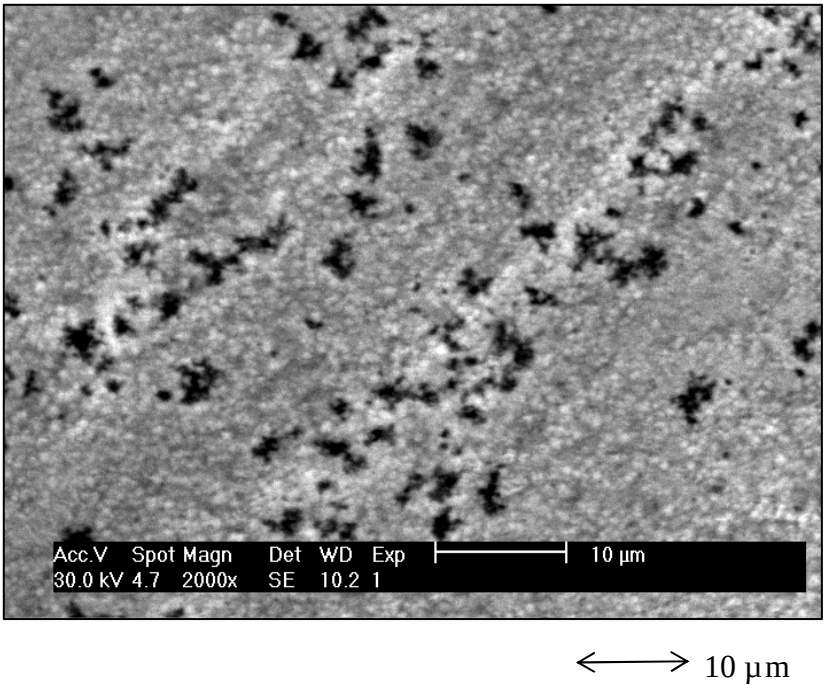

Figure 3.1.4.3 *Surface condition for Ni coated mild steel after 1hour hold in constant potential in phosphoric acid pH 2 at 353K.*

3.1.5 Conclusions:

a) The rate of corrosion of the pure metal decreases along the series Fe > Ni > Cr. The corrosion rates of both Fe and Ni are far too high for application in a bipolar plate without surface modification. Chromium presents the best result in phosphoric acid and this probably results from an existing corrosion film. Modification of Ni by alloying with Cr is a route that could be considered.

b) Stainless steel has been characterised by high resistance to corrosion and low current density in range of µA cm^{-2}, while mild steel undergoes rapid corrosion with current densities in the range of mA cm^{-2}

c) Commercial 3 µm Ni coated mild steel free from pinholes has been found to behave very similarly to bulk Ni. Likewise the inclusion of a heavy loading of graphite particles does not alter the performance significantly.

3.2. A Procedure for Determining the Porosity of Nickel Coatings on Mild Steel

3.2.1 Determination of the porosity of the coating

Impedance [1-9] was investigated as a method to determine the 'quality' of nickel coatings on mild steel, ie. the porosity of the coating and hence the exposure of the substrate mild steel to solutions. In general, it was found that the AC impedance response could be modelled by a very simple equivalent circuit, see Figure 3.2.1.1

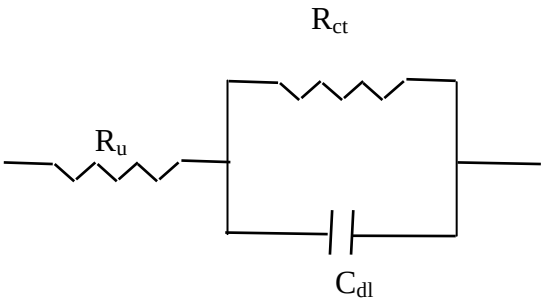

Figure 3.2.1.1 *Simple equivalent circuit for Ni and mild steel at open circuit potential.*

1 M H_2SO_4 at room temperature (~ 293 K) was found to be a suitable medium and the impedance was determined at the open circuit potential using a frequency range 10^{-2} – 10^4 Herz and an amplitude of $\pm$ 5 mV.

3.2.2 Nickel and Mild Steel

The electrochemistry of the bulk materials was first defined. The mild steel and nickel took up open circuit potentials of - 900 mV and – 660 mV vs. Hg/Hg_2SO_4 respectively in 1 M H_2SO_4. Nickel has the more positive corrosion potential than the steel (ie. nickel is the more noble metal) and is therefore likely to be a protective coating for mild steel. On the other hand, if a nickel coating on mild steel has pores or scratches, the situation on the open circuit is set up for accelerated (pitting) corrosion of the steel; oxygen and/or proton reduction will occur over the whole nickel surface and will be matched by enhanced iron dissolution at the faults in the coating.

Figure 3.2.2.1 shows current vs. potential data for the two metals in the form of both a voltammogram and a Tafel plot. It can be seen that both metals show current density for H_2 evolution negative to the open circuit potential and an active corrosion range positive to this potential as well as passivation towards the positive limit. The currents in the active region just positive to the open circuit potential are very large reaching peak current densities of ~ 250 mA cm^{-2} for the mild steel (corresponding to equivalent uniform corrosion rates of > 10 cm/year!) and 100 mA cm^{-2} for Ni. At more positive potentials both passivate with the current densities dropping to low values. It can be clearly seen from the Tafel plots that passivation is significantly more complete at Ni; this is apparent from the lower current density towards the positive potential limit on the forward scan. Even more clearly, on the reverse scans back to negative potentials, higher current densities are seen at the mild steel and the reactivation (seen on the Tafel presentations) approaching the corrosion potential is more significant. At nickel, the passivation leads to a positive shift in the open circuit potential, largely due to a decrease in the H_2 evolution currents. At mild steel, the shift in the corrosion potentials is to more negative potentials perhaps indicating that the potential cycle has led to a more active surface, perhaps by the initiation of pits.

If a second cycle is recorded without renewing the surface, the voltammograms for both metals again show peaks although with a reduced current density.

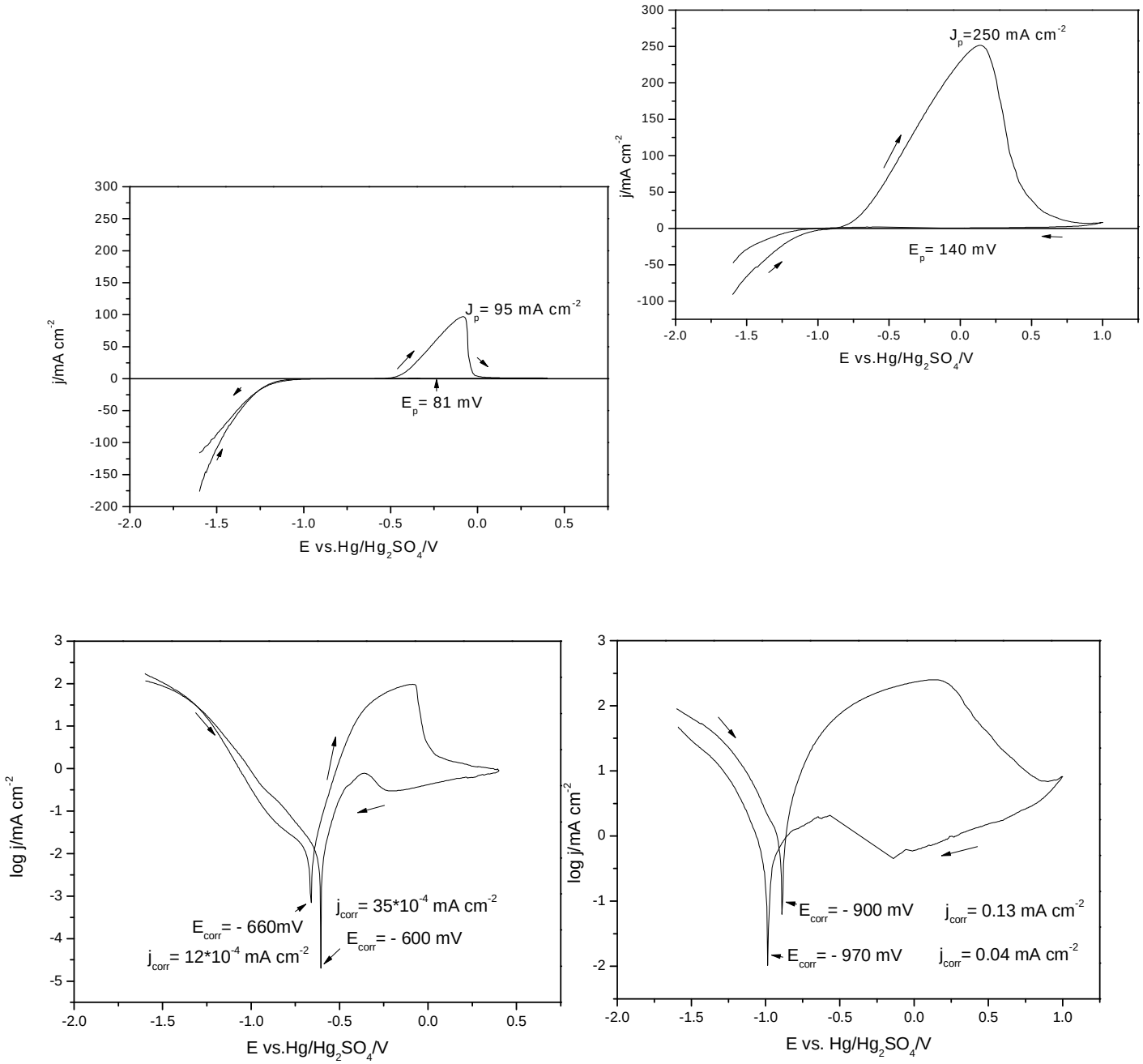

Ni Mild steel

Figure 3.2.2.1 *Current vs. potential data for mild steel and nickel in 1 M H_2SO_4. Potential scan rate 20 mV s^{-1}.*

Table 3.8 *Data taken from cyclic voltammograms and Tafel plots. Potential scan rate 20 mV s^{-1}.*

Material	**Forward**		**Back**	
	E_{corr}/ mV	**R_{corr}/Ω cm^{-2}**	**E_{corr} /mV**	**R_{corr}/ Ω cm^{-2}**
Ni	- 660	2.32	- 600	2.26
Mild steel	- 970	0.02	- 900	0.1

Figure 3.2.2.2 shows Nyquist presentations of the impedance data for the two metals recorded at the open circuit potential in 1 M H_2SO_4. It can be seen that reasonable semicircles are obtained for both metals and data taken from the plots are summarised in Table 3.9. The capacitances indicate similar roughnesses for the two metals and hence the lower charge transfer resistance for the mild steel can be attributed to a higher rate of corrosion.

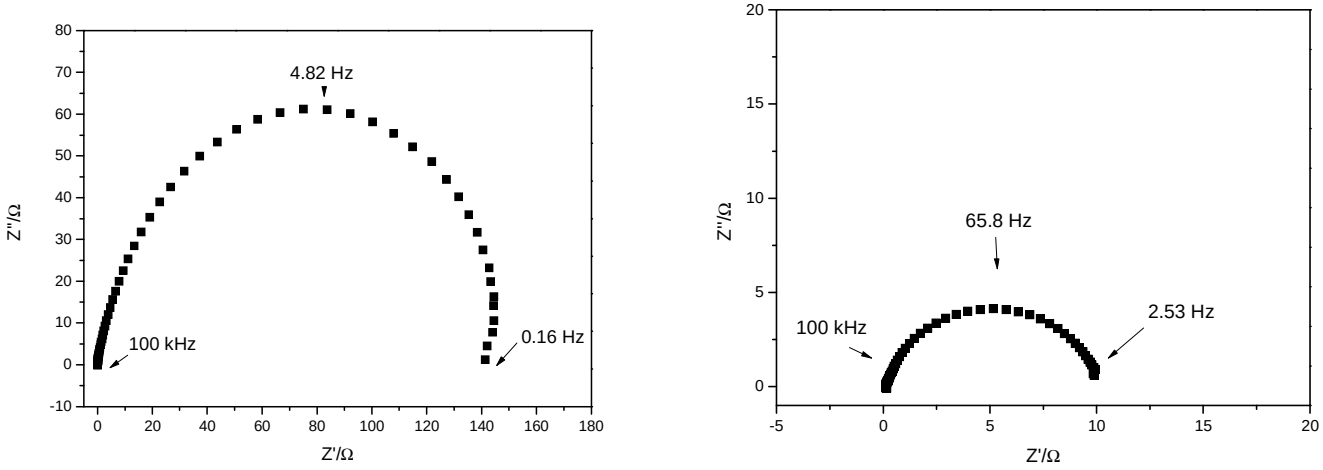

Ni Mild steel

Figure 3.2.2.2 *Nyquist plots for mild steel and nickel at the corrosion potential in 1 M H_2SO_4.*

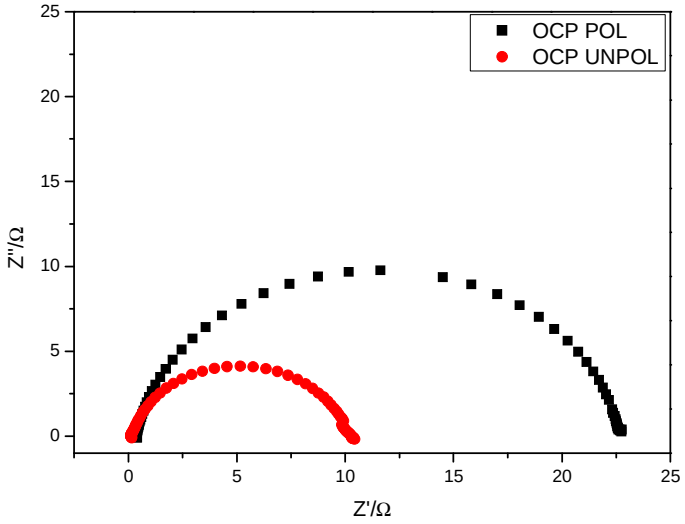

Figure 3.2.2.3 *Comparison of the Nyquist plots in 1 M H_2SO_4 for polished and 'as supplied' mild steel at the open circuit potentials.*

The influence of the surface area on both the capacitance and the charge transfer resistance was confirmed by comparing the impedance response for a polished and 'as supplied' mild steel sample, see figure 3.2.2.3. It can be seen that the polished sample gives a larger semi-circle and to the expected change in R_{ct} and C_{dl}, see Table 3.9.

Table 3.9 *Open circuit potentials, charge transfer resistances and capacitances (at their open circuit potentials) for mild steel and nickel in 1 M H_2SO_4.*

Material	**E_{oc}/ mV vs. Hg/Hg_2SO_4**	**R_{ct}/ Ωcm^{-2}**	**$C_{dl}/\mu F\ cm^{-2}$**
Mild steel	- 900	55	44
Nickel	- 660	725	41
Polished mild steel	- 880	110	36

3.2.3 Nickel Electroplated Mild Steel.

Nickel coatings on mild steel with three thicknesses, 1 μm, 3 μm and 10 μm were prepared (by Jacek Lapinski) by electroplating from the standard Watts bath. Figure 3.2.3.1 reports SEM images for these deposits. With the thinnest deposit, scratches on the underlying steel can still be seen while it is clear that the deposit become rougher as the layer thickens. On the 1 μm and 3 μm layers, black patches are evident and these are though to be pits.

Impedance data were recorded for each of the deposits at their open circuit potentials in 1 M H_2SO_4. Good semi-circles were obtained and their diameter increased with thickness of the Ni deposit (figure 3.2.3.2). Charge transfer resistances and capacitances estimated from these diagrams are included in Table 3.10. The rate of corrosion increases strongly as the deposit is fabricated less thick. With the 10 μm Ni coating, the charge transfer resistance is the same as that found for bulk nickel. With thinner coatings, the charge transfer resistance decreases. This is clear evidence that the thinner Ni coatings do not provide complete coverage of the mild steel, ie. the coatings have faults such as pinholes. This is confirmed by repeating the impedance experiment with a sample with a 10 μm Ni coating that has been scratched; the charge transfer resistance is decreased significantly. In fact, the charge transfer resistance

found for the 1 and 0.1 µm Ni coatings are lower than that found for uncoated mild steel and this implies that an accelerated corrosion mechanism, pitting, or crevice corrosion, occurs with these thinner coatings.

It was also noted that when the impedance experiment was repeated with the nickel coated mild steel samples, the corrosion resistance decreased with each repeat, see figure 3.2.3.3; for example, with the 5 µm Ni coating, the corrosion resistance was 44, 23 and 5 ohms for three experiments without cleaning/treating the sample surface. The same degree of change was not seen with bulk nickel. This further implies that pitting or the formation of corrosion active sites is occurring during each experiment with the plated samples.

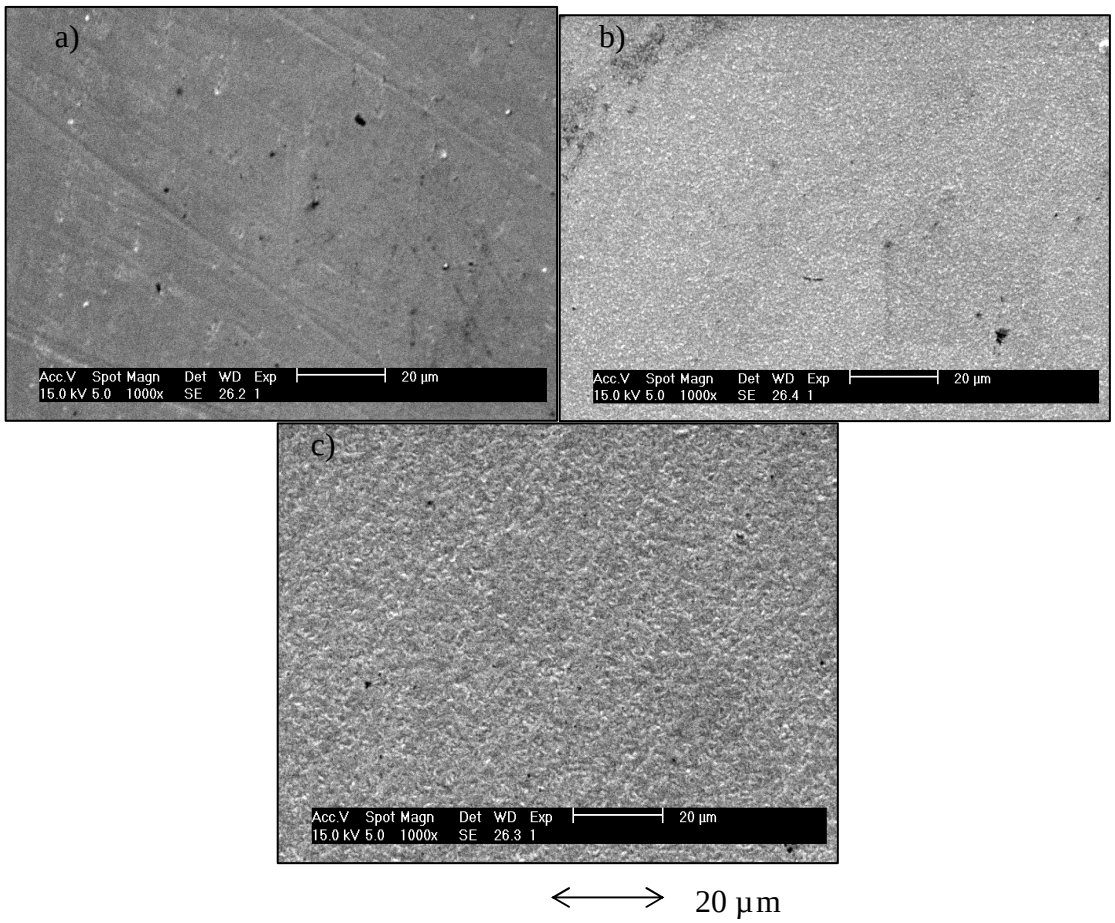

Figure 3.2.3.1 *SEM images of 'as deposited' Ni on mild steel for three different thicknesses a) 1 µm, b) 5 µm, c) 10 µm.*

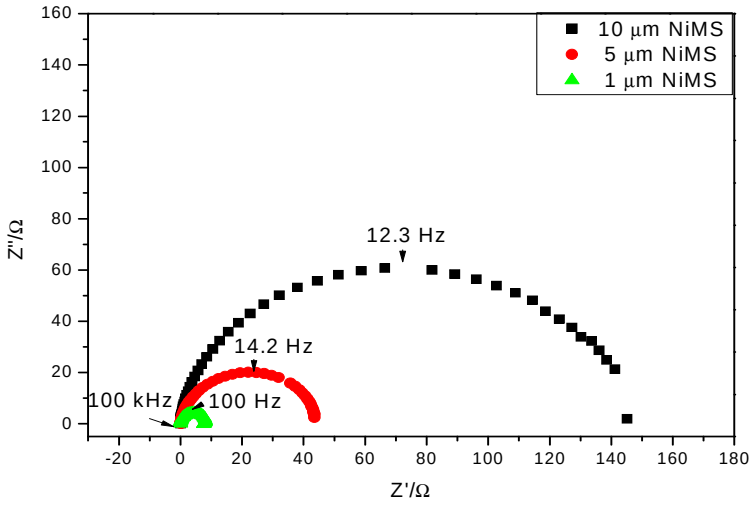

Figure 3.2.3.2 *Nyquist plots for three samples of Ni plated mild steel with different thicknesses of nickel coating.*

Table 3.10 *Open circuit potentials, charge transfer resistances and capacitances for Ni plated samples at their open circuit potential in 1 M H_2SO_4.*

Material	**E_{oc}/ mV vs. Hg/Hg_2SO_4**	**R_{ct}/ Ω**	**C_{dl}/µF cm^{-2}**
Soton 0.1 µm Ni	- 970	<0.2	-
Soton 1 µm Ni	- 840	20	80
Soton 5 µm Ni	- 680	215	52
Soton 10 µm Ni	- 720	155	27
Soton 10 µm Ni Polished	- 660	725	18
Scratched Soton 10 µm Ni	- 780	65	40
Corus 3 µm Ni	- 840	1500	6
Corus Ni/ 40 g/dm^3 C	- 830	675	80
Scratched Corus Ni/ 40 g/dm^3 C	- 860	85	64

The impedance experiment with the 3 µm Ni coated mild steel supplied by Corus also gave a semi-circle Nyquist plot. It can be seen the corrosion resistance is high and the capacitance is low compared to the samples plated in Southampton and, indeed, the bulk nickel. The Corus sample appears to be less prone to corrosion than the Southampton sample indicating a more complete coverage of the mild steel. The data also suggests a smoother surface and this will partly contribute to the higher corrosion resistance.

The smoother surface presumably results from the additives in the commercial plating system.

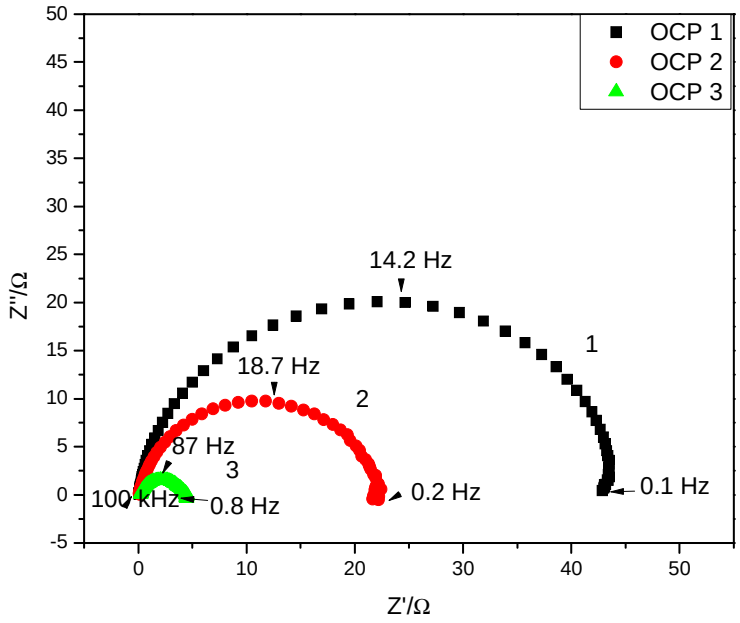

Figure 3.2.3.3 *Three sequential impedance plots for 5 µm Ni coated mild steel in 1 M H_2SO_4.*

The corrosion potentials for the Ni coated mild steels in 1 M H_2SO_4 are also interesting. With the thicker nickel deposits (E_{corr}= - 661 mV for 5 µm), the corrosion potentials are close to that for bulk nickel but the value for the 1 µm Ni coating (E_{corr}= - 730 mV) is much more negative and approaching that for the mild steel. This is further evidence for an incomplete coating. Voltammograms were also recorded for the Ni coated mild steel plated in Southampton.

Figure 3.2.3.4 reports the voltammograms for the 1, 5, and 10 μm Ni coated samples. All show an active corrosion region immediately positive to the corrosion potential and a well defined peak and passivation at more positive potentials. With the thinner coating, passivation is much less complete; the current densities at + 100 mV vs. $Hg/HgSO_4$ are 50, 60 and 2400 μA cm^{-2} for the 10, 5 and 1 μm Ni coatings respectively. It is also clear that, with the 1 μm Ni coating, corrosion at a substantial rate continues on the reverse scan.

This coating provides much less corrosion protection and clearly has faults in the coating. The peak current densities on the forward scan show an unexpected trend with the value increasing with thickness of the deposit and the peak current densities are also low compared with that for bulk Ni. It is possible that this reflects variations in surface area. Certainly, the thin coating has a good reflectivity while the 10 μm Ni has a matt appearance.

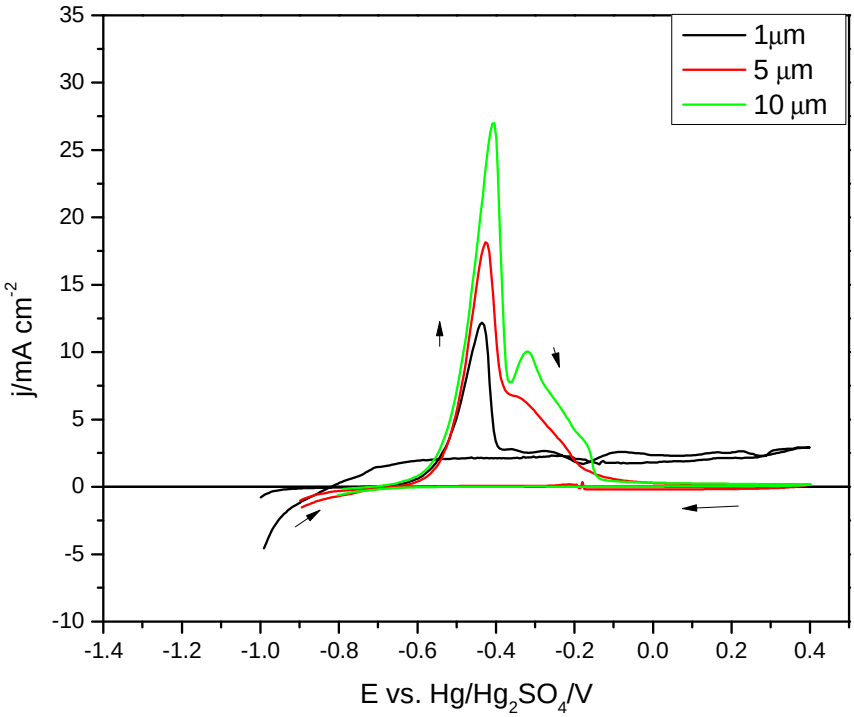

Figure 3.2.3.4 *Voltammograms for 1, 5, and 10 μm Ni coated mild steel in 1 M H_2SO_4. Potentials scan rate 20 mV s^{-1}.*

The study was extended to a sample of Ni/graphite coating fabricated from a bath containing 40 g/dm^3 graphite at Corus (figure 3.2.3.5). This medium leads to high graphite content in the Ni deposit (according to other studies, a C content that is far above that necessary to give an acceptable contact resistance). The Nyquist plot is again semi-circular and the corrosion resistance was 135 ohms (cf. 300 ohms for a similar Ni coating). The capacitance of the Ni/graphite surface is, however, much higher implying a much higher surface area. Hence the impedance does not necessarily suggest an incomplete coverage of the mild steel by the Ni/graphite coating. Also has been observed differences between scratches (figure 3.2.3.6) and non-scratches (figure 3.2.3.5) surface where is well defined deposited line and substrate. Resistance is growing up with increasing thicknesses of the Ni layer, and maximum of frequencies dropping down with changing thickness of layer.

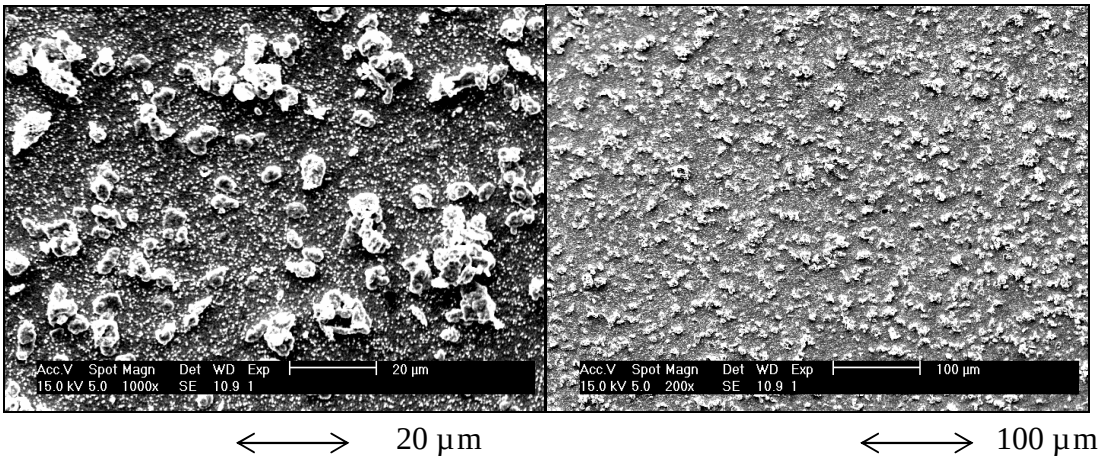

Figure 3.2.3.5 *SEM images of Ni 40 g/dm^{3}with different magnification.*

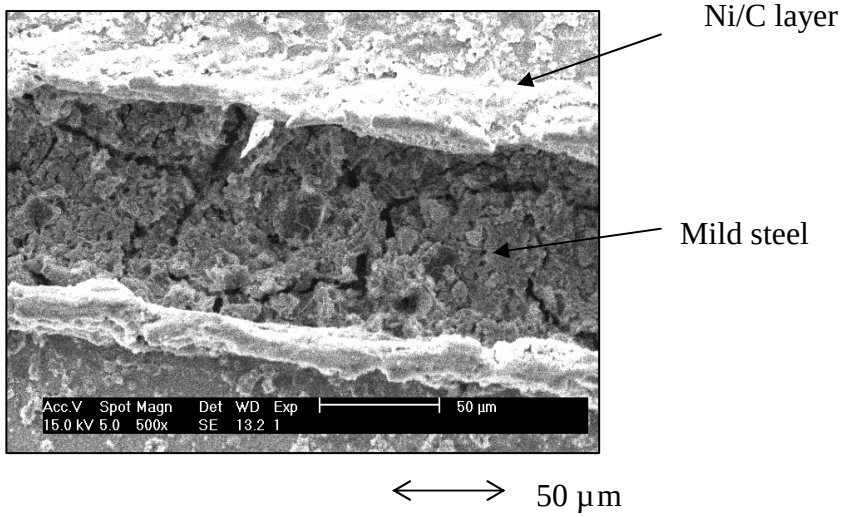

Figure 3.2.3.6 *SEM images of Ni 40g/dm^3 for after open circuit potential impedance measurement at Open Circuit Potential.*

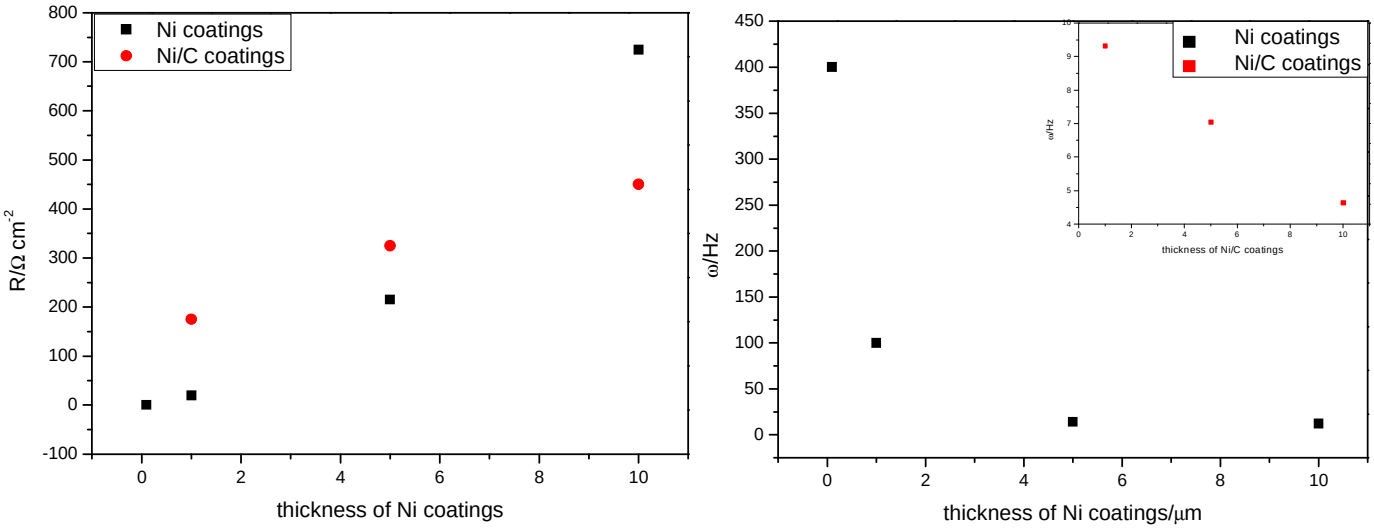

Figure 3.2.3.7 *Influence of Ni coatings on ω vs. C_{dl} and R_{ct} in 1 M of sulphuric acid.*

3.2.4 Conclusion:

- The AC impedance provides a convenient procedure for quality control of the deposition of Ni and Ni/graphite coatings on mild steel.
- Moreover, the results correlate well with measurements of open circuit potentials and cyclic voltammetric data.
- A corrosion resistance < 100 ohms is an indication that the coverage is incomplete and that mild steel is exposed to the solution. Components manufactured with such coatings are unlikely to give an acceptable performance in a fuel cell stack.

Of course, all our data from experiments with a phosphoric acid medium at 353 K would show that Ni itself is not a material to be exposed in the fuel cell stack. Hence the Ni surfaces would require modification to improve substantially their corrosion resistance before application in fuel cells. The impedance in sulphuric acid at room temperature only provides a check that the surfaces are worth such modification.

3.3 The influence of graphite particles on the corrosion rate

3.3.1 Nickel graphite deposited on Ni SS 904L

In order to gain further insight into the properties of Ni/graphite layers in the absence of effects resulting from substrate corrosion, samples were prepared of Ni/graphite coatings on 904 L stainless steel, replacing mild steel. Samples were prepared from the Watts containing 1, 5 and 10 g/dm^3 graphite particles by Jacek Lapinski and it was known from his work [10] that the graphite particles in the Ni layer decreased strongly as the loading of graphite in the electrolyte was decreased. Since the substrate was stainless steel, the steel was first coated with a Wood's strike, then a layer of Ni before the Ni/graphite layer was deposited, see figure 3.3.1.1. Further details may be found in the thesis by Lapinski [10].

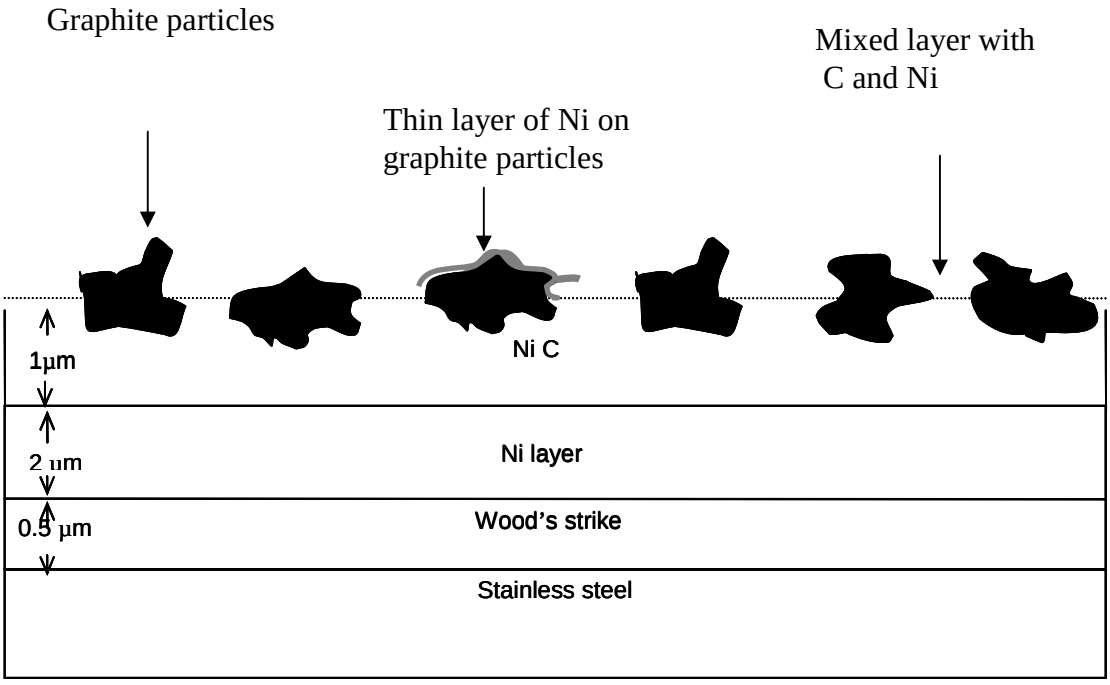

Figure 3.3.1.1 *Sketch of the layer structure on stainless steel 904 L.*

Figure 3.3.1.2 presents SEM images recorded for deposits onto 904 L stainless steel from the electrolytes containing 1, 5 and 10 g/dm^3 of graphite particles. It can clearly be seen that the number density of graphite particles increases with graphite content of the solution. With the lowest loading the particles are well spaced over the surface while with the highest loading the particles are closely spaced with some tendency to form agglomerates.

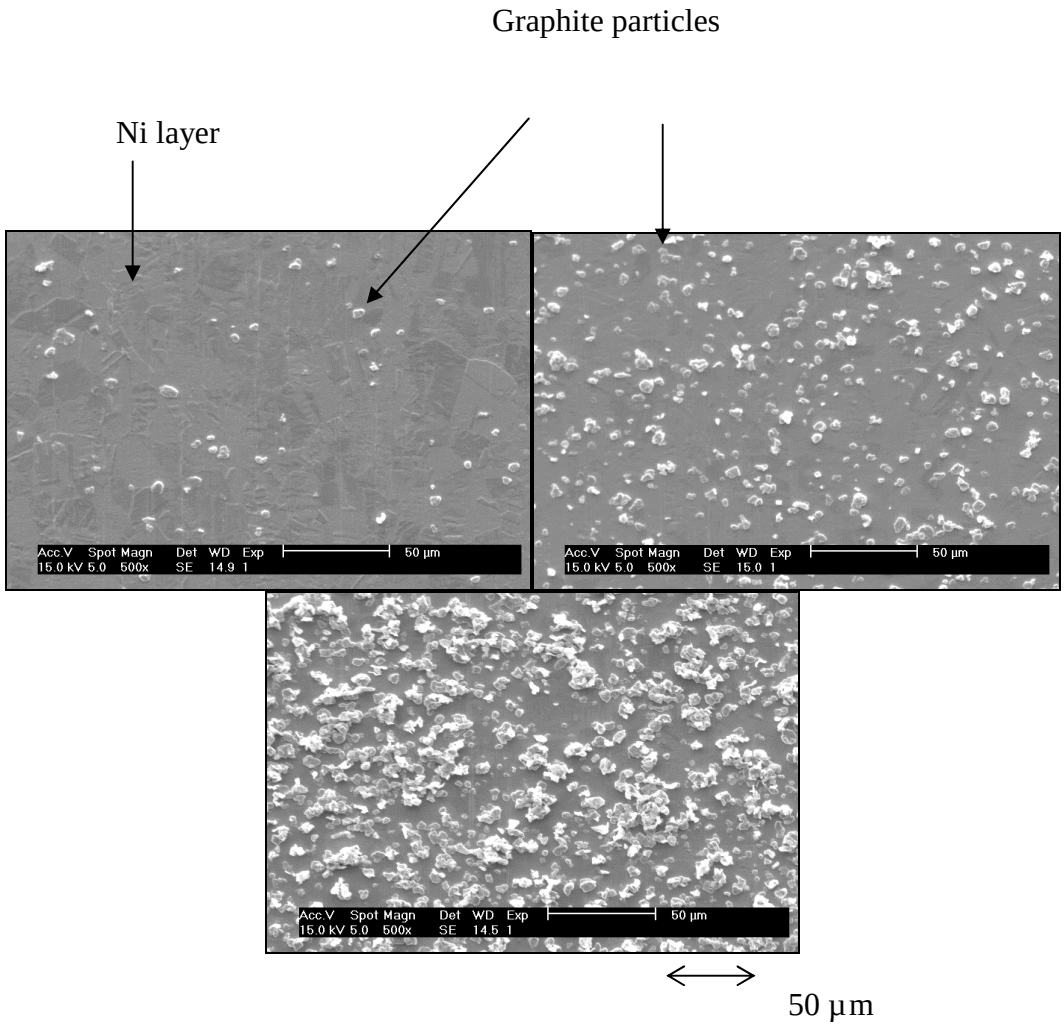

Figure 3.3.1.2 *SEM images as deposited Ni graphite/ Ni/SS 904 L a) 1 g/dm^3 b) 5g/dm^3, c) 10 g/dm^3 of graphite.*

3.3.2 Voltammetry of Ni/ Graphite Layers

Cyclic voltammograms were recorded for the three Ni/graphite surfaces in phosphoric acid pH 2 at 353 K. The voltammograms are shown in figure 3.3.2.1 and the data is represented at a Tafel plot in figure 3.3.2.2. At the initial potential of – 900 mV vs. Hg/Hg_2SO_4, hydrogen evolution occurs on all three samples; also on the forward scan,

the corrosion potentials are very similar. Positive to the corrosion potential, two anodic peaks (A and B) are seen and the peak current densities are large. The first peak (A) for all three samples is at - 480 mV vs. Hg/Hg_2SO_4 and this coincides with the peak potential for the Ni electrodeposits discussed earlier. Also the peak current density is similar for all three samples are similar. Peak B occurs at more positive potentials and clearly this peak increases in height with the graphite loading in the layer. The origin of this peak was studied further below. Beyond peak B, passivation occurs and the current densities drop to a relatively low values. The current densities in the passive region decrease along the series 10 g dm^{-3} > 5 g dm^{-3} > 1 g dm^{-3} and a similar trend is seen on the reverse scan; passivation is more complete with the low C loading. Also some reactivation is seen on the reverse sweep close to the corrosion

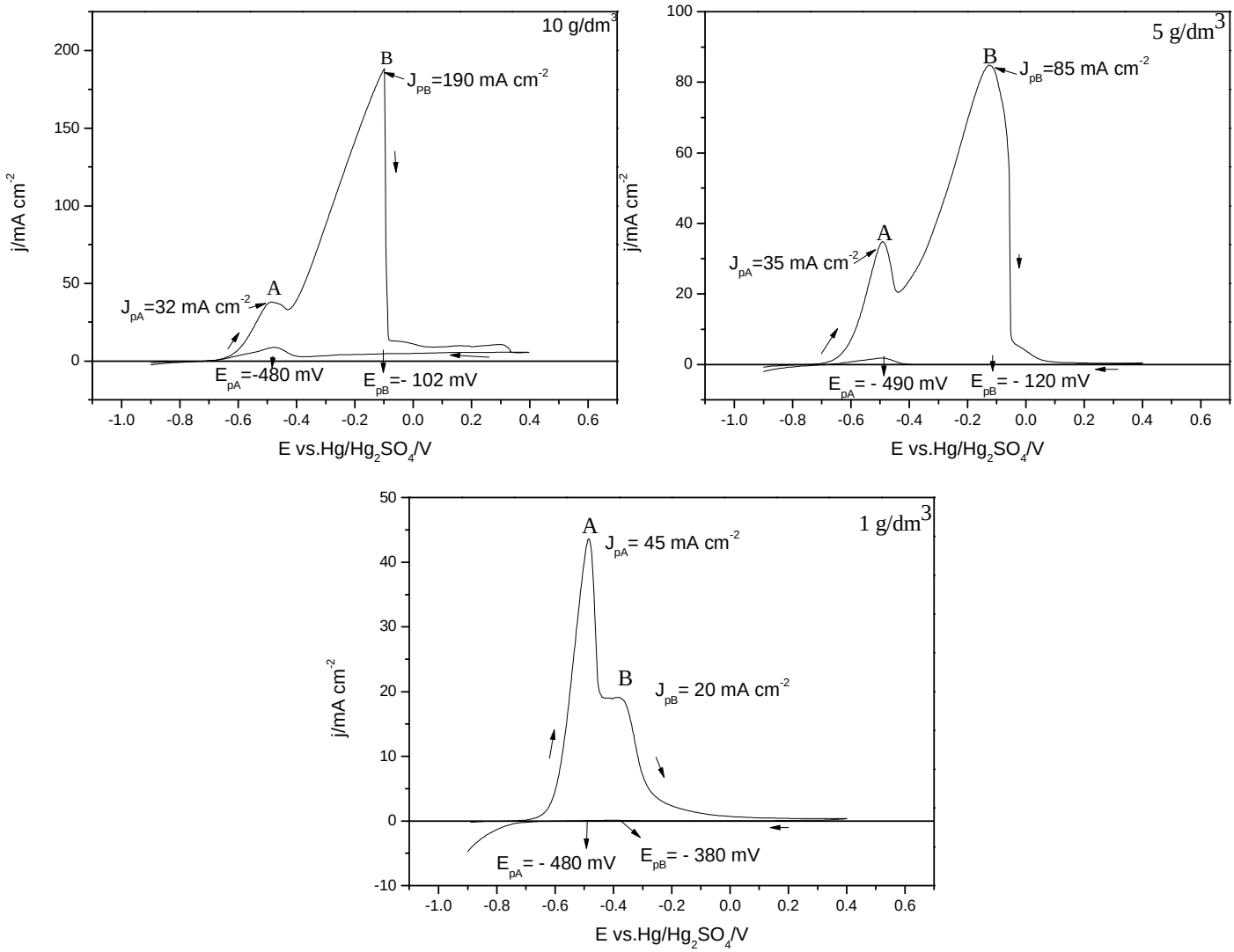

Figure 3.3.2.1 *Cyclic voltammograms of Ni/C deposits from Watts bath with C particles loading of a) 10 g/dm^3, b) 5 g/dm^3 ,c) 1 g/dm^3, in phosphoric acid, pH 2, at 353 K. Potential scan rate 20 mV s^{-1}.*

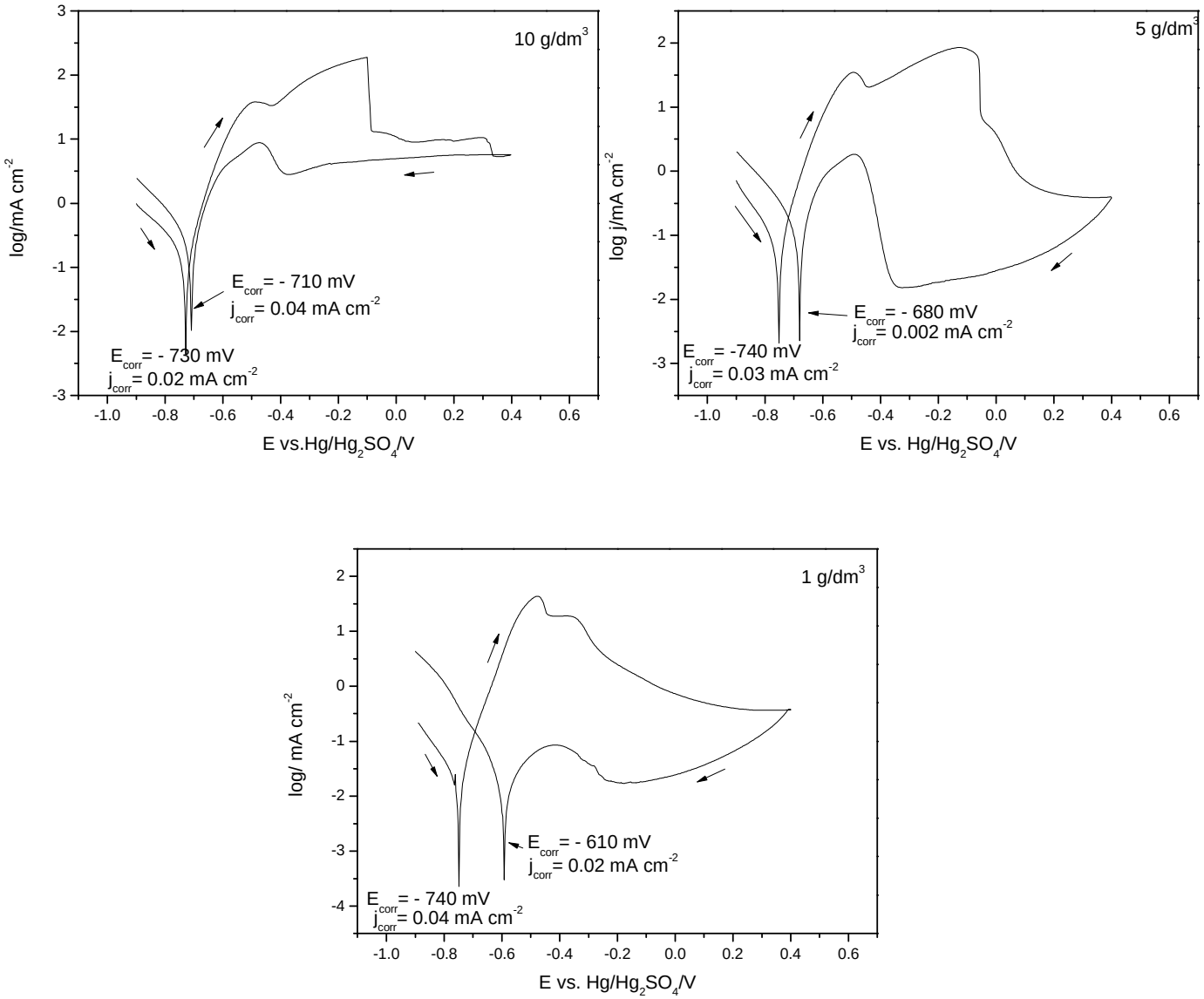

Figure 3.3.2.2 *Data of figure 3.3.2.1 presented as Tafel plots for the three as deposited 1, 5 and 10 g/dm^3 of Ni/C composites, in phosphoric acid pH 2 at 353 K.*

potential. The corrosion potentials from the reverse scan are shifted positive but the shift decreases with graphite loading – another indication that passivation is more complete with the lowest graphite loading. Table 3.11 summarises the data from these voltammograms.

Table 3.11 *Data taken from the voltammograms for the three different C particles loading and two thicknesses of Ni coated mild steel in phosphoric acid, pH 2, at 353 K. Potential scan rate 20 mV* s^{-1}.

Material	**Peak A** **j/mA** cm^{-2}	**Peak B** **j/mA** cm^{-2}	**Q_p/ C** cm^{-2}		**E_{corr}/mV**	
			Q_{pA}	**Q_{pB}**	**Forward Scan**	**Reverse Scan**
1 g/dm^3 C	45	20	0.9	0.4	- 740	- 610
5 g/dm^3 C	35	85	0.5	2.5	- 740	- 680
10 g/dm^3 C	32	190	0.6	4.3	- 730	- 710

When a second cycle voltammogram was recorded, all the anodic peaks were smaller. With the surface prepared from the Watts bath with 1 g dm^{-3} graphite, peak B was absent while with surfaces with a higher graphite loading the current density for peak B was much diminished and the ratio of the peak heights A/B was significantly changed.

In order to test whether oxidation of the graphite itself was responsible for peak B, a voltammogram was recorded for (a) a graphite disc and (b) a layer of graphite particles supported on a Pt disc, both in phosphoric acid, pH 2. The voltammograms are presented in figure 3.3.2.3. In neither case was there a peak comparable to peak B in figure 3.3.2.1. Both the forward and reverse scans were rather featureless except for small oxidation and reduction peaks around – 200 mV. The voltammograms, especially that for the powder, show large charging currents, as expected for a high surface area material. The literature would assign the pair of small oxidation/reduction peaks to the electrochemistry of functional groups on the graphite surface [11-15], most likely for a quinine/hydroquinone couple.

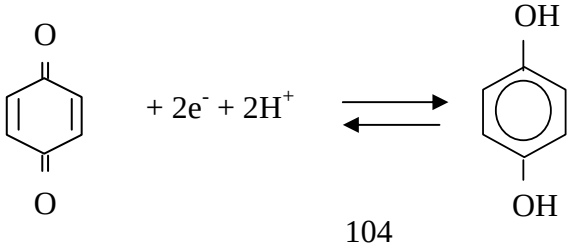

(3.3)

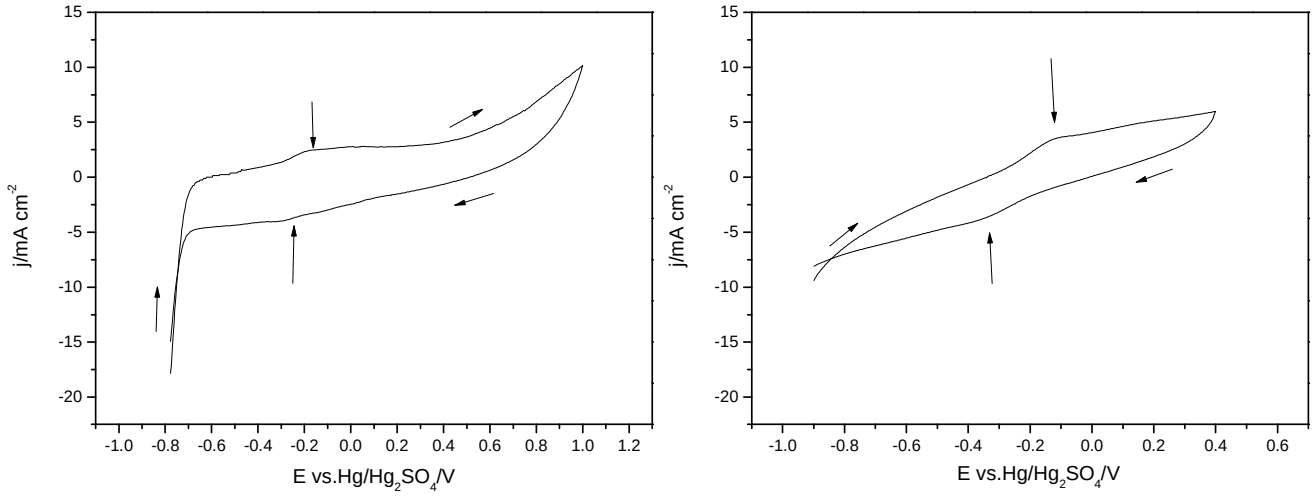

Figure 3.3.2.3 *Cyclic voltammograms of graphite a) bulk of C on Pt ring b) graphite sheet in phosphoric acid, pH 2 at 353 K.*

Certainly, the voltammograms show no evidence for major irreversible peaks that would arise from oxidation of the graphite by mechanisms such as [16-17]:

$$C + H_2O \longrightarrow C(O)_{ads} \qquad (3.4)$$

followed by

$$2C(O)_{ads} \longrightarrow CO_2 + C \qquad (3.5)$$

or/and

$$C(O)_{ads} + H_2O \longrightarrow CO_2 + 2H^+ + 2e^- \qquad (3.6)$$

or peaks that could be assigned to the intercalation of a phoshate or biphosphate anion into the graphite structure

$$C + PO_4^{3-} \longrightarrow C^+PO_4^{3-} \qquad (3.7)$$

Such reactions are known, for example sulphate intercalates into graphite [18-21] although at quite positive potentials.

It is also possible to consider the possibility that nickel catalyses the oxidation of graphite, presumably via nickel oxide species that otherwise lead to passivation of the

nickel surface. It is difficult to believe, however, that this could occur at the very high rates necessary to observe the large peaks, B.

Perhaps the most likely explanation for B is that it arises from the dissolution of nickel on or within pores in the graphite particles. Such metal is certainly in a different environment to the nickel within the layer and is likely to be in a high area, dispersed form. This would lead to the very high current densities for dissolution and the marked decrease in charge on the second cycle. What is not clear is why this nickel should be more difficult to oxidise (it occurs at more positive potential) than the nickel layer. Figure 3.3.2.4 stresses that the height of peak A changes little with graphite loading while that for peak B is strongly dependent on the graphite loading. This would be consistent with peak B arising from oxidation of Ni on the graphite surface.

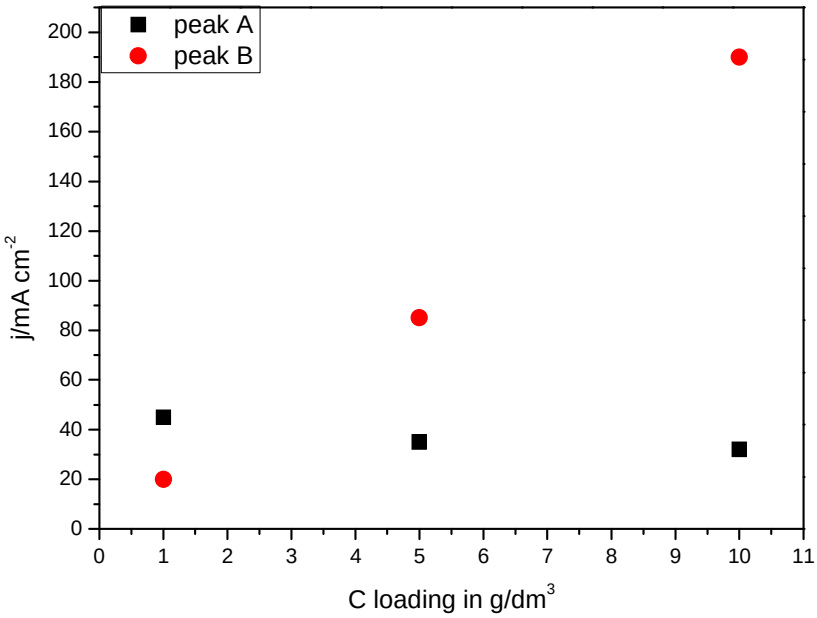

Figure 3.3.2.4 *Correlation between A and B peaks for different C particles loading in 1, 5 and 10 g/dm^{3}onto Ni/stainless steel in phosphoric acid pH 2 at 353 K.*

The three nickel/graphite samples on stainless steel were also monitored during a one hour hold at + 100 mV in phosphoric acid, pH 2, and the conditions selected to mimic the situation of a bipolar plate in a fuel cell. The current densities as a function of time are shown in figure 3.3.2.5. It can be seen that the currents decrease with time and the currents after 1 hour are reported in Table 3.12. The current densities increase

strongly with the graphite content of the Ni/C layer and it is clear that the graphite enhances the rate of corrosion. The extent to which this results only from the additional Ni surface over the graphite particles is uncertain. Certainly, the current densities early in the experiment are low compared to those seen in voltammetry and this implies that passivation is much faster at + 100 mV than at the negative potentials of the voltammetric peak B and therefore, if peak B results from dissolution of the Ni on the graphite, then metal will remain on the surface for a much longer period.

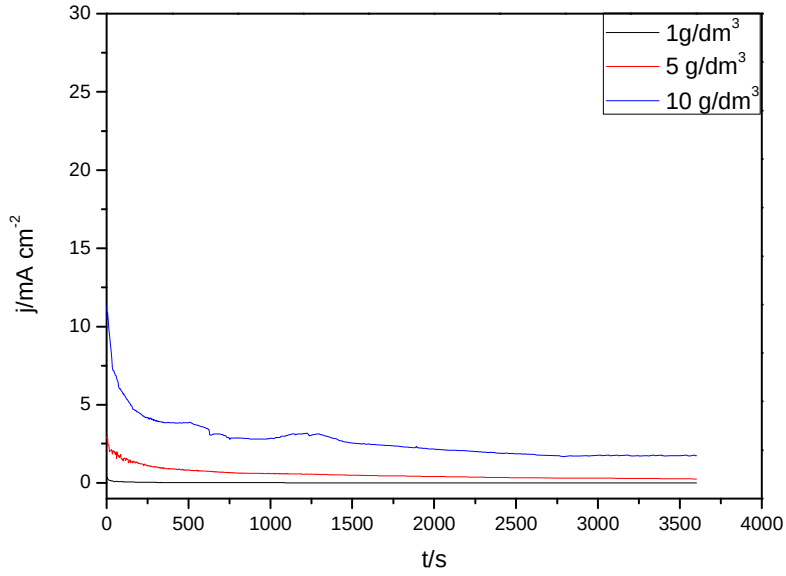

Figure 3.3.2.5 *I-t response for a potential step experiment of 1, 5 and 10 g/dm^3 Ni graphite /Ni/SS 904 L, at E $_=$ + 100 mV vs. Hg/Hg_2SO_4 in phosphoric acid pH 2.*

Table 3.12 *Simulation of cathode condition for different loadings of C in Ni/C layer onto stainless steel in phosphoric acid pH 2 at 353 K.*

Material	**E $_{+ 100\ mV}$ j/ mA cm^{-2}**	**Corrosion rate / mmy^{-1}**
1 g/dm^3	0.01	0.1
5 g/dm^3	0.2	2.8
10 g/dm^3	1.7	29

Figure 3.3.2.6 presents a voltammogram for a sample of Ni/graphite on mild steel prepared by deposition from a Watts bath containing 30 g/dm^3 of graphite particles. The medium is again phosphoric acid, pH 2. It can be seen that the response is significantly different to the samples on stainless steel. Active corrosion/passivation is seen as a single, broad, but large anodic peak. Passivation only occurs over a range of potential and, even in the passive region, the rate of corrosion is substantial, ~ 2 mA cm^{-2}. The reason for the difference in response between the two steel substrates is not known although it is likely that faults in the layer on mild steel contribute to the differences.

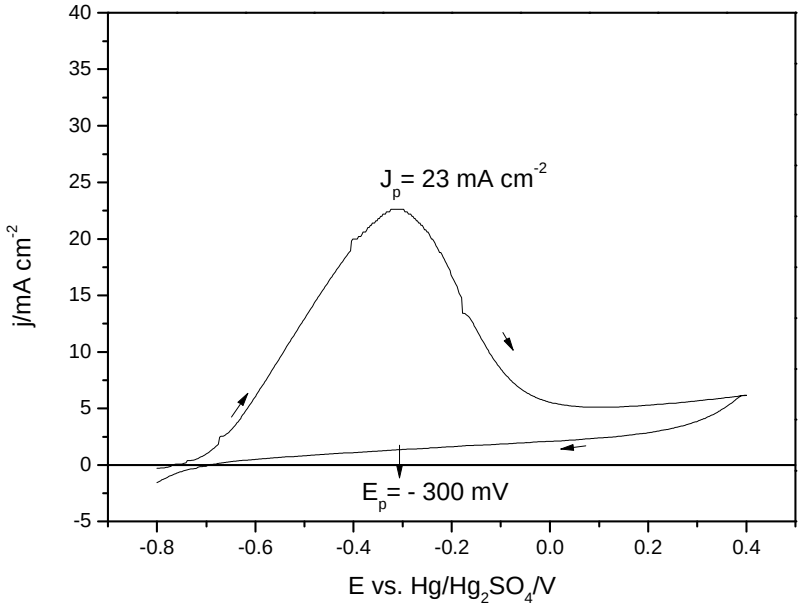

Figure 3.3.2.6 *Cyclic voltammogram of 30 g/dm^3 of Ni/C graphite deposited onto mild steel in phosphoric acid pH 2 at 353 K. Scan rate 200 mV s^{-1}.*

3.3.3 Impedance Investigations of Ni/graphite layers on stainless steel

Impedance spectra were recorded for the three samples with different loadings of graphite particles in Ni/C coated Ni stainless steel 904 L in phosphoric acid pH 2 at 353 K. The data were recorded at the open circuit potentials using a frequency range 10^{-2} – 10^4 Herz and amplitude of $\pm$ 5 mV and the results are presented as Nyquist plots [26-29].

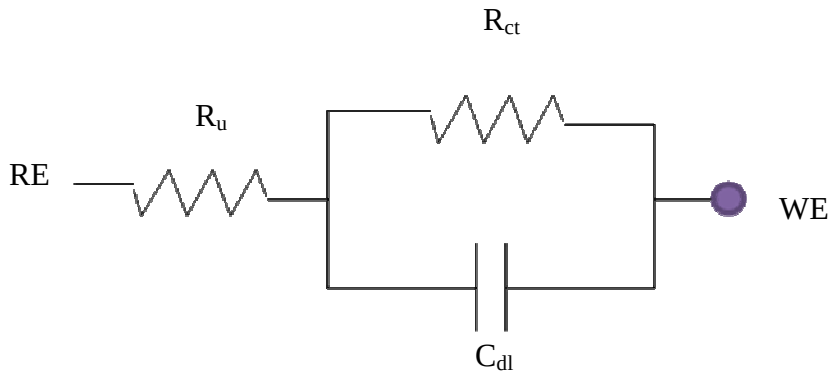

Figure 3.3.3.1 *A simple equivalent circuit.*

Figure 3.3.3.2 presents the results for (a) freshly prepared surfaces and (b) surfaces after they had been held at + 100 mV for 1 hour. Reasonable semi-circles were obtained for all samples and hence the data may again be interpreted in terms of the simple equivalent circuit of figure 3.3.3.1. The corrosion resistances for the fresh samples show little variation with the graphite loading. The values for the samples prepared with 5 and 1 g/dm^3 of graphite particles in the Watts bath are identical but that for 10 g/dm^3 of graphite is slightly lower. After again recording the impedance at open circuit after holding the potential at + 100 mV for 1 hour, the corrosion resistances can be seen to increase.

The surface has been passivated. Moreover, the corrosion resistance now depends on the graphite loading, the passivation being less with the higher loading of graphite. This is consistent with the current densities measured after the 1 hour hold, see Table 3.12.

There is, however, little change to the corrosion potential, see Table 3.13. The corrosion potential is also insensitive to the graphite loading and does not change during the collection of the impedance data. This does not necessarily imply that the rate of corrosion is unchanged; the corrosion potential will not change if the anodic and cathodic processes involved in the corrosion process are equally impeded.

For comparison, the impedance spectra were obtained for uncoated stainless steel both before and after a 1 hour hold at + 100 mV. The spectra are shown in figure 3.3.3.3.

The corrosion resistance of the untreated stainless steel is comparable to the nickel metal discussed earlier but after the more positive potential is applied, the corrosion resistance increases very substantially and it is clear that a passive film that impedes corrosion very effectively. Table 3.14 summarises all the data from the samples in

phosphoric acid, pH 2. This table also includes the data for a commercial sample of Ni/graphite on mild steel and it can be seen that it performs reasonably well and this sample is presumable largely free of pits.

a)

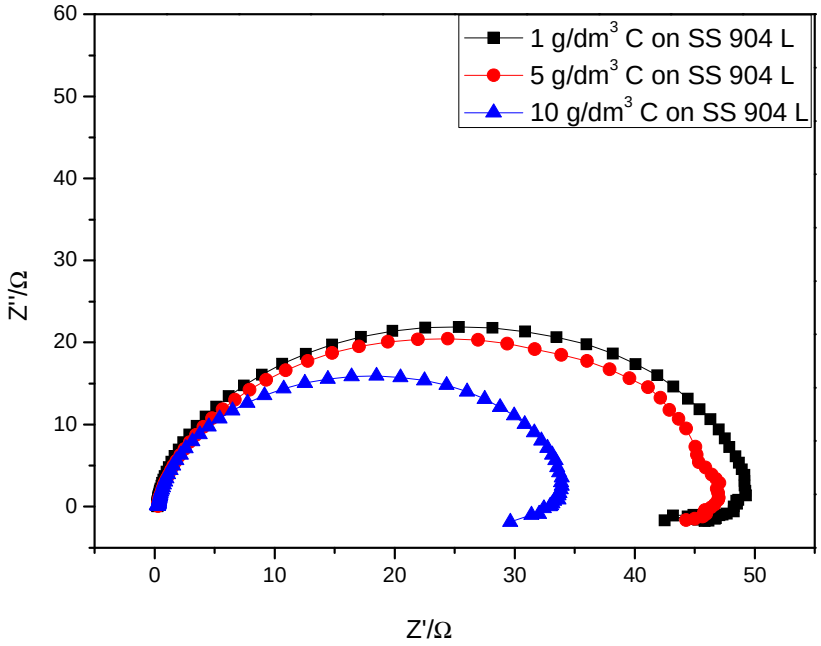

b)

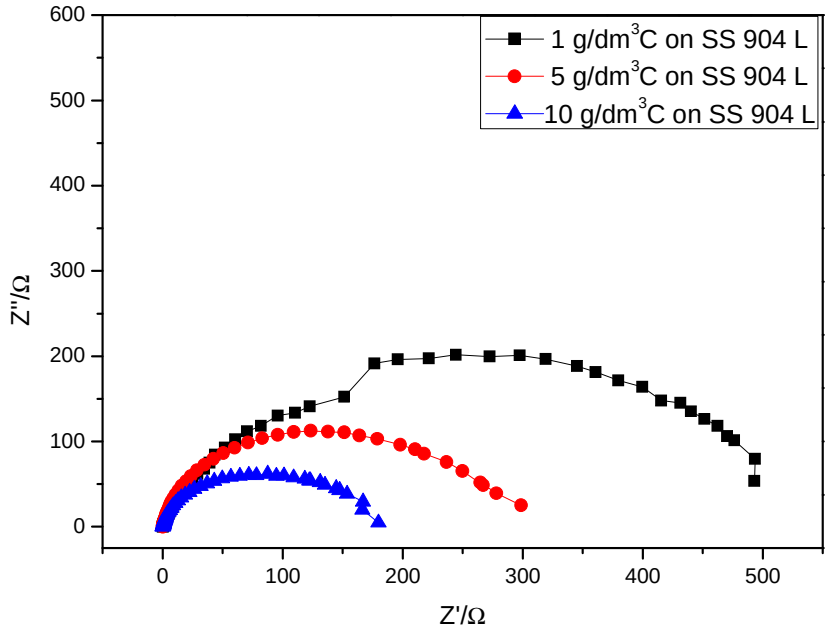

Figure 3.3.3.2 *Nyquist plots of different C particles loadings 1, 5 and 10 g/dm^3 at Open Circuit Potential a) before and b) after hold sample 1 hour at + 100 mV in phosphoric acid pH 2. Temperature 353 K.*

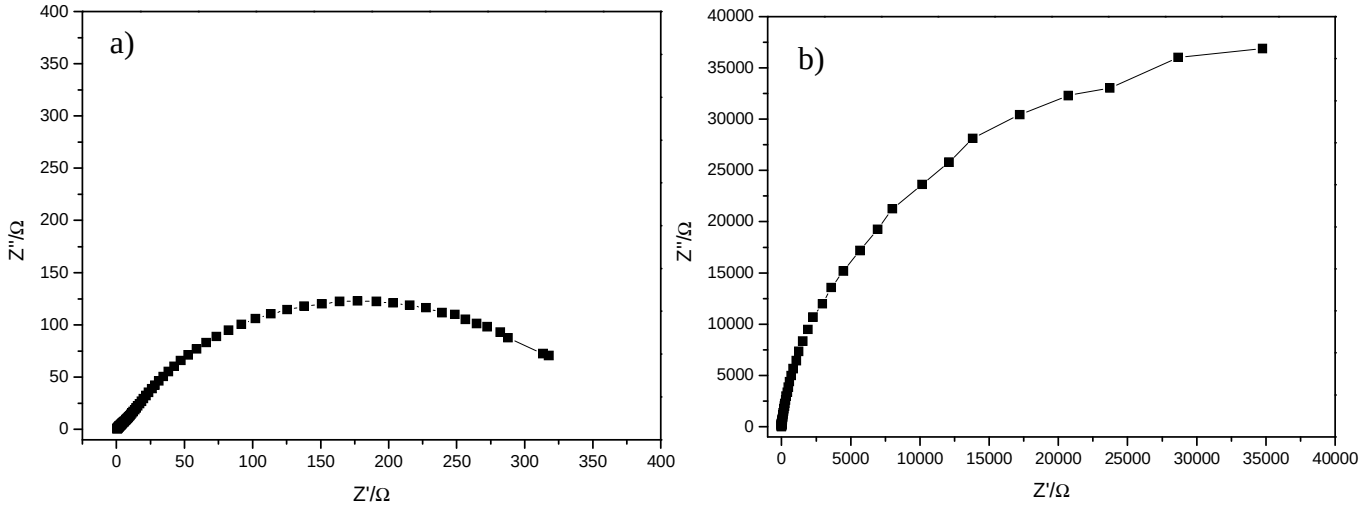

Figure 3.3.3.3 *Nyquist plots of stainless steel at Open Circuit Potential for conditions: a) before and, b) after 1 hour at + 100 mV in phosphoric acid pH 2.*

Table 3.13 *Open Circuit Potentials measured before and after EIS experiments.*

Material	**OCP/ mV**		
	Before	**After**	**After 1 hour at $E_{=+100\ mV}$**
1 g/dm^3	- 780	- 780	- 770
5 g/dm^3	- 770	- 770	- 770
10g/dm^3	- 780	- 770	- 790

Table 3.14 *Charges transfer resistance, maximum of frequencies and capacitances for different of C loadings at open circuit potential and after 1 hour in phosphoric acid pH 2 at 353 K.*

Material	**OCP**			**OCP/After 1 hour at $E_{+100\ mV}$**		
	R_{ct}/Ω cm^{-2}	**C_{dl}/ μFcm^{-2}**	**ω_{max}/Hz**	**R_{ct}/Ω cm^{-2}**	**C_{dl}/ μFcm^{-2}**	**ω_{max}/Hz**
1 g/dm^3	240	96	7.05	2500	90	0.7
5 g/dm^3	235	71	9.33	1500	50	2.1
10g/dm^3	165	21	4.64	900	38	4.6
40g/dm^3	260	100	6.14	1600	240	0.4
Stainless Steel	1500	536	0.19	175000	900	0.01

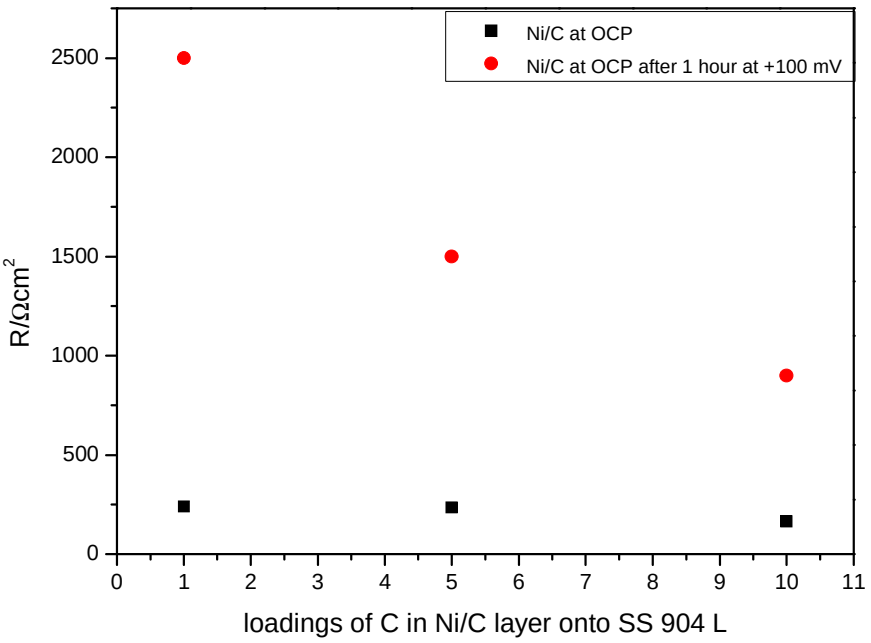

Figure 3.3.3.4 *Influence of C loading in the deposited layer on corrosion resistance at open circuit potential.*

To allow direct comparison with the impedance experiments for the Ni coated mild steel in the previous section, the Ni/graphite surfaces were also studied in 1 M sulphuric acid at 293 K (figure 3.3.3.5). Table 3.15 presents the data obtained at open circuit. Compared with phosphoric acid, the open circuit potential is shifted to a more positive potential.

For sulphuric acid electrolyte a trend in R_{ct}, is found, the value increasing with increase in the loading of graphite particles. The charge transfer resistance for these samples with a stainless steel substrate show are of a similar magnitude to those found for Ni suggesting that the behaviour of the samples is dominated by nickel alone. When the substrate is mild steel any imperfections in the coating lead to a large enhancement in the rate of corrosion.

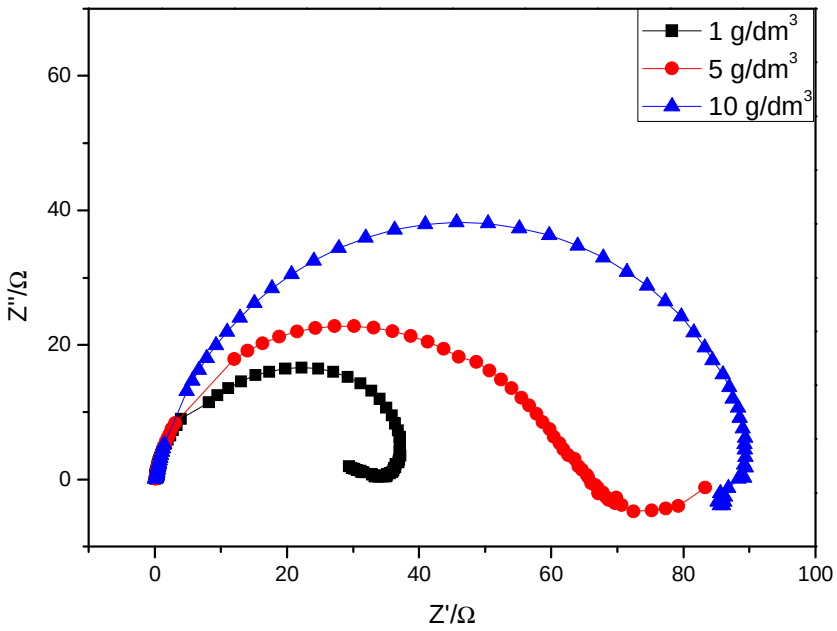

Figure 3.3.3.5 *Nyquist plots of different C particles loadings 1, 5 and 10 g/dm^3 at open circuit potential in 1M sulphuric acid. Temperature 293 K.*

Table 3.15 *Open circuit potentials, charge transfer resistances, and capacitances for Ni/C on stainless steel samples at their open circuit potential in 1 M H_2SO_4. Temperature 293 K.*

Material	**E_{oc}/ mV vs. Hg/Hg_2SO_4**	**R_{ct}/ Ω cm^{-2}**	**C_{dl}/μF cm^{-2}**
Ni/1 g/dm^3 C	- 710	175	112
Ni/5 g/dm^3 C	- 720	325	60
Ni/10 g/dm^3 C	- 740	450	44

3.3.5 Conclusions.

With respect to corrosion, the experiments throughout this chapter comment upon four quite different situations

- The corrosion of fresh samples at their open circuit (corrosion) potential.
- Corrosion in the active corrosion region where dissolution is taking place at a rapid rate.
- Corrosion at + 100 mV where the surface is passivated but there is still a strong driving force for dissolution.
- Corrosion at the open circuit potential for the passivated surface.

In this final section the corrosion behaviour study of different loadings of graphite particles onto Ni deposited on stainless steel in phosphoric acid pH 2 allows the following conclusions:

- With a stainless steel substrate, the high rates of corrosion resulting from pitting are avoided.
- With samples containing graphite particles, the voltammetry in the active corrosion region shows two, high current density peaks. One appears to be due to the dissolution of the Ni in the Ni zones. It is suggested that peak B results from the dissolution of dispersed Ni on the graphite particles.
- With decreasing C particles loading, the corrosion potentials shift to more positive potentials and the second peak decreases.
- The Impedance measurements showed better resistance after holding the sample for 1 hour at constant potential E =+ 100 mV, when passivation film is formed on the surface.

3.4 Reference

[1] D. D. Macdonald *Electrochimica Acta* **51** (2006) 1376- 1388
[**2]** D.E. Tallman *Electrochemical Impedance Spectroscopy*, February 2 (2009)
[3] M.E. Orazem, B. Tribollet *Electrcocimica Acta* **53** (2008) 7360-7366
[4] J.M MacDonald *Electrochimica Acta*, **Vol.35**, No. 10 (1990) 1483-1492
[5] M.E. Orazem, B. Tribollet, N. Pébère *Journal of the Electrochemical Society* **153** (4) B 129-B 136 (2006)
[6] P. L. Bonora,F . Deflorian, L. Fedrizzi *Ectrochimica Acta***Vol. 41**. Nos. l/8. pp. 1073. 108.2, 1996
[7] P. Agarwal, M.E. Orazem *J. Electrochem. Soc*.,**Vol. 139**, No. 7 (1992)
[8] D. Loveday, P.Peterson, B. Rogers Part 1 Fundamental of Electrochemical Impedance Spectroscopy *JCT Coatings Tech* **October 2004**
[9] D. Loveday, P.Peterson, B. Rogers Part 2 Applications of EIS to Coatings JCT *Coatings Tech* **October 2004**
[10] J. Lapinski *Optimization of protective coating for steel-based bipolar plates in PEM fuel cell*, 2010
[11] A.B. Dongil, B. Bachiller-Baeza, A. Guerrero-Ruiz, I. Rodríguez-Ramos, A. Martínez-Alonso, *Journal of Colloid and Interface Science* **355** (2011) 179–189
[12] T. Szabò, E. Tombácz, E. Illés, I. Dékány *Carbon* **44** (2006) 537–545
[13] Z. Klusek, P.K. Datta, W. Kozlowski *Corrosion Science* **45** (2003) 1383–1393
[14] M. Rueffer, D. Bejan, N.J. Bunce *Electrochimica Acta* **56** (20110 2246-2253
[15] S.K. Sharma, F.J. Vastola, P.L. Walker Jr. *Carbon* **Vol. 35**, No.4 pp. 529-533, 1997
[16] V.V. Parshutin, N.L.Bogdashkina, G.P. Chernova *Protection of Metals* **Vol. 43** (2007) 59-65
[17] H. Iken, R. Basseguy, A. Guenbour, A. Ben Bachir *Electrochimica Acta* **52** (2007) 2580-2587
[18] M. Noel, R. Santhanam *Journal of Power Sources* **72** (1998) 53-56
[19] F.Kang, T-Y.Zhang, Y.Leng *Carbon* **Vol. 35**, No.8 pp. 1137-1173, 1997
[20] M. S. Dresselhause *Materials Science and Engineering, BI* (1988) 259-277
[21] A. Moissette, H. Fuzellier, A. Burneau, J. Dubessy, M. Lelaurain *Carbon*, Vol. **33,** No. 2, pp. 123-1281, 995

Chapter 4

Corrosion of Ni –Cr alloys.

In this chapter corrosion of Ni-Cr alloys in phosphoric acid is presented. Topics covered:

- The structure and composition of Ni-Cr alloys.
- The passivation process.
- Investigations of the microstructure of the alloys.
- X-ray Diffraction study and characterisation of the surface of the alloys.

4.1 A comparison of the corrosion rates on Nickel/Chromium Alloys in phosphoric Acid Media at 353 K

4.1.1 Nickel/Chromium Alloys as foils

In this chapter, we seek to compare the corrosion behaviour of chromium, nickel and their alloys (Ni90Cr10, Ni80Cr20, and Ni50Cr50) in phosphoric acid pH 2 (no other electrolytes added) at a temperature of 353 K. The solutions were thoroughly deoxygenated with a fast stream of N_2 before each experiment. In addition Ni80Cr20 alloys were tested in two forms, rod, and foil. Table 4.1 presents the compositions of the materials studied. In view of the results found, it is important to note that the chemical composition of two Ni80Cr20 sample (as stated by the supplier) are identical.

Ni, Cr, and Ni80Cr20 were tested as foils (figure 4.1.1.1). Results for pure Ni and Cr have been described in detail in a previous chapter. It should be noted that the volatmmogram for Ni foil shows very large current densities in the active corrosion region just positive to E_{corr} and the current density positive to the peak is substantial. Oxidation continues to be rapid even on the reverse scan back towards negative potentials. The surface of nickel is poorly passivated and in the region from – 300 to + 400 mV. The presence of the anodic current during the reverse scan indicates the high corrosion activity of the partially passivated surface.

On the other hand the voltametric response of pure Cr (see figure 4.1.1.1b) shows only a low corrosion activity with a defined passivated region at the higher potentials. The cyclic voltammogram for the Ni80Cr20 alloy was commenced at - 800 mV where there is a current corresponding to the hydrogen evolution. The corrosion potential is located at E_{corr} - 660 mV. The active corrosion region is located approximately at - 600 to - 550 mV. An anodic peak lies at - 590 mV with a maximum of the current density j_p~ 120 µA cm^{-2}. The charge under the oxidation peak Q_p ~ 2.4 mC cm^{-2} much lower than the charge for Ni oxidation. Beyond the peak, the current densities are low. On the reverse scan, the surface is strongly passivated. The current density crosses zero at - 110 mV and there is a small cathodic wave close to this potential. The Tafel plot for Ni80Cr20, see figure 4.1.1.1d emphasises the strong hysteresis between forward and reverse scans. The surface is strongly passivated, although the large

positive shift in the zero current potential results from the small cathodic wave on the reverse scan.

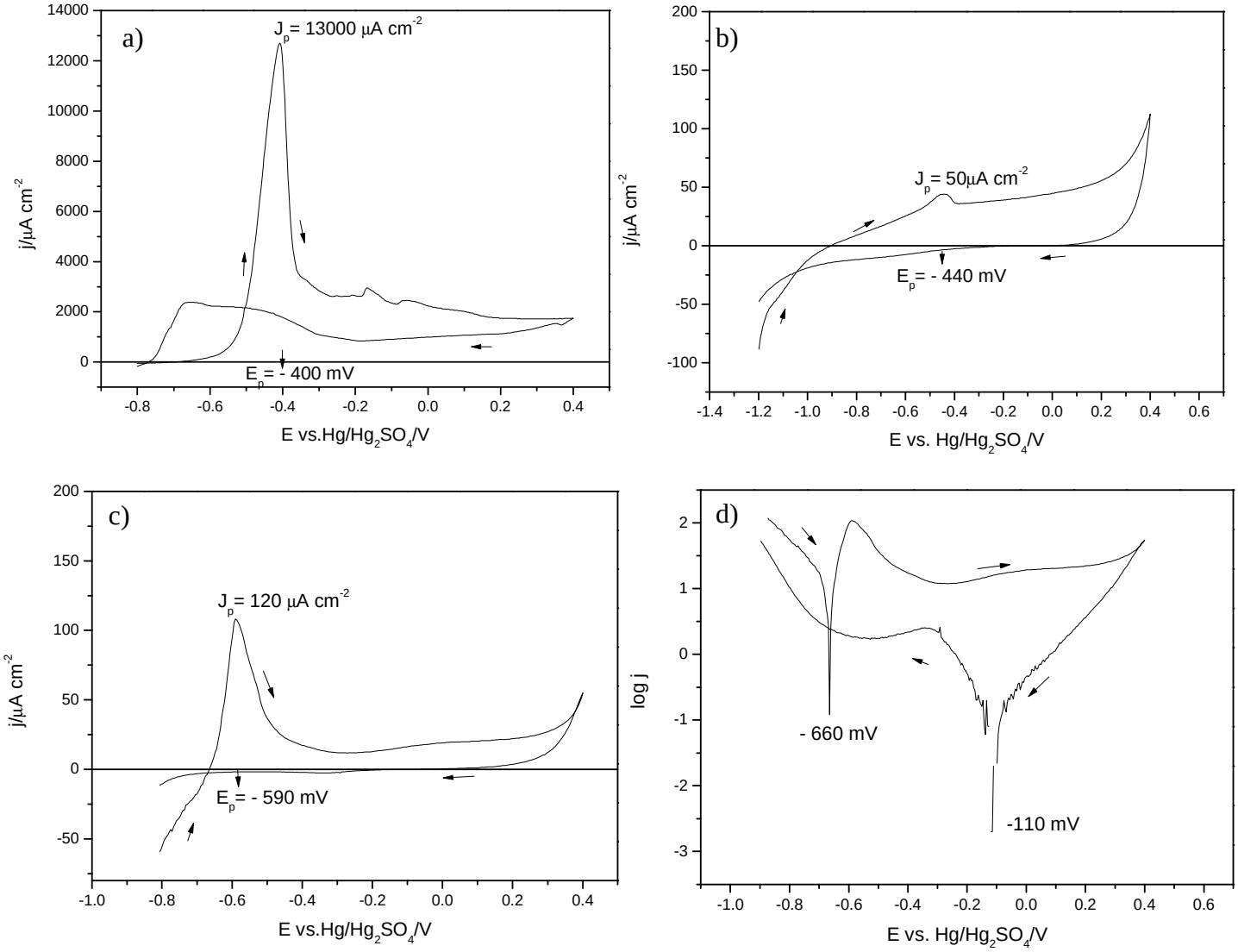

Figure 4.1.1.1 *Cyclic voltammograms of foils a) Ni, b) Cr c) Ni80Cr20 and d) Tafel plot of Ni80Cr20 in phosphoric acid pH 2. Temperature 353 K. Potential scans rate 20 mVs^{-1}.*

Table 4.1 *Compositions of the materials studied as provided by the suppliers.*

Material	**Cr**	**Ni**	**Si ppm**	**Al ppm**	**Fe ppm**	**Mn ppm**	**Mg ppm**	**Ca ppm**	**Cu ppm**	**Sn ppm**	**Ag ppm**
Ni	<1	balance	2	1	15	<1	<1	1	3	< 2	1
Ni90Cr10	9.5%	balance	5000	-	1500	-	-	-	-	-	-
Ni80Cr20 rod	18-20%	balance	1.5 %	1000	2000	2000	-	-	-	-	-
Ni80Cr20 foil	18-20%	balance	1.5%	1000	2000	2000	-	-	-	-	-
Ni50Cr50	~50%	balance	40	75	115	-	1	5	80	-	-
Cr	Balance	-	-	<1	1	-	<1	5	3	-	<1

4.1.2. Nickel/Chromium Alloys as rods.

Figure 4.1.2.1 compares voltammograms recorded at 20 mVs^{-1} for the three alloys Ni90Cr10, Ni80Cr20, and Ni50Cr50 (all rods) in phosphoric acid pH 2, at 353 K. The electrodes discs were well polished prior to each voltammogram. Data taken from these voltammograms is reported in Table 4.2. Both 10% and 20% of chromium alloys show well defined active corrosion regions positive to the corrosion potential with the passivation at more positive potentials. In addition, the anodic peak potentials shift negatively as the concentration of Cr changes from 0 to 10 to 20%. With Ni90Cr10 and Ni80Cr20, the current density positive to the peak is much lower than for Ni, particularly on the reverse scan; the surfaces are much more fully passivated and the current densities are very low. The peak current densities, but not peak potentials for the foil and rod samples of Ni80Cr20 are quite different despite the fact that the chemical compositions are the same; this implies can be an importance for structure as well as composition in determining the rate of corrosion. It also appears that the addition of Cr to Ni enhances the cathodic current density associated with H_2 evolution. Negative to – 600 mV, the voltammograms for the Ni - Cr alloys are complex and the potential ranges for H_2 evolution and metal oxidation may overlap. The alloys with 10% and 20% Cr give similar H_2 evolution current. Figure 4.1.2.1c shows cyclic voltammogram recorded at the Ni50Cr50 disc electrode. The shape of the response is quite different and there is the formation of anodic peak at - 700 mV is seen. This is however unclear whether the dissolution of alloy shifted negative by a continuation of the trend with Cr content or oxidation of H_2 is responsible for the formation of the peak. Particularly the Ni90Cr10 voltammogram shows anodic current positive to – 780 mV and this may be due to H_2 oxidation.

Table 4.2 *Data taken from the voltammograms for the two metals and three alloys in phosphoric acid, pH 2, at 353 K. Potential scan rate 20 mV* s^{-1}*. Potential measured vs.* Hg/Hg_2SO_4*.*

Material	**$E_{corrosion}$/mV**		**Anodic Oxidation Peak**			**$j_{E=100\ mV}$(reverse) /µA cm^{-2}**
	Forward	**Reverse**	**E_p/mV**	**j_p/µA cm^{-2}**	**Q_p/mC cm^{-2}**	
Ni *foil*	- 690	- 760	- 400	12700	200	1070
Ni90Cr10 *rod*	- 720	- 420	- 480	630	20	40
Ni80Cr20 *foil*	- 660	- 110	- 590	120	2.4	3
Ni80Cr20 *rod*	- 730	- 550	- 600	4500	70	75
Ni50Cr50 *rod*	- 790	- 670	- 690	190	5	30
Cr *foil*	- 900	- 120	- 440	45	1.4	0.1

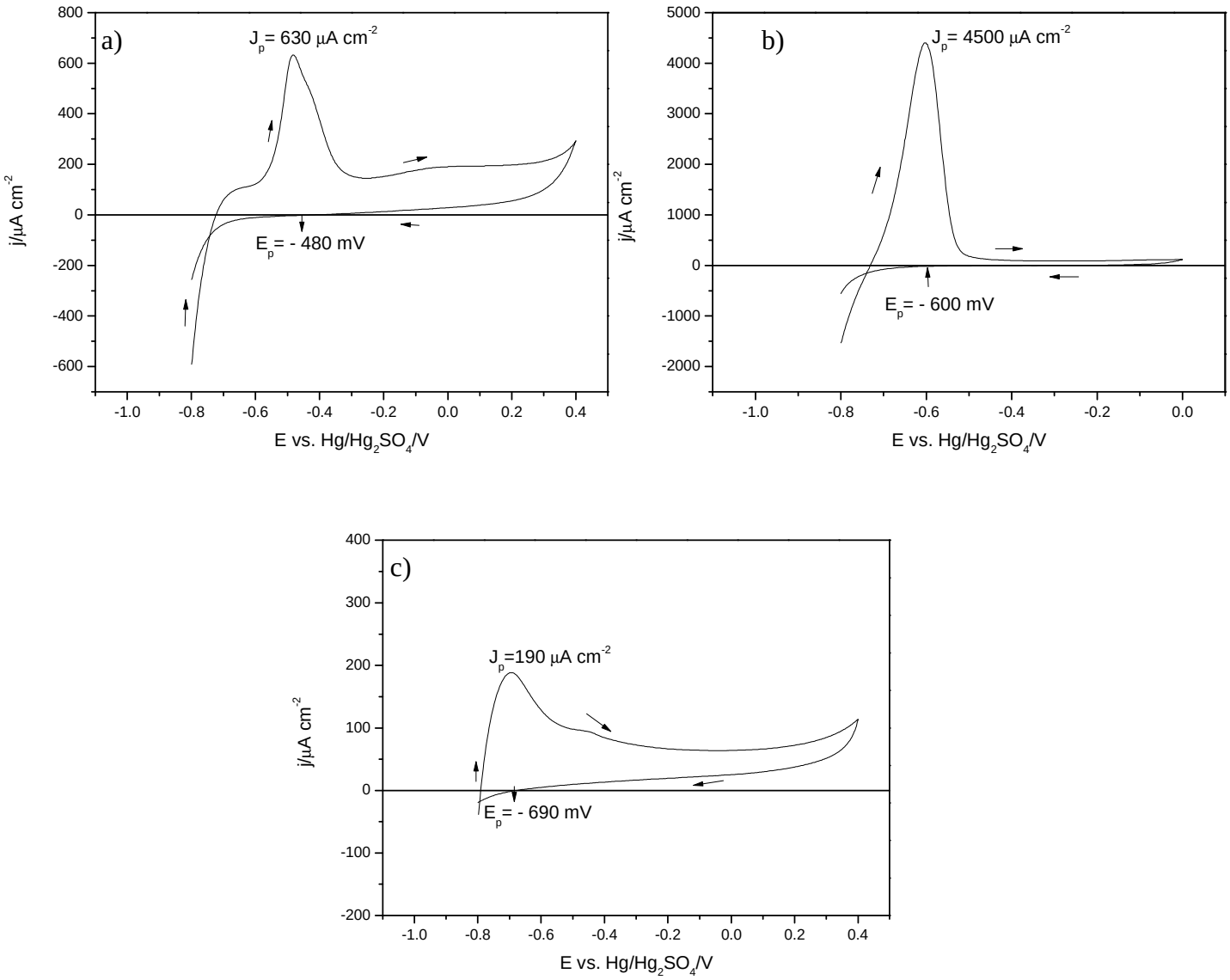

Figure 4.1.2.1 *Cyclic voltammograms of Ni-Cr rods a) Ni90Cr10, b) Ni80Cr20 c) Ni50Cr50, in phosphoric acid, pH 2. Temperature 353 K. Potential scans rate 20 mVs^{-1}.*

Further studies were focused on investigating the corrosion potential of the different compositions. Figure 4.1.2.3 reports the voltammetric data of the three Ni-Cr alloys replotted as Tafel plots. These show small shifts in the corrosion potentials but no trend with the alloy composition. The voltammograms also show large hysteresis

between forward and reverse scan characteristic for all studied alloys in the condition employed. It also noticed that the large shifts in the open circuit potentials have occurred after alloy passivation. This shift largely results from a small cathodic current seen for the passivated surface at more positive potential, see figure 4.1.2.2. This wave results from some change in the passivating layer as it does not correspond to either oxygen or proton reduction (voltammograms for an oxygenated solution or one of lower pH do not show an increased current density). The absolute values of the current densities at the positive potentials as well as the largest shift in corrosion potential indicate that Ni80Cr20 (foil) is the alloy with the lowest corrosion rate after passivation.

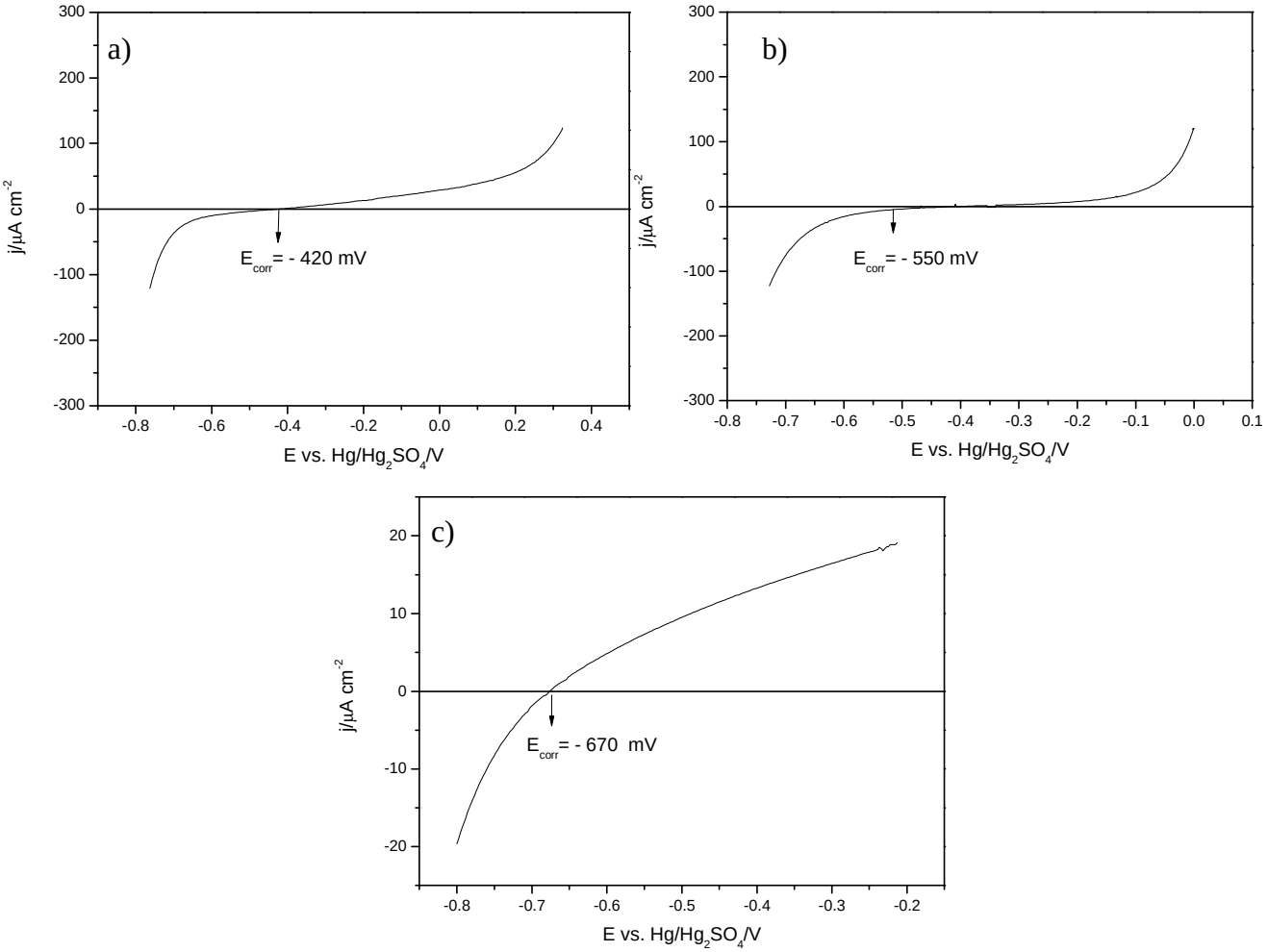

Figure 4.1.2.2 *Reverse potential scans for the three Ni-Cr alloys as discs a) Ni90Cr10, b) Ni80Cr20 rod, d) Ni50Cr50 in phosphoric acid pH 2, and temperature 353 K.*

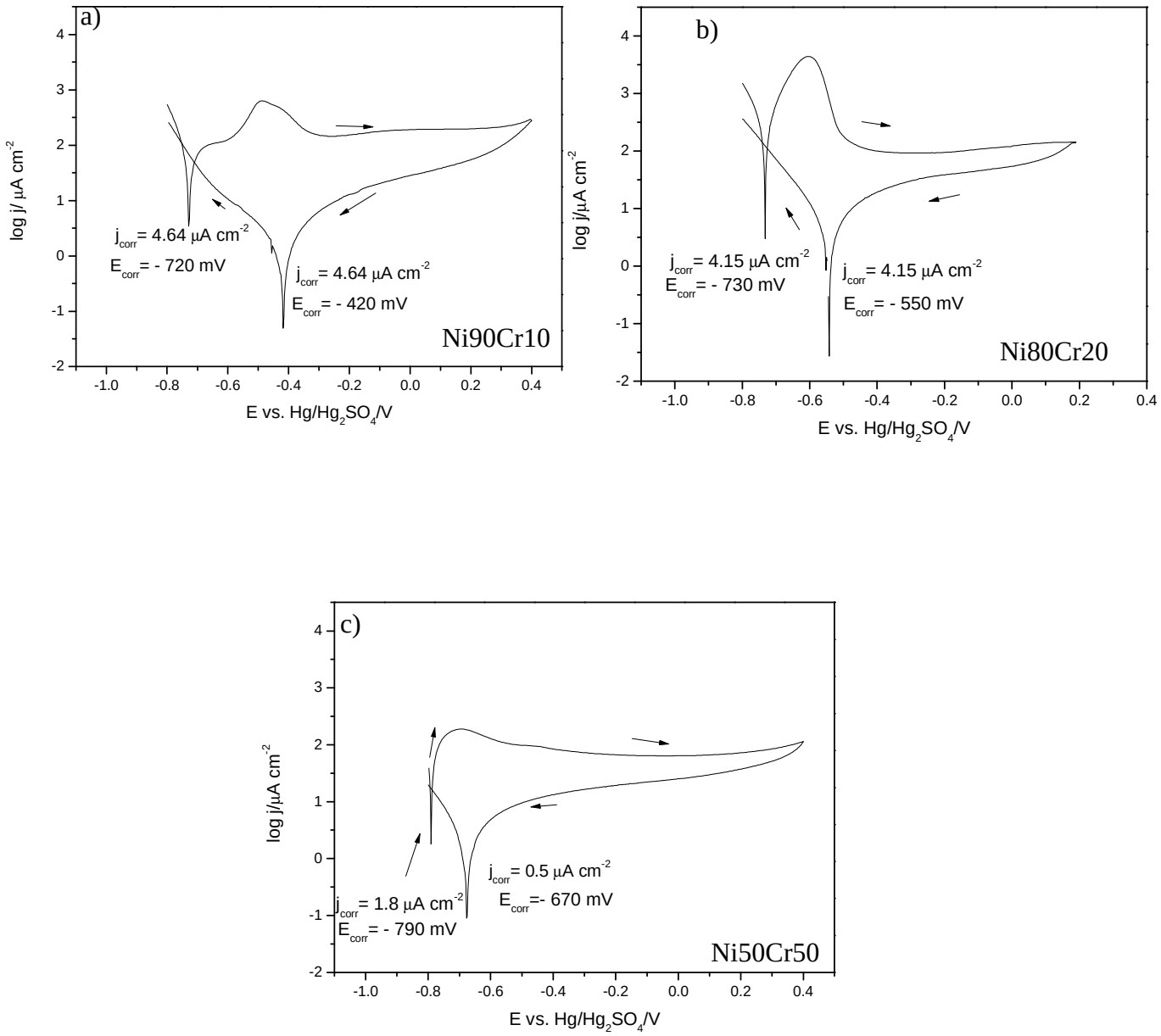

Figure 4.1.2.3 *Data of figure 4.1.2.1 presented as Tafel plots for the three Ni-Cr alloys as discs a) Ni90Cr10, b) Ni80Cr20 rod, d) Ni50Cr50 in phosphoric acid pH 2, and temperature 353 K.*

4.1.3 Further studies of the Ni-Cr alloys.

The behaviours of the Ni-Cr alloys are more complex than the pure metals.
The difference in the preparation of the materials could affect the corrosion behaviour of the alloys. In particular, production of a foil includes rolling of the raw materials which in turn could result in the substantial structural changes. This may explain the differences between Ni80Cr20 as rod and foil.

a) Voltammetry of passivated surfaces.

Multiple potential cycles without surface polishing were recorded. For all samples, polished electrodes were employed. For the pure Ni the anodic peak current density decreases slowly with the repetitive cycling. In contrast the peak heights for the Ni-Cr alloys decrease much more rapidly and the voltammograms become increasingly featureless (figure 4.1.3.1). Table 4.3 presents results collected for second scans of Ni-Cr alloys as rods. In a further experiment, holding the materials for on 1 hour at constant potential +100 mV, all alloys showed very little electrochemical activity, indicating the effective and irreversible passivation of the analysed surfaces**.**

Table 4.3 *Data taken from the voltammograms for the second scans of the Ni-Cr alloys as rods, in phosphoric acid, pH 2, at 353 K. Potential scan rate 20 mV* s^{-1}*. Potential vs.* Hg/Hg_2SO_4*.*

Alloy	**E_{corr}/mV**		**E_p/mV**	**j_p/ µA cm^{-2}**	**Q_p/mC cm^{-2}**
	Forward	**Reverse**			
Ni90Cr10	- 770	- 370	- 720	94	0.94
Ni80Cr20	- 770	- 550	- 740	103	1.4
Ni50Cr50	- 670	- 160	- 510	14	0.4

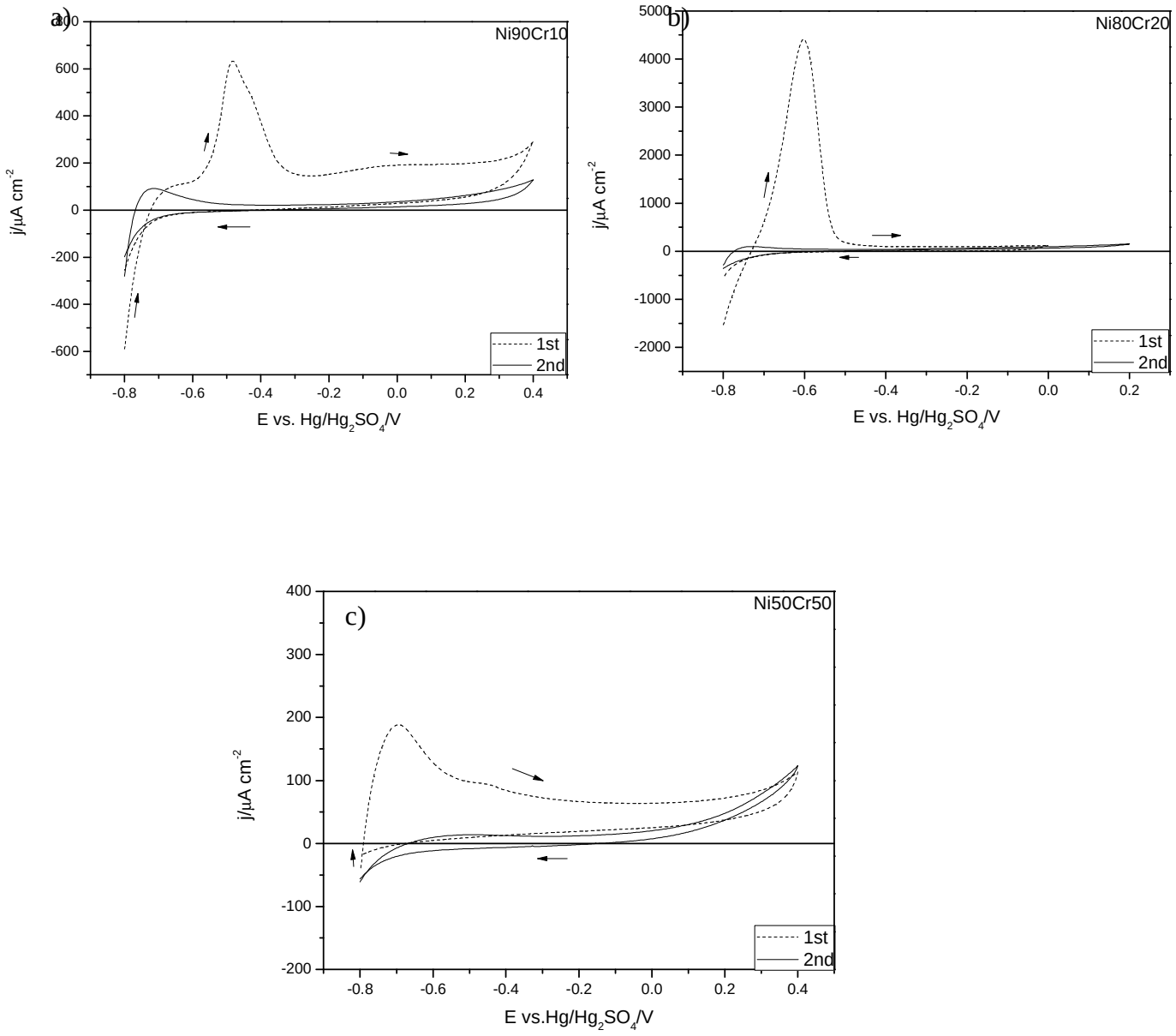

Figure 4.1.3.1 *Cyclic voltammograms of second scans of Ni-Cr alloys rods of a) Ni90Cr10, b) Ni80Cr20 and c) Ni50Cr50, in phosphoric acid, pH 2. Temperature 353 K. Potential scans rate 20 mV* s^{-1}.

b) Corrosion at the Open Circuit Potential.

The data close to the corrosion potential was also examined to investigate the corrosion rate of the 'unpassivated' surface. The alloy's corrosion resistance R_{corr} can estimated from the linear I/E data around the corrosion potential

$$R_{corr} = \frac{1}{slope}$$

Figure 4.1.3.2 shows typical data which has been employed to calculate R_{corr} for the studied materials. Table 4.4 presents R_{corr} for Ni - Cr alloys from forward and back scans. The data shows a large increase in corrosion resistance resulting form passivation.

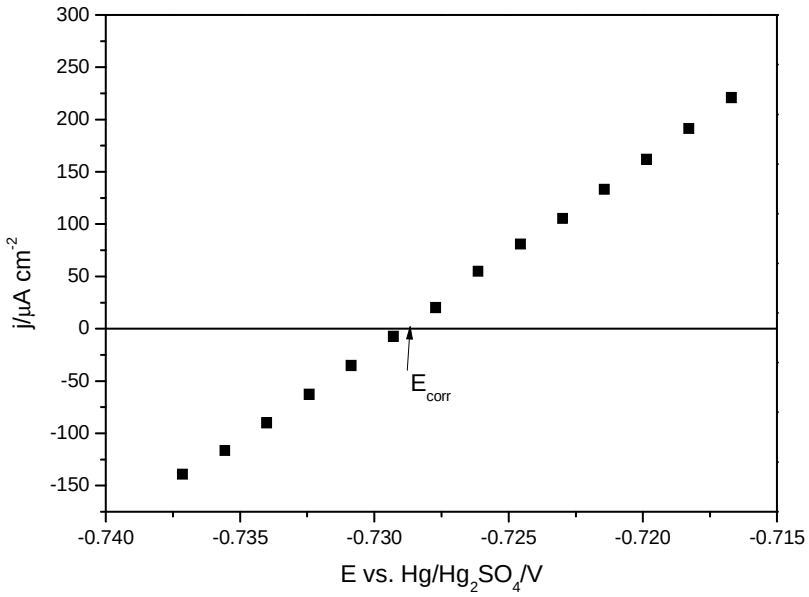

Figure 4.1.3.2 *Slope for Ni80Cr20 (rod) with E_{corr} potential ± 10 mV.*

Table 4.4 *Data taken from linear sweep around ± 10 mV of cor rosion potential.*

Material	**R_{corr} / Ω cm^{-2}**	
	Forward	**Back**
Ni90Cr10 rod	317	21186
Ni80Cr20 rod	56	16282
Ni80Cr20 foil	1753	153465
Ni50Cr50 rod	193	13076

c) Corrosion in the Passivation Region

It was important to investigate the behaviour of the alloys close to the PEM fuel cell environment. This was examined by applying the potential of + 100 mV vs. Hg/Hg_2SO_4, the value estimated for oxygen reduction at pH 2, for 1 hour and monitoring the current. Each of the materials showed an initial high current density which rapidly dropped to a lower value and had reached a 'steady state' after one hour. The experiment was repeated at pH 1 and pH 3, all solutions containing only phosphoric acid. The potential for experiment was shifted by 60 mV/pH unit to allow for the change in O_2 reduction potential. The currents after 1 hour increased with acidity, see Table 4.5. Nickel can be characterised by high current density, while Cr shown low current with no influence of pH.

The explanation of this behaviour for Cr can be the fast aerial oxidation and film formation before step experiment. In fact Ni80Cr20 foil and rod have the lowest currents density and much better than of pure Ni. Influence of pH on current density of Ni-Cr alloys are collected on figure 4.1.3.3.

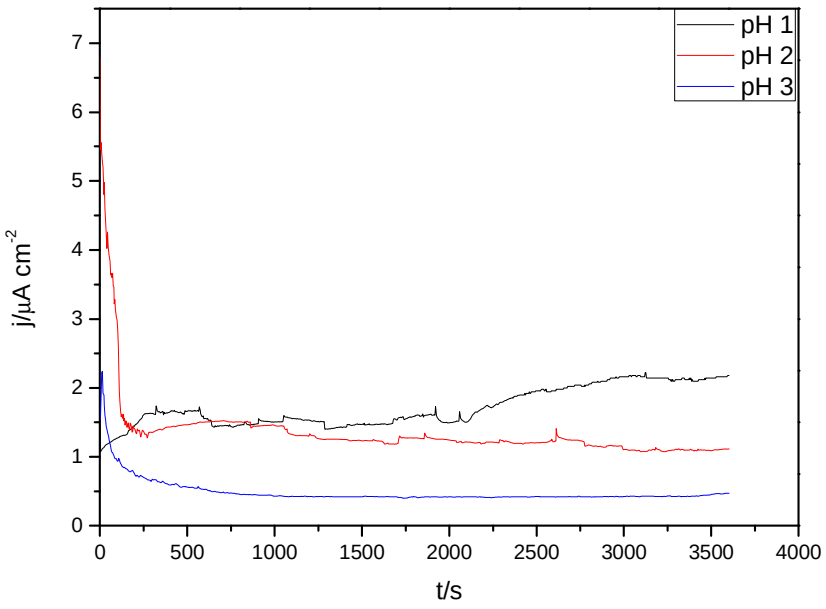

Figure 4.1.3.3 *Influence of pH on behaviour of Ni90Cr10 alloy in phosphoric acid at 353 K.*

Table 4.5 *Current densities after 1 hour at the potentials (vs. Hg/Hg_2SO_4) estimated for the oxygen cathode in a fuel cell at the three pH. Solutions contain only phosphoric acid. Temperature 353 K.*

Material	**pH 1, E =+ 160 mV j/µA cm^{-2}**	**pH 2, E = + 100 mV j/µA cm^{-2}**	**pH 3, E =+ 40 mV j/µA cm^{-2}**
Ni *foil*	2180	1000	470
Ni90Cr10 *rod*	2.4	1.4	0.7
Ni80Cr20 *foil*	0.4	0.3	0.2
Ni80Cr20 *rod*	1.0	0.6	0.4
Ni50Cr50 *rod*	1.3	1.0	0.5
Cr *foil*	0.2	0.2	0.2

It is clear to see that there is a big difference in the current densities even in the passivation region for the Ni80Cr20 foil and rod. The foil gives much lower current density in all investigated cases. For the Ni80Cr20 foil and rod, it is concluded that Ni80Cr20 as foil is oxidized and passivated faster and easier than the same composition as rod.

4.2 Phase compositions of Ni - Cr alloys

The structures of the Ni-Cr alloys have been probed by X-ray diffraction to determine the phase composition. Each sample has been well polished to a very smooth and flat surface. Then the sample has been kept in a holder and placed inside the diffractometer. The beam of X-ray falls on the alloy surface and scatters in all directions. The studies were carried out for Ni-Cr alloys using Cu-K_α radiation (λ=1.5406Å). The scattered X-rays result in Bragg reflections was operating at wide angles 35 - 100 º. The characterisations and identifications of Ni-Cr alloys have been performed with the date base ICCD and literature materials. The diffraction patterns are shown in figure 4.2.1.

Metallic Ni has a face centred cubic structure and pure Cr has the structure of body centred cubic lattice. The characteristic peaks of Ni and Cr are located very close together. Birjega et al [1] suggest that at the equilibrium phase of Ni-Cr alloys the range of 20-35% of Cr in Ni-Cr alloy has only one phase and it is a f.c.c structure with Cr atoms displacing Ni atoms in the lattice for pure Ni. While for higher concentration of Cr in Ni-Cr alloys (35-65% Cr and more) observed two phases: γ-Ni with f.c.c structure and α-Cr with b.c.c structure. This situation is more complicated because the temperature plays important role. Table 4.6 presents influence of temperature and concentration of Cr in Ni-Cr alloys on structure behaviour.

Table 4.6 *Influence of temperature and Cr % on the structure of Ni-Cr alloys* [2].

	% of Cr in Ni-Cr alloy
T/K	20 25 30 35 40 45 50 55 60 65
293	
393	
493	
523	
553	
573	

γ- Ni structure f.c.c

α -Cr structure b.c.c

Amorphuos strcutrure

Table 4.7 *Data taken from the XRD patterns of Ni-Cr alloys.*

Ni foil/2θ	**Cr foil/2θ**	**Ni80Cr20 foil/2θ**	**Ni80Cr20 rod/2θ**	**Ni90Cr10 rod/2θ**	**Ni50Cr50 rod/ 2θ**
-	-	38.26	-	-	-
44.52	44.36	44.34	44.34	44	43.6
51.86	-	51.64	51.68	51.12	50.74
76.4	-	75.88	76.14	75.5	74.82
-	81.68	82.22	-	-	-
89.3	89.34	-	89.7	89.58	89.34
92.98	-	92.16	92.6	91.52	90.86
98.48	98.42	97.58	98.04	97.22	96
-	-	99.02	-	-	-

For the alloys Ni-Cr low Cr content- the Cr atoms replace Ni atoms in a retained f.c.c structure. All investigated samples have the room temperature structure even in experiment at 353 K because of the very slow rate of structured change.

The peaks observed by X-ray diffraction are reported in Table 4.7. All of investigated Ni - Cr alloys have been characterised by a peak at ~ 43-44º what suggest that is a (111) Ni f.c.c or (110) Cr b.c.c plane. Many authors have concluded that this angle is typical of Ni - Cr. Ni-rich Ni-Cr alloy can be described with hkl positions (200), (221), and (222) of the f.c.c structure.

The diffraction patterns for the foil and rod samples of Ni80Cr20 are compared in figure 4.2.2. Foil and rod have five common peaks at ~ 44º, ~ 51.6º, ~ 76º, ~ 92º, ~ 98 º what correspond to (111), (200), (220), (311) and (222). Ni80Cr20 foil has two extra peaks at ~ 38º and ~ 82º corresponding to (100) and (211) planes (figure 4.2.2). In fact Ni80Cr20 as foil presents much sharper peaks than the rod. Vinayak et al [2] investigated Ni-Cr alloys of different compositions, but especially studied Ni80Cr20, Ni50Cr50 and Ni40Cr60 alloys. For Ni80Cr20 the authors found three characteristic peaks at the angle range 44.14º, 51.12º and 75.875º, what are very similar to investigated alloys with composition Ni80Cr20.

Ni50Cr50 presents peak at 43.6º, which is shifted to lower angle compared to Ni90Cr10 and Ni80Cr20. The shift could correspond to Cr_3Ni_2, second characteristic peak at 74.82 º suggest that could be a metastable phase γ – NiCr [2-6].

Ni-Cr alloys indicate shifting of main peaks (figure 4.2.3) compared with major peaks for pure Ni and Cr. Ni80Cr20 alloys have peaks at the same position as Cr (44.36º), Ni90Cr10 alloy is moved to 44º and Ni50Cr50 alloy to 43.6 º vs. original Ni and Cr peaks. The shift is engaged with changes in the crystal lattice structure and strongly depends of the Cr content in lattice structure.

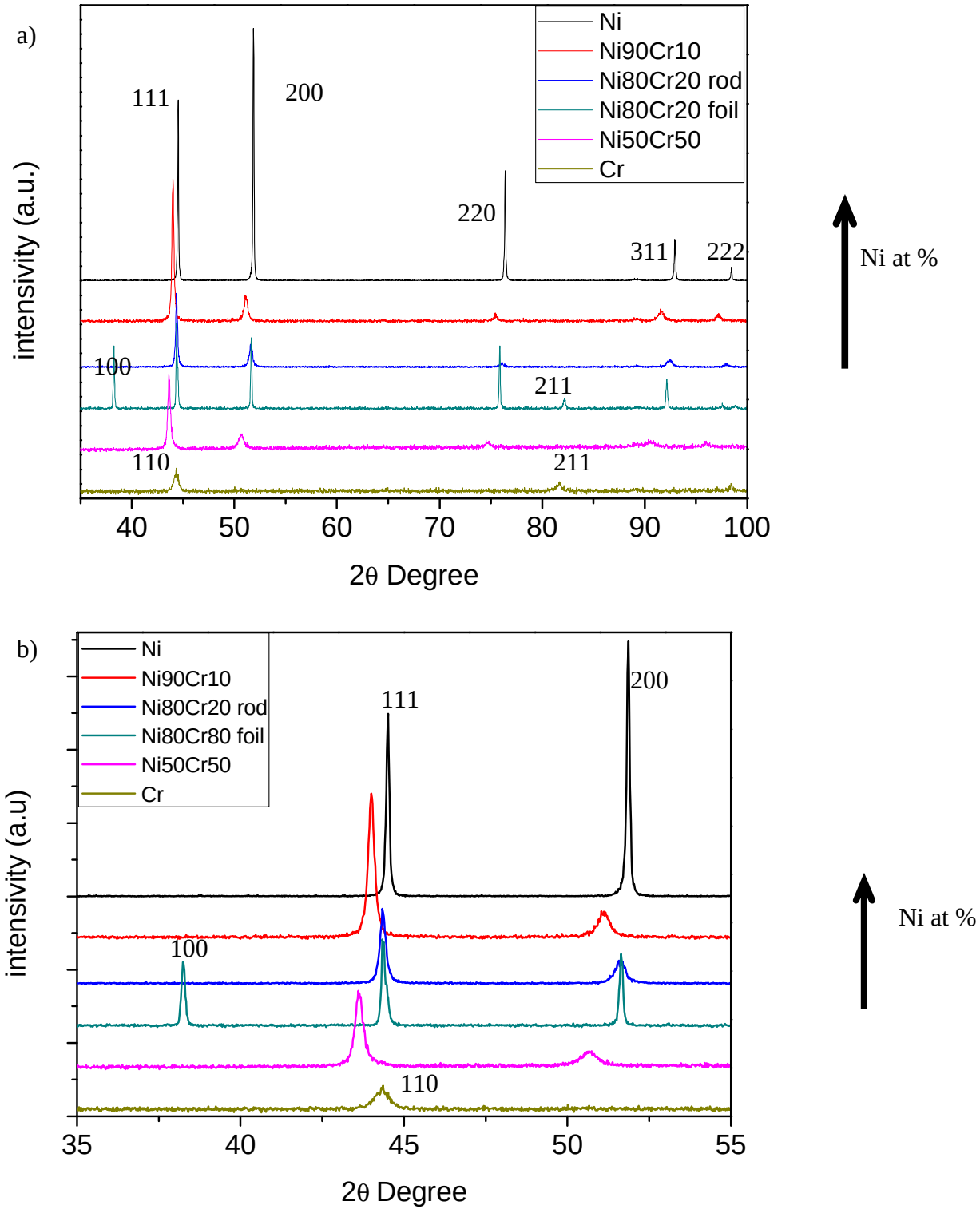

Figure 4.2.1 *XRD patterns of Ni-Cr alloys and pure Ni and Cr a) range 10 - 90 degree, b) range 35-55 degree.*

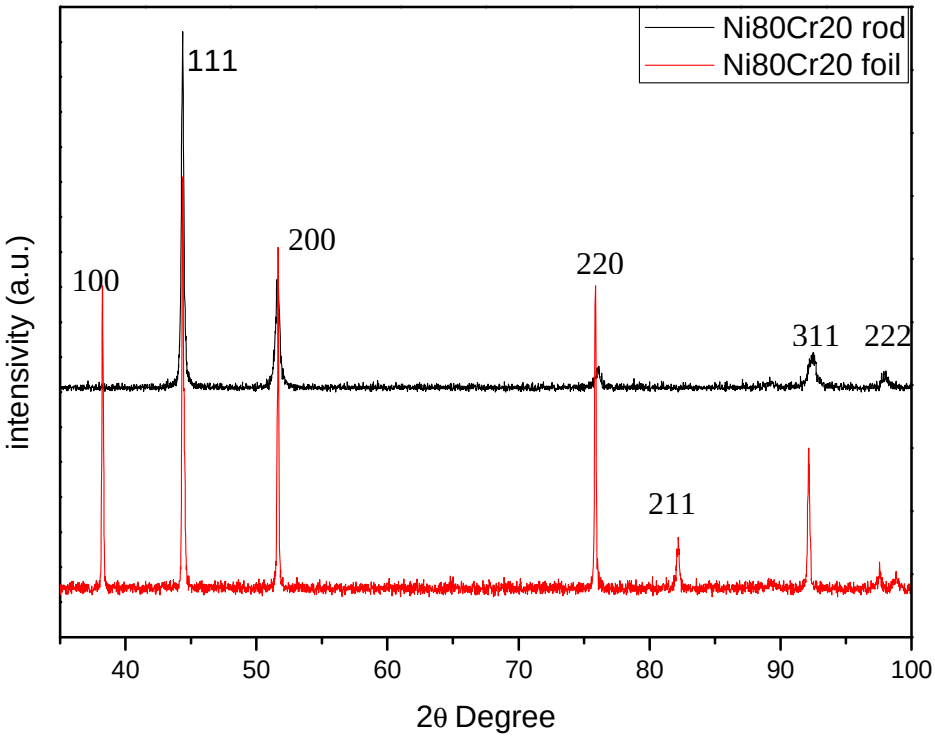

Figure 4.2.2 *XRD patterns showing the differences between rod and foil for Ni80Cr20 alloy.*

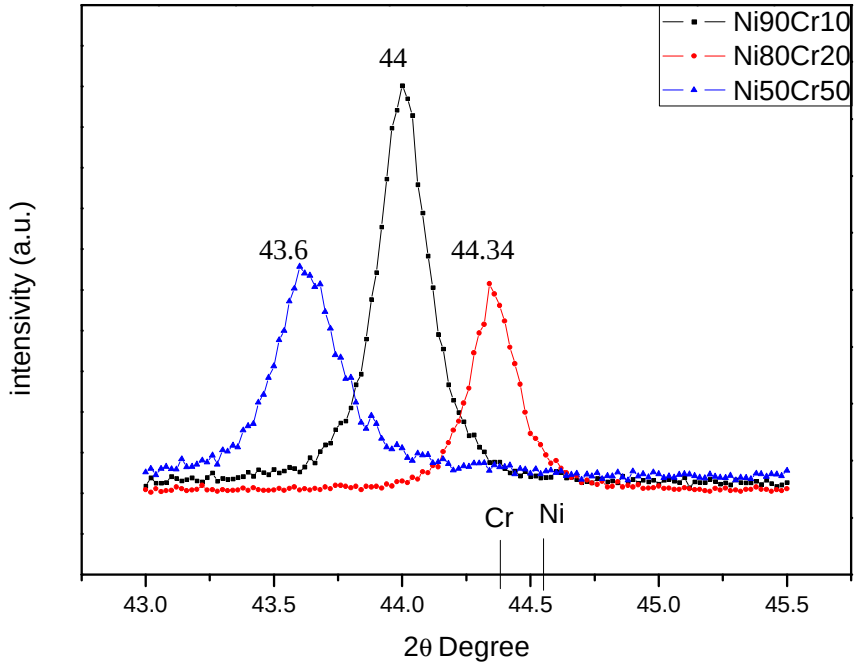

Figure 4.2.3 *Peak position of Ni-Cr alloys (Ni90Cr10, Ni80Cr20, and Ni50Cr50).*

XRD measurements can give important information about the size of the crystallites from the wide angle XRD scans. Grains sizes can be calculated by using Scherer's equation:

$$L = \frac{\lambda}{\beta \cos\theta}$$

Where,

L- The crystallite size

λ- The wavelength of the X-ray beam

β – The full width at half maximum diffraction peak

θ – The scattering angle

Grains sizes strongly depend on the Ni content. The trend with increasing the concentration of Cr in Ni-Cr alloys is for grains sizes getting smaller. Grain size of Ni is approximately ~ 446 nm whereas for Cr ~ 110 nm. For the two forms of Ni80Cr20, foil (372 nm) has much bigger grain size than rod (277 nm). According to the literature the material with the largest grain size should be less prone to corrosion because less grains boundary area would be available for corrosion reactions [7].

The crystal structure of Ni based solid solution changes with increasing Cr in the Ni-Cr alloy. The literature results of Ni and Cr suggesting that Ni lattice parameter [3-4] increasing proportional with increasing % of Cr (decreasing spacing in the crystal). Whereas Cr lattice parameter decreasing with increasing Cr (increasing spacing in the crystal) - Table 4.8.

Table 4.8 *Lattice parameters for Ni and Cr phases* [8-13].

Composition	Ni lattice parameter /Å	Cr lattice parameter/Å
100% Ni	3.5264	-
10% Cr	3.535	-
20% Cr	3.5437	-
50%Cr	3.5457	2.8957
80% Cr	3.5513	2.8908
100% Cr	-	2.8854

4.3 Microstructure of Ni-Cr alloys.

Microstructure is an important element of the structure of materials and to investigate the microstructure of the Ni - Cr alloys, Optical and Scanning Electron Microscopes were used. Alloys were cut on discs and connected to steel wire, for better electrical contact using a silver conductive paint and encapsulated in epoxy resin. The Ni - Cr materials were ground using (120, 600, and 4000 grade emery paper) and polished 6 µm and 1 µ m diamond paste until no scratches could be seen on the surface using [14] optical microscope. Etching of the materials were carried out through electrolytic etching using 10% H_3PO_4 in H_2O with j= 40 mA cm^{-2} for 30-90s at room temperature. Ni-Cr alloys are believed to corrode via intergranular corrosion [15-16]. Considerable verification exists to suggest some influence of the crystallographic structural of grain boundaries and their properties [17].

The crystallographic structure of Ni-Cr alloys strongly depends of concentration Cr ions into the crystal lattice.

For Ni-Cr rods, simple behaviour with increasing Cr content was observed with in the crystal lattice the grain size decreasing (figure 4.3.1). Ni90Cr10 and Ni80Cr20 have rather uniform grain size whereas Ni50Cr50 alloy has both smaller and bigger grains. Also it has been observed that grain boundary of Ni80Cr20 in both forms (rod and foil) are more regular than the others.

Comparisons of the two forms of Ni80Cr20 - rod and foil (figure 4.3.2) have presented differences of grain dimensions. Foil has well defined and much bigger grains than the rod. Indeed on the rod's surface exist white lines (seems like noodle), what is probably connected with dislocations in the crystal lattice. Mapping characterisation of Ni80Cr20 has been shown, that on the alloy surface exist cations Cr^{3+} and Ni^{2+} (figure 4.3.2 a). Figure 4.3.3 shows samples etched in 1 M H_2SO_4 at 353 K. Studied sample can be identified with well defined crystal structure. Also noted some twin crystals what were not observed previously. The high magnification has showed grain boundary line.

XRD showed crystal sizes that were sub-micron while the SEM disclosed whole grain much larger. The large grains are in fact composed of smaller grains.

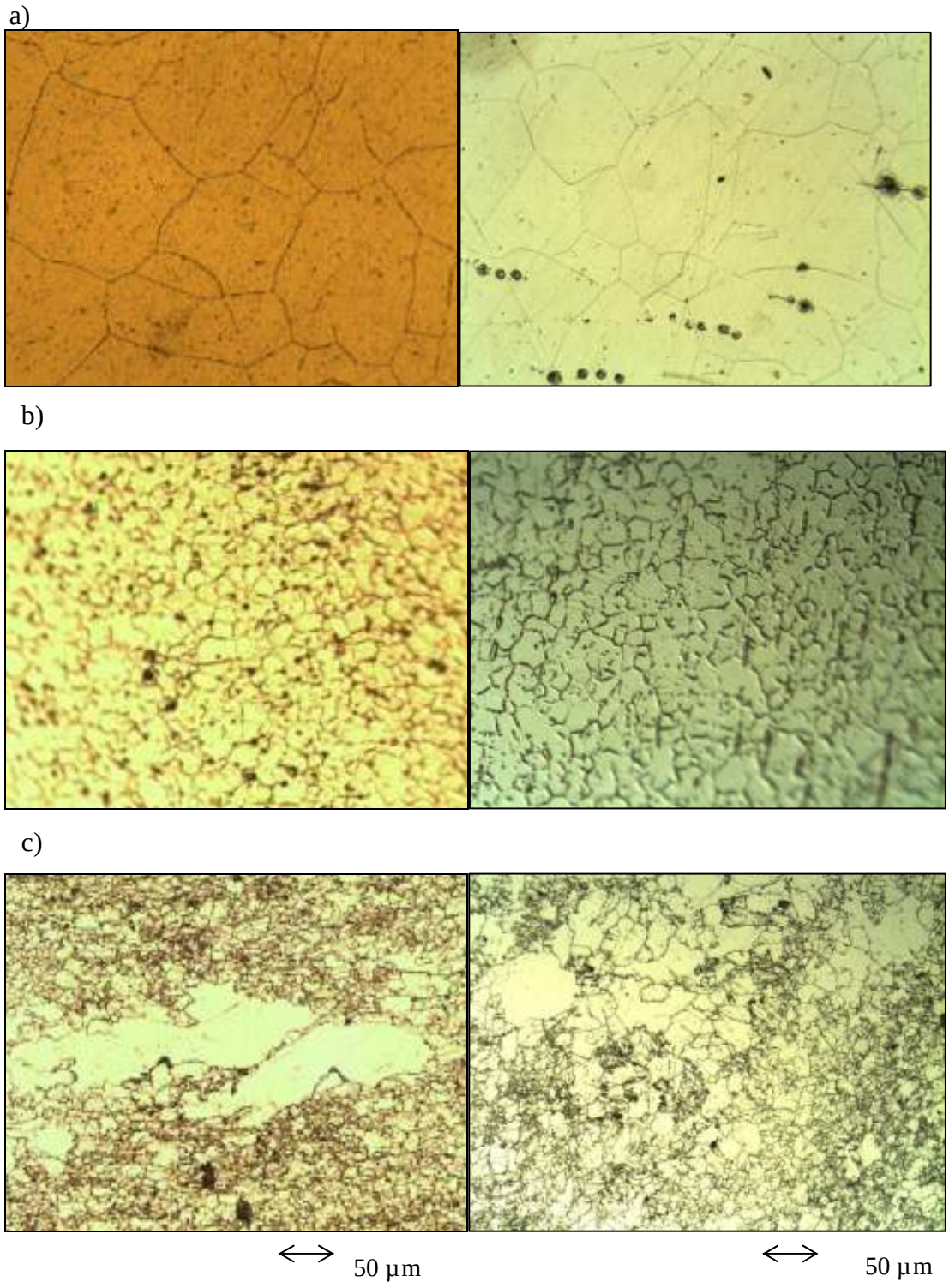

Figure 4.3.1 *Optical Microscope images of intergranular corrosion and cross sections of Ni-Cr rods a) Ni90Cr10 b) Ni80Cr20, c) Ni50Cr50, after electro- etched*

alloys in 10% phosphoric acid. The left and right images are for the rods cut at different angles.

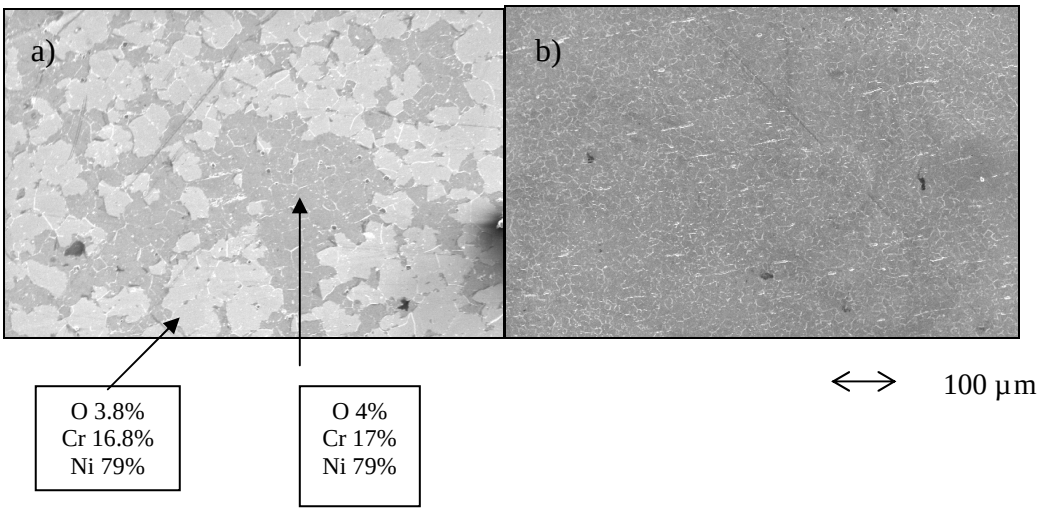

Figure 4.3.2 *SEM images of Ni80/20Cr alloys for a) foil, b) rod after electro-etch in 10 % phosphoric acid.*

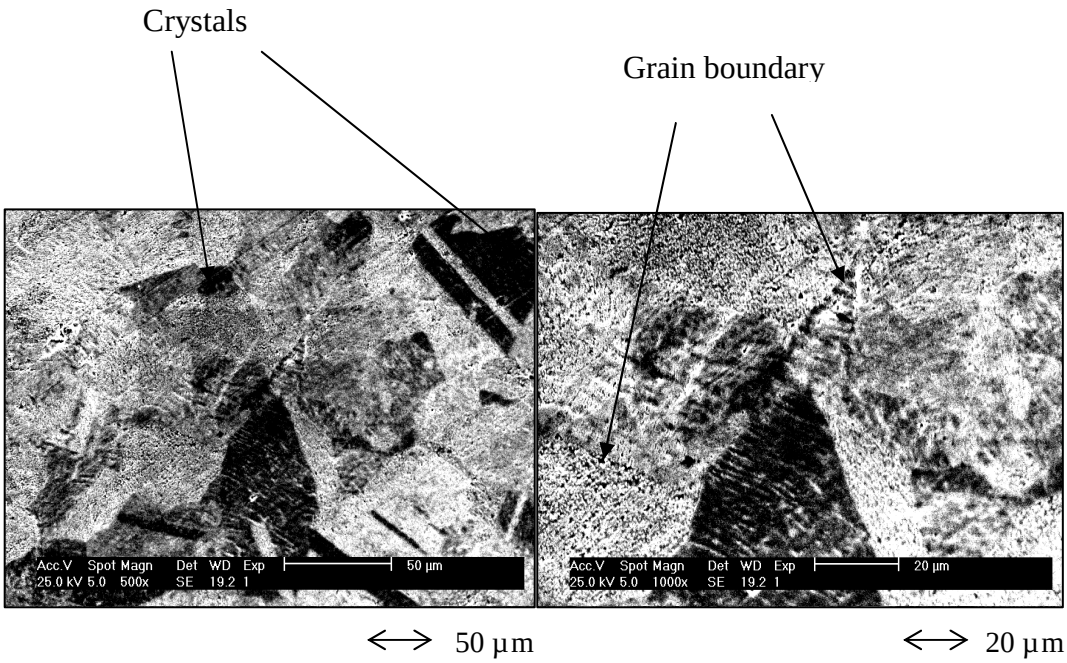

Figure 4.3.3 *SEM images grain boundary of Ni80Cr20 in sulphuric acid at 353 K.*

4.4 Conclusions

It is concluded, that:

- The Ni - Cr alloys are less prone to corrosion than Ni, at both the corrosion potential and the passivated surface. In the passivated state the lowest current density has been noted for Ni80Cr20 as foil, j~ 0.3 μA cm^{-2}.
- A current density of 1 μA cm^{-2} is equivalent to a metal loss rate by uniform corrosion of ~ 10 μm/year, still not negligible when dealing with the corrosion of coatings.
- A charge for Ni80Cr20 is approximately 3 mC cm^2 for the dissolution of the metals corresponds to the loss from the surface equivalent to a small number of monolayers.
- Manufacturing process has a strong influence on the structure of Ni80Cr20.
- The increase of %Cr in Ni-Cr alloy changes the lattice and the grain size.

4.5 References

[1] M. I. Birjega, M. Alexe, *Thin Solid Films* **275** (1996) 152-154
[2] S. Vinayak, H. P. Vyas, V. D. Vankar, *Thin Solid Films*, **515** (2007) 7109
[3] A. A. Edigaryan, G. E. Goryunov, E. N. Lubnin, and Yu. M. Polukarov *Russian Journal of Electrochemistry*, **Vol. 40, No. 12,** 2004, pp. 1266–1271.
[4] O.V. Kasprova, *Protection of Metals*, **Vol. 36**, No.6, 2000, pp
[5] M. Danismand, N. Cansever, *J. Alloy Cpds* **493** (2010) 649
[6] M.B. Vollaro, D.I. Potter, *Thin Solid Films* **239** (1994) 37
[7] W.D. Callister *Materials Science and Engineering an Introduction* seventh edition, USA, 2007.
[8] T. D. Xiao, S. Torban, P. R. Strutt, B. H. Kear *Nanostructured Materials*, Vol.7, No.8 pp 857-871 (1996)
[9] Ochiai, S.;Mishima, Y.;Suzuki, T.(1984)
[10] X. Peng, A. Morrone, K. Nikolaev, M. Kief, M. Ostrowski *Journal of Magnetism and Magnetic Materials* **321** (2009) 2902–2910
[11] A. A. Edigaryan, G. E. Goryunov, E. N. Lubnin, and Y. M. Polukarov *Russian Journal of Electrochemistry*, **Vol. 40,** No. 12, 2004, pp. 1266–1271.
[12] M. J. Mehl, D. A. Papaconstantopoulos *Physical Review B* **Vol. 54**, Num. 7, 15 (1996)
[13] Z. Lockman, X. Qi, A. Berenov, W. Goldacker,R. Nast, B. deBoer, B. Holzapfel, J.L.MacManus-Driscoll *Physica C* **383** (2002) 127-139
[14] D. Landolt, P.F. Chauvy, O.Zinger *Electrochimica Acta* **48** (2003) 3185-3201
[15] E.M. Lehockey,G. Palumbo, P.Lin, A.M. Brennenstuhl, *Scripta Mineralia*, **Vol. 36**, No.10, pp. 1211-1218, 1997
[16] F. Xiao, R. Yang, L. Fang, C. Zhang *Materials Science and Engineering* **B 132** (2006) 193-196
[17] E. M. Lehockey, G. Palumbo, P. Lin, A.M. Brennenstuhl *Scripta Materialia*, **Vol. 36**, No. 10, pp. 1211-1218, 1997

Chapter 5

Ni – Cr alloys deposited by Physical Vapour Deposition.

This chapter presents collected results for Ni-Cr alloys deposited by PVD.

- Influence of Cr content on the corrosion rate.
- XRD investigations of the alloy structure.
- Effect of heat treatment on behaviour of Ni-Cr deposited alloys.

5.1. Coated Mild Steel Surfaces

The literature and results earlier in this thesis show that mild steel corrodes rapidly in acidic media but coatings of Ni and/or Cr slow the rate of corrosion. It was therefore decided to investigate surfaces produced with 20nm and 80nm of Cr on 3µm Ni electroplated onto mild steel. The rate of corrosion was established at the potential of + 100 mV vs. Hg/Hg_2SO_4 in deoxygenated phosphoric acid, pH 2 at a temperature of 353 K, the environment selected to simulate the conditions seen by the bipolar plate in contact with the positive electrode of an O_2/H_2 fuel cell.

Layers of Cr were sputtered onto the 3µm Ni electroplated onto mild steel. SEM images (Figure 5.1.1) showed that the surfaces were rather featureless and largely reflected the smoothness of the Ni electrodeposits. The intention was also to heat treat these structures with the objective of forming a surface layer of Cr Ni alloy.

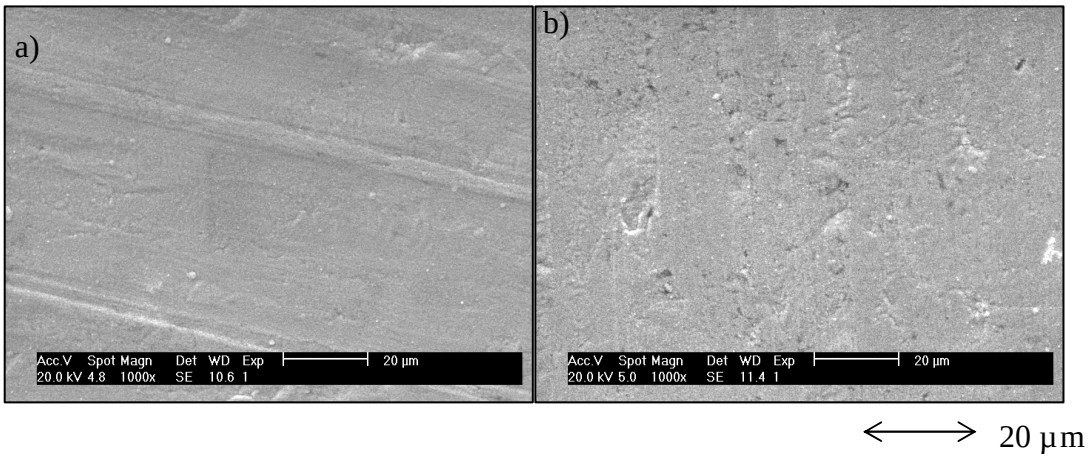

Figure 5.1.1 *SEM images of Cr deposited on 3 µm Ni/mild steel, samples 'as deposited', a) 20 nm Cr/3 µm Ni/mild steel , b) 80 nm Cr/ 3 µm Ni/mild steel.*

A typical cyclic voltammogram for 20 nm Cr/ 3µm Ni/mild steel is presented in figure 5.1.2. The major features are a cathodic current negative to – 800 mV during both the forward and reverse scans resulting from proton reduction to give hydrogen gas and an anodic peak at E_p = - 180 mV vs. Hg/Hg_2SO_4. The latter peak is similar in shape to that observed for Ni in this medium but the peak potential is slightly more positive and the peak current density, ~ 2000 µA cm^{-2}, is much lower. Certainly, the voltammogram is unlike that for Cr and suggests that the thin layer has many pores or other imperfections. The anodic peak arises from active corrosion just positive to the corrosion potential and passivation beyond the peak; it is probably the corrosion of the Ni layer that leads to this current but some contribution from Cr corrosion may also be present. At the positive limit of + 400 mV, the anodic current has dropped to a low value and it decreases further on the reverse scan. At + 100 mV on the reverse scan the current density is down to 121 µA cm^{-2}. The surface is well passivated with the measured charge under the oxidation peak being ~ 622 µC cm^{-2}, which is much smaller compared to that obtained for pure Ni.

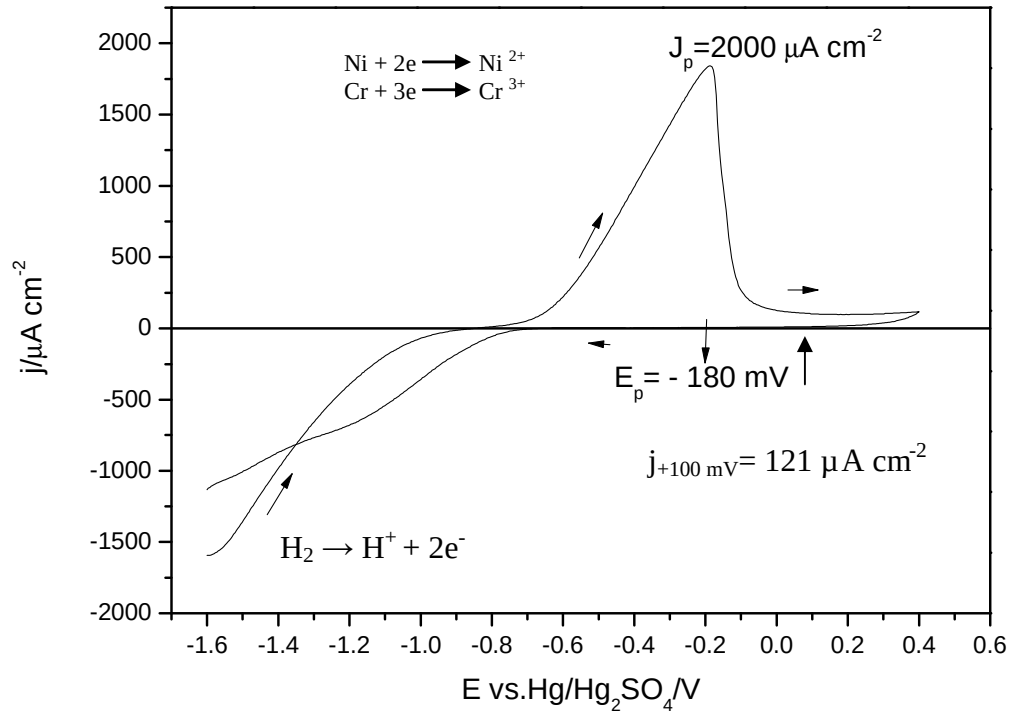

Figure 5.1.2 *Cyclic voltammogram of 20 nm Cr/3 µm Ni/mild steel in phosphoric acid pH 2, potential scan rate 20 mVs^{-1}, temperature 353 K.*

Heat treatment in an Ar/5% H_2 atmosphere was investigated as a method to form the surface Ni-Cr alloy. The 20 nm Cr/3µm Ni/mild steel sample was heat treated for 1 hour at 973 K. With this heat treatment, and indeed, with repeated treatments in related conditions, a coloured surface was produced (often light blue). This is a clear indication that the Cr layer had been oxidized. At such a high temperature some of the Cr may also have been evaporated. Figure 5.1.4 reports data for the 1 hour corrosion test at + 100 mV. The as deposited sample has a lower corrosion rate than the heat treated sample. Neither sample approaches the performance of the bulk alloy, see Table 5.1.

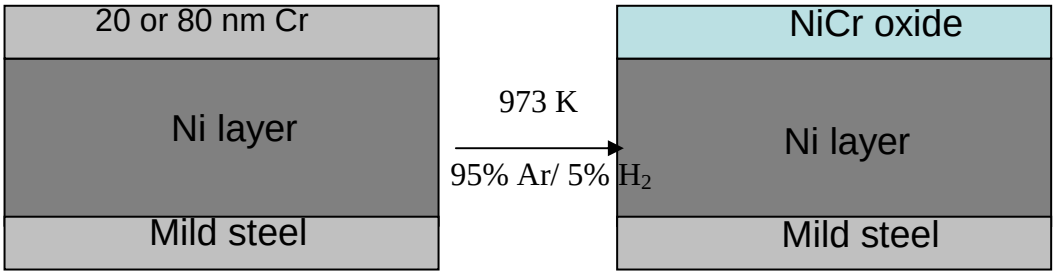

Figure 5.1.3 *Simple graphical presentation of the concept.*

Table 5.1 *Influence of heat treatment on the surface condition.*

Condition	**Current density After 1 hour at E= + 100 mV j/µ A cm^{-2}**
Alloy	0.3
20 nm Cr/3 µm Ni/mild steel	3.0
20 nm Cr/3 µm Ni/mild steel After 1 hour at 973K	9.0

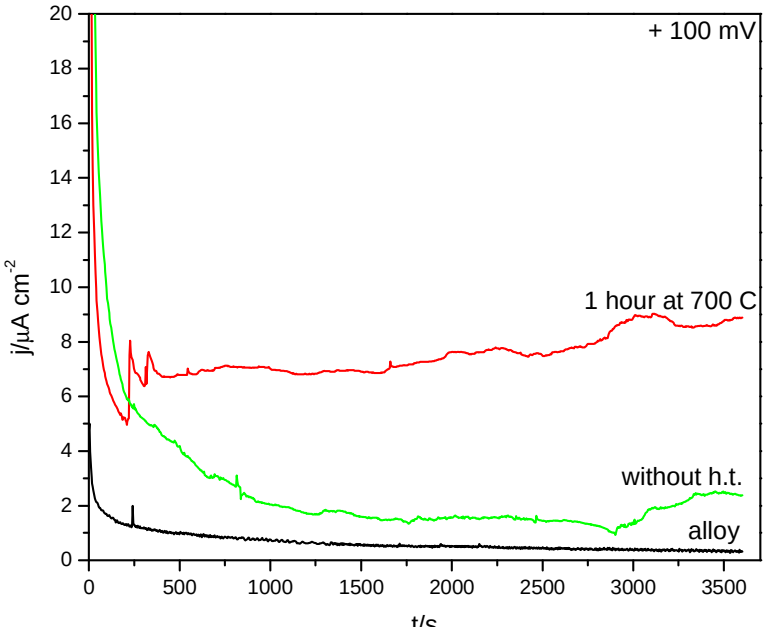

Figure 5.1.4 *I transient t for Ni80/Cr20 alloy, 20nm Cr/3µmNi/mild steel with heat treatment (1 hour at 700°C) and 20nm Cr/ 3µmNi/ mild steel without heat treatment in phosphoric acid pH 2 at temperature 353 K, applied potential E =+ 100 mV vs. Hg/Hg_2SO_4.*

5.2 Ni – Cr alloys deposited by PVD

Cr-Ni layers of various compositions were deposited onto 10x10 arrays of gold micropads by PVD. The 'wedge' technique was used to give variable compositions across the array [1-4]. With some samples, after deposition, a heat treatment of 2 hours at 523 K in Ar/ 5% H_2 was carried out in order allow the formation of the equilibrium Ni-Cr alloy structure within the whole thin layer. Typically the layers deposited by PVD were 250 nm thick. This is a relatively thick layer for PVD but it was recognised that corrosion might lead to oxidation of a significant fraction of such layers.

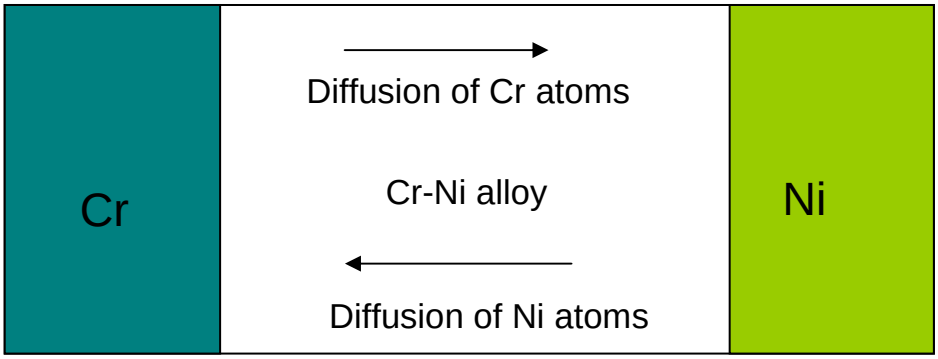

Figure 5.2.1 *Theoretical scheme of Ni-Cr alloys for heat treated sample with diffusion zone*[1].

The electrochemistry was carried out in the special cell with the software that allowed simultaneous voltammetry at all 100 electrodes (each 0.014 cm^2).

5.2.1 'As deposited' sample

Experiments (cyclic voltammograms and step experiments) were carried out in phosphoric acid pH 2 deoxygenated at temperature 323 K.

Since it was recognised that every electrochemical experiment could lead to a significant change in the thin film layer of Ni-Cr a strict protocol was followed: (a) first a cyclic voltammogram was recorded over the potential range - 800 mV to + 200 mV with the potential scan rate 20 mV s^{-1}, (b) a step experiment at the constant potential E= + 100 mV vs. Hg/Hg_2SO_4 during 10 minutes, (c) cyclic voltammogram with the same condition of potential range and scan rate as the previous.

The cyclic volatmmograms 'before' and 'after' the step experiments compare the surface condition and give basic electrochemical data. Also for the as deposited sample, the region close to the corrosion potential has been investigated. In the deposition, the Ni and Cr sources are at an angle and one does not obtain a simple and predictable wedge arrangement of compositions. Hence it was necessary, after deposition, to determine, the composition of each alloy in the 10x10 array by EDX. This elemental analysis was repeated at the end of the electrochemical experiments. The results are reported in figure 5.2.1.1. Over most compositions in the array, there was little change in the Ni:Cr ratio producing evidence that the voltammetric experiments do relate to the stated compositions. The exceptions were the high Ni compositions where dissolution occurred: this was in line with the dissolution charges observed from the voltammograms.

Figure 5.2.1.2 presents volatmmograms of Ni-Cr deposited, 'before' and 'after' the step experiment. At the Cr rich electrodes (top LH corner) the cyclic voltammograms are featureless with rather low currents. At intermediate Cr levels (10-80%) well defined anodic peaks with passivation at more positive potentials in seen. At lower Cr (bottom RH corner) the responses are erratic and this arises from rapid loss of material. After the 10 minute hold at + 100 mV, the currents are generally lower at all potentials and certainly the anodic peaks an absent, see figure 5.2.1.2b. The surfaces are passivated.

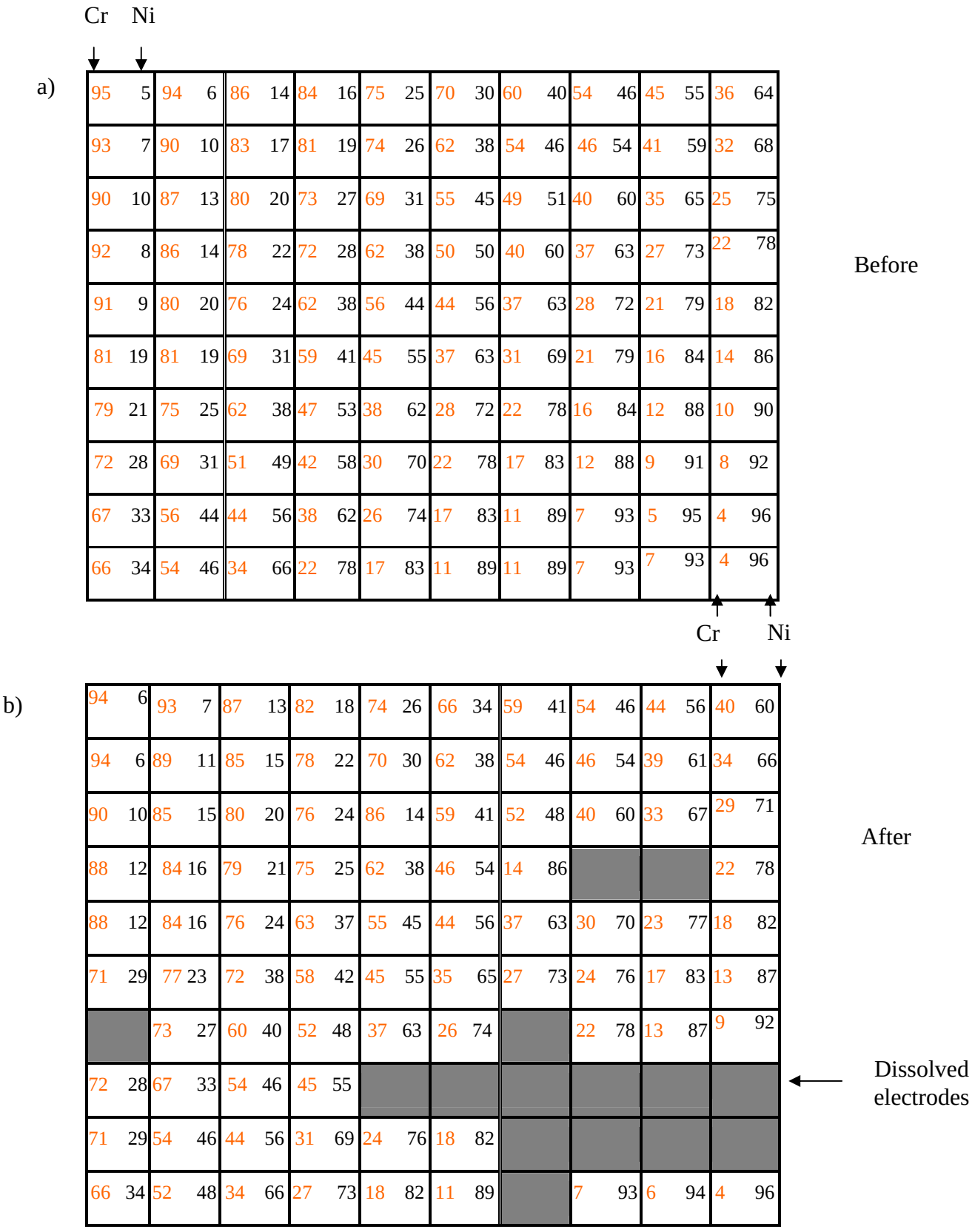

Figure 5.2.1.1 *EDX data for Ni-Cr alloys 'as deposited' sample with percentage of Ni and Cr a) before experiment, b) after cyclic voltammograms and step experiment in phosphoric acid pH 2 at 323 K.*

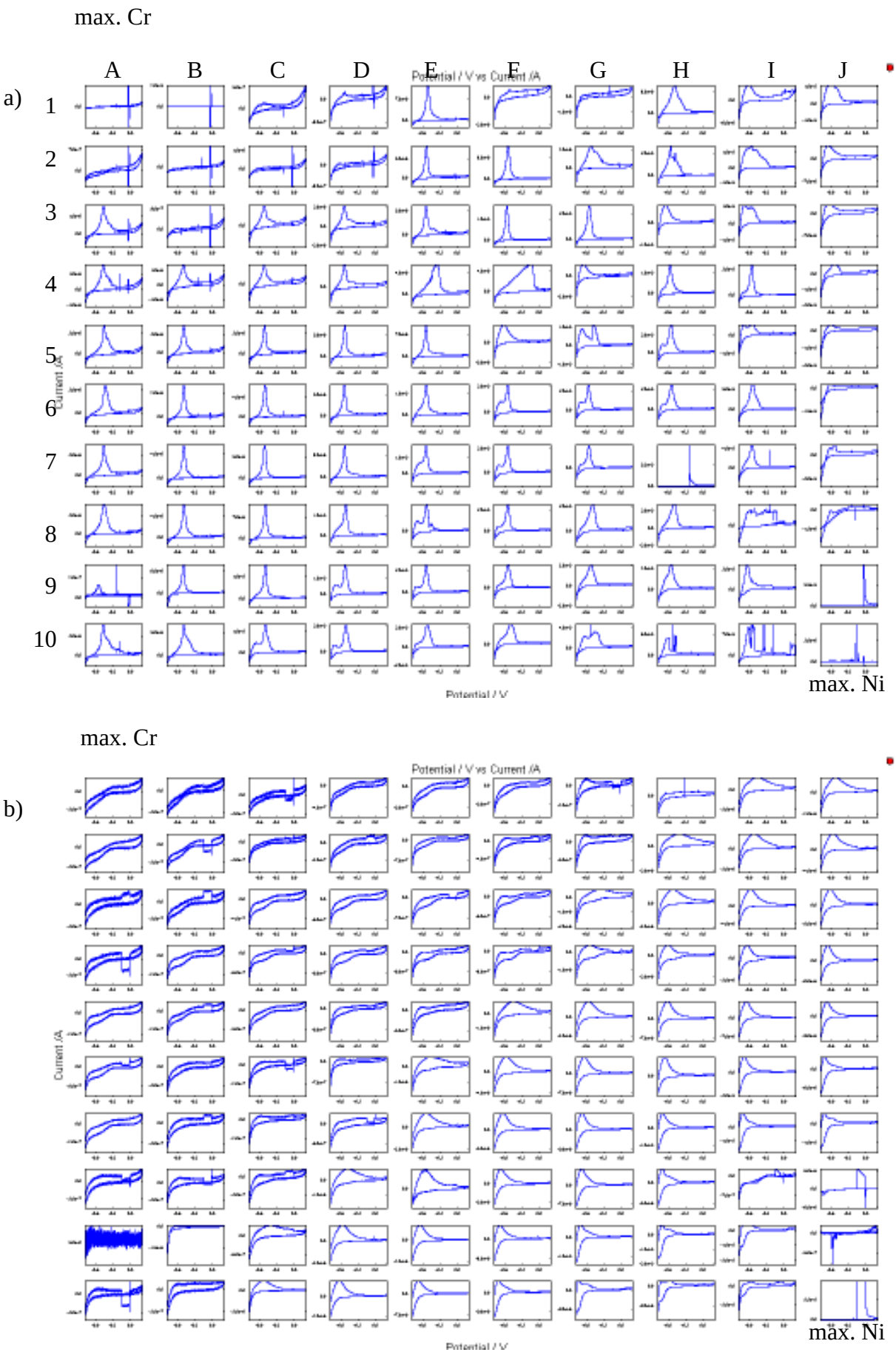

Figure 5.2.1.2 *Cyclic voltammograms of 100-electrodes array Ni-Cr alloys in phosphoric acid pH 2 at 323 K for a) first scan, b) scan after step experiment. Potential scan rate 20 mV* s^{-1}*, potential range: - 800 mV to + 200 mV vs.* Hg/Hg_2SO_4.

Figure 5.2.1.3 presents cyclic voltammograms results for selected electrodes in the array corresponding to the compositions Ni93Cr07, Ni78Cr22, Ni51Cr49, and Ni05Cr95. These electrodes have been chosen to compare with the commercial Ni-Cr alloys (Ni90Cr10, Ni80Cr20, and Ni50Cr50). There are striking similarities between this array voltammetry and the previously reported data for bulk samples. At the initial potential for Ni93Cr07 alloy there is a characteristic current density for hydrogen evolution. The corrosion potential E_{corr} for the forward scan equals - 720 mV. Using the data close to the corrosion potential, the corrosion resistance R_p ~ 34 Ωcm^{-2}. Ni rich deposited alloy has two peaks: first at E_{pA} ~ - 640 mV and second at E_{pB} ~ - 556 mV with the current densities j_{pA} ~ 2427 and j_{pB} ~ 4760 µA cm^{-2}. The first peak might result from H_2 oxidation. The charges under the oxidation peaks Q_p ~ 100 mC cm^{-2} (equivalent to the oxidation of a layer~ 20 nm thick of the 250 nm alloy layer). Then the passivation process takes place. On the reverse scan E_{corr} ~ - 320 mV has been found and there is a small cathodic current at - 750 mV.

For Ni78Cr22, as previously, at the beginning potential there is a hydrogen evolution current with E_{corr} ~ - 750 mV. On the forward scan the region close to the corrosion potential is characterised by R_p and equals ~ 50 Ω cm^{-2}. Also interesting is the fact that for this composition of Ni-Cr alloy exist two anodic peaks at: E_{pA} ~ - 711 mV and E_{pB} ~ - 546 mV with following current density j_{pA} ~ 470 and j_{pB} ~ 2567 µA cm^{-2}. The first peak may suggests that it results from hydrogen oxidation or/and dissolution of Ni-Cr alloy. The charges under the oxidation peaks correspond to the amount of the dissolution process and equals Q_p ~ 50 mC cm^{-2}. Then Ni-Cr alloy passivates with low current density (j ~ 165 µA cm^{-2} at + 200 mV). On the back scan E_{corr} has been found at - 150 mV. Also it is interesting that the first anodic peak depends strongly on the Ni concentration and with increasing % of Cr in Ni-Cr alloy has disappeared. This behaviour is clearly shown for Ni51Cr49 alloy, which has only one peak. At the initial potential has been observed a hydrogen evolution and corrosion potential at E_{corr} ~ - 730 mV. The region close to the corrosion potential is characterised by R_p ~ 188 Ω cm^{-2}. There is a sharp anodic peak at E_p ~ - 557 mV and the charge under the oxidation peak Q_p ~ 45 mC cm^{-2} results from the dissolution process. Then passivation occurs and the current density drops down to the value j ~ 50 µA cm^{-2}.

As previously, at the initial potential for Ni05Cr95 has been noted a hydrogen evolution and corrosion potential at E_{corr} ~ - 440 mV on the forward scan. The resistance polarisation equals R_p 21760 Ω cm^{-2} and hence a much lower corrosion

rate. There is no anodic peak, current density growing up to j ~ 55 µA cm^{-2} at + 200 mV, where the oxygen evolution occurs. The charge describes the oxidation process equals ~ 5 mC cm^{-2}. On the reverse scan is an E_{corr} at -100 mV. This composition presents the lowest current density and is very similar to the pure Cr.

For the selected electrodes the main anodic peak position is similar and lies at ~ - 550 mV. All selected alloys shown well defined passivation region approximately from - 450 mV to + 200 mV vs. Hg/Hg_2SO_4, what correspond to results of Ni-Cr alloys and pure metals commercial materials (Ni90Cr10, Ni80Cr20, Ni50Cr50, pure Ni, and Cr).

The corrosion potentials on the reverse scans are shifted to more positive potential with increasing the % of Cr in Ni-Cr alloys (figure 5.2.1.4).

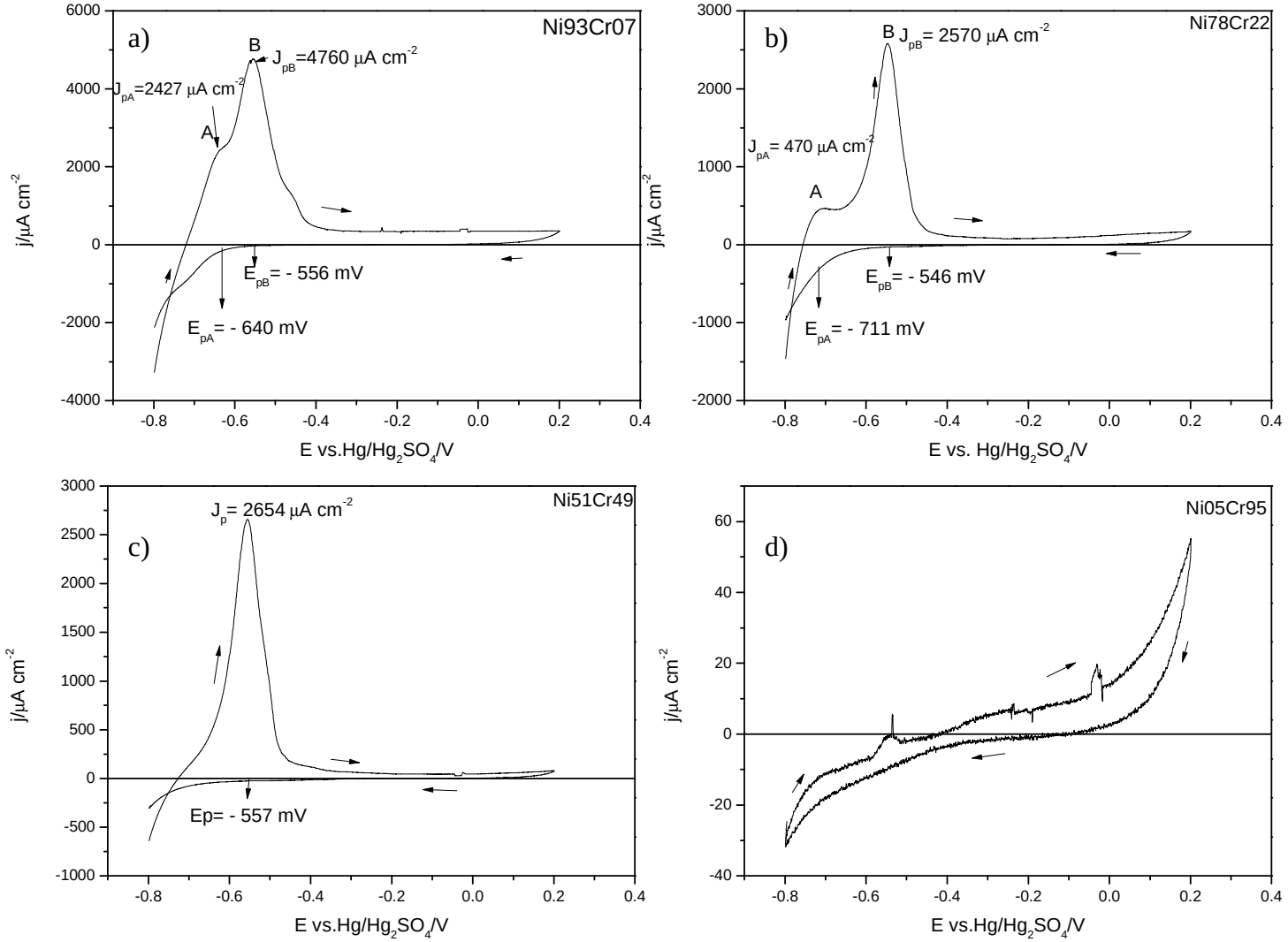

Figure 5.2.1.3 *Cyclic voltammograms of selected electrodes sample as deposited first scan for a) Ni93Cr07(H9) b) Ni78Cr22 (F8), c) Ni51Cr49 (G3), d) Ni05Cr95(A1) in phosphoric acid pH 2 at 323 K.*

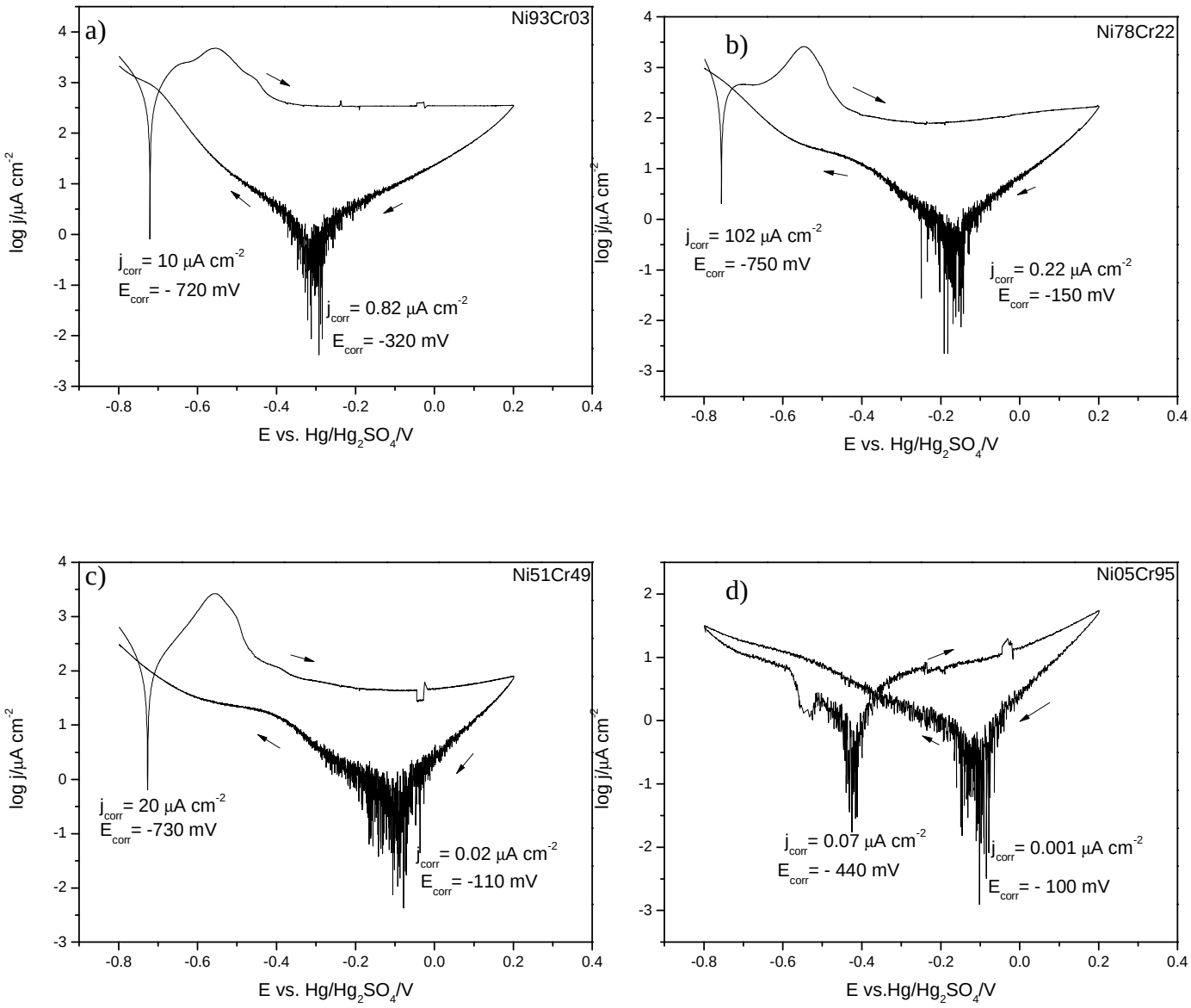

Figure 5.2.1.4 *Tafel plots for data on Figure 5.2.1.3 for Ni-Cr alloys a) Ni93Cr07, b) Ni78Cr22, c) Ni51Cr49, and d) Ni05Cr95 in phosphoric acid pH 2 at 323 K.*

Differences between cyclic voltammograms before and after test at constant potential are presenting on figure 5.2.1.5. The current densities after the 10 minute test are much lower and resulting from the passivation process. Peak positions of Ni93Cr07 and Ni78Cr22 are shifted to the more negative potential, while for Ni51Cr49 to the more positive potential. Similar behaviour has been observed for the corrosion potentials (figure 5.2.1.6). Only Ni-Cr with the composition of Ni05Cr95 has in both

cases the same corrosion potential. The maximum of the current densities and the charges are much lower compared with the previous voltammograms.

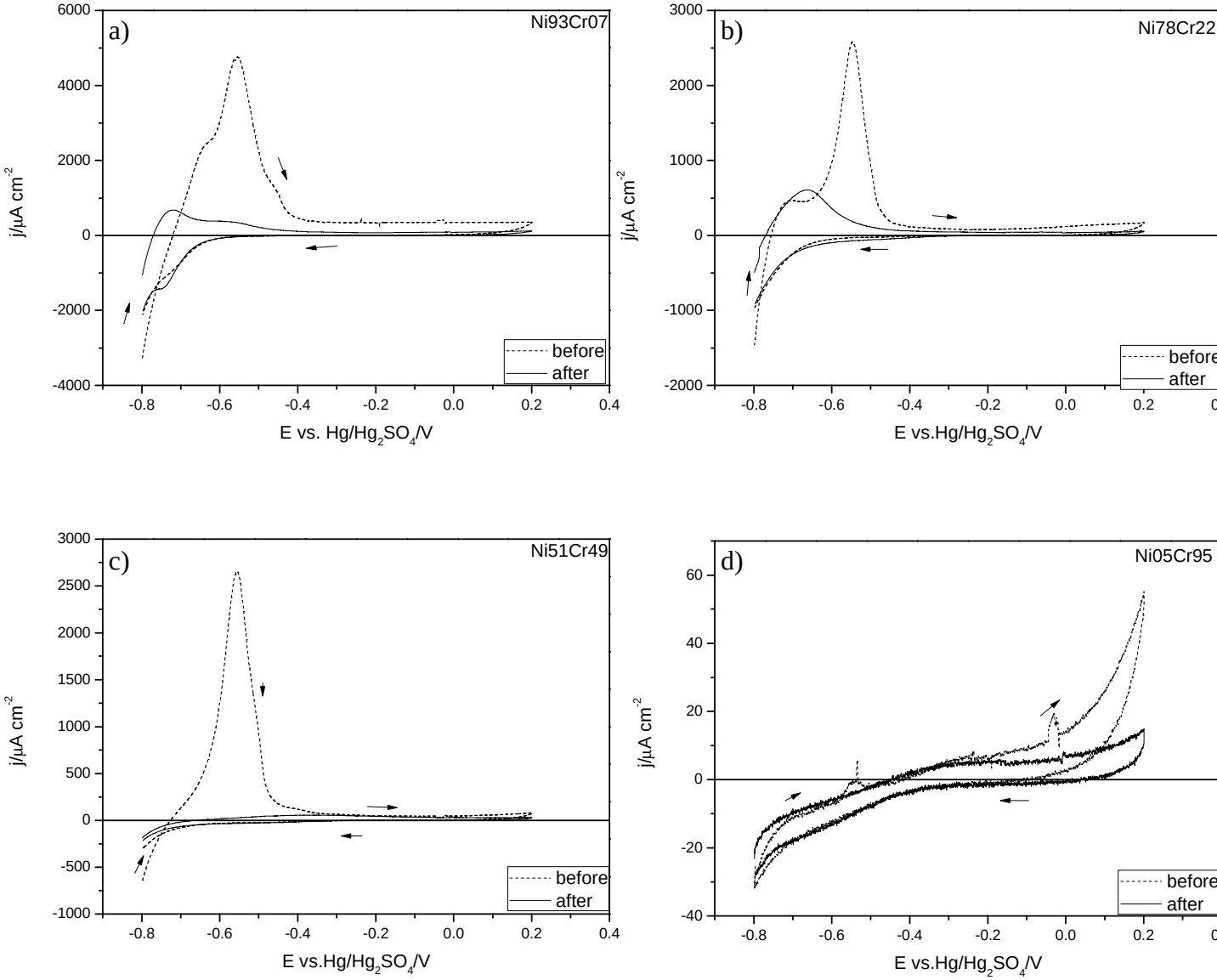

Figure 5.2.1.5 *Cyclic voltammograms of selected electrodes of Ni-Cr alloys 'as deposited' sample for a) Ni93Cr07, b) Ni78Cr22, c) Ni51Cr49 and d) Ni05Cr95 after hold sample at constant potential, in phosphoric acid pH 2 at 323 K.*

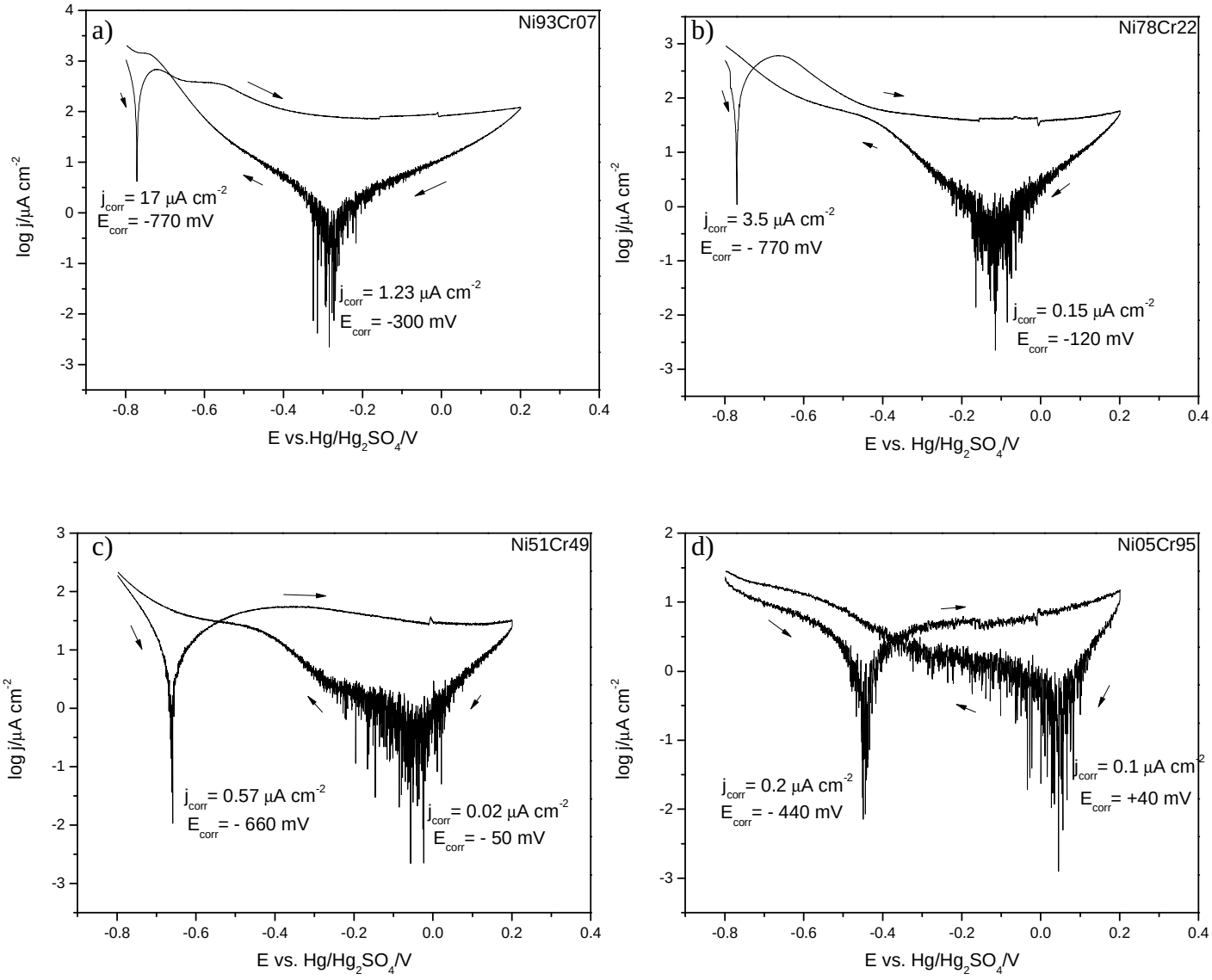

Figure 5.2.1.6 *Tafel plots of data collected in Figure 5.2.1.5 for Ni-Cr alloys a) Ni93Cr07, b) Ni78Cr22, c) Ni51Cr49, and d) Ni05Cr95 in phosphoric acid pH 2 at 323 K. Data for samples after hold at + 100 mV for 10 minutes.*

Figure 5.2.1.7 reports the anodic charge as a function of % Cr for all electrodes in the array. The data is reported both for the initial cyclic voltammogram and the cyclic voltammogram after the 10 minutes hold at + 100 mV. The charges for the latter experiments are, of course, much lower but the trends are similar; the charges are high at low Cr levels and drop sharply with increasing Cr. Both plots show scatter but this trend is clear and the scatter is typical of array experiments

a)

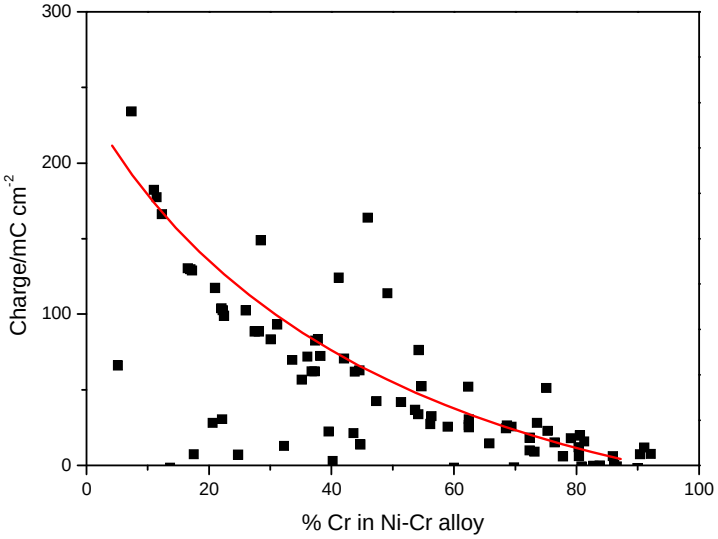

b)

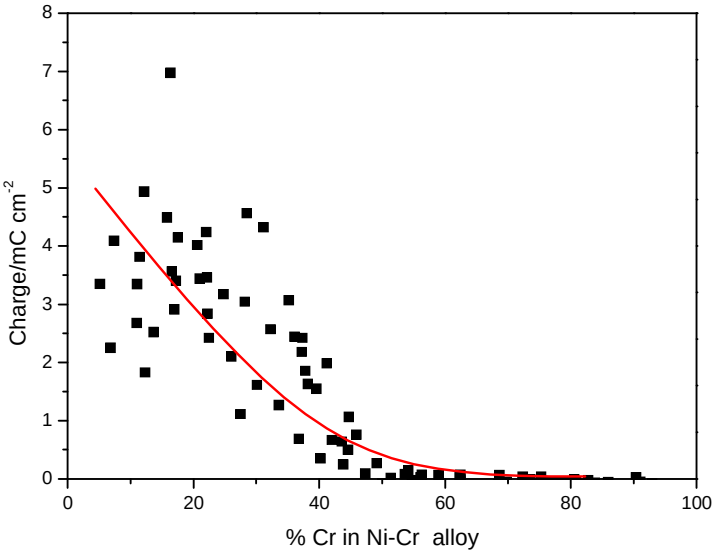

Figure 5.2.1.7 *Q_p vs. % Cr of as deposited sample for a) first scan b) last scan in phosphoric acid pH 2 at 323 K.*

Table 5.2 compare the results of resistance polarisations, charges, corrosion potentials and of selected alloys, before and after step experiment. The resistance polarisation increases after passiavation process.

Table 5.2 *Influence of Cr additions on surface condition of Ni-Cr alloys deposited by PVD, in phosphoric acid pH 2 at 323 K.*

First CV-before exp.							**Second CV-after exp.**					
Alloy	**E_p/ mV**	**j_p/ µA cm^{-2}**	**E_{corr}/mV**		**Rp/ Ω cm^{-2}**	**Q_p/ mC cm^{-2}**	**E_p/ mV**	**j_p/ µA cm^{-2}**	**E_{corr}/mV**		**Rp/ Ω cm^{-2}**	**Q_p/ mC cm^{-2}**
			Forward	**Reverse**					**Forward**	**Reverse**		
Ni93Cr07	- 640 - 556	2427 4760	- 720	- 320	34	100	- 720 - 570	680 358	- 770	- 300	37	10
Ni78Cr22	-711 - 546	470 2570	- 750	- 150	50	50	- 710	465	- 770	- 120	97	7
Ni51Cr49	- 557	2654	- 730	- 110	188	45	- 400	54	- 660	- 50	31847	3
Ni05Cr95	No	-	- 440	- 100	21760	2	-	-	- 440	+ 40	40214	0.5

Also the 'as deposited' samples have been tested for the oxygen cathode conditions by monitoring the current with time at + 100 mV vs. Hg/Hg_2SO_4 in phosphoric acid pH 2 at 323 K. With the arrays, the hold time was limited to 10 minutes because of software limitations. Figure 5.2.1.8 presents results of selected electrodes of Ni-Cr alloys (Ni93Cr07, Ni72Cr28, and Ni45Cr55). It has been observed that for Cr rich Ni-Cr alloy current density is much lower. Table 5.4 presents data of current densities at 600 s.

Table 5.4 *Influence of Cr addition on surface condition.*

Alloy	**$j_{\text{at 600s}}$/ µA cm^{-2}**
Ni93Cr07	65
Ni72Cr28	4
Ni45Cr55	0.5

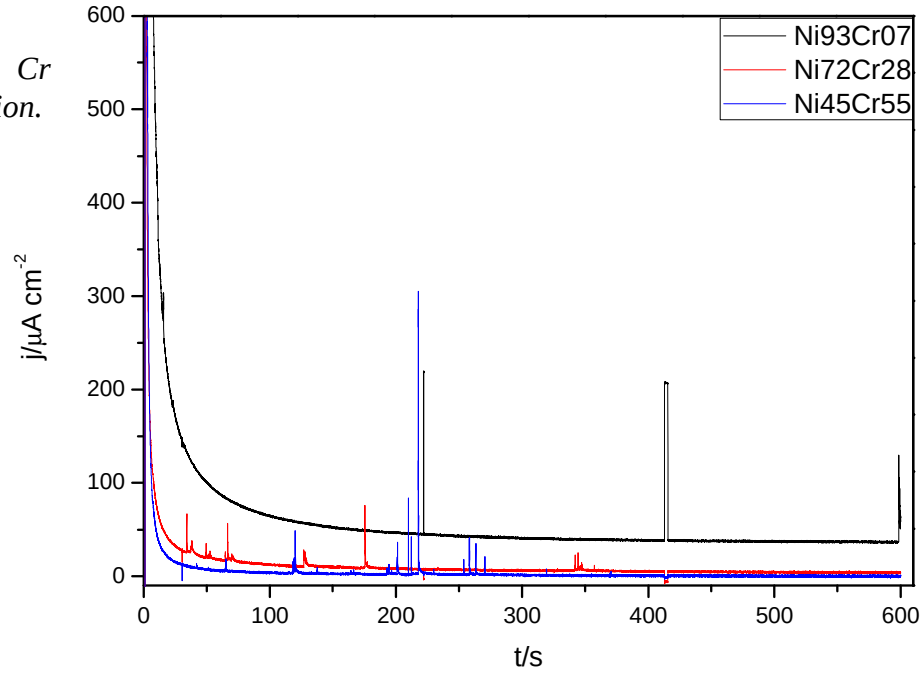

Figure 5.2.1.8 *I vs. t for selected electrodes of 'as deposited' sample Ni-Cr alloys: Ni93Cr07, Ni72Cr28, and Ni45Cr55 after 10 minutes at constant potential + 100 mV vs. Hg/Hg_2SO_4 in phosphoric acid pH 2 at 323 K.*

5.2.2 Heat treated sample

During the heat treatment process, atoms of each element are diffusing into the other element, leading to a change in structure. The sample ‘as deposited’ has been heat treated for 2 hours at 523K in Ar 95%/(5% H_2) atmosphere. In the high vacuum deposition chamber, the heat treatment was achieved without developing coloration indicative of Cr oxidation. Heat treated sample with 100 electrodes was then studied in phosphoric acid pH 2 at 323 K, deoxygenated with N_2. Figure 5.2.2.1 (a) reports the EDS analysis for the array after the heat treatment and the Ni/Cr ratios are essentially unchanged by the heat treatment.

Figure 5.2.2.1 (b) reports the EDS analysis after the electrochemical experiments. Unlike the ’as deposited’ sample, the electrochemistry leads to some changes in composition with a trend to loss of Ni. Figure 5.2.2.2 reports the voltammetry for the array, both the initial cycle and the voltammogram after passivation. In the initial cycle, rather sharp anodic peaks are seen over a wide range of % Cr but at low Cr the responses are again totally erratic with large currents flowing (the Ni rich layer is dissolving). After the 10 minutes of holding at + 100 mV, the anodic peaks are no longer evident and the cyclic voltammograms become rather featureless. The voltammetry does indicate some change in layer structure during the heat treatment. This global presentation is, however, suitable for identifying trends. More detected analysis requires a different approach.

a)

Cr	Ni																		
92	8	85	15	83	17	70	30	62	38	55	45	39	61	32	68	19	81	12	88
94	6	88	12	72	28	70	30	64	36	47	53	35	65	23	77	16	84	11	89
85	15	79	21	70	30	65	35	55	45	39	61	29	71	18	82	13	87	8	92
83	17	78	22	66	34	59	41	47	53	33	67	21	79	15	85	8	92	5	95
77	23	65	35	59	41	55	45	39	61	27	63	16	84	8	92	4	96	3	97
79	21	70	30	51	49	46	54	26	74	16	84	10	90	4	96	2	98	1	99
65	35	57	43	42	58	29	71	20	80	9	91	4	96	3	97	2	98	1	99
57	43	54	46	31	69	21	79	12	88	9	91	4	96	2	98	1	99	1	99
40	60	26	74	23	77	14	86	6	94	3	97	3	97	0	100	2	98	1	99
38	62	9	91	13	87	15	85	7	93	4	96	2	98	2	98	2	98	0	100

Before

b)

Cr	Ni																		
92	8	89	12	89	11	85	15	69	31	49	51	43	57	36	64	30	70	24	76
89	11	88	12	82	18	67	33	61	39	52	48	39	61	33	67	23	77	21	79
90	10	86	14	81	19	72	28	53	47	42	58	30	70	26	74	23	77	18	82
93	7	81	19	72	28	65	35	48	52	61	39	26	74	23	77	17	83	14	86
84	16	83	17	70	30	57	43	44	56	29	71	23	76	17	83	14	86	11	90
83	17	74	26	64	36	45	55	36	64	25	75	18	82	13	87	11	89	8	92
69	31	70	30	57	43	39	61	28	72	20	80	14	86	9	91	6	94	5	95
75	25	59	41	47	53	33	67	21	79	13	87	10	90	7	93	7	93	4	96
60	40	50	50	36	64	25	75	15	85	8	92	4	96	5	95	6	94	3	97
45	55	33	67	28	72	19	81	12	88	7	93	5	95	4	96	2	98	2	98

After

Figure 5.2.2.1 *EDX data for Ni-Cr alloys 'heat treated' sample with percentage of Ni and Cr a) before experiment, b) after cyclic voltammograms and step experiment.*

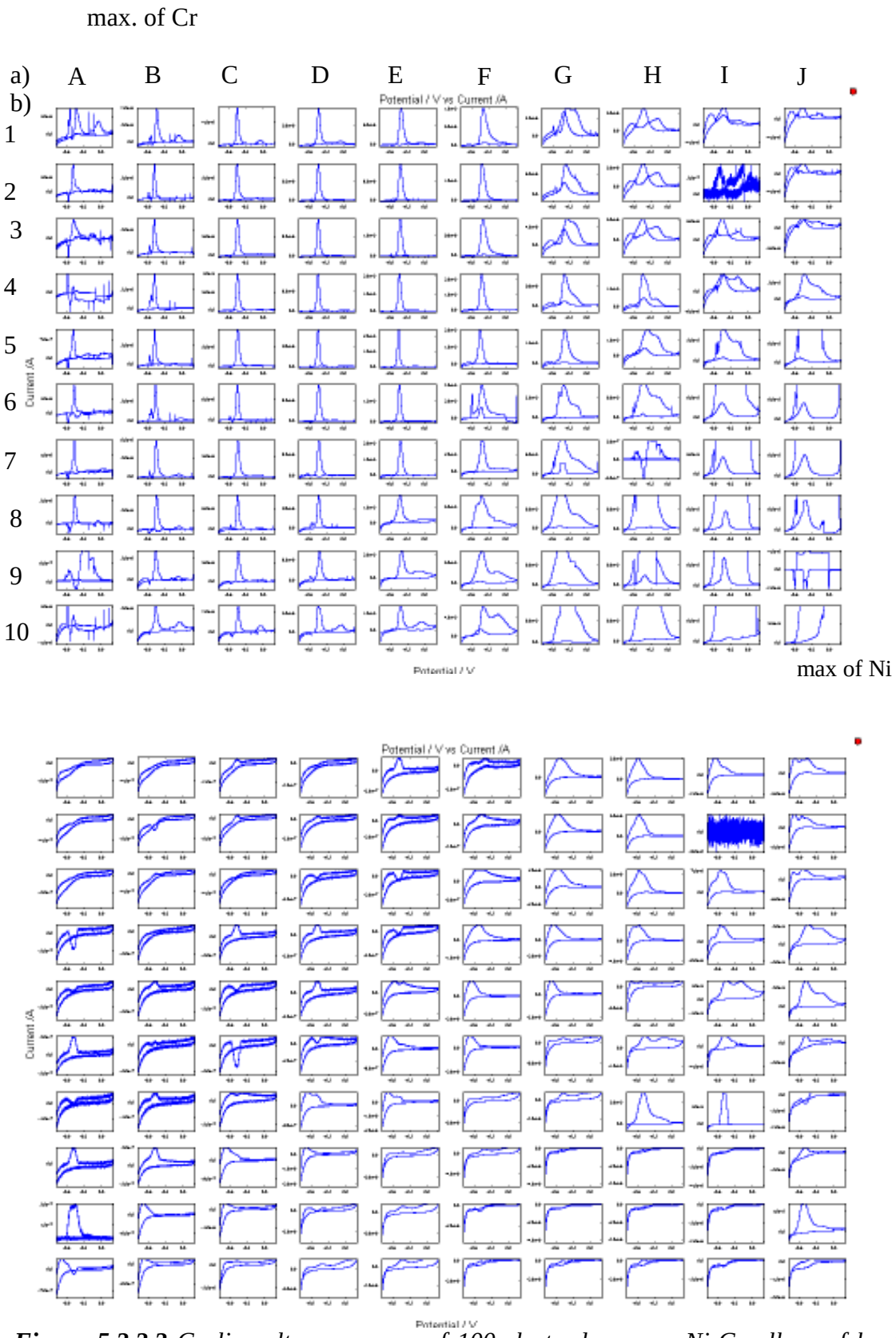

Figure 5.2.2.2 *Cyclic voltammograms of 100-electrodes array Ni-Cr alloys of heat treated sample in phosphoric acid pH 2 at 323 K for a) first scan, b) scan after step experiment. Potential scan rate 20 mV* s^{-1}.

Selected electrodes (figure 5.2.2.3) with different composition of Cr and Ni have been investigated: Ni79Cr21, Ni52Cr48, and Ni17Cr83. The voltammograms for the hest treated sample show some changes form the 'as deposited' sample. The Ni rich sample at the initial potential current gave a cathodic current characteristic for hydrogen evolution. Also on the forward scan the corrosion potential E_{corr} ~ - 680 mV has been found. The region close to the corrosion potential is characterised by R_p ~ 394 Ω cm^{-2}. A large anodic peak at – 410 mV corresponds to massive dissolution. In fact for this alloy composition second peak exists at - 180 mV with current density j ~ 3 mA cm^{-2}. The charge under the oxidation peaks equal Q ~ 400 mC cm^2. Then the passivation process takes place with the corrosion process continuing slowly on the reverse scan with a small anodic current. At the potential region from - 320 to - 600 mV corrosion is more active. The corrosion potential on the back scan equals - 620 mV, and is shifted to the more positive potential compared with the forward scan.

Ni52Cr48 is characterised with hydrogen evolution on the forward scan and the corrosion potential at E_{corr} ~ - 720 mV and R_p ~ 1375 Ω cm^{-2}. A sharp anodic peak has been noted at E_p ~ – 440 mV with maximum of the current density j_p ~ 3 mA cm^{-2} and the charge under the oxidation peak Q ~ 30 mC cm^{-2}. Then the passivation process occurs. During the potential range from - 350 to + 400 mV current density is very low. On the reverse scan E_{corr} has been found at ~ -70 mV, shifted to more positive potential compared with forward scan.

At the initial potential for Ni17Cr83 exists a hydrogen evolution current. On the forward scan the corrosion potential has been observed at E_{corr} ~ - 550 mV. The region close to the corrosion potential is characterised by resistance polarisation and equals R_p ~ 367 Ω cm^{-2}.

An anodic peak at – 460 mV with current density j_p ~ 0.9 mA cm^{-2} has a sharp shape. The charge under the oxidation peak equals ~ 10 mC cm^{-2}. Then the passivation process occurs. On the reverse scan there is a low current density and E_{corr} ~ - 110 mV.

All investigated alloys present an anodic peak. Also with increasing concentration of Cr in Ni- Cr alloys the peak position is shifted to more negative potential. The current density corresponds to the j_p decreasing with increasing % of Cr. Also, in fact, there is no trend for the resistance polarisation and surprisingly the alloy with concentration Ni52Cr48 presents high resistance. The corrosion potential for the reverse scans for

all investigated materials is shifted to the more positive potential. Compared with non-heat treated sample: (a) the peak position is shifted to the more positive potential, (b) the peaks occurs at much higher current density, (c) corrosion potential shifted to the more positive potential for the forward scan, while reverse scan presented the opposite trend.

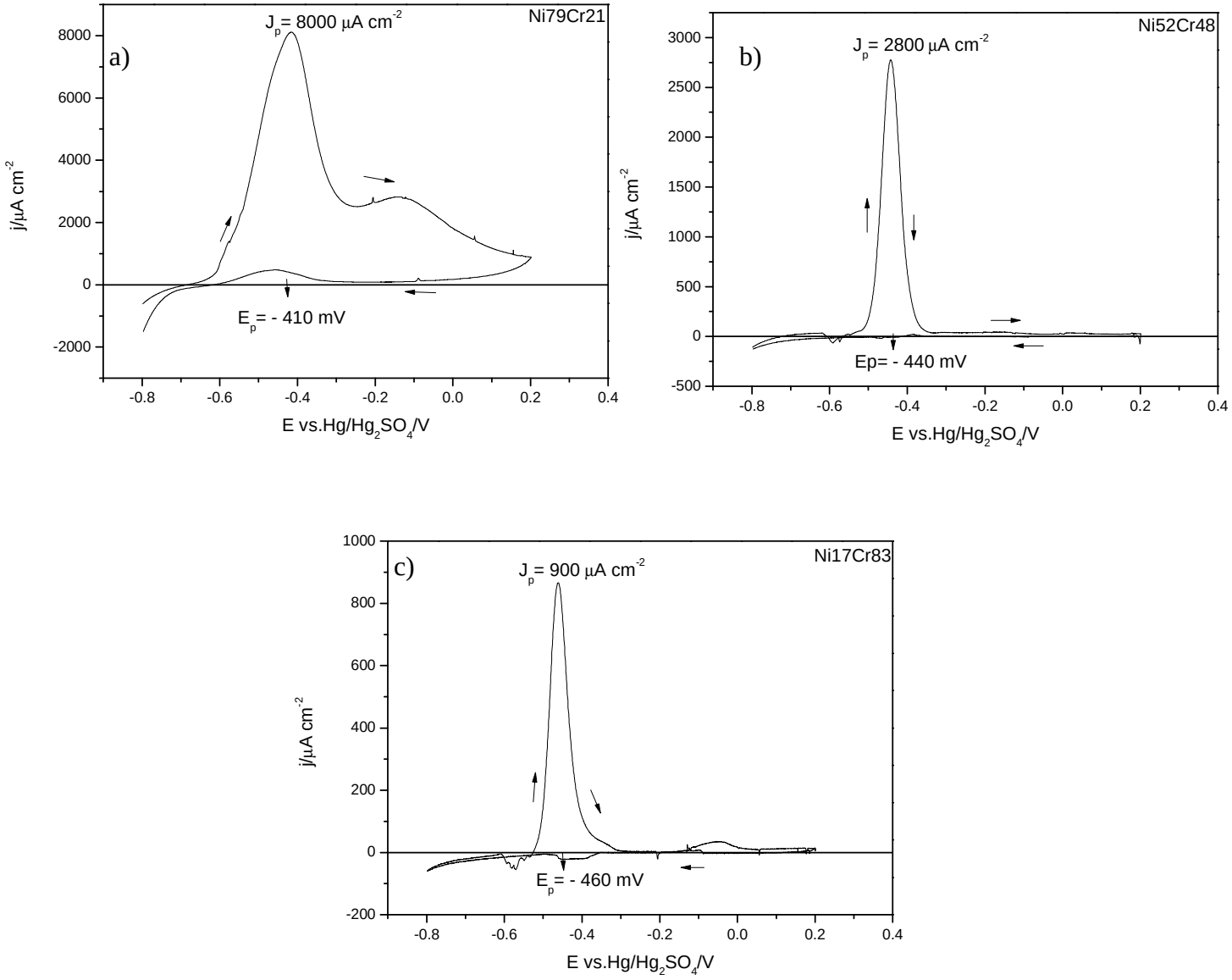

Figure 5.2.2.3 *Cyclic voltammograms of 'heat treated' sample for selected electrodes a) Ni79Cr21 (G4), b) Ni52Cr48 (C7) and c) Ni17Cr83 (C1) in phosphoric acid pH 2 at 323 K.*

On figure 5.2.2.4 has been collected results for cyclic voltammograms of selected electrodes after 10 minutes step experiment at a constant potential of + 100 mV (oxygen cathode region in fuel cell). For all cyclic voltammograms the current density

is much lower compared with first scans. With increasing the concentration of Cr in the composition of Ni-Cr alloys the current density of j_p decreases. As previously, the charge characteristic for the oxidation process decreases with the increasing % Cr. It is clearly to see that after the potential step experiment, the polarisation resistance is much higher, excluding Ni52Cr48.

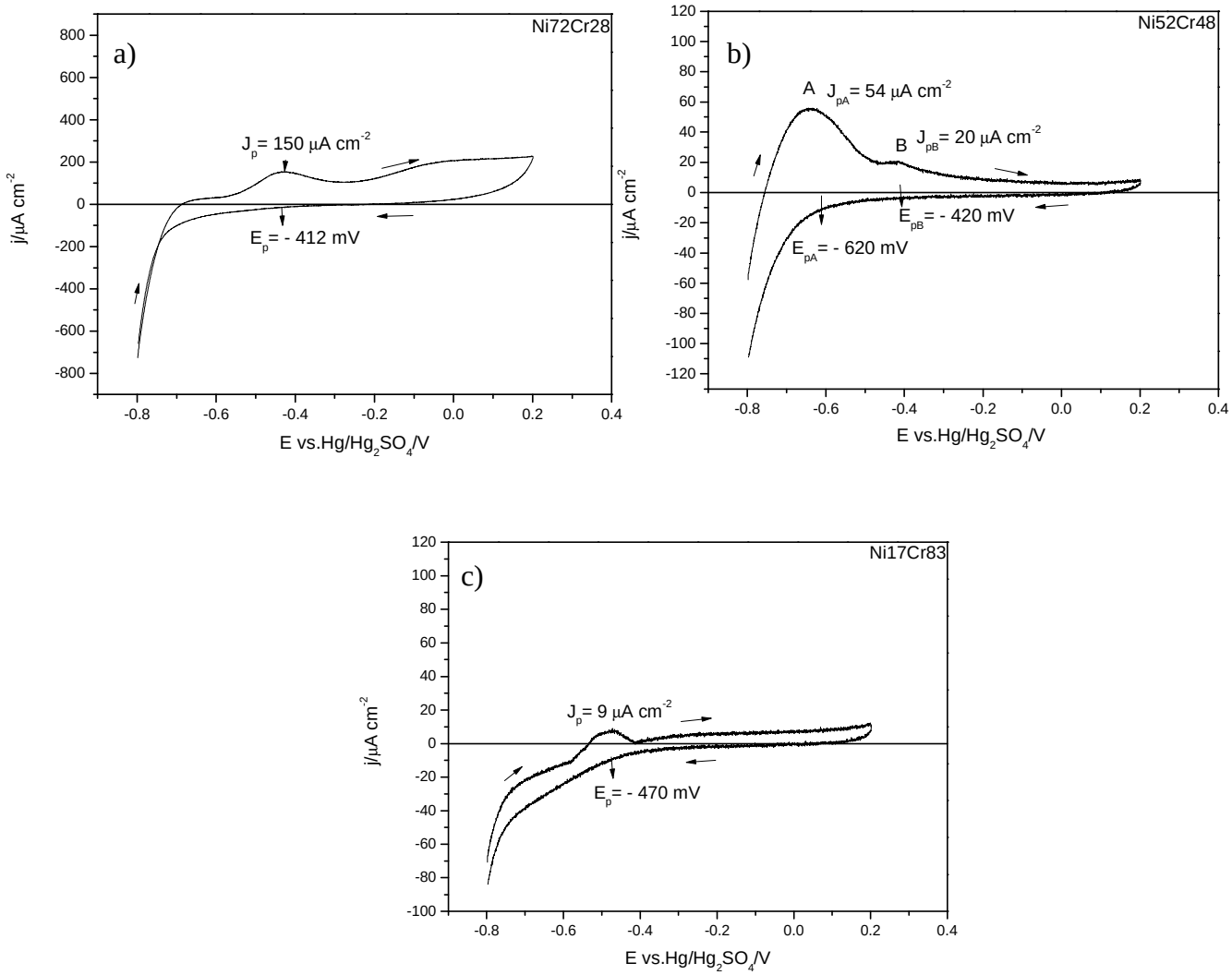

Figure 5.2.2.4 *Cyclic voltammograms of heat treated sample for selected electrodes a) Ni79Cr21 b) Ni52Cr48 c) Ni17Cr83, in phosphoric acid at 323 K.*

The differences of the charges under the oxidation peaks between the first and last scan can be explained by the formation of a corrosion film richer in Cr. Also there are changes to the surfaces. The apparent charge for higher Ni in Ni-Cr alloys (up to 10 %

of Cr) is very high and approximately is in the range between 140 – 40 mC cm^{-2} (figure 5.2.2.5).

From 10 – 95 % of Cr, the charge drops and this is comparable with trend presented on Figure 5.2.2.4. After step experiment (Figure 5.2.2.5b) the charges are much smaller and at the highest point equals 0.8 mC cm^{-2}. Part of high Ni content in Ni-Cr alloys is dissolved (marked on plot). It is a region between 0- 15 % of Cr.

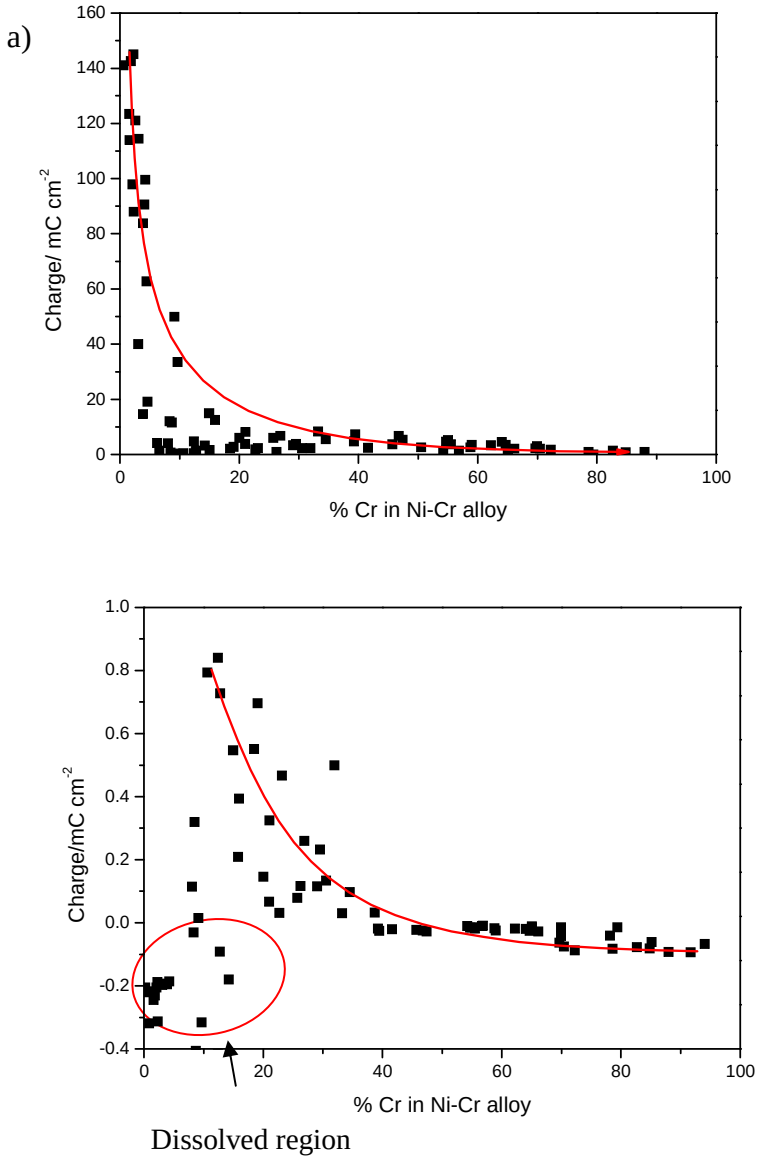

Figure 5.2.2.5 *Charge vs. % Cr in Ni-Cr alloys at condition for 'heat treated' sample a) first scans, b) last scans in phosphoric acid pH 2 at 323 K.*

Table 5.5 *Influence of Cr additions on surface condition of heat treated sample of Ni-Cr alloys deposited by PVD, in phosphoric acid pH 2 at 323K.z*

First CV-before exp.							**Second CV-after exp.**						
Alloy	**E_p/ mV**	**j_p/ µAcm^{-2}**	**E_{corr}/mV**		**Q_p/ mC cm^{-2}**	**R_p/ Ω cm^{-2}**	**Alloy**	**E_p/mV**	**j_p/ µA cm^{-2}**	**E_{corr}/ mV**		**Q_p / mC cm^{-2}**	**R_p/ Ω cm^{-2}**
			Forward	**Reverse**						**Forward**	**Reverse**		
Ni79Cr21	- 410	8000	- 680	- 620	400	394	Ni72Cr28	- 412	150	- 680	- 210	5	840
Ni52Cr48	- 440	2800	-720	-70	30	1375	Ni52Cr48	- 620 - 420	54 20	- 750	- 70	2	1014
Ni17Cr83	- 460	900	-550	-110	10	367	Ni17Cr83	- 470	9	- 530	- 66	0.1	3064

Table 5.6 presents results for Ni-Cr selected electrodes compared with commercial alloys.

As earlier noted for Ni rich Ni-Cr alloys the current density is much higher. In case of Ni-Cr alloy with composition Ni50Cr50 observed that for the commercial alloy current density is higher than Ni80Cr20 in both cases: foil and rod. While for deposited alloys noted opposite situation. Differences are affected of temperatures and the condition of production process.

Table 5.6 *Comparison of commercial materials and selected deposited on array in phosphoric acid pH 2.*

Alloy	**Current density / µA cm^{-2} j at 600 s**
Ni90Cr10 *(353 K)* rod	16
Ni80Cr20 *(353 K)* rod	1.8
Ni80Cr20 *(353 K)* foil	0.9
Ni50Cr50 *(353K)* rod	6
Ni96 Cr04 *(323K)* array	33
Ni88Cr12 *(323 K)* array	30
Ni45Cr55 *(323 K)* array	1.6

5.3 XRD studies of Ni-Cr deposited alloys

XRD spectra were used to characterise the phase structure for Ni-Cr alloys and Ni-Cr alloys deposited by PVD. The phase compositions of Ni-Cr alloys were determined by X-ray diffraction (XRD). Data were collected using a diffractometer, Siemens D5000 in a 2θ configuration. The X-ray source was a monochromatic copper radiation $K_{\alpha 1}$ (1.5406Å) passed directly onto a sample. The EDS analysis for this array was reported in figure 5.2.1.1 a. The scattered X-rays result in Bragg reflections was operating at wide angles 30 - 75 º (figure 5.3.1). The identification of Ni-Cr alloy and pure Ni and Cr phases were performed with the ICDD database and literature. Figure 5.3.1 presents XRD patterns for 100 electrodes of deposited Ni-Cr alloys.

max of Cr

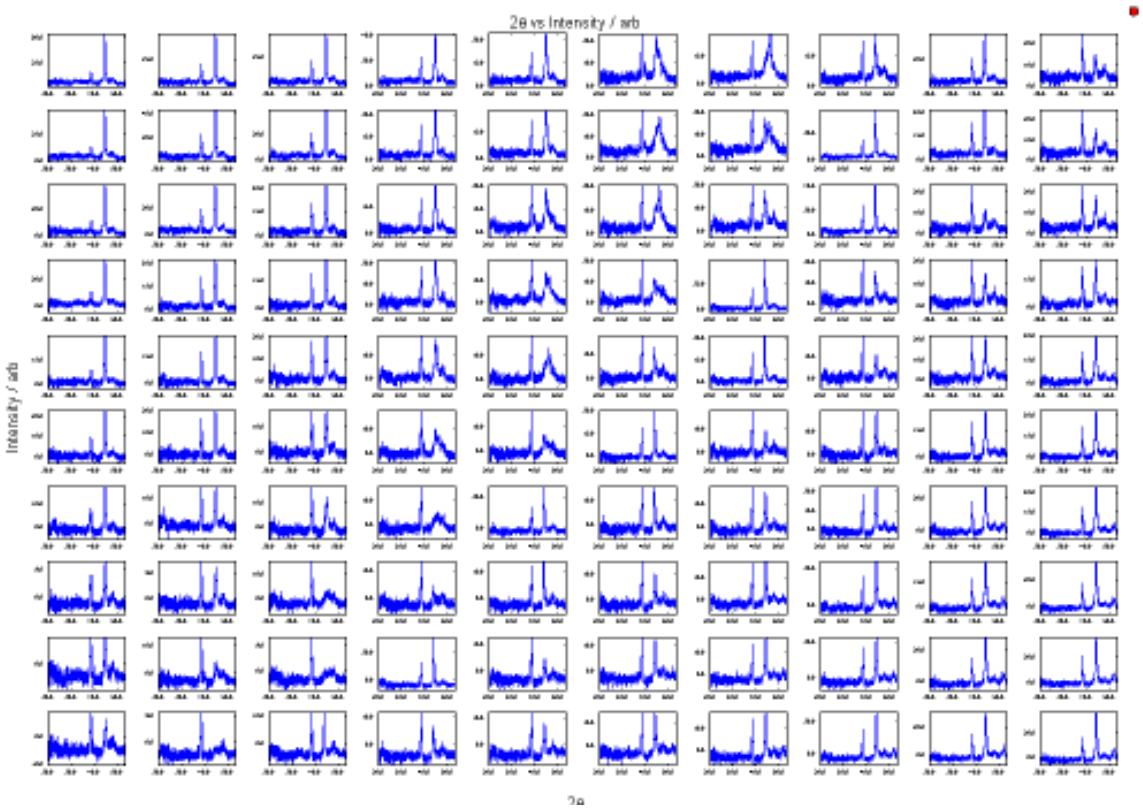

max of Ni

Figure 5.3.1 *XRD patterns for 100 – electrodes Ni-Cr alloys deposited.*

X-ray patterns for as deposited sample (figure 5.3.1) present a main peak at approximately ~ 44 - 45º, which strongly depends of the concentration of Cr in the lattice structure (γ- Ni f.c.c and α- Cr b.c.c). High Ni content Ni96Cr04 has been characterised by peak at ~ 44.5º Ni (111) with structure of f.c.c and a small peak at ~ 53º corresponds to Ni (200). Ni67Cr33 has only one peak at ~ 44º, but with very high intensity. With increasing concentration of Cr up to 50% in Ni50Cr50 alloy second peak has been noted at ~ 40º, what suggests that is probably a δ-phase with cubic structure. Ni47Cr53 has been described by two peaks: one at ~ 40º and second at 44º, while Ni38Cr62 has two peaks at 38º and 45º. Ni32Cr68 has three peaks 38º, 45º and 66º. Ni24Cr76 and Ni11Cr89 present similar behaviours two peaks at 44º and 65º. S. Vinayak and co-workers [6] concluded that for deposited sample of Ni50Cr50 alloy exist two peaks at ~ 43.45º described as tetragonal Cr_3Ni_2 and 74.49º called δ Ni-Cr cubic phase. Also the same authors [7-9] observed for Ni-Cr deposited alloys metastable σ-phase at the concentration range 50-70 % of Cr. The as deposited samples have been heat treated 523 K selected as a temperature where structural change will occur but the metals will not evaporate. In fact heat treatment changes the crystal structure only for ~ 50 % of Cr (not on the picture) and the most important thing is applying the right temperature. W. Pitschke [10] investigated the phase formation process for deposited layer of Ni-Cr alloy with concentration of Ni37Cr63. He concluded that with increasing temperature during annealing process lattice parameter increases. In fact observed [10-11] three steps of crystallization process, first at 673 K bcc structure formed for Cr rich alloys, second at 873 K and 923 K with crystallization of the metastable Ni-Cr phase (figure 5.3.2).

Table 5.7 presents characteristic peaks of Ni-Cr alloys for selected electrodes: Ni96Cr04, Ni67Cr33, Ni50Cr50, Ni47Cr53, Ni38Cr62, Ni32Cr68, Ni24Cr76, and Ni11Cr89.

The influence of temperature on structure changes has been shown in Table 5.8.

Table 5.7 *Data taken from the XRD patterns of Ni-Cr alloys deposited by PVD.*

Ni96Cr04/ 2θ	**Ni67Cr33/ 2θ**	**Ni50Cr50/ 2θ**	**Ni47Cr53/ 2θ**	**Ni38Cr62/ 2θ**	**Ni32Cr68/ 2θ**	**Ni24Cr76/ 2θ**	**Ni11Cr89/ 2θ**
-	-	-	-	38	38	-	-
-	-	40	40	-	-	-	-
	44	44	44	-	-	44	44
44.5	-	-	-	-	-	-	-
-	-	-	-	45	45	-	-
53	-	-	-	-	-	-	-
-	-	-	-	-	-	65	65
-	-	-	-	-	66	-	-

Table 5.8 *Influence of temperature on structure changes* [6].

Alloy	**As deposited**	**Heat Treated 2 h at ~ 525K**	**Heat Treated 3 h at ~ 625 K**
Ni80Cr20	Structure f.c.c	f.c.c and γ NiCr at ~76º	f.c.c and γ NiCr at ~75º
Ni50Cr50	Cr_3Ni_2~ 43 º δ NiCr 74º	Cr_3Ni_2~ 43.58 º δ NiCr 74.53 º	Cr_3Ni_2~ 43.67 º δ NiCr 74.80 º
Ni40Cr60	Cr_3Ni_2 44.13 º Cr_3Ni_2 65.8 º δ NiCr 74.86º	Cr_3Ni_2 44.36 º Cr_3Ni_2 65.67 º δ NiCr 74.68º	Cr_3Ni_2 44.63 º Cr_3Ni_2 64.88 º δ NiCr 74.33º

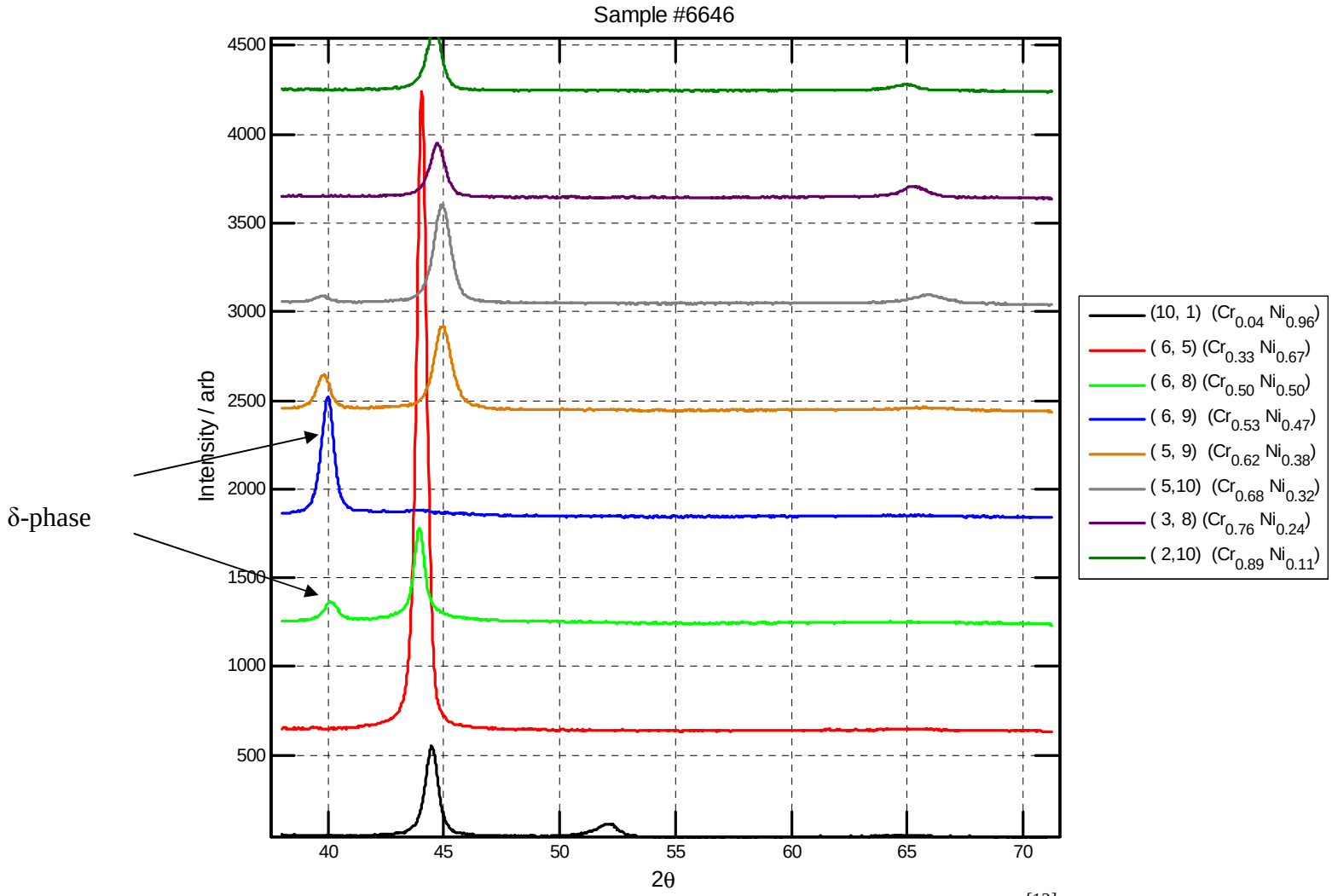

Figure 5.3.2 *XRD patterns of Ni-Cr alloys deposited by PVD for 'as deposited' sample- T. Aljohani* [12]

For both as deposited and heat treated samples it was observed that the peak position for 10 - 45 % Cr in Ni-Cr alloy is shifting to lower angle range but from 45 % until 60 % of the Cr peak shifts to a higher 2θ. For 65 % - 95 % (figure 5.3.3), the shift is again reversed.

a)

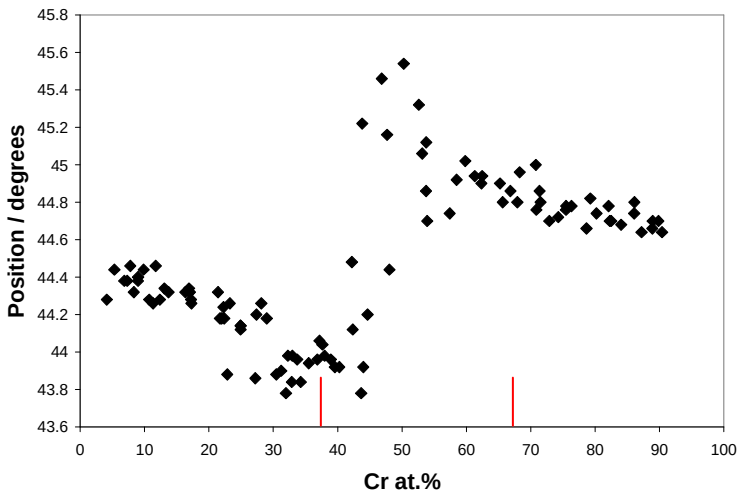

b)

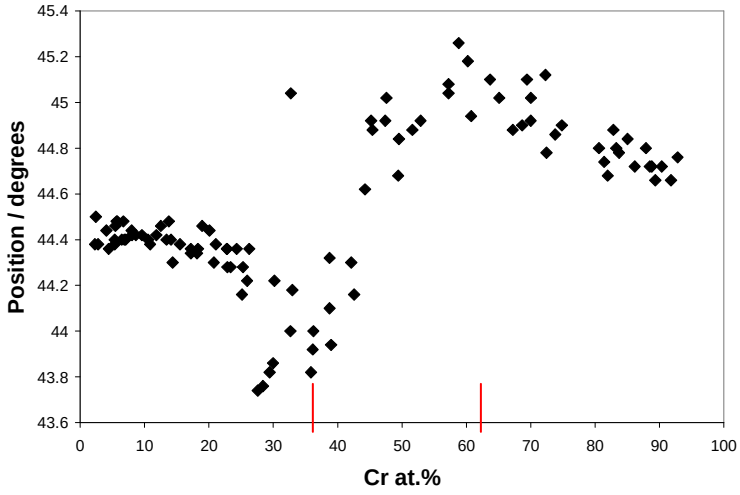

Figure 5.3.3 *Position degree of the main peak vs. Cr % for a) as deposited b) heat treated Ni-Cr alloys.*

Phase formation can be investigate with the equilibrium phases diagram, which recommend two phases started at approximately with 50% of Cr in Ni-Cr alloy (figure 5.3.4). Phase formation strongly depends on the annealing temperature- figure 5.3.5.

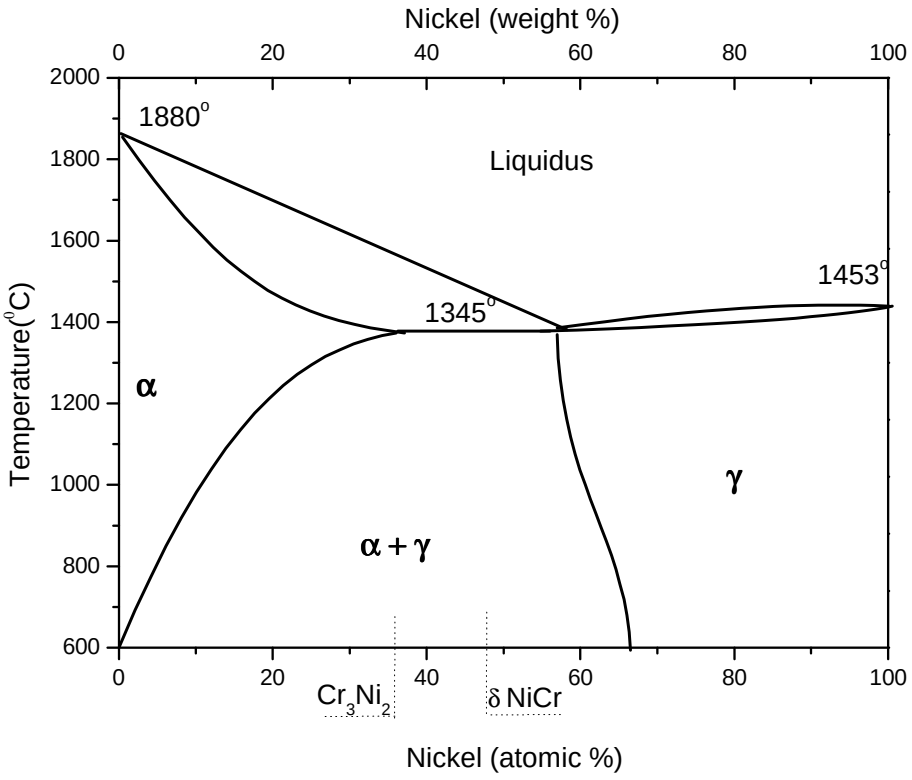

Figure 5.3.4 *Phases in the equilibrium phase diagram* [6, 13].

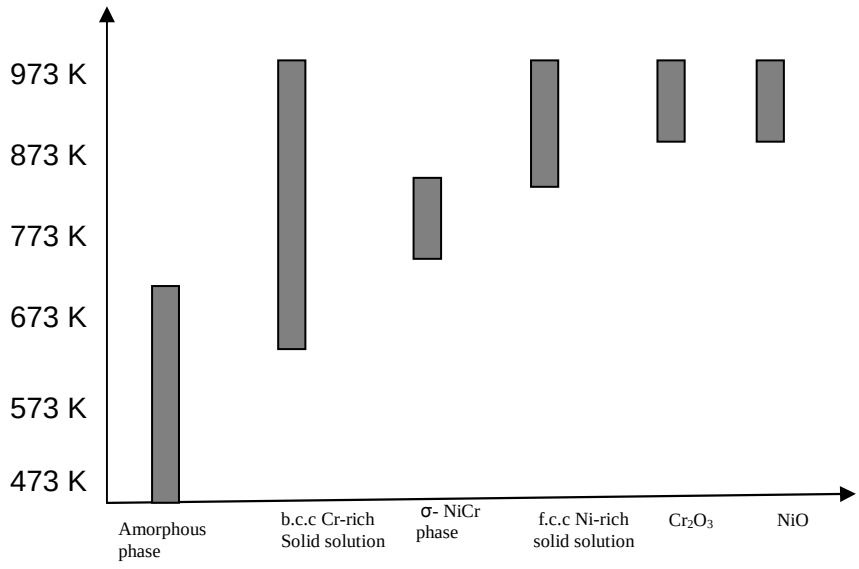

Figure 5.3.5 *Influence of temperature on phase formation* [10].

5.4 Conclusions

The corrosion behaviour studies of Ni-Cr alloys for ‘as deposited’ and ‘heat treated’ samples deposited by PVD method in phosphoric acid pH 2 allow the following conclusions:

- Modified surfaces prepared by PVD and heat treatments are showing promise. This method gives possibility to check different compositions at the same time, in the same conditions, but deposits not necessarily same structure as bulk.
- The corrosion potential is shifted to more positive potentials with increasing % Cr in the Ni-Cr alloys.
- The surfaces of the Ni - Cr alloys in both cases ‘as deposited’ and heat treated samples, passivated easier and faster with increasing % Cr in the Ni-Cr alloys.

  Also Ni-Cr alloys corrode much more slowly than pure Ni at the condition for the fuel cell cathode (+ 100 mV). Also observed that Ni50Cr50 deposited presents good results and better resistance to corrosion than Ni80Cr20, as reported in Chapter 4 the opposite trend was observed for the commercial materials. This indicating that the formation of the δ-phase observed for the PVD is important in finding the best corrosion protection.

5.5 References

[1] S. Guerin, B. E. Hayden, D. C. A.Smith *J. Phys. Chem*. B 2006, **110**, 14355-14362.
[2] S. Guerin, B. E. Hayden *J.Comb.Chem*.2006, **8**, 66-73.
[3] B. E. Hayden, D. Pletcher, J-P. Suchland, L. J. Williams *Physical Chemistry Chemical Physics* 2009, **11,** 9141-9148.
[4] S. Guerin, B. E. Hayden, C. E. Lee, C. Mormiche, J. R. Owen, A. E. Russell, *J. Comb. Chem*. 2004, **6**, 149-158.
[5] W. D. Callister Jr. *Materials Science and Engineering an Introduction,* 7th edition, John Wiley and Sons, 2007, USA.
[6] S. Vinayak, H. P. Vyas, V. D. Vankar, *Thin Solid Films*, **515** (2007) 7109.
[7] M. B. Vollaro, D. I. Potter, *Thin Solid Films* **239** (1994) 37-46.
[8] P. Mengucci, M. Costato, G. Majni, *Thin Solid Films* **209** (1992) 67-72.
[9] M. Danismand, N. Cansever, *Journal of Alloys and Compounds s* **493** (2010) 649-543.
[10] W. Pitchke, W. Brùkner *J. Anal. Chem.* (1998) **361**:608-609.
[11] M. I. Birjega , M. Alexe, *Thin Solid Films* **275** (1996) 152-154.
[12] T. Aljohani '*Combinatorial corrosion screening of novel thin film alloys prepared by high-throughput physical vapour deposition method'*.
[13] D. R. F West, N. Saunders *Ternary Phase Diagrams in Material Science,* 3rd edition, Maney Material Science, London 2002.

Chapter 6

Conclusions

The objective of this project was to investigate the corrosion of materials that could be used for bipolar plates in fuel cells based on a poly(benzimidazole) membrane filled with H_3PO_4. In addition to mild steel, stainless steel, nickel, electroplated Ni and Ni/graphite the focus was on Ni-Cr alloys and the influence of composition on the rate of corrosion.

The graphite in the nickel layer was designed to lower the contact resistance between the bipolar plate and the electrocatalyst layers of a MEA. The medium chosen was phosphoric acid pH 2 at 353 K and a potential of + 100 mV was considered in order to mimic, the conditions at an oxygen cathode in a fuel cell.

Pure metals were tested and it was found that the corrosion rate decreased along the series of Fe > Ni > Cr. Ni and Fe gave relatively high current densities at + 100 mV with a poor passivation film, making them unsuitable for application in a fuel cell stack. In contrast, Cr gives only a very low current density probably because of the pre-existence of a highly protective passivating film. The steels were also quantified. Stainless steel is characterised by very low current density but mild steel corrodes rapidly, confirming the need for a protective coating if it is to be used in a fuel cell. In fact, the electrodeposition of a thin layer of Ni is enough to cover and reduce the corrosion rate of the mild steel but not to the extent essential for practical application in the fuel cell. Hence, the interest in NiCr alloys since Cr itself has a high contact resistance. In a parallel project, the electroplated Ni layer was modified by addition graphite with different loading of graphite particles and the project foresaw the modification of the Ni/graphite layer with Cr. The modification with Cr was never achieved but it was shown that the Ni/C layer with loading of 40 g/dm^3 graphite had a similar corrosion rate to the Ni deposited on mild steel.

Since the overall project required the deposition of Ni and Ni/graphite layers onto mild steel, a procedure to access the quality of the deposit was required. AC impedance carried out in 1 M H_2SO_4 at 293 K temperature proved an appropriate procedure. The mild steel and the electroplated layers gave impedance plots with well formed semi-circles and the corrosion resistances were easily read from the data. With electroplated layers > 3 μm, the corrosion resistance was similar to bulk nickel. Very thin layers, < 1 μm, gave corrosion resistances less than mild steel showing the existence of pits and pitting corrosion.

The impedance procedure is a quick and reliable way to check for complete layers but it cannot be described as non-destructive as repeated impedance scans showed a decrease in corrosion resistance.

The corrosion of NiCr alloys has been investigated in two ways. The first used bulk, commercial alloys. The second was more innovative. The high throughput technique developed by Hayden and co-workers [1-3] for the optimisation of electrocatalyst composition has been extended to the study of corrosion. The procedure involves the application of the 'wedge' technique during physical vapour deposition to deposit alloys with variable but controlled compositions over an array of 10x10 gold micropads and the simultaneous recording of voltammograms for each of the 100 Ni/Cr ratios [2]. Software to rapidly determine composition (by EDX) and structure (by XRD) of each of the alloys in the 10 x 10 array allows the influence of structure as well as composition to be defined. The structure of the layers can be changed by an appropriate heat treatment and in this work, the as deposited alloys were modified by heat treatment at 523 K under Ar/5%H_2 atmosphere. The high throughput array method is excellent for defining the trends in corrosion rates with, for example, the Cr content of the alloys. For the study of corrosion, however, the approach does have drawbacks.

(i) It is not possible to polish or otherwise prepare the surfaces of the alloys in the array. A single potential scan can lead to the oxidation of a substantial fraction of the layer deposited by PVD, typically < 250 nm. Hence, each array may be limited to a single electrochemical experiment. Certainly in this work, it was clear that Ni and very low Cr content were completely dissolved in a single scan to + 100 mV, the potential wanted for most of the electrodes in the array – the charge density was that required to remove all the Ni and the gold pad beneath the coating was visible. The arrays are expensive to prepare and, certainly it is not possible to check reproducibility of the voltammetry in the same way as is possible at bulk electrodes.

(ii) The experiments at each array electrode may not be the optimum for its composition. For example, the corrosion potential may vary by several hundred millivolts over the compositions of the array. However, the same potential range (and potential scan rate) must be applied to all 100 electrodes in the array. It can be difficult to select the potential range so that the important features are included for all electrodes. Also, the potential range at the NiCr alloy array

inevitably includes H_2 evolution at some electrodes at this could also change the surfaces of these electrodes.

(iii) As shown from the Ni/20Cr rod and foil bulk samples, the structure, as well as composition, can have a large influence on the corrosion rate. The PVD deposition adds a further uncertainty about the structure.

Hence, the results from the high throughput procedure should always be viewed alongside results from bulk samples. In this work the trends and, indeed, the absolute values of corrosion rates showed good consistency.

Both types of sample, confirm that with increasing % Cr in the Ni-Cr alloy, the (open circuit) corrosion potential, $E_{corr,}$ is shifted to more positive potentials. This could result from an increase in the rate of proton reduction or a decrease in the rate of metal oxidation. The latter seems more likely. In all the voltammograms, the alloys gave lower anodic dissolution current densities than nickel, the anodic peak current density and charge density was diminished and the current densities at + 100 mV the alloys again gave lower current densities.

To summarise the results on the influence of the Cr content on the rate of corrosion, the results are further discussed in terms of the two different potentials, the open circuit corrosion potential and the potential of + 100 mV where passivation has occurred.

(a) The Open Circuit, Corrosion Potential

As noted above, E_{corr} shifts significantly positive with increase in the Cr content. With the bulk materials, the influence of Cr content on the corrosion resistance is complicated by the large difference in the values for the foil and rod with the composition Ni80Cr20. Even so, it is clear that the low Cr content alloys are, at most, marginally more corrosion resistant than the pure nickel. The data from the array experiments show that the corrosion resistance increases significantly above 50 % Cr, see figure 6.1. The heat treatment of the alloys had little influence on these conclusions.

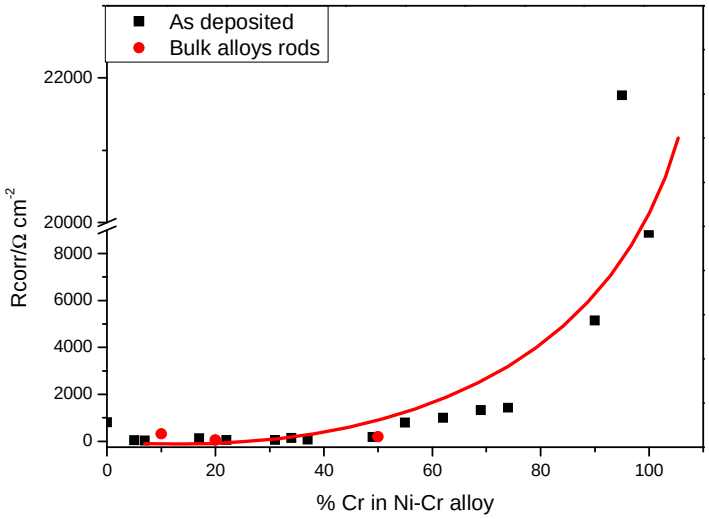

Figure 6.1 *Influence of % Cr in Ni-Cr alloy on open circuit corrosion rate.*

(b) Passivated surface

Once passivated, the rate of corrosion drops dramatically. In contrast to the behaviour at the corrosion potential, when the surfaces are passivated the NiCr alloys show much greater corrosion resistance than pure Ni. The 'steady state' current density at + 100 mV drops from 1000 µA cm^{-2} at Ni to < 0.3 µA cm^{-2} at the alloys. There is a big decrease in current density in going from Ni to Ni80Cr20 but there appears to be no advantage in taking the Cr content above 50 %, see figure 6.2. The trends after heat treatment are similar but the absolute values of the corrosion rates are lower.

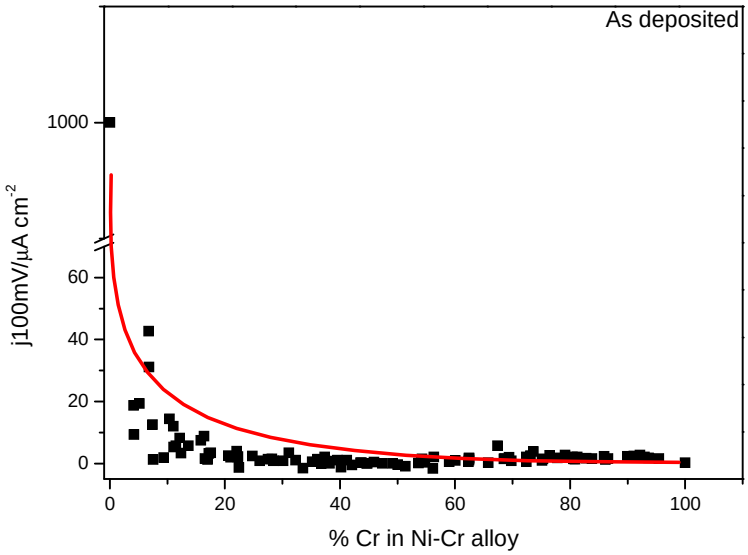

Figure 6.2 *Influence of % Cr on current density in the oxygen cathode conditions at +100 mV in phosphoric acid.*

6.1 References

[1] S. Guerin, B. E. Hayden, D. C. A.Smith *J. Phys. Chem*. B 2006, **110**, 14355-14362.
[2] S. Guerin, B. E. Hayden *J.Comb.Chem*.2006, **8**, 66-73.
[3] B. E. Hayden, D. Pletcher, J-P. Suchland, L. J. Williams *Physical Chemistry Chemical Physics* 2009, **11,** 9141-9148.